MORPHOMETRIC ANALYSIS OF HIPPOCAMPAL SUBFIELDS

A Dissertation

Submitted to the Faculty

of

Purdue University

by

Shan Cong

In Partial Fulfillment of the

Requirements for the Degree

of

Doctor of Philosophy

December 2019

Purdue University

West Lafayette, Indiana

THE PURDUE UNIVERSITY GRADUATE SCHOOL
STATEMENT OF DISSERTATION APPROVAL

Dr. Maher Rizkalla, Co-Chair

Department of Electrical and Computer Engineering, IUPUI

Dr. Edward J. Delp, Co-Chair

School of Electrical and Computer Engineering, Purdue University

Dr. Li Shen

Perelman School of Medicine, University of Pennsylvania

Dr. Paul Salama

Department of Electrical and Computer Engineering, IUPUI

Dr. Zhongming Liu

School of Electrical and Computer Engineering, Purdue University

Approved by:

Dr. Dimitrios Peroulis

Head of The Graduate Program

This dissertation is dedicated to my beloved parents Xiang Li and Xubo Cong.

For their endless love, support, and encouragement.

ACKNOWLEDGMENTS

Special thanks to my advisor Dr. Li Shen from the Department of Biostatistics, Epidemiology and Informatics, Perelman School of Medicine, University of Pennsylvania for his constant support to my studies and research work.

I would like to express my appreciations to my committee chairs Dr. Rizkalla and Dr. Delp, I also feel appreciated to my advisors Dr. Salama and Dr. Liu for their guidance.

Thanks to my research collaborators Mark Inlow for his theoretical support on statistical analyses, Shannon L. Risacher and Long Xie for providing pre-processed experimental data, John D. West for providing technical supports. Thanks to Yu-Chien Wu, Liana Apostolova, Eileen Tallman and Andrew J. Saykin for their valuable advice.

I also want to thank my lab mates: Jingwen Yan, Danai Chasioti, Zhi Huang, Linhui Xie, Huang Li, Kefei Liu for their encouragement and help.

Last but not least, I would specially thank my fiancée Xiaohui Yao. Thank you for giving me the chance to spend my rest of life with you, and thank you for your support and encouragement.

TABLE OF CONTENTS

Page

Page

LIST OF TABLES

LIST OF FIGURES

SYMBOLS

$\angle$	Angle
Ψ	A mapping function
$*$	Convolution
γ	Hidden transformation
Δ	Laplacian operator
Reg	Regularization term
Γ	Spatial transformation
TS^2	Tangent space
v	Velocity
$\circ$	Vector composition

ABBREVIATIONS

AD	Alzheimer's Disease
ADNI	Alzheimer's Disease Neuroimaging Initiative
ASHS	Automatic segmentation of hippocampal subfields
BA	Brodmann areas
CA	Cornu ammonis
Comb	Combined
CS	Collateral sulcus
DG	Dentate gyrus
DSC	Dice similarity coefficient
Diff-like	Diffusion-like
EMCI	Early mild cognitive impairment
ERC	Entorhinal cortex
FOE	First order ellipsoid
FIRST	Functional magnetic resonance imaging of the brains integrated registration and segmentation tool
HC	Health control
HE	Harmonic energy
Hippo	Hippocampus
IADC	Indiana Alzheimer Disease Center
ICCs	Intraclass correlation coefficients
LMCI	Late mild cognitive impairment
LM	Levenberg Marquardt
MRI	Magnetic resonance imaging
Momen SD	Momentum-based spherical demons

MTL	Medial temporal lobe
ROI	Region of interest
RMSE	Root mean square error
SBM	Surface-based morphometry
SD	Spherical demons
SPHARM	Spherical harmonics
SNP	Single nucleotide polymorphism
Symm SD	Symmetric spherical demons
SUB	Subiculum
T	Tesla
T-maps	Maps of t statistics
VBM	Voxel-based morphometry

ABSTRACT

Cong, Shan Ph.D., Purdue University, December 2019. Morphometric Analysis of Hippocampal Subfields. Major Professors: Maher Rizkalla, Edward J. Delp.

Alzheimer's disease (AD) is an irreversible neurodegenerative brain disease distinguished by progressive impairment of memory and decline in cognitive abilities. The hippocampus is widely recognized to play essential roles in forming and gradually transferring information from short-term memory into long-term memory, and it is involved in the onset of the neuropathological pathways of the brain to suffer neuron loss in the rise of AD. Thus, hippocampal information obtained from magnetic resonance imaging (MRI) scans have been established as crucial AD biomarkers. The hippocampus is composed of multiple subfields, and the neuron loss is not uniformly distributed on the whole hippocampus. However, this critical subfield information is not addressed by the existing surface-based morphometry (SBM) and voxel-based morphometry (VBM) studies. Due to the size, complexity, heterogeneity, and folding anatomy of the hippocampus, acquiring volumetric and morphometric measures of hippocampal subfields usually presents not only technical challenges in quantitative neuroimaging but also analytical challenges. To address these challenges and deeply understand the relationships between hippocampal shape changes and brain disorders, especially to examine the degeneration of hippocampal subfields, this thesis focuses on constructing a hippocampal subfield morphometric analysis framework including the following aspects: 1) hippocampal subfield segmentation; 2) 3D shape modeling; 3) feature formulation; 4) diffeomorphic surface registration; 5) surface shape reconstruction; and 6) association analytics. The goals include developing ac-

curate hippocampal subfield guided registration methods, extracting useful features and identifying significant subfields on the hippocampus that are highly related to cognitive disabilities, and using such information to assist early detection of AD.

1. INTRODUCTION

1.1 Background and Motivation

Alzheimer's disease (AD) is an irreversible neurodegenerative brain disease distinguished by progressive impairment of memory and decline in cognitive abilities. Patients with AD experience difficulty in memory, language, learning, problem-solving, and other cognitive abilities, which can profoundly affect their daily lives. These problems occur due to the damage or loss of nerve cells (neurons), which are involved and associated with cognitive functions, including those that allow a person to carry out fundamental bodily behaviors such as walking, vocal expression and swallowing. Patients in the final stages of the illness are bed-ridden or chair-bound and require around-the-clock care. AD is ultimately fatal, and there is currently no cure to slow or stop the damage and destruction of neurons caused by AD. As summarized in Figure 1.1, which is based on the statistics from the 2019 Alzheimers disease facts and figures [1], AD is the 6th leading cause of death in United States. Currently there are more than 5 million Americans living with Alzheimer's, and one thirds of seniors die with Alzheimer's or another dementia. In addition, this disease will cost the nation 290 billion in 2019. As the most common type of age-related dementia, AD is widely studied using neuroimaging approaches with particular emphasis on critical memory structures.

The hippocampus is a complex brain subcortical structure embedded deeply into the temporal lobe. It is widely recognized to play essential roles in forming and gradually transferring information from short-term memory into long-term memory, and it is involved with the neuropathological pathways of the brain that suffer various cognitive impairment diseases such as AD. Hippocampal information can be obtained with magnetic resonance imaging (MRI, Figure 1.2) techniques such as structural

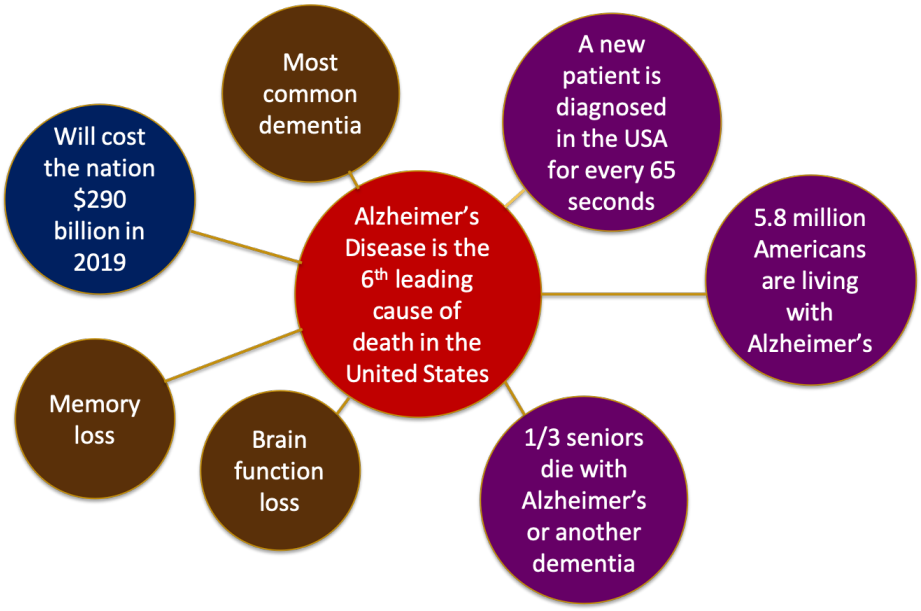

Fig. 1.1.: A summary of the statistics from 2019 Alzheimer's disease facts and figures.

MRI and functional MRI, and it has been widely studied in neuroimaging analysis given the value of hippocampus in cognition and memory. The structural changes of hippocampus observed from MRI scans are found to be sensitive/indicative to the progression of dementia, which makes it as a potential biomarker to detect brain disorders such as AD, mild cognitive impairment (MCI) which is a prodromal stage of AD [2], epilepsy [3, 4], and schizophrenia [5]. Thus, the hippocampus is widely analyzed to discover the status of AD or MCI [6–9] and to infer cognitive status [10]. Furthermore, hippocampal volumetry and morphometry have been employed to detect the presence and progression of cognitive disorders in quantitative neuroimaging [11,12]. However, the complex and heterogeneous folding anatomy of the hippocampus usually present challenges in neuroimaging studies.

The hippocampus is composed of multiple subfields [13], and neuron loss is not uniformly distributed on the whole hippocampus [14]. Many hippocampal studies have indicated that subfields play an essential role in brain functions, e.g., the cornu ammonis 1 (CA1) is selectively more vulnerable and related to autobiographical mem-

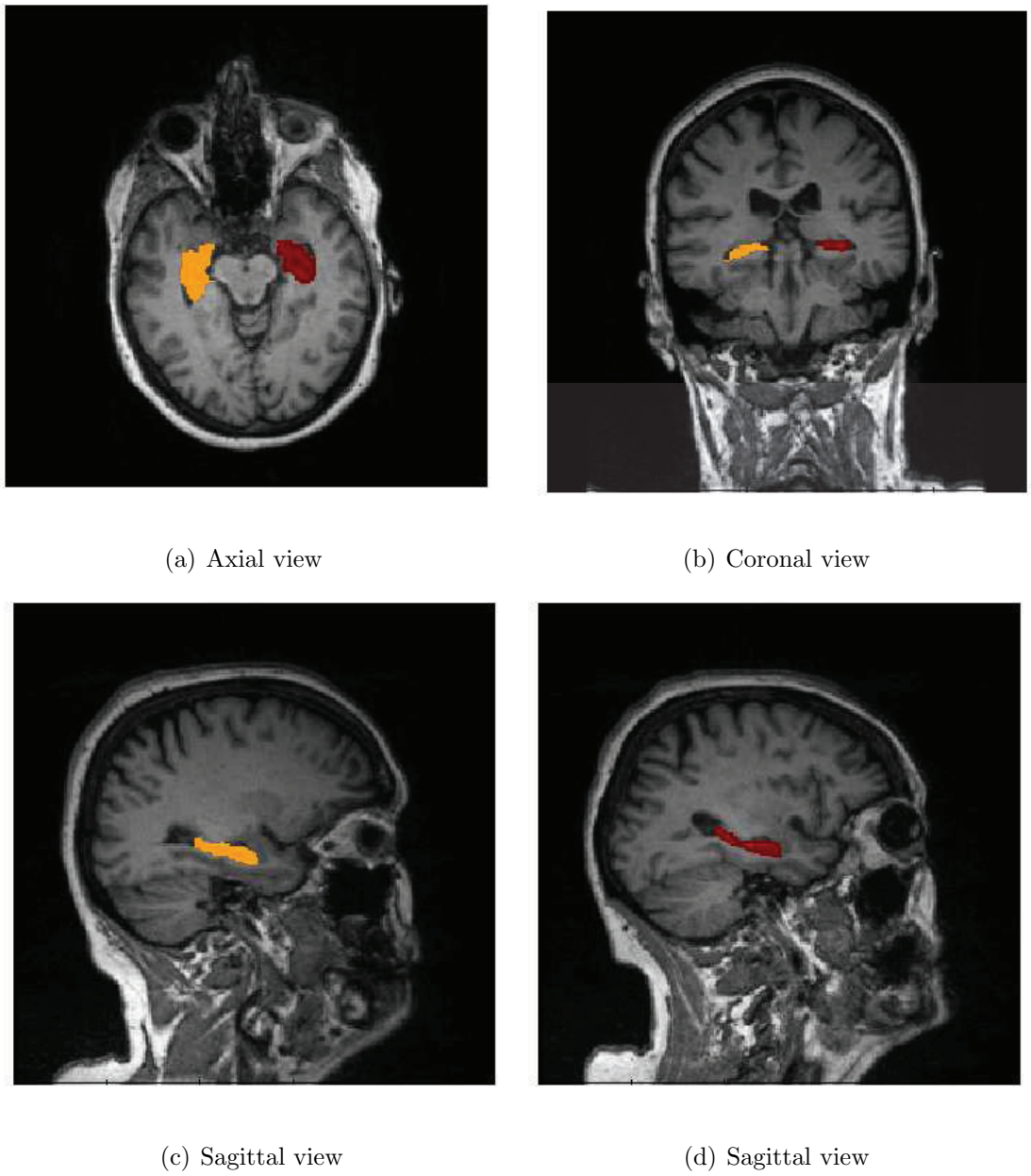

(a) Axial view

(b) Coronal view

(c) Sagittal view

(d) Sagittal view

Fig. 1.2.: MRI scan with highlighted left (brown) and right (red) hippocampi.

ory retrieval [15], CA3 and dentate gyrus (DG) are involved in memory encoding and early retrieval [13], and the subiculum and CA1 are predominantly affected in AD patients [16]. However, this critical subfield information is typically not addressed by the existing surface-based morphometry (SBM) and voxel-based morphometry

(VBM) studies [7,10]. Due to the size, complexity, heterogeneity, and folding anatomy of the hippocampus, acquiring detailed volumetric and morphometric measures of hippocampal subfields usually presents not only technical challenges in quantitative neuroimaging but also analytical challenges.

Currently, the most popular and widely used strategy for morphometric analysis is volumetric analysis [17–20]. Since volume-based analysis can take the input directly from the output of segmentation techniques, it is a convenient and efficient way to conduct shape analyses. However, volumetric analyses only utilize hippocampal volume measurements whereas detailed shape changes such as local deformation are ignored in volumetric studies. Thus, volumetric analyses are not able to locate the areas with most severe atrophy and cannot evaluate how severe the atrophy is for a local region. To overcome this problem and conduct detailed hippocampal shape analyses, surface-based analyses are adopted in this thesis. A surface-based representation provides the capability of capturing detailed shape information, which can be composed of geometric information such as curvatures and thickness, as well as additional surface signals such as segmented labels and landmarks. These surface features are helpful in localizing clinical biomarkers on the surface, which is typically ignored in volumetric studies.

The major challenges and goals in this thesis are summarized as follows:

1) The creation of a reference (atlas) to enable group shape analyses and group comparisons. The framework for generating a surface atlas is comprised of two major steps: segmentation and 3D surface shape modeling. Segmentation is needed to extract the hippocampal regions of interest, and surface shape modeling is used to generate 3D surface models. In addition, a 3D model of the surface atlas allows visual inspection of the hippocampal sub-regions.

2) As mentioned earlier, common volumetric analyses take the whole hippocampal volume as the only measurement while ignoring local changes in shape. Thus, the second goal of this study is to conduct surface-based analyses that can clearly indicate where the atrophy is, and how severe it is.

3) Important hippocampal subfields are not only ignored in most existing hippocampal shape analyses, but also in shape modeling where most studies ignore subfield measurements during the process of surface registration. With the goal of achieving better alignment locally on hippocampal subfields, a surface registration strategy is developed in this study.

4) The fourth challenge is to determine surface information, which typically characterizes the local or global shape, and organize the extracted information into a representation of the surface. A properly defined representation of surface features is capable of describing hippocampal subfield information and ultimately guiding registration.

5) The fifth challenge is that existing surface registration methods are yet to be fully explored. In this study we propose a new surface registration method and design experiments to compare the registration results.

Another goal of this thesis is to understand the relationships between hippocampal shape changes and brain disorders, especially the degeneration of hippocampal subfields, through hippocampal surface shape analyses such that the correlations between cognitive diseases and local deformation on hippocampal subfields can be revealed.

The framework of the analyses include the following components: 1) hippocampal subfield segmentation and 3D shape modeling; 2) surface registration; 3) surface shape reconstruction and building a surface atlas; and 4) morphometric analyses on hippocampal subfields. As a result, the expected outcomes of this study include:

1. Utilizing hippocampal subfield information to guide surface registration instead of solely using geometric information. Thus, a better alignment of subfields has to be achieved. In addition, subfield information is an excellent feature that can guide registration especially when the shape information is not complete due to the quality of MRI scans.

2. Creating a 3D surface atlas of the hippocampus through surface modeling and surface registration. In this case the deformation fields can be obtained by computing the distance from each individual surface to the atlas.

3. Building a framework for hippocampal morphometric analysis and identifying statistical significance of associations among hippocampal morphometry, diagnosis, and genetic information.

1.2 Related Work

Given the importance of subcortical structural changes such as the atrophy of the hippocampus in the progression of AD, there has been notably expanded interest in recent literature in examining the subfields of the hippocampal structure using magnetic resonance imaging (MRI). As mentioned earlier, shape analysis is widely used and contains several key steps such as segmentation, shape modeling, feature representation, shape registration and statistical group analysis. In this section, current hippocampal morphometric analyses are categorized and summarized based on these steps, and each step will be explained individually.

1.2.1 Hippocampus Segmentation

The task of segmentation is to extract a target region from raw MRI scans, and it is essential for any shape analyses. However, in our study the size, complexity, heterogeneity and complex folding anatomy of hippocampus present analytical challenges, and due to the low resolution of regular T1-weighted MRI images at 1.5T or 3T, the hippocampal subfield information is often hard to extract. Some existing studies [21–26] use manually delineated hippocampi or semi-automated segmentation [6,27,28] for their studies. Manual labeling often requires tedious work by professionals with extended processing time, and thus do not apply to large-scale datasets. One of the most popular methods for automated hippocampal subfield segmentation is presented in [29]. As a subroutine integrated in the latest FreeSurfer 6.0 [30], it has recently finished a major update that enables the possibility of handling either T1 or T2-weighted MRI images individually, or both T1 and T2-weighted MRI scans at the same time [30]. Another popular and validated method is Automatic Segmentation of

Hippocampal Subfields (ASHS) [9]. Compared to the previous method [29] employed in earlier versions (5.1 and 5.3) of Freesurfer, the new methods [30] and [9] the utilization of high-resolution T2-weighted MRI scans, makes these methods effective in evaluating particular hippocampal subfields as well as adjacent related cortices. The use of this automated hippocampal segmentation with high-resolution T2-weighted images may lead to better prognostic predictions and selections of treatment, and a fuller understanding of cognitive disorders [31]. Other automated segmentation methods and related work include multi-atlas and joint label fusion method [32, 33], patch-based label fusion [34], and anatomically-guided EM [35].

1.2.2 Shape Descriptors

After segmentation and before any morphological studies, a proper representation of data should be defined as they characterize local or global shape. The most direct and convenient way to represent shape is based on the segmentation result which is a 3D volume [17–20]. Another common representation for shape analyses is to generate 3D surfaces [36–38].

Volumetric studies only utilize hippocampal volume measurements whereas the detailed shape changes such as local deformation are ignored in volumetric studies. Thus, volumetric analyses are not able to locate the areas with most severe atrophy, also it cannot evaluate how severe the atrophy is for a local region. In this study, one of the goals is to conduct detailed hippocampal shape analyses. Thus, surface-based analysis is the main focus in this thesis. A surface represented shape can provide more informative features compared to volumetric studies, and these features among different subjects should be determined in the purposes of searching correspondences and measuring differences between a pair of subjects or a subject and image template. The surface features include but not limited to: 1) structural information such as points (vertex), lines, faces [39], 2) geodesic information such as radial distance (thickness), curvatures and manifolds [11, 40], 3) clustering information such as hip-

pocampal subfield distributions and surface or volumetric clustering [41], 4) spectral features obtained from eigenvalues of the Laplace-Beltrami operator [42, 43], and 5) landmark information based on prior knowledge [44].

For computational convenience, 3D surfaces sometimes are required to be parameterized and reconstructed. The popular surface parameterization methods include conformal mapping by holomorphic 1-forms [45] and spherical mapping using spherical harmonics [46, 47]. By applying the surface parameterization techniques, it introduces a common space across all objects, which makes registration easier to identify correspondences across the groups.

1.2.3 Image and Shape Registration

Since the goal is to investigate degeneration occurring on hippocampal subfields, a natural intuition is to investigate the deformation field between case group (patients) and control group (healthy people). In order to compute the deformation field between two 3D objects, we can use the feature information discussed in the earlier section 1.2.2 for image registration (alignment). A registration problem is a task of finding spatial correspondences for two or more images. To achieve this goal, a registration algorithm should apply a transformation on the source image to make it matches the target image locally or globally. Registration techniques are widely used in computer vision and medical imaging analyses, in order to numerically measure shape changes, all of the objects are required to be well aligned.

Image registration algorithms can be categorized in many ways. For example, when we consider the types of transformation, it can be classified into two major categories: linear rigid transformations and elastic (non-rigid or deformable) transformations. We can also categorize registration methods according to the types of feature correspondences including landmark-based registration and landmark-free registration. Registration problems can also be categorized based on the types of image

modalities such as surface registration and volumetric registration. As registration is a major component in this thesis, and for a better understanding on registration techniques, we further explain each category in the following paragraphs.

At first, we introduce the categories based on the types of transformations. The linear transformation is a wide category, it applies uniform mapping between or among objects including rotation, scaling, as well as other affine transforms. Since the linear transformations are global, this method cannot model local geometric differences between images [48, 49]. Elastic transformations are also known as non-rigid transformation or deformable transformation, which employs local warping that transforms a source image to align with the target image (template or reference image). Elastic transformations include radial basis functions [50], physical continuum models (viscous fluids) [45, 51], and large deformation models (diffeomorphisms) [37, 52].

The second way to categorize registration methods is based on the types of features. Usually, landmark-based registration requires some pre-knowledge of structural or functional features, and landmarks should be placed on objects in advance of the registration process. Studies such as [53, 54] take advantages of landmarks in shape analyses. Compared to landmark-based methods, landmark free registration strategies do not require any landmarks. The studies such as [37, 55] utilize geometric features and define a registration problem as an optimization problem. These studies try to resolve this optimization problem to minimize the differences between objects in either Euclidean space or non-Euclidean geometry aspect (such as Riemannian geometry), a smaller difference usually means a better correspondence between two objects.

Another way to categorize registration methods is based on image modalities. The most popular image modalities in medical imaging analyses are 2D medical imaging scans and 3D shape models. The common 2D medical imaging techniques include magnetic resonance imaging (MRI), functional MRI, computed tomography (CT), positron emission tomography (PET) and ultrasound. Registration methods usually extract imaging features from image intensities, a registration algorithm can handle

the image intensity directly [56,57] or reformulate these intensity features as geometric features [58,59], spectrum [60] or diffusion tensor [61,62]. It is common for a patient to have two or more different types medical imaging scans. Thus, there is a wide interest focusing on multi-modality registration by taking the mutual information [63–65].

3D shape models have two major branches: voxel-based shape modeling and surface-based shape modeling, both can be represented as polygon meshes. Surface registration methods [51, 66–69] usually extract morphological and topological measurements from anatomical structures such as the neocortex, and to redefine the complex correspondence searching problem into a surface matching scheme. Similar to 2D image registration, voxel-based registration [50, 70] usually extends the registration methods from 2D into 3D, it applies a 3D transformation to obtain a deformation or vector velocity field according to either voxel intensity or features derived from intensity information of raw image.

To compare surface-based registration and volumetric registration, some existing studies [71, 72] demonstrate that surface-based methods can achieve more accurate registration results in aligning highly complex folded human brain cortex. Because a higher quality of alignment leads to a better correspondence among objects, it results in getting functionally homologous regions across the groups. An obvious and direct benefit in aligning functionally homologous regions is that the results of group analyses show enhanced statistical power by identifying more sensitive biomarkers, this motivated us in exploring a registration strategy of aligning hippocampal surface based on subfield measurements as the functionality varies in each individual subfield. Conversely, volumetric registration aims to find correspondences across the whole brain instead of only considering the surface areas. Rather than ignoring, it embraces the interior information in searching correspondences. However, geometric information and folding patterns are typically not easily handled in volumetric registration studies.

1.2.4 Morphometric Analysis of Hippocampal Shape

Morphometric analyses are ready to perform after all of the objects are well aligned. As mentioned, the quality of registration can directly affect the power of statistical analysis. Statistical morphometric analysis is widely employed in biomedical imaging studies with the goal of understanding physiological structures and identifying pathological abnormalities associated with structural changes, demographics and diagnosis information. Zhang et al. [73] defined and extracted surface multivariate tensor-based morphometry and radial distance on each hippocampal surface vertex, they then applied Hotelling's T2 test in order to identify significant morphometric differences in both hippocampus and lateral ventricle between normal and clinically declining subjects. They found the left hemisphere was more severely affected than the right during the early stage of cognitive disease. Shi et al. [74] explored pathological abnormalities associated with genetics information, and showed that Apolipoprotein E (APOE) e4 carriers exhibited accelerated hippocampal atrophy using Hotelling's T2 test. They concluded meaningful morphological atrophy in APOE e4 carriers related to noncarriers in the whole cohort as well as in the nondemented (pooled MCI and HC) subjects, that affects the left hippocampus more than the right, and this conclusion was more pronounced in e4 homozygotes than heterozygotes . Gold et al. [75] employed volumetric and surface shape analyses of the hippocampus to characterize neuroanatomical correlates of depression in multiple sclerosis.

Chen et al. [76] performed volumetric analyses in posttraumatic stress disorder, and they observed that neuron loss was not uniformly distributed on hippocampus and indicated that smaller hippocampal CA1 had significantly statistical associations with increased anxietylike behavior from repeated exposure to acute stress. There are more studies focusing on hippocampal subfield using morphometric information. Scher et al. [21] use radial distance as a feature, and suggest the AD pathology involvement with the CA1 region, adjacent portions of CA2 and distal CA3, subiculum (SUB), and additionally, with the dentate gyrus-hilar (DG) region. Haukvik et

al. [77] concluded that patients with bipolar disorder and schizophrenia consistently displayed smaller SUB volumes, and their evidence showed that these patients were related to worse verbal memory. Yushkevich et al. [9] conclude that most significantly different hippocampal subregions between amnestic MCI and healthy control (HC) are observed mutually in the hippocampal subregion CA1 and the left Brodmann area 35 based on volumetric analyses. The volumetric study results from Mueller et al. [78] show that subiculum, CA1, and CA2 are significantly affected in AD pathology.

Other than identifying group associations in morphometric analyses, functional and structural information of hippocampus are also widely studied in the areas of machine learning and data mining, the tasks include classifying and predicting the diagnostic status of the subjects, especially for the prognostics to detect abnormalities in the early stage of brain cognitive diseases. Costafreda et al. [79] predict the transition from MCI to AD based on hippocampal morphology, and they conclude that the initial degeneration area associated with severe atrophy is CA1. In their study, a Support Vector Machine (SVM) is employed with variants of normalized hippocampal volume and radial distance. Hett et al. [39] adopt patch-based grading approach to capture structural deformation of hippocampus, and build a graph of hippocampal subfields grading to distinguish AD patients from clinically normal participants. Ning et al. [80] adopt the popular convolutional neural network (CNN) framework, they take both of single nucleotide polymorphism (SNP) information and structural MRI images as predictors to identify AD risk factors.

1.3 Limitations

Given the awareness of the recent development of segmentation techniques (mentioned in Section 1.2.1), most methods mentioned in Section 1.2.4 are based on volumetric measurement. Volumetric analyses take the input directly from segmentation outputs, and are a convenient way to conduct shape analyses. However, volumetric analyses only takes hippocampal volume as one measurement, so it measures

the global shape changes in nature. In the meanwhile, it ignores the local shape changes. Conversely, surface-based analysis can capture and utilize detailed shape information, which contains geometric information such as curvatures and thickness, and additional surface signals such as regional subfield distribution and landmarks. These surface feature descriptors characterize both local and global shape, and are helpful in locating clinical biomarkers that are typically ignored in volumetric studies.

Another issue is, most existing studies employed regular T1-weighted MRI scans; thus, they cannot clearly capture the critical hippocampal subfields as well as their neighboring cortical subregions. With the goal of better subfield alignment, typical registration methods which are based on geometric information may not be sufficient. To the best of our knowledge, there is currently no image registration method that is based on hippocampal subfield distribution information, while most of the registration studies only focused on geometry information such as radial distance and local patches. Since we model hippocampus with a smooth surface, it typically provides limited geometric information. Thus, taking advantage of hippocampal subfield measurements will lead to a more accurate hippocampal surface registration. Also, as mentioned previously, the functionality varies in each individual subfield, it is important to align functionally homologous regions across the groups. This can dramatically help to reduce errors in statistical group analyses, as well as to enhance statistical power.

The last issue in the existing shape analyses is that identifying AD from HC is not a challenging problem. The investigation of hippocampal morphometry as an early biomarker for detecting early MCI (EMCI) is an important but yet under-explored topic. Since the EMCI is a very early MCI in AD pathology, deformation signals are too weak to be well captured. A computational framework that can address this issue using hippocampus information is to be studied. Biomarkers on hippocampal subfield are to be explored and validated in statistical analyses.

1.4 Proposed Framework and Main Contributions

Based on the issues mentioned above, a novel computational framework is proposed for group shape analysis in this thesis. As stated previously, shape analysis is a wide concept containing several key image processing techniques such as target segmentation, quantification and shape modeling, and they are essential areas in medical image processing. By combining these techniques, researchers can find valuable ways to extract and represent details on user-desired structures, which can function as the basis for subsequent analyses such as feature classification, regression, and prediction. This thesis presents a new framework for building a three-dimensional (3D) hippocampal atlas model with subfield information mapped onto its surface, with which hippocampal subfield guided surface registration can be performed, group comparison and statistical analysis can be facilitated, and results can be clearly visualized.

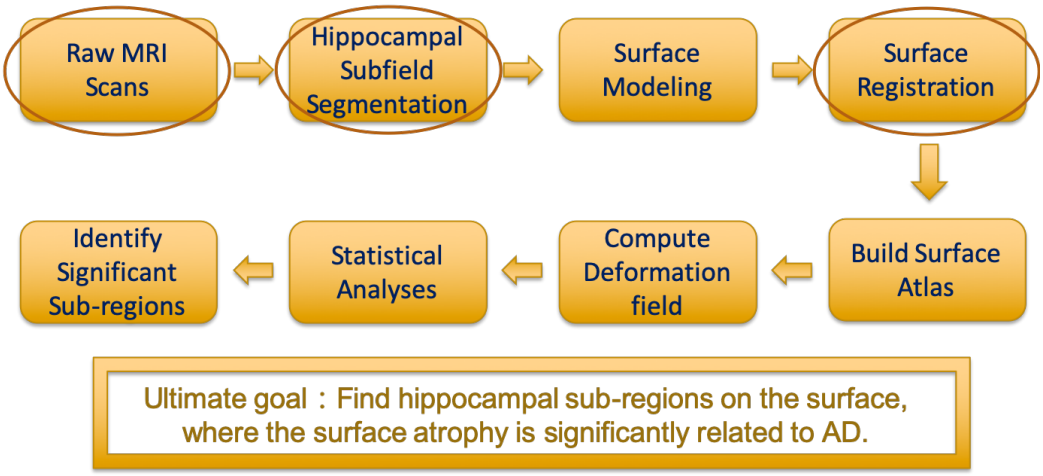

Fig. 1.3.: Working procedures of the proposed approaches.

To deeply understand the relationships between hippocampal shape changes and brain disorders, especially to examine the degeneration of hippocampal subfields, this study focuses on constructing a hippocampal subfield morphometric analysis framework including the following aspects: 1) hippocampal subfield segmentation;

2) 3D shape modeling; 3) surface registration; 4) surface shape reconstruction and building atlas; 5) association analytics. In this thesis, two frameworks that share the same structure will be described as shown in Figure 1.3. The working procedures start by taking raw MRI scans as inputs. Next hippocampal subfield segmentation extracts subfield measures followed by surface modeling that models the segmentation results as 3D surfaces, after which surface registration is applied to align all of the surfaces together. By averaging the aligned surfaces from a control group, a surface atlas of the hippocampus can be obtained. The framework treats this atlas as a template and surface deformation field from each object surface to this template is found. By obtaining the deformation field surface morphometric analysis can be performed and correlations between surface shape changes and cognitive diseases found. Tihis will allow for some vulnerable hippocampal sub-regions to be identified as potential biomarkers for detecting AD. The major modifications of the second approach compared to the first approach are circled in Figure 1.3.

The first framework shows our initial efforts in hippocampal subfield morphometric analyses, and it has two major goals: building a surface atlas of hippocampal subfields and identifying vulnerable hippocampal subfields in AD pathology. It is composed of existing and powerful tools for automatic subcortical segmentation and 3D surface modeling. In particular, Freesurfer 5.3 and Functional magnetic resonance imaging of the brain's Integrated Registration and Segmentation Tool (FIRST) are employed for hippocampal segmentation and quantification, while SPherical HARMonics (SPHARM) is employed for parametric surface modeling. This framework is shown to be effective in creating a hippocampal surface atlas using the Alzheimer's disease Neuroimaging Initiative Grand Opportunity and phase 2 (ADNI GO/2) dataset.

The other framework adopted the same working scheme as shown in Figure 1.3. The major differences and improvements include: 1) it is capable of capturing more detailed hippocampal subfield changes with high-resolution MRI scans. Detailed comparisons of image quality will be shown in Chapter 5 and Figure 5.8. 2) Merging two segmentation approaches in the first approach may introduce errors because their par-

titions of the hippocampus are not exactly the same. Our solution is to replace FIRST and FreeSurfer by a newly released and widely recognized package named Automatic Segmentation of Hippocampal Subfields (ASHS), which can handle high resolution T2-weighted MRI scans while T1-weighted MRI scans are treated as complementary information. 3) Hippocampal subfield information is taken into consideration in the surface registration process. It aims to match the subfield locally, while the registration strategy adopted in the first approach only applies a global transformation. Spherical demons [37] and other demons algorithm variants [60, 81, 82] are employed to perform landmark free registration.

The common parts of the two proposed approaches are: 1) SPHARM is kept unchanged in the second framework for parametric surface modeling. 2) Same strategies are adopted for association analyses. The experimental results of the second framework demonstrate the feasibility of building a hippocampal surface atlas using high-resolution data by developing new methods and employing some recently developed methods.

In summary this study is motivated by several goals including: 1) establishing a computational framework to build a 3D hippocampal subfield surface atlas; 2) developing accurate hippocampal subfield guided registration methods, and 3) extracting useful features and identifying statistically significant biomarkers such as identifying sub-regions on the hippocampus that are highly related to cognitive disabilities.

The main contributions of this study as summarized in Table 1.1 fall into two major categories, namely shape analyses and surface alignment. In the area of shape analyses, as our goal is to perform group analyses, we need a reference for group comparisons, so the first contribution of this study is to propose a novel computational framework that integrates several existing shape segmentation and surface modeling methods to build surface atlas as a reference. The generated 3D surface atlas can demonstrate detailed and accurate hippocampal subfield partitions for visual inspection. The second contribution in shape analysis is the utilization of each individual surface vertex as a measurement that can clearly indicate the atrophy and

Table 1.1.: Main contributions in this study

Category	Needs	Gaps	Solutions
Shape analyses	Perform detailed shape analyses on hippocampal subfields	No reference for group comparisons	Build surface atlas as a reference
	Locate shape changes on hippocampus	Volumetric analyses cannot locate significant regions specifically	Surface shape analyses
Surface alignment	Achieve better subfield matching	No geometric information on surface for subfield matching	Subfield-guided registration
	Elaborate proper subfield representations	Integer labels may introduce errors	Binary maps , distance maps and probability maps
	Improve the existing registration methods	The trade-offs between similarity and regularity	A newly proposed surface registration method

severity level. The next major contribution of this study is in the area of surface registration. In this regard the contribution of this study is alignment of hippocampal subfields in the absence of informative surface geometric information. In this study, we demonstrate the feasibility of the procedures for fast and accurate landmark free registration using hippocampal subfield information. Since hippocampal subfield measures are obtained directly from segmentation results, and using integer labels directly for registration can introduce errors, one contribution is to generate proper surface feature representations such as binary maps, distance maps and probability maps. The final contribution is a new surface registration method based on demons algorithm, and detailed experimental results will illustrate the advantages of our methods compared to the classical methods.

1.5 Organization

The rest of the thesis is organized as follows, as illustrated in Figure 1.3: Chapter 2 introduces the processes of data preparation such as segmentation and surface shape modeling, Chapter 3 describes the fundamental theories of several popular surface registration methods and the proposed methods. In Chapter 4, we apply the methods mentioned in Chapter 2 and 3 with the goal of building a hippocampal surface atlas. Morphometric analyses such as volumetric analyses, surface-based analyses, and genetic analyses are discussed in Chapter 5. In Chapter 6, we summarize the studies and discusses several possible future directions. A diagram shown in Figure 1.4 demonstrates the relations between Chapters 2-5 and the goals of this study.

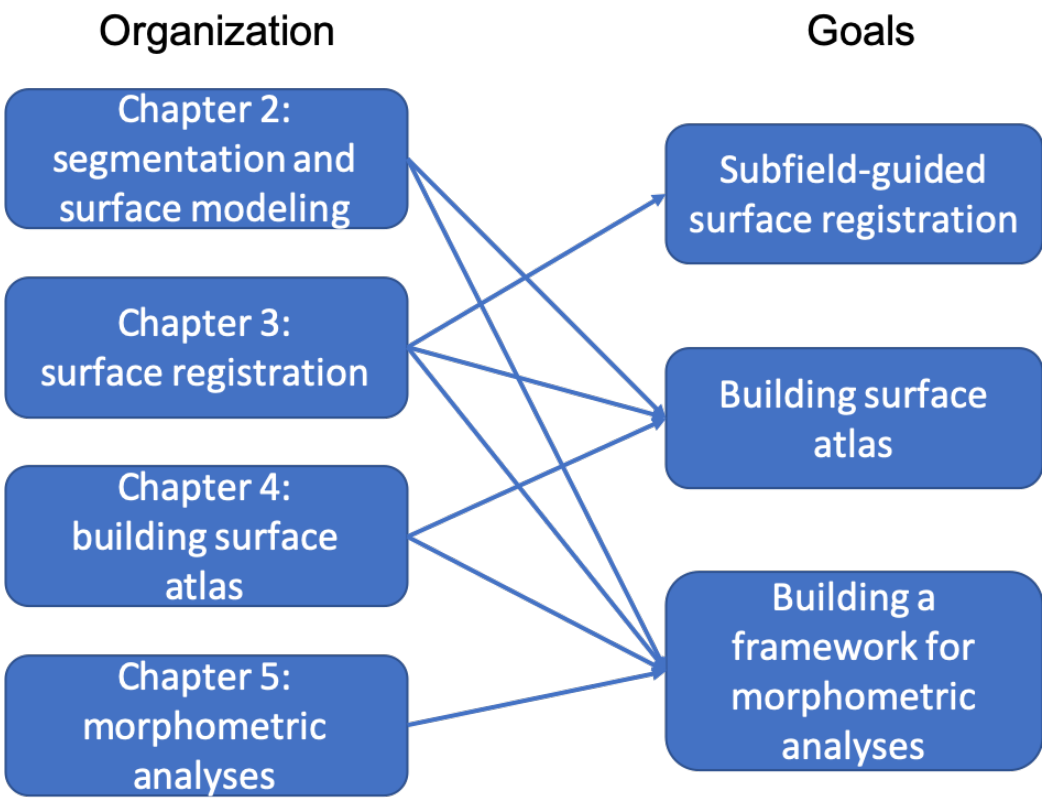

Fig. 1.4.: Organization and goals of the thesis.

2. SURFACE SHAPE MODELING

2.1 Background

The goal of this chapter is to introduce several methods used in the initial data preparation and processing such as segmentation of the hippocampus and 3D surface modeling approaches that will be used to generate the hippocampus surface atlas. The 3D surface model is a polygon representation that describes the geometric characteristics of an object. It defines topological relations on the surface such as vertex, face, and edge, which can provide a series of shape correspondences across different objects. It makes geometric operations (such as Euclid geometry and Riemannian geometry) feasible for surface shape analyses by numerically evaluating shape variations and structural differences among objects. This allows for a region of interest such as a region with severe atrophy on the surfaces to be identified.

The 3D surface modeling process usually contains two major steps: the first step is to extract a region of interest (ROI); the second step is to generate 3D polygon representations. This strategy is widely applied and discussed in the areas of computer graphics and computer vision, and widely applied in the areas of medical-imaging analysis, 3D animation, industrial design and earth science [83–85].

As a focus of this study, the complex folding anatomy of the hippocampus often presents analytical challenges. In particular, the critical hippocampal subfield information is usually ignored in hippocampal morphometric studies. Most existing subfield studies employ high-field MR technologies, post-mortem data, and long scan times for extracting hippocampal subfield information [25, 86–88], which can not be applied to a large cohort. Automated extraction of hippocampal subfields from 1.5T

or 3T MRI brain scans is still a challenging task [89] and there are very few tools available. In this section, several tools that fulfill automatic hippocampal and subfields segmentation are introduced.

After the information of the hippocampus and its subfields are obtained, the next step is to obtain morphometric changes. As voxel-based hippocampal objects cannot be compared directly across subjects, the SPHARM method [90] is employed to model the surfaces so that group analysis (e.g., computing an average shape) can be facilitated. This work extends the analysis on single object cases to multiple objects cases and allows the analysis not only on the individual shape information of each object but also on spatial relations between or among objects. The SPHARM parametric surface modeling was initially proposed by Brechbuhler et al. [91] to model 3D objects with arbitrary shape but required to be simply connected. It is basically a parametric surface modeling method based on Fourier transform method, which describes a 3D surface utilizing three spherical functions and transforms them into three sets of Fourier coefficients in the frequency domain [92]. Three steps are involved in our SPHARM processing framework: (1) spherical parameterization, (2) SPHARM expansion, and (3) SPHARM registration.

2.2 Data and Materials

The data used in this study was downloaded from the ADNI database [93]. One goal of ADNI has been to test whether serial MRI, positron emission tomography (PET), computed tomography (CT), biological markers, and clinical and neuropsychological evaluation can be combined to measure the progression of AD and MCI (an early stage of AD).

We downloaded baseline 3T MRI scans of 172 HC, 267 early MCI (EMCI), 140 late MCI (LMCI), and 108 AD participants aging between 55 and 90, along with demographic and diagnostic information. All the raw data are 3D T1-weighted scans with $1.2 \times 1.0 \times 1.0\, mm^3$ voxel resolution, and dimension of $196 \times 256 \times 256$.

2.3 Image Segmentation and Quantification

Freesurfer and FIRST (published as a part of FSL) are automatic segmentation tools based on Bayesian models, and they are widely recognized in the field of medical imaging analyses. The automated segmentation technique in FreeSurfer [94] is based on a statistical model of image formation around the hippocampal area using Bayesian inference. It firstly builds an explicit computational model by incorporating a prior which is based on a generalization of probabilistic atlases to describe the formation around the hippocampal area in ultra-high resolution MRI scans, then a likelihood distribution completes the model by predicting and assigning integer labels to each voxel according to a maximum a posteriori estimate, which indicates a subfield it belongs to. Thus, hippocampal subfield segmentations can be obtained.

For more specific details, in the first step, the goal of FreeSurfer algorithm is to create a generative model that incorporates a prior distribution, which is learned from manually labeled partition of hippocampal subfields. Assume a labeled image $L = \{l_i, i = 1, \ldots, I\}$ with a total of I voxels and K classes of subfield labels, the region of interest (ROI) is covered by a tetrahedrical mesh with N mesh nodes $\mathbf{x}^r = \{\mathbf{x}_n^r, n = 1, \ldots, N\}$ and each node has K probability values for each label $l_i \in \{1, \ldots, K\}$, so we have $\alpha = \{\alpha_n\,, n = 1, \ldots, N\}$ and $\alpha_n = \left\{\alpha_n^1, \ldots, \alpha_n^K\right\}$ with the conditions that $\alpha_n^k \geqslant 0$ and $\sum_k^K \alpha_n^k = 1$ which counts the frequency a label l_i occurs at a node $\mathbf{x}^r$ in the training data. Then, the algorithm models the the probability of having label k in an image pixel i with a mesh node $\mathbf{x}$ as the followings:

$$p_i(k|\mathbf{x}) = \sum_{n=1}^{N} \alpha_n^k, \Phi_n\left(\mathbf{x}_i\right), \tag{2.1}$$

where $\Phi_n(\cdot)$ is defined as the interpolation basis function for a mesh node n. With the assumption of the conditional independence, the FreeSurfer algorithm models the probability of obtaining label image L by

$$p(L|\mathbf{x}) = \prod_{i=1}^{l} p_i\left(l_i|\mathbf{x}\right). \tag{2.2}$$

The second step is to employ a likelihood distribution to measure the mean and variance of the normal distribution associated with different tissue categories. For an intensity image $Y = \{y_i, i = 1, \ldots, I\}$,

$$p(Y|L, \boldsymbol{\theta}) = \prod_{i=1}^{l} p_{l_i}\left(y_i|\boldsymbol{\theta}\right), \tag{2.3}$$

where $\boldsymbol{\theta}$ is defined as likelihood distribution parameters, and the algorithm models each of the distributions $p_k(y|\boldsymbol{\theta})$ as a normal distribution:

$$N\left(y|\mu, \sigma^2\right) = \frac{1}{\sqrt{2\pi\sigma^2}} \exp\left(-\frac{(y_i - \mu)^2}{2\sigma^2}\right). \tag{2.4}$$

For tissue types $G(k)$ and $k \in \{\mathrm{GM}, \mathrm{WM}, \mathrm{CSF}, \mathrm{CP}\}$, each of the distributions

$$p_k(y|\boldsymbol{\theta}) = N\left(y|\mu_{G(k)}, \sigma^2_{G(k)}\right) \quad \forall k. \tag{2.5}$$

The third step is to perform parameter optimization for the maximum a posteriori (MAP) parameter estimate. The goal is to obtain parameters $\{\hat{\mathbf{x}}, \hat{\boldsymbol{\theta}}\}$ that can maximize $p(\mathbf{x}, \boldsymbol{\theta}|Y) \propto p(Y|\mathbf{x}, \boldsymbol{\theta})p(\mathbf{x})$ using a generalized expectation maximization (EM) algorithm [95].

The last step of FreeSurfer (v5.3) hippocampal subfield segmentation algorithm is to assign anatomical labels to testing data with the trained MAP model. For each voxel, the highest posterior probability is obtained by

$$p_i(k|y, \hat{\mathbf{x}}, \hat{\boldsymbol{\theta}}) \propto N\left(y|\hat{\mu}_{G(k)}, \hat{\sigma}^2_{G(k)}\right) p_i(k|\hat{\mathbf{x}}). \tag{2.6}$$

Similar to the FreeSurfer (v5.3), FIRST [96] is also a Bayesian model based approach for the hippocampus segmentation. The major differences are 1) FIRST is not capable to provide any subfield estimation, and 2) FIRST algorithm introduces the shape appearance in addition to the image intensity. The FIRST algorithm adopts the shape and appearance models created from manually traced and labeled MRI images partitioned by the Center for Morphometric Analysis in Boston, USA. Then these labels are parameterized as vertices of tetrahedrical polygon meshes. The shape

and appearance model within a Bayesian framework allows a full exploitation of probabilistic relationships between image intensity and the shape of hippocampus. The shape is described as a mean with singular value decomposed principal components. Based on the MAP models learned from the training process, the segmentation algorithm seeks through linear combinations of appearance modes of variation for the most probable shape instance with the highest maximum a posteriori value given the observed intensities in an input MRI image.

For more specific details, in the first step, the FIRST algorithm aims to model the joint distribution $p(\boldsymbol{x}_I, \boldsymbol{x}_s)$ of intensity and shape appearance as a multivariate normal distribution, where $\boldsymbol{x}_I$ denotes image intensity and $\boldsymbol{x}_s$ denotes the image shape with Euclidean coordinates of vertices.

The second step is to calculate the conditional posterior probability $p(\boldsymbol{x}_s|\boldsymbol{x}_I, \mathcal{Z})$, given $\boldsymbol{x}_I$ and $\mathcal{Z}$:

$$p(\boldsymbol{x}_s|\boldsymbol{x}_I, \mathcal{Z}) = \frac{p(\boldsymbol{x}_s, \boldsymbol{x}_I|\mathcal{Z})}{p(\boldsymbol{x}_I|\mathcal{Z})}, \tag{2.7}$$

where $\mathcal{Z} = \{X_1 \dots X_{n_s}\}$ denotes a set of manually traced training data. MAP maximizes $p(\boldsymbol{x}_s|\boldsymbol{x}_I)$ such that $p(\boldsymbol{x}_s|\boldsymbol{x}_I) \propto p(\boldsymbol{x}_I|\boldsymbol{x}_s)\, p(\boldsymbol{x}_s)$ and this equation is solvable by logarithm transformation:

$$-\ln p(x_s|x_I) = -\ln p(x_I|x_s) - \ln p(x_s) + \ln p(x_I)\,. \tag{2.8}$$

The third step of the FIRST algorithm is to model the shape partition by approximating the testing image to training data using the shape and appearance models:

$$\hat{\boldsymbol{x}} = \overline{\boldsymbol{x}} + \boldsymbol{U}\frac{\boldsymbol{D}_\epsilon\sqrt{\gamma_v}}{\sqrt{(n_s-1)}}\boldsymbol{b}, \tag{2.9}$$

where $\boldsymbol{U}$ are the eigenvectors of the covariance matrix, b are model parameters that weight the linear combination of eigenvectors, $\boldsymbol{D}_\epsilon^2$ is a diagonal matrix consisting of the eigenvalues, γ is a scalar such that $\gamma = (n_s - n_s^{-1})\,/\,(n_s - n_s^{-1} - 2)$.

Given the intensities from a testing MRI scan, the final shape partition is modelled using Equation 2.9. The parameters of the new shape instance $\mathbf{b}_\mathrm{s}$ can be estimated from the posterior conditional distribution $p(\mathbf{x}_s|\mathbf{x}_I, \mathcal{Z})$.

We first perform an initial segmentation of the subfields of the hippocampus from each MRI scan using FreeSurfer (see Figure 2.2). The result includes eight probability maps, one for each subfield. Then, we use FIRST to extract the left and right hippocampi, and the result is a 3D binary image (see Figure 2.4). As we can see from Figure 2.4, FIRST yielded a less noisy boundary than FreeSurfer. Although FreeSurfer can produce reliable hippocampal subfield volume measures, it tends to yield noisy hippocampal boundary which is not suitable for detailed shape analysis. Conversely, FIRST generates successful hippocampal boundary results, but it does not offer the capability for segmenting subfields. So a strategy we will adopt in the following sections is to combine these two segmentation approaches: for the same subject, we take the segmentation result from FIRST as a binary mask, and apply it on the results from FreeSurfer, it is a process of mapping subfield information from FreeSurfer to FIRST segmentation results.

As the segmentation results cannot always be perfect, there may exist some unnoticeable vacancies or discontinuities between image voxels, it is necessary to check and eliminate the topological errors of the segmentation results. In the next step, we perform a topology fix for the FIRST result (as it is the mask) to make sure the hippocampal object is simply-connected, and its surface has a spherical topology. A simply-connected object means: 1) each face contains four edges, and each pair of vertices is connected by an edge; 2) each vertex can be connected by three to six edges based on the local connectivity; 3) the total number of vertices should be greater than the total number of faces by two, which follows the Euler's rule of relation: $n_{vert} = n_{face} + 2$ [47, 91, 97, 98].

Topology fix is a crucial step required by spherical parameterization which will be introduced in Section 2.6.1. We assume the segmentation results are binary images, we assign values equal to one for the hippocampus and zero for the background, then the topology fix corrects hippocampal topology in the following aspects: 1) for the isolated or disconnected small components, they are removed changing their values from 1 to 0; 2) for the holes inside the object which are zeros completely surrounded

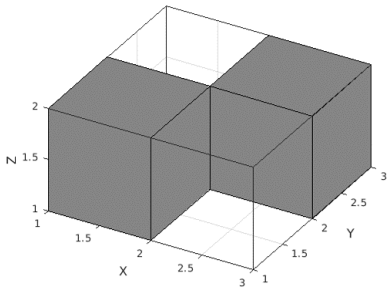

(a) An example of bad topology: bad edge connectivity

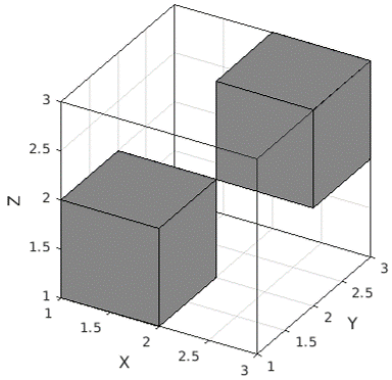

(b) An example of bad topology: bad vertex connectivity type I

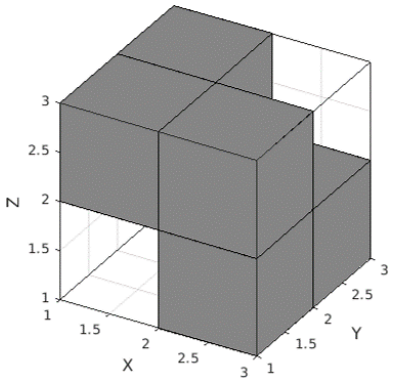

(c) An example of bad topology: bad vertex connectivity type II

Fig. 2.1.: Some examples of bad topology.

by ones, they are removed by changing the values from 0 to 1; 3) for the bad edge connectivity shown in Figure 2.1(a), the topology fix chooses one candidate from four voxels and replaces the voxel value based on maximum number of different neighbours, the result is either removing an existing voxel or adding a new voxel; 4) for the type I bad vertex connectivity shown in Figure 2.1(b), a voxel may be removed by changing the value from 1 to 0 based on maximum number of different neighbours; 5) for the type II bad vertex connectivity shown in Figure 2.1(c), a voxel may be added by changing the value from 0 to 1 based on maximum number of different neighbours.

After the topology correction, we use the fixed hippocampus to mask the 8 probability maps (i.e., values outside the mask are set to 0). We also identify "holes" in the mask, where all the 8 probability maps have 0 values. We smooth each probability map with a Gaussian kernel (Kernel size is [5 5 5] in our experiments) to get nonzero values and assign these values to voxels in the holes. We denote these updated probability maps as $P_1 - P_8$. Thus, for each hippocampus, the result of this step includes (1) a binary object to represent the entire hippocampus (its surface has a spherical topology), and (2) 8 probability maps $P_1 - P_8$, one for each subfield (see Figure 2.3 for mapping it onto the surface, where nonzero values are colored in red). These are the input data to the next step.

2.4 Reproducibility Test

To test if FIRST and Freesurfer are reliable tools for our studies, in this section, we perform a reproducibility analysis on hippocampal subfield segmentation using FreeSurfer and FIRST, aiming for identifying reliable subfield measures for further investigation. Thus, This study has two goals: (1) evaluating the reproducibility of hippocampal subfields segmented by FreeSurfer; (2) examining whether combining FreeSurfer and FIRST can yield reliable subfield measures with the potential for further shape analysis.

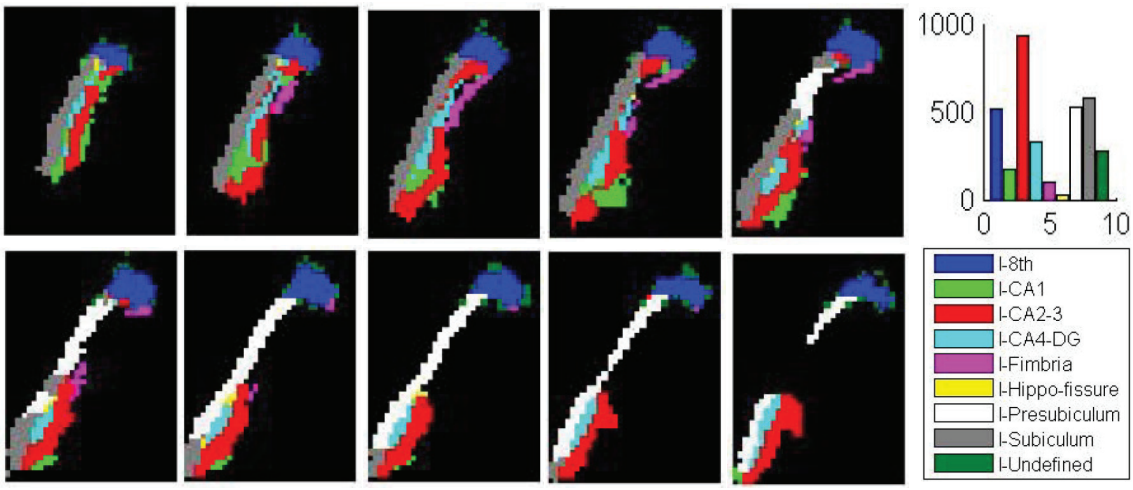

Fig. 2.2.: FreeSurfer subfield segmentation: example slices of the left hippocampus. Histogram shows the number of voxels in each subfield.

Participants include 30 healthy controls from the Alzheimer's disease Neuroimaging Initiative (ADNI) GO/2 cohort, same scanning protocols are discussed in 2.2. Two repeated baseline 3T magnetic resonance imaging (MRI) scans were downloaded for each participant. Using these two sets of repeated MRI scans, intraclass correlation coefficients (ICCs, more details can be found in section 4) were calculated to evaluate the reproducibility of the volume measures of these extracted structures. Each subfield map was further masked by the entire hippocampus generated by either FreeSurfer or FIRST to obtain two new sets of subfield volume measures. After that, two more sets of ICCs were calculated based on these new measures.

Comparing FIRST and FreeSurfer (Figure 2.4) segmentation results of the entire hippocampus, we observed that FIRST yielded a less noisy boundary than FreeSurfer. The reproducibility tests for measuring subfield volume resulted in ICCs ranging from 0.4 to 0.9, and using FIRST to mask the subfields produced ICCs higher or similar to the original ones.

Although FreeSurfer can produce reliable hippocampal volume measures, it tends to yield noisy hippocampal boundaries which are not suitable for detailed shape analysis. While FIRST generates successful hippocampal segmentation results, yet it

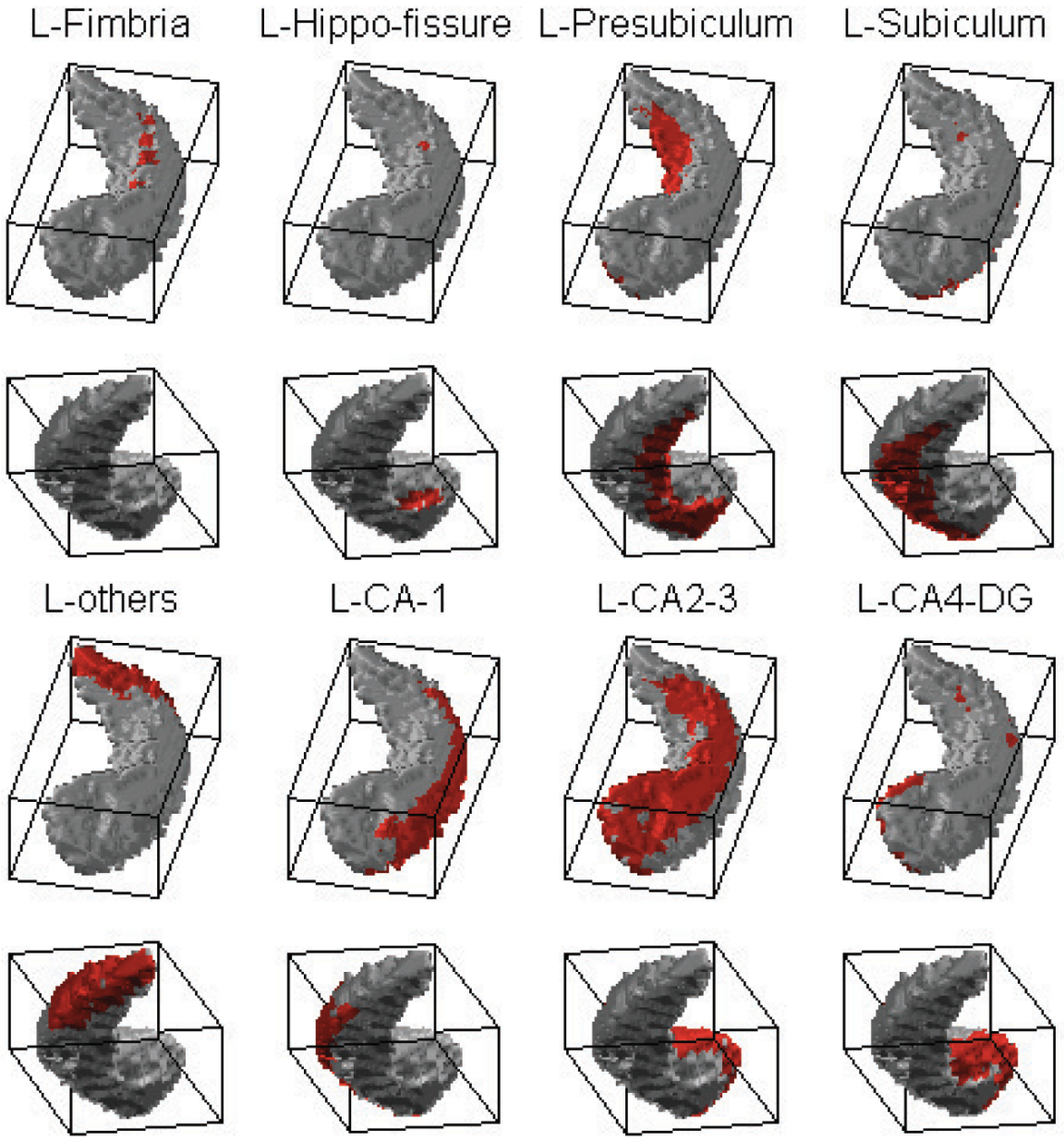

Fig. 2.3.: Subfields information measured using FreeSurfer is mapped on left hippocampal surface segmented by FIRST. "L-others" is the tail region of the hippocampus which contains "l-8th" and "l-undefined" on Figure 2.2.

does not offer the capability for segmenting subfields. Based on the reproducibility measures, using FIRST to mask the subfields yields a set of ICCs that are better than or similar to the original ones, while the most ICCs results of using FreeSurfer

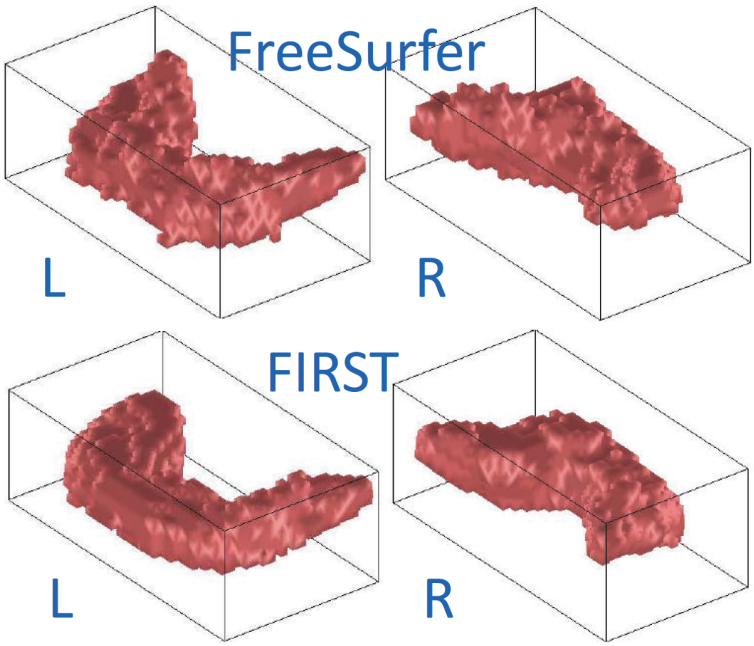

Fig. 2.4.: Hippocampal segmentation: FIRST versus FreeSurfer.

to mask subfields are similar or worse than the original ones. This promising result suggests that FIRST-masked subfields may have the potential to be used in detailed shape analysis, and guarantees the validation of the experimental results.

2.5 Surface Mesh Representations

Surface shape modeling is a major branch in computer vision and medical imaging, which has proved valuable in the tasks of object representation, recognition, classification, and registration. This part focuses on shape modeling of 3D surfaces extracted from volumetric images.

Surface mesh is a polygon structure that describes a geometric shape by a set of vertices, edges, and faces. Figure 2.5 gives two examples showing cortical [99] and facial [100] surface meshes.

As seen in Figure 2.6, a vertex is defined as a node or an intersection for two line segment on the surface mesh. An edge is defined as a line segment that joins two vertices. A face is defined as a closed area within edges. Representations of polygon meshes have many variants; the surface models are usually represented by triangular mesh, quadrilaterals mesh, or other simple convex polygons for different applications and goals, or as a result of the simplification level of rendering.

As shown in Figure 2.6(a) and 2.6(b), we take 9 vertices from a surface with N vertices, a vertex is a 1×3 vector indicating its spatial coordinates x, y and z (Figure 2.6(c)), while a face is described as a 1×3 vector (triangle mesh, as shown in Figure 2.6(d)) or 1×4 vector (quadrilaterals mesh), which indicates indices of vertex. With a certain structure, the surface mesh can provide geometric information as each vertex contains geometric coordinates in one space. This helps examine structural deformation in group studies.

Other than simple geometric surface information, a polygon structure may contain additional signals that can provide useful information. For example, when the medial curve is calculated, the thickness can be defined as the shortest distance from a specific vertex to the medial curve, this is also seen as an indicator of surface deformation when performing group comparisons. Another example is surface curvature; it can be evaluated along surface normal. By introducing the concept of surface curvature, many mathematical tools such as differential geometry can be applied. More details can be found in [101–104].

2.6 3D Hippocampal Surface Modeling

After hippocampi and subfields are extracted from segmentation tools such as FIRST and Freesurfer, a procedure of hippocampal surface modeling is required for surface-based morphometric analyses. This procedure includes two steps: (1) spherical parameterization, and (2) SPHARM expansion.

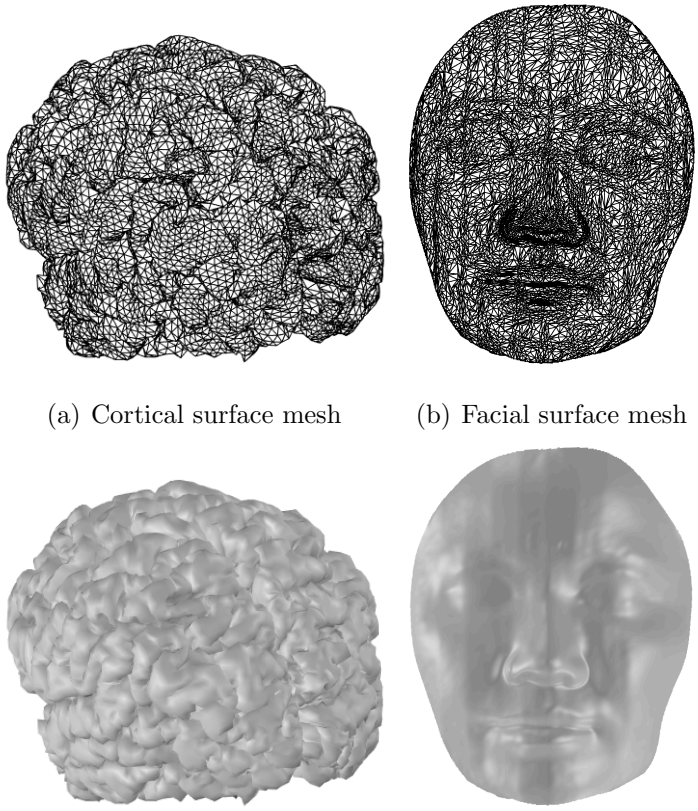

(a) Cortical surface mesh

(b) Facial surface mesh

(c) Shaded rendering for cortical surface

(d) Shaded rendering for facial surface

Fig. 2.5.: An example of surface mesh: (a) describes an example of cortical surface mesh; (b) describes an example of facial surface mesh; (c) describes the shaded rendering for cortical surface; and (d) describes the shaded rendering for facial surface.

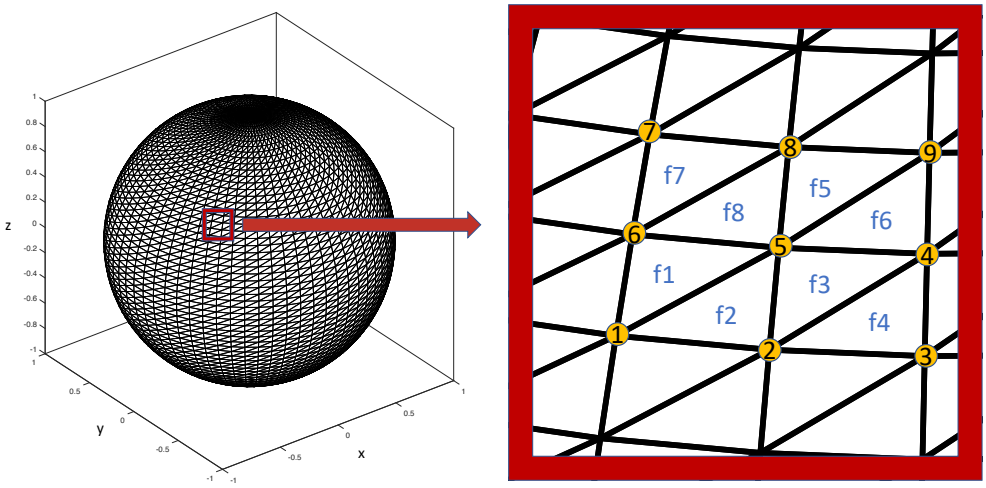

(a) Spherical mesh

(b) Zoom-in view of spherical mesh

Face ID	Vertex ID		
f1	1	5	6
f2	1	2	5
f3	2	4	5
f4	2	3	4
f5	5	9	8
f6	5	4	9
f7	6	7	8
f8	6	5	8

(c) A list of faces

Vertex ID	X	Y	Z
1	-0.76	-0.41	0.51
2	-0.71	-0.48	0.51
3	-0.66	-0.54	0.51
4	-0.64	-0.53	0.56
5	-0.69	-0.46	0.56
6	-0.73	-0.39	0.56
7	-0.71	-0.38	0.6
8	-0.67	-0.45	0.6
9	-0.62	-0.51	0.6

(d) A list of vertices

Fig. 2.6.: Structures of surface meshes: (a) describes the complete surface mesh; (b) describes the zoom-in view of mesh structures; (c) describes the faces and vertices; and (d) describes the spatial coordinates of surface vertices.

2.6.1 SPHARM Parameterization

In order to describe a voxel-based hippocampal surface using spherical harmonics, spherical parameterization was introduced. It embedded the voxel-based hippocampal surface graph onto a surface of the unit sphere, and it created a continuous and uniform mapping from the object surface to the surface of a unit sphere. Thus, it resulted in a bijective mapping between each point v on a surface and a pair of spherical coordinates θ and ϕ that matched the definition of spherical harmonics [105]:

$$\mathbf{v}(\theta, \phi) = (x(\theta, \phi), y(\theta, \phi), z(\theta, \phi))^T, \tag{2.10}$$

where θ is defined as the polar (or co-latitudinal) coordinate with $\theta \in [0, \pi]$, and ϕ is taken as the azimuthal (or longitudinal) coordinate with $\phi \in [0, 2\pi)$, as shown in Figure 2.7. Thus, the north pole is defined as $\theta = 0$ and the south pole has $\theta = \pi$. Figure 2.8 shows an example spherical parameterization. This closed-surface parameterization is achieved through an area-preserving mapping by implementing Brechbuhler's method [91].

2.6.2 SPHARM Expansion

SPHARM expansion expands the object surface in a full set of spherical harmonic basis functions Y_l^m, where Y_l^m indicates the spherical harmonic of degree l and order m, and it is actually a Fourier basis function defined on the sphere. Each function is independently decomposed in terms of SPHARM as:

$$x(\theta, \phi) = \sum_{l=0}^{\infty} \sum_{m=-l}^{l} c_{lx}^m Y_l^m(\theta, \phi), \tag{2.11}$$

$$y(\theta, \phi) = \sum_{l=0}^{\infty} \sum_{m=-l}^{l} c_{ly}^m Y_l^m(\theta, \phi), \tag{2.12}$$

$$z(\theta, \phi) = \sum_{l=0}^{\infty} \sum_{m=-l}^{l} c_{lz}^m Y_l^m(\theta, \phi). \tag{2.13}$$

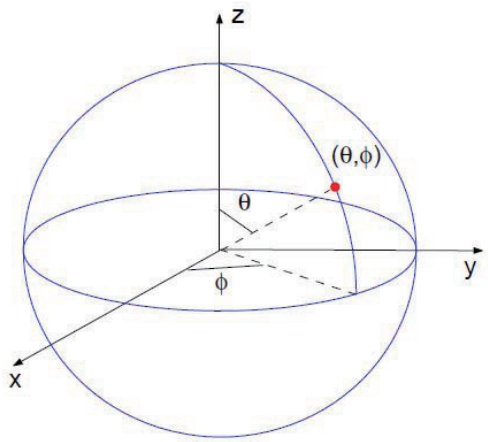

Fig. 2.7.: A spherical unit: θ is defined as the polar (or co-latitudinal) coordinate with $\theta \in [0, \pi]$, and ϕ is taken as the azimuthal (or longitudinal) coordinate with $\phi \in [0, 2\pi)$.

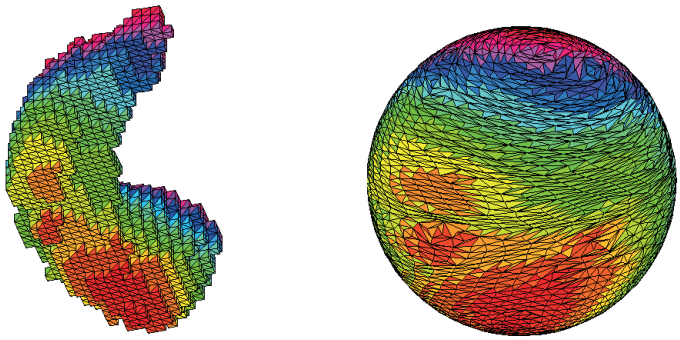

Fig. 2.8.: Hippocampal surface (left) and its spherical parameterization (right). Color indicates the correspondence between the surface and parameterization.

The expansion can be bundled as a single vector-valued form:

$$v(\theta,\phi) = \begin{pmatrix} x(\theta,\phi) \\ y(\theta,\phi) \\ z(\theta,\phi) \end{pmatrix} = \sum_{l=0}^{\infty} \sum_{m=-l}^{l} \begin{pmatrix} c_{xl}^m \\ c_{yl}^m \\ c_{zl}^m \end{pmatrix} = \sum_{l=0}^{\infty} \sum_{m=-l}^{l} c_l^m Y_l^m(\theta,\phi), \tag{2.14}$$

where,

$$v(\theta,\phi) = \begin{pmatrix} x(\theta,\phi) \\ y(\theta,\phi) \\ z(\theta,\phi) \end{pmatrix}, \tag{2.15}$$

and,

$$c_l^m = \begin{pmatrix} c_{xl}^m \\ c_{yl}^m \\ c_{zl}^m \end{pmatrix}. \tag{2.16}$$

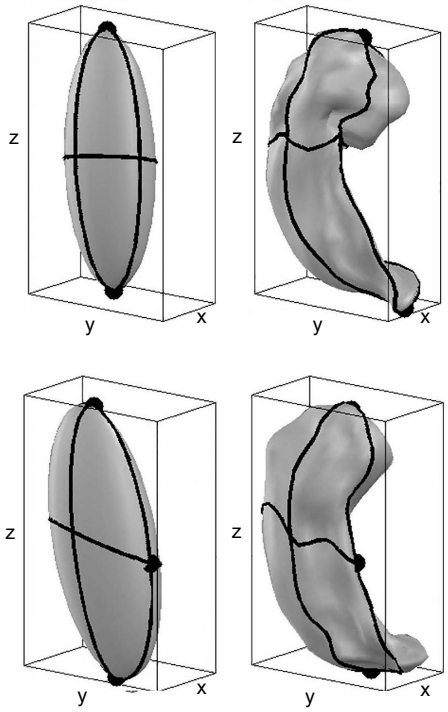

Fig. 2.9.: An example of degree 1 reconstruction (an ellipsoid) and the degree 15 reconstruction of the same object.

The prerequisite for SPHARM expansion is to finish spherical parameterization in advance, as it was introduced in the last section. As the results of spherical parameterization shown in Equation 2.6.2, $x(\theta,\phi)$,$y(\theta,\phi)$,$z(\theta,\phi)$ are functions that define the location relationship between the voxel-based object and spherical unit. Based on this theory, the object surface can be described through expanding these three spherical functions using SPHARM, as shown in Equation 2.6.2.

The Fourier coefficients c_l^m are determined using standard least-square estimation and can be estimated by solving a linear system. To describe how to calculate it, we can pick one dimension, $x(\theta,\phi)$ as an example. The goal is to compute the coefficients c_{lx}^m up to a user-desired maximum degree L_{max}. When an input spherical function $x(\theta,\phi)$ is described by a set of spherical samples (θ_i,ϕ_i) and their function values $x_i = x(\theta_i,\phi_i)$, for $1 \leqslant i \leqslant n$. Based on Equation 2.6.2, a linear system can be described as follows:

$$\begin{pmatrix} y_{1,1} & y_{1,2} & y_{1,3} & \cdots & y_{1,k} \\ y_{2,1} & y_{2,2} & y_{2,3} & \cdots & y_{2,k} \\ \vdots & \vdots & \vdots & \ddots & \vdots \\ y_{n,1} & y_{n,2} & y_{n,3} & \cdots & y_{n,k} \end{pmatrix} \begin{pmatrix} a_1 \\ a_2 \\ a_3 \\ \vdots \\ a_k \end{pmatrix} = \begin{pmatrix} x_1 \\ x_2 \\ x_3 \\ \vdots \\ x_n \end{pmatrix}, \tag{2.17}$$

where $y_{i,j} = Y_l^m(\theta_i,\phi_i)$, $j = l^2 + l + m + 1$, and $k = (L_{max}+1)^2$. For every pair (l,m), an indexing scheme j is the unique number assigned to these pairs. The above system is solved by least square fitting for $(a_1, a_1, \cdots, a_k)^T$ as for most cases $n \neq k$. As each $a_j \equiv \hat{c}_{lx}^m$ is an estimation of the original coefficients c_{lx}^m, for the unique index $j = l^2 + l + m + 1$, the original function can be reconstructed as the form:

$$\hat{x}(\theta,\phi) = \sum_{l=0}^{\infty} \sum_{m=-l}^{l} \hat{c}_{lx}^m Y_l^m(\theta,\phi) \approx x(\theta,\phi). \tag{2.18}$$

The object surface can be reconstructed utilizing these coefficients, and the more degrees (i.e. larger values of L_{max}) the user uses, the more coefficients are generated and the more precise and detailed reconstruction $\hat{x}(\theta,\phi)$ will be achieved. Applying

least-squares estimation in a same way onto $y(\theta, \phi)$ and $z(\theta, \phi)$, the results c_{ly}^m and c_{lz}^m are determined individually. Thus, a series of bundled coefficients c_l^m can be used for approximating the original surface and also used to represent and reconstruct an approximated surface. Figure 2.9 shows the degree 1 remodeling and the degree 15 remodeling for the same object.

The SPHARM parametrization and expansion process is demonstrated in Figure 2.10, the surface of an object (hippocampus) was first bijectively mapped onto the spherical surface (done by SPHARM parameterization), then this object was reconstructed by applying spherical harmonic functions and using the calculated spherical coefficients and user-desired degree (done by SPHARM expansion).

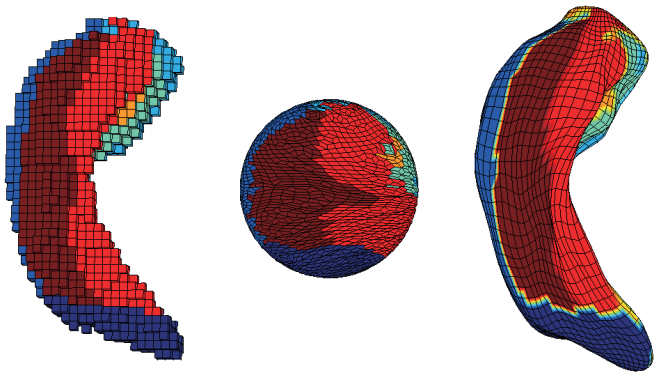

Fig. 2.10.: The object on left is the original hippocampus, the object in the middle is the unit sphere, and the object on the right (FOE aligned, in Chapter 3 is the reconstructed hippocampus using SPHARM expansion.

2.7 Summary of Chapter 2

In this section, we introduced two segmentation tools: FIRST for hippocampi segmentation, and Freesurfer for hippocampal subfield segmentation. We also described the procedures to parameterize a 3D object on a unit sphere, and then reconstruct the 3D object surface using Fourier basis expansion. SPHARM expansion makes

each object surface has the same number of vertices and faces under the same reconstruction degree level; thus, it makes all surface objects comparable. However, the surfaces are still not comparable since they are not well aligned. An additional step should be performed to align those surface-based objects together for the goal of group comparisons. A reference or template (atlas) is required for such a step.

3. SURFACE REGISTRATION

3.1 Background

Surface shape registration is an extension of image registration, which is also known as image matching. It aims to discover the spatial correspondences between two or more images of a scene by seeking an optimal global or local transformation that best aligns the structures or functionalities of interested regions homogeneously across the given images. By registering images, a correspondence can be determined and the structural changes in the scene can be detected. This basic capability is needed in various medical image analysis applications.

Image features can be extracted from 2D or 3D images as introduced in Chapter 1, and they are unique image properties that can describe geometric and other shape features. This information can be useful to establish a correspondence between two 2D images or 3D surfaces. Surface registration is intended to align all surface shape models in a common scheme of reference to enable the shape comparisons. It produces a standardized geometric representation to describe the shape after standardizing measurements of size, position, and orientation (i.e. excluding scaling, translation as well as rotation).

While image registration is deemed as one of the most critical topics in image processing and analysis, surface registration plays a likewise significant role in computer graphics and shape analysis. One important application of surface registration is surface-based morphometry (SBM); it is commonly used in biomedical imaging and other fields to locate shape changes related to distinct conditions.

The registration of 3D surfaces represents an essential area of research in image-based tasks, and it is widely studied in medical imaging literature as it is an essential tool for surface analysis. To specifically explains this, surface registration is

fundamental in geometric modeling and 3D shape analytics that aims to find surface correspondence between two objects in polygon mesh representation. Thus, a transformation which best superposes one surface with another can be found. It is extensively applied in medical imaging and analytics aspects such as human cerebral cortex analysis, cortical connectome analysis, and soft tissues analysis. Surface registration in medical imaging employs anatomical information to achieve fast and efficient registration.

Compared with point registration, surface registration features for more informative surface correspondences, which combines geometric information such as curvatures and thickness, and additional surface signals such as regional subfield distribution and landmarks. These features make surface registration as an identical tool to find ideal correspondence (when no correspondences are pre-defined).

To manually pre-define correspondent points or trace landmark points frequently requires professional pre-knowledge on anatomy and pathology. It often requires heavy labor work; thus, it is a time-consuming, error-prone, and subjective process, which makes manual landmarking impractical for the studies with a large scale of data set. To overcome this limitation, some surface based automated registration methods are proposed [106–108]. These methods usually utilize geometric features such as radial distance and shape curvature, and this naturally makes surface boundaries and surface regions distinct patterns in distinguishing different tissues or finding common geometric features in group studies. As mentioned before, a registration problem is essentially a problem that we try to find correspondence between subjects, surface registration utilizing geometric information can resolve a medical image registration problem in an automatic sense. However, the complex anatomy is often not only provide geometric information but also brings challenges for accurate registration.

In this chapter, the goal is to introduce the basic theories for surface registration and describe the proposed surface-guided registration strategy. It present a set of effective surface registration methods that are suitable for SBM processing. Different applications may require different registration methods and criteria for obtaining

optimal registration results. The remainder of this section is organized into four major parts. The first subsection aims to introduce surface registration theories, algorithms, and variants. In the second subsection, four types of popular registration quality evaluation methods will be discussed. In the third subsection, different surface registration strategies will be tested on synthetic data. At the end of this section, discussions, and conclusions will be summarized.

3.2 Methods

In this thesis, surface registration methods are categorized into two classes: one is based on surface geometric information; the other is based on non-geometric features. Geometry based methods benefit from the object's spatial characteristics. Thus, the algorithms can catch local or global geometric patterns. The most discussed non-geometric features include landmarks and clusters, instead of matching geometric features, these methods aim to match correspondent landmarks together or align similar clusters.

3.2.1 Register Surface Meshes using Geometric Information

First Order Ellipsoid Registration

Section 2.6.1 and 2.6.2 described the working procedures of SPHARM parameterization and expansion. As a result, a 3D hippocampal surface based on computing coefficients and user-desired degrees is introduced. Since the goal is to compare different subjects across groups, a method that can align all these objects into a common reference system should be introduced; with the consideration of utilizing geometric information, the registration task can be handled by First Order Ellipsoid (FOE). It generates a shape descriptor (i.e., excluding translation, rotation, and/or scaling) from a standardized set of SPHARM coefficients, which are comparable across objects.

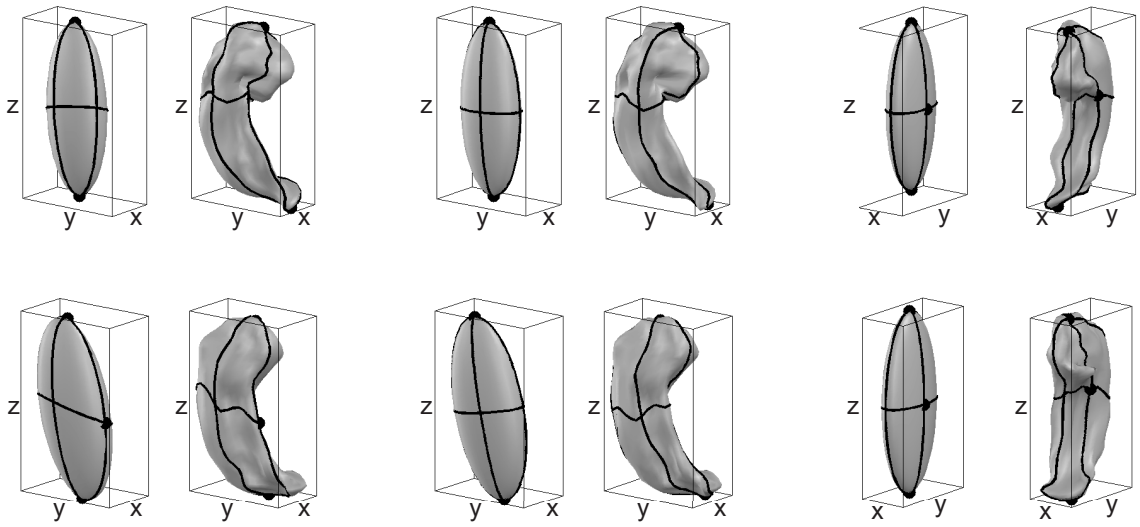

(a) original objects (b) aligned parameterizations (c) aligned objects

Fig. 3.1.: First order ellipsoid (FOE) registration. There is one identical sample hippocampus on each row. The ellipsoids are FOE representations of the sample, while the hippocampi are reconstructed using SPHARM expansion with degree of 15. Parameterization correspondences (solid lines and dots) are indicated on each surface: the Equator is defined as $\theta = \pi/2$, and each longitudinal line is separately defined as $\phi = -\pi/2$, 0, $\pi/2$, π. The north and south poles and the point ($\pi/2$, 0) are shown as dots. (a) shows initial parameterization and pose of the two surfaces. (b) shows the alignment in parameter space (parameter net adjustment). (c) shows the alignment in subject space (pose adjustment).

Figure 3.1 illustrates the registration procedures for SPHARM models by aligning the first order reconstruction of the hippocampus. There are two samples of the hippocampus used in this test and each row demonstrates the exact procedures of shape alignment. For each pair of (a-c), it demonstrates the reconstructed hippocampal surfaces: on the left side, it is the first degree reconstruction (an ellipsoid); and on the right side, it is the 15th degree reconstruction (a more accurate approximation of hippocampus). In this scenario, we assume surface parameterization is performed, and spherical coefficients are calculated. Figure 3.1(a) shows one hippocampus's original

gesture(on the right side), surface parameterization (simplified as lines and crossing points) and its first order reconstruction (FOE, on the left side). To further explain this, the correspondence between two SPHARM models is intimated by the underlying parameterization on the surface: two surface dots with a pair of same surface parameter (θ, ϕ) on two different surfaces are identified to be a corresponding pair. Thus, in Figure 3.1(b), the FOE algorithm is used to match the surface parameterization in the parameter space, it establishes the surface correspondence by rotating parameter net: although the pose of the hippocampus stays unchanged, the surface mesh on each FOE is rotated to a canonical position such that the north pole is at one end of the longest primary axis, and the crossing point of the zero meridians and the equator is at one end of the shortest primary axis. A transformation that aligns the parameterization of FOE to a canonical position also aligns the degree 15 (or any other degree) reconstruction to a canonical position correspondingly. Figure 3.1(c) shows the final step of FOE. The FOE is applied to adjust the hippocampus's orientation in the object space: the FOE is rotated such that its main axes coincide with the coordinate axes, putting the shortest axis along x and longest along z. Thus, We can define the north pole as the point at one end of the longest main axis, and the crossing point of the zero meridians and the equator is at one end of the shortest main axis. By completing the above two steps, we successfully registered the two samples of the hippocampus to a canonical position in both parameter space and object space. More complete theories and implementation details of the algorithm can be found in Brechbuhler et al. [91, 109].

However, this alignment technique works with a restriction that only when the first order reconstruction is a real ellipsoid, as we showed the hippocampus data used in this study. If this restriction is broken, for example, if our experimental object is an ellipsoid of revolution or a sphere, FOE will be failed. There are also other scenarios in which FOE registration may not work well. Even though this limitation will not cause a problem in this thesis, a more general method that can be applied in broader study scenarios is desired.

3.2.2 Register Surface Meshes using Clustered Labels

Image Registration: demons Algorithm

Demons algorithm was widely used in 2D MRI and CT image registration, it was proposed by Thirion et al. [110], which was inspired by Maxwell's demons functions. Then Vercauteren et al. [111] further validated theoretical basis of demons algorithm. With the recent development of demons algorithm, several variants [36,60,81,82,112] were proposed to improve the performance of demons algorithm, and Yeo et al. [37] extended the 2D image-based demons algorithm to 3D spherical space.

Demons algorithm is based on a two-step optimization scheme, and it can be seen as an optimization scheme on the whole space of displacement fields. In the first step, it intends to search for the update direction of each node. While in the second step, it seeks to regularize the generated displacement fields and form the new warp.

Given a fixed image $F(.)$ and a moving image $M(.)$, we assume they are scalar-valued images. The transformation $\Gamma(.)$: $p \rightarrow \Gamma(p)$, models the spatial mapping of vertices from the fixed image space to the moving image space. Spatial transformations are represented by a displacement field Γ, which is added to an identity transformation to get the transformation:

$$\Gamma : \quad p \rightarrow p + \Gamma(p).$$

We define a similarity criterion $Sim(.,.)$, it measures the commonality of two surfaces. In the following parts, we take the mean squared error to measure the similarity between $F(.)$ and $M(.)$:

$$Sim(F, M \circ \Gamma) = \frac{1}{2}\|F - M \circ \Gamma\|^2 = \frac{1}{\Omega_p} \sum_{p \in \Omega_P} \|F(p) - M(\Gamma(p))\|^2, \qquad (3.1)$$

where Ω_P is the area of intersection between F and $M \circ \Gamma$. However, with no regularization, Equation 3.1 causes an ill-posed problem with unstable and non-smooth solutions. To avoid this issue and apply to add some possible apriori knowledge, a

regularization term $Reg(s)$ can be added to resolve this problem. Then we can define the global energy:

$$E(\Gamma) = \frac{1}{\sigma_i^2} Sim(F, M \circ \Gamma) + \frac{1}{\sigma_T^2} Reg(\Gamma), \tag{3.2}$$

where σ_i^2 states for the noise on the image intensity, and σ_T^2 adjusts the amount of regularization we need. We further introduce a hidden transformation γ and formulate an optimization objective function, it seeks:

$$\begin{aligned}(\gamma^*, \Gamma^*) = \underset{\gamma,\Gamma}{\operatorname{argmin}} \|\Sigma^{-1}(F - M \circ \Gamma)\|^2 \\ + \frac{1}{\sigma_x^2} dist(\gamma, \Gamma) + \frac{1}{\sigma_T^2} Reg(\gamma),\end{aligned} \tag{3.3}$$

where:

$$dist(\gamma, \Gamma) = \|\gamma - \Gamma\|^2, \tag{3.4}$$

$$Reg(\gamma) = \|\nabla(\gamma - Id)\|^2, \tag{3.5}$$

and σ_x and σ_T are parameters that control the trade-off between the image similarity and regularity of the registration process. For a group registration issue, Σ is a diagonal matrix that illustrates the variability of a feature at a particular vertex across the group. Equation 3.4 suggests the geodesic distance from hidden transformation to optimized transformation. Equation 3.5 indicates regularization penalization on gradient magnitude of the displacement field $\gamma - Id$ of γ. Algorithm 1 shows the demons algorithm, where $\vec{v}$ is a stationary velocity field that indicates transformation velocity. Detailed parameter explanations can be found in [37, 111]. The energy function shown here can lead to a mathematically solid scheme to resolve the problem, but it is intend to bring an intensive computational burden by mixing of the similarity and the regularization terms and trying to optimize those two terms at the same time.

To summarize up, this computational scheme creates a two-step optimization procedure that separately optimizes the similarity and regularity in first two (first and second) and last two (second and third) terms of Equation 3.3. The first two terms are formulated as a nonlinear least-squares problem, which can be efficiently optimized

Algorithm 1 Demons Registration Algorithm

1: **Input:** A fixed image F and moving image M.

2: **Output:** Transformation Γ so that $\min dist(F - M \circ \Gamma)$ achieved.

3: Initialize $\gamma^0 =$ identity transformation

4: **repeat**

5: Step 1: Given $\gamma^{(t)}$

6: Minimize the first two terms of 3.3

$$u^{(t)} = \underset{u}{\operatorname{argmin}} \|\Sigma^{-1}(F - M \circ \left\{\gamma^{(t)} \circ u\right\})\|^2 + \frac{1}{\sigma_x^2} dist(\gamma, \Gamma) \tag{3.6}$$

7: Compute $\Gamma^{(t)} = \gamma^{(t)} \circ u^{(t)}$

8: Step 2: Given $\Gamma^{(t)}$

9: Update $\gamma^{(t+1)}$ by minimizing the last two terms of 3.3

$$\Upsilon^{(t+1)} = \arg\min_{\Upsilon} \frac{1}{\sigma_x^2} \operatorname{dist}\left(\Upsilon, \Gamma^{(t)}\right) + \frac{1}{\sigma_T^2} \operatorname{Reg}(\Upsilon) \tag{3.7}$$

10: **until** Convergence

via Gauss-Newton scheme; and last two terms can be resolved by a single convolution of the displacement field Γ using a Gauss Kernel. As summarized in Algorithm 1, the demons method begins with an identity transformation γ^0 as the initial displacement field, then it iteratively optimizes an update transformation, which can update the current transformation by composing with the current estimate.

Spherical Demons Algorithm

With the basic idea of demons algorithm working procedures, we further explain the extended work in 3D spherical space. We assume two unit spheres with identical surface mesh distribution, one of both is fixed sphere $F(.)$ and the other is moving sphere $M(.)$. Recall demons Algorithm in 2D image registration, each update is calculated on individual vertex; now in Spherical demons Algorithm, a coordinate chart is introduced for each surface vertex to update displacement field. Usually, at least six coordinate charts are required to cover a sphere. With the considerations that 1) we hope to reduce formula complexity and simplify derivations; 2) SD algorithm can update the velocity vector individually on each vertex, we choose N coordinate charts to cover a spherical image, where N is the total number of vertices. So we can obtain a set of N tangent vectors $\left\{\vec{\Gamma}_n\right\}_{n=1}^{N}$ that transforms N vertices $\{x_n\}_{n=1}^{N}$ to new locations $\{\Gamma(x_n)\}_{n=1}^{N}$.

Optimization of Step 1 in Algorithm 1: To more specifically explain this, let $T_{x_n}S^2$ be the tangent space at x_n, $\vec{\Gamma}_n \in T_{x_n}S^2$. The step 1 in Algorithm 1 formulates a minimization problem for solving least-squares with respect to the velocity field

$\vec{v} \triangleq \{\vec{v}_n \in T_{x_n}S^2\}_{n=1}^N$. By substituting $u = \exp(\vec{v})$ and $\text{dist}(\Upsilon, \Gamma) = \sum_{n=1}^N \left\| \vec{\Upsilon}_n - \vec{\Gamma}_n \right\|^2$ in Equation 3.6:

$$\begin{aligned}
\vec{v}^{(t)} &= \arg\min_{\vec{v}} f(\vec{v}) \\
&= \arg\min_{\vec{v}} \left\| \Sigma^{-1} \left(F - M \circ \left\{ \Upsilon^{(t)} \circ \exp(\vec{v}) \right\} \right) \right\|^2 \\
&+ \frac{1}{\sigma_x^2} \text{dist} \left(\Upsilon^{(t)}, \left\{ \Upsilon^{(t)} \circ \exp(\vec{v}) \right\} \right) \\
&= \arg\min_{\vec{v}} \sum_{n=1}^N \frac{1}{\sigma_n^2} \left(F\left(x_n\right) - M \circ \left\{ \Upsilon^{(t)} \circ \exp(\vec{v}) \right\} \left(x_n\right) \right)^2 \\
&+ \frac{1}{\sigma_x^2} \sum_{n=1}^N \left\| \vec{\Upsilon}_n^{(t)} + G_n^2 \left\{ \Upsilon^{(t)} \circ \exp(\vec{v}) \right\} \left(x_n\right) \right\|^2,
\end{aligned} \tag{3.8}$$

where $\circ$ denotes transformation vector composition. Equation 3.8 is a mapping from the tangent bundle TS^2 to the real numbers $\mathbb{R}$. Each tangent vector $\vec{v}_n$ is treated as a 3×1 vector in $\mathbb{R}^3$, and it is tangent to the spherical surface at a point x_n. Therefore $\vec{v}_n$ only have 2 directional constrains in the plane of TS^2, which means it has 2 degrees of freedom. Thus, Equation 3.8 can be seen as a constrained optimization problem, which is not ideal in solving the problem. Rather than working with the constraints, one possible solution is to introduce coordinate charts which are diffeomorphisms between open sets in $\mathbb{R}^2$ and and open sets on S^2, as important and nice properties of diffeomorphisms, the mappings will be smooth and invertible. Refer to [37], let $\vec{e}^{n1}$ and $\vec{e}^{n2}$ be any two orthonormal 3×1 vectors tangent to the sphere at x_n, a local coordinate chart $\Psi_n : \mathbb{R}^2 \mapsto S^2$ is defined as:

$$\Psi_n\left(x'\right) = \frac{x_n + E_n x'}{\left\| x_n + E_n x' \right\|}, \tag{3.9}$$

where $E_n = [\vec{e}^{n1} \quad \vec{e}^{n2}]$.

Let $\vec{z}_n$ be a 2×1 tangent vector at the origin of $\mathbb{R}^2$, the corresponding tangent vector at x_n is given by the differential of the mapping $D\Psi_n(\cdot)$ evaluated at $x' = 0$:

$$\begin{aligned} \vec{v}_n &= D\Psi_n(0)\vec{z}_n \\ &= \frac{I_{3\times 3} - \Psi_n(0)\Psi_n^T(0)}{\|\Psi_n(0)\|} E_n \vec{z}_n \\ &= \frac{I_{3\times 3} - x_n x_n^T}{\|x_n\|} E_n \vec{z}_n \\ &= E_n \vec{z}_n = \begin{bmatrix} \vec{e}^{n1} & \vec{e}^{n2} \end{bmatrix} \vec{z}_n. \end{aligned} \tag{3.10}$$

The formulas above determines the mapping of a tangent vector $\vec{z}_n$ at the origin of $\mathbb{R}^2$ to the tangent vector $\vec{v}_n$ at x_n via coordinate chart $D\Psi_n$ at $x' = 0$.

Substituting Equation 3.10 into Equation 3.8, we obtain an unconstrained optimization problem:

$$\begin{aligned} \left\{\vec{z}_n^{(t)}\right\} &= \arg\min_{\{\vec{z}_n\}} \sum_{n=1}^{N} \frac{1}{\sigma_n}^2 \left(F(x_n) - M \circ \left\{\Upsilon^{(t)} \circ \exp\left(\{E_n \vec{z}_n\}\right)\right\}(x_n)\right)^2 \\ &+ \frac{1}{\sigma_x^2} \sum_{n=1}^{N} \left\| \vec{\Upsilon}_n^{(t)} + G_n^2 \left\{\Upsilon^{(t)} \circ \exp\left(\{E_n \vec{z}_n\}\right)\right\}(x_n) \right\|^2 \\ &\triangleq \arg\min_{\{\vec{z}_n\}} \sum_{n=1}^{N} \frac{1}{\sigma_n^2} f_n^2(\vec{z}) + \frac{1}{\sigma_x^2} \sum_{n=1}^{N} \|g_n\|^2 (\vec{z}). \end{aligned} \tag{3.11}$$

We can efficiently resolve the above nonlinear least-squares with Levenberg Marquardt (LM) algorithm [113]. LM algorithm engages the best advantages of both the gradient-descent and the Gauss-Newton methods to optimize and resolve a least square problem. More specifically, the LM algorithm behaves more like a gradient-descent algorithm when the parameters are far away from the optimal value. Conversely, it behaves more like the Gauss-Newton algorithm if the parameters are close to the optimal value.

Optimization of Step 2 in Algorithm 1: The optimization in Step 2 is to regularize the transformation such that the transformation can be as smooth as possible, which will directly reduce mesh distortion caused by registration. The following equation describes the process of the second step in the spherical demons algorithm:

$$\vec{\Upsilon}^{(t+1)} = \arg\min_{\vec{\Upsilon}} \frac{1}{\sigma_x^2} \sum_{n=1}^{N} \left\| \vec{\Upsilon}_n - \vec{\Gamma}_n^{(t)} \right\|^2 + \frac{1}{\sigma_T^2} \|\vec{\Upsilon}\|_V. \tag{3.12}$$

As discussed earlier, it attempts to minimize the function such that a vector field $\vec{\Upsilon} \in V$ can smoothly approximates the tangent vectors $\left\{\vec{\Gamma}_n^{(t)}\right\}_{n=1}^{N}$. Motivated by the convolution methods to optimize the second step in the demons algorithm [110, 111, 114] and the fast fluid registration methods based on convolution in the Euclidean space [115], In a recent work [36, 37], they adopted an step-by-step approximation strategy to resolve the spherical vector spline interpolation problem by iterative smoothing. In order to achieve the minimization with a convolution, the regularization term $Reg(\vec{\Upsilon})$ is typically taken as a norm of a differential operator. As a well-known example, applying a Gaussian kernel of smoothing on the displacement field can lead to a minimum of the harmonic energy in $\mathbb{R}^n$. [116].

Thus, for the computational convenience and efficiency, in practice, this optimization problem can be resolved by a single convolution of the displacement field Γ using a Gauss Kernel [36, 37].

Computation for Matrix Exponential: In practice, we adopted the scaling and squaring method [117, 118] to compute $\exp\left(\vec{v}^{(t)}\right)$ for $\Gamma^{(t)} = \gamma^{(t)} \circ \exp\left(\vec{v}^{(t)}\right)$ and $u^{(t)} = \exp\left(\vec{v}^{(t)}\right)$. It employs Pade approximants to calculate $u \approx e^v$. For $e^v = \left(e^{v/\sigma}\right)^{\sigma}$, where $v \in \mathbb{C}^{n\times n}$ and $\sigma \in \mathbb{C}$, it numerically integrates the smoothly interpolated velocity field v and requires the following steps:

1. $v \leftarrow v/2^s$ so $\|v\|_\infty \approx 1$
2. $r_m(v) = [m/m]$ Pade approximant to e^v
3. $u = r_m(v)^{2^s}$

where $r_m(x) = p_m(x)/q_m(x)$ can be obtained by:

$$\begin{aligned} p_m(x) &= \sum_{j=0}^{m} \frac{(2m-j)!m!}{(2m)!(m-j)!} \frac{x^j}{j!}, \\ q_m(x) &= p_m(-x). \end{aligned} \tag{3.13}$$

To explain this, the first step is to choose σ an integral power of 2. Thus, $\sigma = 2^s$ and $v/2^s$ has norm of order 1. The second step is to calculate Pade approximant to e^v by $e^{v/2^s} \approx r_m\left(v/2^s\right)$, where r_m is a $[m/m]$ Pade Approximant. Thus, in the third step, we take $e^v \approx r_m\left(v/2^s\right)^{2^s}$, then $u = r_m(v/2^s)^{2^s}$ is obtained by s repeated squarings.

Now the framework of the spherical demons method is fully introduced and can be summarized as the following Algorithm 2:

Demons Variants

Other than the basic demons method and spherical demons, a variant of the demons-based algorithms were proposed for a wide of application scenarios. For example, the symmetric demons force was reported that it outperformed compositive and additive demons forces in [111,119]; Han et al. demonstrated a momentum term could help in convergence in [81]; Zhao et al. employed a deep learning framework for demons registration [120]. In this section, the fundamental theories of different types of regularization strategies and several demons forces will be introduced.

Two Types of Regularization: Regularization terms are usually employed to ensure the smoothness of the displacement field Γ and have a high impact on mesh regularity and registration accuracy. In our framework, regularization is applied by a single convolution of the displacement field Γ using a Gauss Kernel smoothing. Common instances of regularization are modeling of physical processes. For exam-

Algorithm 2 Spherical Demons Registration Algorithm

Input: A fixed spherical image F and moving spherical image M.

Output: Transformation Γ so that $\min dist(F - M \circ \Gamma)$ achieved.

Initialize γ^0 = identity transformation

repeat

    Step 1: Given $\gamma^{(t)}$

    for each vertex k **do**

        Compute the velocity $\vec{v}_n^{(t)}$ stated in Equation 3.8

    end for

    $\Gamma^{(t)} = \gamma^{(t)} \circ \exp(\vec{v}^{(t)})$ using "scaling and squaring".

    Step 2: Given $\Gamma^{(t)}$

    for each vertex k **do**

        Update $\gamma^{(t+1)}$ using iterative smoothing.

    end for

until Convergence

ple, smoothing the accumulated displacement field usually leads to a "diffusion-like regularization" and smoothing the update usually leads to a "fluid-like regularization" [111, 121].

Additive Demons: In the additive demons method showing in the Algorithm 3, the demons algorithm is conducted within the whole space of transformation by adding additive updates $s + u$. This form is inspired by the classic update rules employed in the Newton methods on vector spaces. However, this type of update rules is abandoned in this thesis as we work on spatial transformations and adding additive updates has no geometrical meanings. This method was adopted in several studies of 2D non-rigid image registration [114, 122] given the advantages of less computationally expensive.

Algorithm 3 Additive Demons Algorithm

1: **Input:** A fixed image F and moving image M.

2: **Output:** Transformation Γ so that $\min dist(F - M \circ \Gamma)$ achieved.

3: Initialize $\gamma^0 =$ identity transformation

4: **repeat**

5: Given $\gamma^{(t)}$, optimize the energy function:

$$\begin{aligned} u^{(t)} = \underset{u}{\operatorname{argmin}} \, & \|\Sigma^{-1}(F - M \circ \{\gamma^{(t)} + u^{(t)}\})\|^2 \\ & + \frac{1}{\sigma_x^2} dist(\gamma^{(t)}, \Gamma^{(t)}) + \frac{1}{\sigma_T^2} \operatorname{Reg}(\gamma^{(t)}) \end{aligned} \tag{3.14}$$

6: For a fluid-like regularization, $u^{(t)} = K_{fluid} * u^{(t)}$. Typically K_{fluid} is a Gaussian Kernel.

7: Compute $\Gamma^{(t+1)} = \gamma^{(t)} + u^{(t)}$

8: For a diffusion-like regularization, $\gamma^{(t+1)} = K_{diff} * \Gamma^{(t+1)}$. Typically K_{diff} is a Gaussian Kernel.

9: **until** Convergence

Compositive Demons: The idea of compositive demons is similar to the additive demons given the awareness that in a vector space, instead of addition, it is more reasonable to iteratively composite the updates with the spatial transformations or the displacement fields. The compositive demons algorithm can then be described in Algorithm 4.

Algorithm 4 Compositive Demons Algorithm

1: **Input:** A fixed image F and moving image M.

2: **Output:** Transformation Γ so that $\min dist(F - M \circ \Gamma)$ achieved.

3: Initialize $\gamma^0 =$ identity transformation

4: **repeat**

5: Given $\gamma^{(t)}$, optimize the energy function:

$$u^{(t)} = \underset{u}{\operatorname{argmin}} \|\Sigma^{-1}(F - M \circ \gamma^{(t)} \circ \left\{Id + u^{(t)}\right\})\|^2 + \frac{1}{\sigma_x^2} dist(\gamma^{(t)}, \Gamma^{(t)}) + \frac{1}{\sigma_T^2} \operatorname{Reg}(\gamma^{(t)}) \tag{3.15}$$

6: For a fluid-like regularization, $u^{(t)} = K_{fluid} * u^{(t)}$. Typically K_{fluid} is a Gaussian Kernel.

7: Compute $\Gamma^{(t+1)} = \gamma^{(t)} \circ (Id + u^{(t)})$

8: For a diffusion-like regularization, $\gamma^{(t+1)} = K_{diff} * \Gamma^{(t+1)}$. Typically K_{diff} is a Gaussian Kernel.

9: **until** Convergence

Diffeomorphisms in Demons Algorithm: In the work of [111] diffeomorphism was introduced into demons algorithm. Assume there are two manifolds S_a and S_b, a differentiable map $f : S_a \to S_b$ is defined as a diffeomorphism if the mapping is bijective and the inverse mappinng $f^{-1} : S_b \to S_a$ is also differentiable. To summarize it, a diffeomorphic transformation is a continuously differentiable bijective and invertible

mapping with inverse mapping is differentiable as well. Diffeomorphic registration is a non-rigid registration method, it features for 1) no foldings, 2)topology preservation and 3) sound assumption if no privileged direction.

Symmetric Demons Forces: Let Im_0 be the target image and Im_1 be a source image. We can define the general form of global energy as the following function:

$$E\left(Im_0, Im_1, \Gamma, \gamma\right) = \frac{1}{\sigma_i^2}\,\mathrm{Sim}\left(Im_0, Im_1, \Gamma\right) + \frac{1}{\sigma_x^2}\,\mathrm{dist}(\gamma, \Gamma)^2 + \frac{1}{\sigma_T^2}\,\mathrm{Reg}(\gamma). \quad (3.16)$$

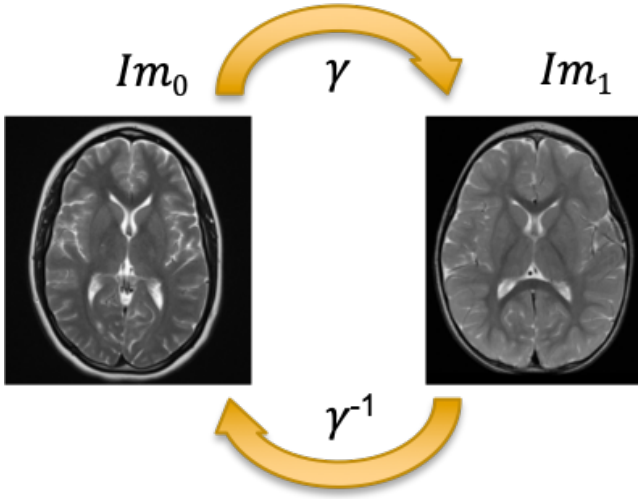

Fig. 3.2.: A diagram of forward and backward transformations between Im_0 and Im_1: the transformation $\gamma = \exp(v)$, the inverse transformation is the backward computation $\gamma^{-1} = \exp(-v)$.

As we assume the transformation is diffeomorphic by applying the strategy introduced in [37, 111]. There must exists an unique and differentiable inverse mapping of the spatial transformation. As the transformation can be termed as $\gamma = \exp(v)$, the inverse transformation can be obtained from the backward computation $\gamma^{-1} = \exp(-v)$. This process is illustrated in the Figure 3.2. A symmetric registration framework tries to optimize the global energy regarding the forward and backward

transformations at the same time. Thus, the combined transformation can be more smooth:

$$\left[\gamma_{opt}, \gamma_{opt}^{-1}\right] = \arg\min_{[\gamma,\gamma^{-1}]} E\left(Im_0, Im_1, \Gamma, \gamma\right) + E\left(Im_1, Im_0, \Gamma^{-1}, \gamma^{-1}\right). \tag{3.17}$$

We formulate it as a constrained optimization using two diffeomorphisms:

$$\left[\gamma_{opt}, \gamma_{opt}^{-1}\right] = \arg\min_{[\gamma,\gamma^{-1}]} E\left(Im_0, Im_1, \gamma\right) + E\left(Im_1, Im_0, \gamma^{-1}\right). \tag{3.18}$$

The symmetric force is defined by averaging the difference value of the forward transformation and the backward transformation, K_{diff} is typically a Gaussian kernel to smooth the update:

$$\boldsymbol{v} \leftarrow \frac{1}{2} K_{\text{diff}} * \left(Z\left(\boldsymbol{v}, K_{\text{fluid}} * \boldsymbol{u}^{\text{forw}}\right) - Z\left(-\boldsymbol{v}, K_{\text{fluid}} * \boldsymbol{u}^{\text{back}}\right)\right). \tag{3.19}$$

Algorithm 5 Symmetric Demons Algorithm

1: **Input:** A fixed image F and moving image M.
2: **Output:** Transformation Γ so that $\min dist(F - M \circ \Gamma)$ achieved.
3: Initialize $\gamma^0 =$ identity transformation
4: **repeat**
5: Given $\gamma^{(t)}$
6: Compute the demons forces $\boldsymbol{u}^{\text{forw}}$ to optimize $E\left(I_0, I_1, \exp(\boldsymbol{v}), \boldsymbol{u}^{\text{forw}}\right)$
7: Compute the demons forces $\boldsymbol{u}^{\text{back}}$ to minimize $E\left(I_1, I_0, \exp(-\boldsymbol{v}), \boldsymbol{u}^{\text{back}}\right)$
8: For a fluid-like regularization, $u^{(t)} = \frac{1}{2} K_{fluid} * (u^{\text{forw}} - u^{\text{back}})$. Typically K_{fluid} is a Gaussian Kernel.
9: Compute $\Gamma^{(t+1)} = \gamma^{(t)} \circ (Id + u^{(t)})$
10: For a diffusion-like regularization, $\gamma^{(t+1)} = K_{diff} * \Gamma^{(t+1)}$ else $\gamma^{(t+1)} = \Gamma^{(t+1)}$. Typically K_{diff} is a Gaussian Kernel.
11: **until** Convergence

Momentum Term: Gradient descent optimization can be stimulated using a momentum term calculated from past updates as a predictive step for subsequent iterations. The momentum-based strategy can accelerate convergence, damped oscillation, and potentially avoid local optima [81].

The momentum term $\mathbf{p}^{[n]}$ is based on the past update field $\boldsymbol{u}^{[n-1]}$ and adjusts the current iteration $[n]$ according to:

$$\begin{aligned} \mathbf{p}^{[n]} &= \alpha \boldsymbol{u}^{[n-1]}, \\ \boldsymbol{u}^{[n]} &\leftarrow \boldsymbol{u}^{[n]} \circ \mathbf{p}^{[n]}, \end{aligned} \tag{3.20}$$

where α is a parameter managing the force ("amount") of momentum in the current iterationa constant ranging between $[0, 1]$ that balances the update field. As shown in the Algorithm 6, the momentum term $\mathbf{p}$ increases the step size when the previous update has the same direction as the current update, and it inhibits sudden changes that can be generated by noise or artifact. Since the momentum term is a diffeomorphic transformation multiplied by a scalar, composing it with the current update maintains diffeomorphism.

3.2.3 Stopping Criteria

A fundamental argument in deformable image registration and shape alignment is to perform a robust matching result at an inexpensive computational cost. Given the iterative nature of the optimization scheme, a well-designed algorithm must automatically detect convergence and stop the iterative process when most appropriate. The most basic and commonly used strategy is to terminate the algorithm after a predetermined number of iterations. It is a straightforward idea adopted by many Gauss-Newton (GN) based algorithms as GN features for the fast convergence. However, this method is only weakly related to the actual convergence, especially when a trade-off between image similarity and mesh distortion is considered, unnecessarily additional iterations may increase mesh distortion rapidly, but image similarity does not reduce visibly. Other than assigning a constant number of iterations, the com-

Algorithm 6 Momentum-Based Demons Algorithm

1: **Input:** A fixed image F and moving image M.

2: **Output:** Transformation Γ so that $\min dist(F - M \circ \Gamma)$ achieved.

3: Initialize γ^0 and $\mathbf{p}$ = identity transformation

4: **repeat**

5: Given $\gamma^{(t)}$, optimize the energy function:

$$u^{(t)} = \underset{u}{\operatorname{argmin}} \|\Sigma^{-1}(F - M \circ \{\gamma^{(t)} + u^{(t)}\})\|^2 + \frac{1}{\sigma_x^2} dist(\gamma^{(t)}, \Gamma^{(t)}) + \frac{1}{\sigma_T^2} \operatorname{Reg}(\gamma^{(t)}) \tag{3.21}$$

6: Apply momentum to $u^{(t)}$ using Equation 3.20

7: For a fluid-like regularization, $u^{(t)} = K_{fluid} * u^{(t)}$. Typically K_{fluid} is a Gaussian Kernel.

8: Compute $\Gamma^{(t+1)} = \gamma^{(t)} + u^{(t)}$

9: For a diffusion-like regularization, $\gamma^{(t+1)} = K_{diff} * \Gamma^{(t+1)}$. Typically K_{diff} is a Gaussian Kernel.

10: Update momentum $\mathbf{p}$

11: **until** Convergence

monly used stopping criteria are: 1) velocity field update step size, 2)mean squared error of the distance between two subjects, and 3) harmonic energy. Each stopping condition should be numerically formulated so that a threshold can be defined and adjusted. A properly chosen stopping criterion will help in keeping a proper convergent rate and saving computational power.

Quantity of Update

The first stopping criteria is based on quantity of update (QU) between current iterative step and last step. It measures the difference in step sizes between current warp and previous warp. The QU we used in this study is modified from the method defined by Yang et al. [123] as:

$$\mathrm{QU}_i = \frac{\sum |Uw_i|}{\sum |w_{i-1}|}, \tag{3.22}$$

where i indicates the "ith" iteration, w_{i-1} is the step size of the warp in the previous iteration and Uw_i is the updated step size of the warp at current iteration. As QU_i decreases with convergence, we can compute:

$$\left| \frac{\mathrm{QU}_{i-1} - \mathrm{QU}_i}{\mathrm{QU}_0} \right| < \varepsilon_{QU}. \tag{3.23}$$

We expect that the difference between current update QU_i and previous update QU_{i-1} normalized by the original update QU_0 can decrease with convergence. Thus, it stops the algorithm when this ratio below the threshold ε_{QU}.

Root Mean Squared Error

An alternative convergence criterion is based on pixel intensity (in 2D) or voxel value (in 3D) disparity between the warp in current iteration with respect to the warp in the previous step. We set root mean square error (RMSE) as a sufficiently small threshold $\varepsilon_{\mathrm{RMSE}}$, quantifying the error reduction between iterations, this process is formulated as the following equation:

$$\mathrm{RMSE}(F, M) = \sqrt{\frac{1}{k}\sum_{i=1}^{k} \|F(x_i) - M(x_i)\|^2} \tag{3.24}$$

where k is the total vertex number for each interpolated surface, and $F(x_i)$ and $M(x_i)$ are the corresponding label values at vertex x_i of template and individual respectively.

$$\frac{\mathrm{RMSE}_n - \mathrm{RMSE}_{n-1}}{\mathrm{RMSE}_0} > \varepsilon_{\mathrm{RMSE}}, \tag{3.25}$$

where n indicates the "nth" iteration. On the left side of the equation, values close to zero represent convergence; hence, a positive ratio indicates divergence. In this situation, the registration can be allowed to continue provided that non-convergence remains below the user-defined threshold $\varepsilon_{\mathrm{RMSE}}$.

Harmonic Energy

The last condition to examine is harmonic energy (HE), it is also called Dirichlet Energy [124]. Given a function $F = (f_1, \ldots, f_m) : D \subset R^n \rightarrow R^m$, the Dirichlet Energy is a measure of how much the function F changes over D:

$$E(F) = \int_D |dF(p)|^2 dp = \sum_{i=1}^{m} \int_D |\nabla f_i(p)|^2 \, dp. \tag{3.26}$$

In our case of discrete vertices on surfaces, HE is defined as the average over all vertices of the squared Frobenius norm of the vector field Jacobian and is correlated to the smoothness of the field [125]. In this study, we adopted the method proposed in [126] and implemented HE using the following equations:

$$HE = \sum_{[u,v] \in K} \theta_{uv} \|\Gamma(u) - \Gamma(v)\|^2, \tag{3.27}$$

where u and v are two vertices that define an edge, K is the triangle that contains u and v, and Γ is a transformation of current warp. Coefficients $\theta_{uv} = \cot\alpha + \cot\beta$, where α and β are the angles opposite to the edge $[u, v]$.

If the registration is converging, HE_i would than be greater than HE_{i-1} and as such the escape condition becomes:

$$\frac{\mathrm{HE}_i - \mathrm{HE}_{i-1}}{\mathrm{HE}_{i-1}} < \varepsilon_{\mathrm{HE}}. \tag{3.28}$$

The harmonic energy was found to give the best trade-off between robustness and convergent rate for the analyzed registration method at coarse registration but was outperformed by mean squared error when using all the original voxel information in [127]. HE will be treated as an important parameter to evaluate the quality of registration in this thesis.

3.2.4 The Proposed Method

With the awareness of the benefits brought from different demons methods, a surface registration method that combines all of the benefits and extends the 2D demons Algorithm to 3D spherical domain is demanded. Thus, a method is designed to align surface labels usually returned from segmentation tools and can be applied in a wide range of surface-based morphometric studies.

As shown in Figure 3.3, it demonstrates the work flow of the proposed registration method based on demons algorithm. The whole process is organized into 4 parts: data preparation, initial processing, update calculating and regularization. In the data preparation, we extract surface features such as binary maps and distance maps. Then in the initial processing, we firstly adopt a multi-level interpolation scheme which interpolates both F and M to a subdivided icosahedron meshes, from coarsest to finest. To increase the efficiency of the algorithm, we do a rotation in the beginning of each level to roughly match F and M. Then we calculate the symmetric demons force, and apply the momentum term on it. Lastly, we apply regularization terms on both the update u and the final deformation field capital gamma. We keep this iterative process until it converges. The detailed working procedures are described in Algorithm 7.

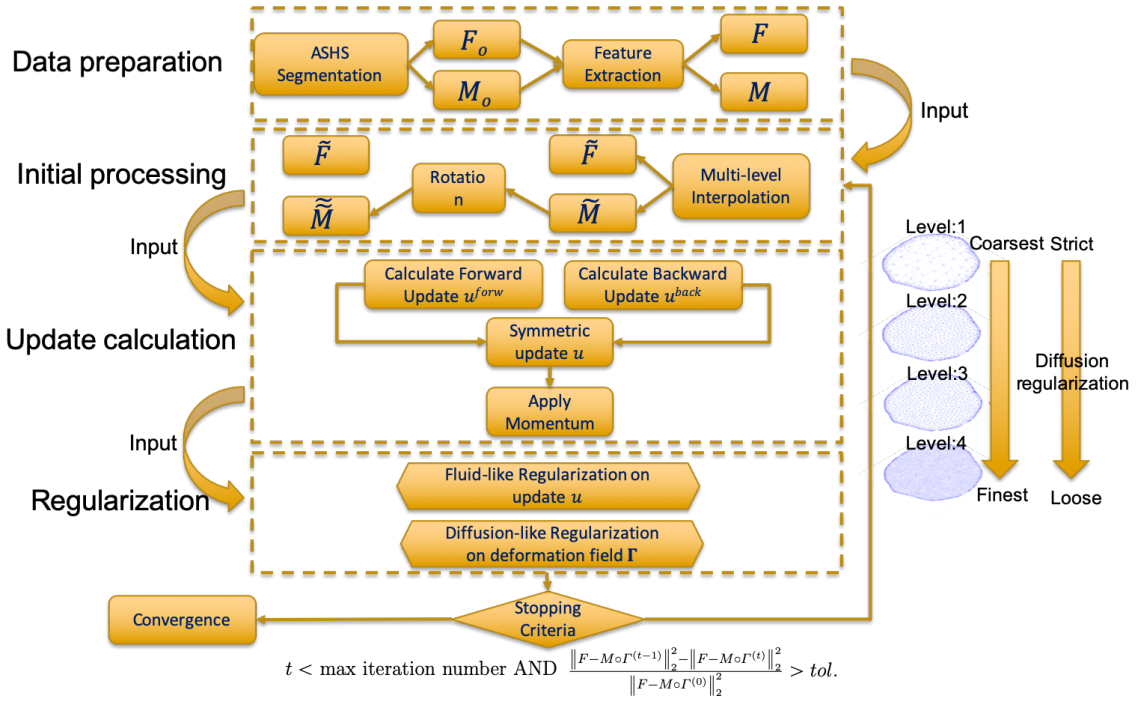

Fig. 3.3.: Structure of the proposed registration algorithm.

From Figure 3.3 we can see, the proposed surface registration method adopted a multiscale scheme from coarsest to finest. At the beginning of the multiscale scheme, a downsampling interpolation is applied on the original surface meshes to reduce resolution of the surface vertices to "ic4". This strategy is motivated by the assumption that large deformations on the surface mesh are usually related to coarse geometric information. Then beginning from the second level, an upsampling interpolation is applied on the original surface meshes to increase resolution of the surface vertices to "ic5","ic6","ic7" respectively at each level. With a higher resolution of surface mesh, finer details of geometric information such as a more precise local shape change can be better captured with a higher scaled interpolation. By combining both coarse and fine scaled registration, the multiscale registration scheme tackles the registration problem in both macroscopic and microcosmic views.

To demonstrate the advantages of employing a multi-resolution scheme, we designed a test to compare the registration results of multi-resolution and single resolution (highest resolution, "ic7") scheme. We applied both methods to register 80 hippocampal surfaces with same parameters including stopping criteria, the only difference is about the resolution: in the multi-resolution scheme, surface vertices were interpolated to "ic4", "ic5", "ic6" and "ic7" gradually, while in the single resolution scheme, surface vertices were interpolated to "ic7" directly. We compared the dice similarity coefficient (DSC, it will be explained in Chapter 4.) and root mean square error (RMSE) between two methods, the results with group mean and variance are shown in Figure 3.4. As we can see from the results, the multi-resolution based method scored lower RMSEs and higher DSCs in general, which means it achieved better registration results.

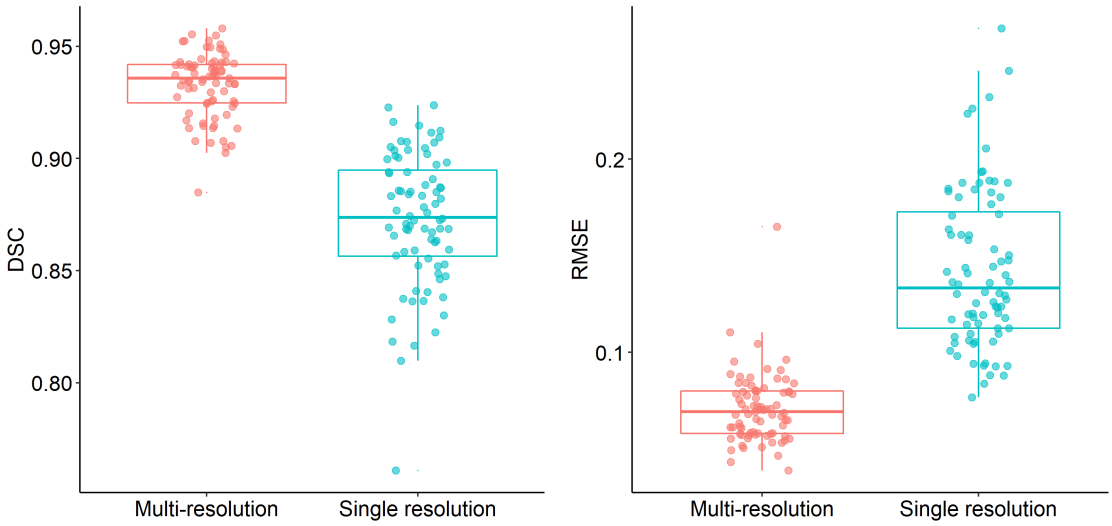

Fig. 3.4.: Comparisons between multi-resolution based method and single resolution based method. DSC: dice similarity coefficient; RMSE: root mean square error.

Algorithm 7 Label-guided Spherical Demons Registration Algorithm

Input: A fixed spherical image F and moving spherical image M.

Output: Transformation Γ so that $\min dist(F - M \circ \Gamma)$ achieved.

Initialize γ^0 = identity transformation

while $t <$ max iteration number AND $\frac{\left\|F-M\circ\Gamma^{(t-1)}\right\|_2^2-\left\|F-M\circ\Gamma^{(t)}\right\|_2^2}{\left\|F-M\circ\Gamma^{(0)}\right\|_2^2} > tol.$ **do**

    Step 1: Given $\gamma^{(t)}$

    for each vertex k **do**

        Optimize $\boldsymbol{u}^{\text{ forw}}$ for the first two terms in $E\left(F, M, \exp(\vec{\boldsymbol{v}}^{(\boldsymbol{t})}), \boldsymbol{u}^{\text{ forw}}\right)$ stated in Equation 3.16

        Optimize $\boldsymbol{u}^{\text{ back}}$ for the first two terms in $E\left(M, F, \exp(-\vec{\boldsymbol{v}}^{(\boldsymbol{t})}), \boldsymbol{u}^{\text{ back}}\right)$ stated in Equation 3.16

    end for

    Let $u^{(t)} = \frac{1}{2}(u^{\text{ forw}} - u^{\text{ back}})$, apply momentum term using Equation 3.20

    For a fluid-like regularization, $u^{(t)} = K_{fluid} * u^{(t)}$. Typically K_{fluid} is a Gaussian Kernel.

    $\Gamma^{(t)} = \gamma^{(t)} \circ \exp(\vec{v}^{(t)})$ using "scaling and squaring".

    Step 2: Given $\Gamma^{(t)}$

    for each vertex k **do**

        Update $\gamma^{(t+1)}$ by minimizing:

$$\gamma^{(t+1)} = \arg\min_{\gamma} \frac{1}{\sigma_x^2} \operatorname{dist}\left(\gamma^{(t)}, \Gamma^{(t)}\right) + \frac{1}{\sigma_T^2} \operatorname{Reg}(\gamma^{(t)}) \tag{3.29}$$

    end for

    For a diffusion-like regularization, $\gamma^{(t+1)} = K_{diff} * \Gamma^{(t+1)}$. Typically K_{diff} is a Gaussian Kernel.

    Update momentum **p**

end while

Convergence

3.3 Evaluation Measurements

It is common that registration results are never perfect. This is why we need to quantitatively measure the quality of registration. There are several properties of triangular or quadrilateral surface mesh to measure, such as the length of the edge, triangular or quadrilateral area and angle. Root mean square error (RMSE) is commonly used for distance measurement in Euclidean space. It measures the spatial distance between two surfaces or the distance of surface signals on two corresponding meshes. It can be used in measuring line distortion. For deformable models, an objective function is typically used to evaluate registration results. It measures the overall cost or energy of the predefined objective function and aims to achieve a local or global minimum in an optimization sense.

To better explain this, we assume several landmarks are pre-defined. Registration methods aim to match the landmark points of an individual object in a spatial domain to the corresponding landmark points of the reference object and subsequently transform the underlying parametric mesh of the individual object. Non-rigid registration distorts the surface mesh of the individual object, for a SPHARM implementation mentioned in Chapter 2.6.2, some severe and irregular mesh distortion caused by improper registration can introduce additional errors to the SPHARM reconstructed shape of the original object. Therefore, we define a mesh distortion cost function C, it is seen as an ideal reference for mesh quality control.

Mesh distortion cost function C can be measured by calculating the area distortion cost (ArDC), the length distortion cost (LDC) and the angle distortion cost (AnDC).

Length Distortion Measures: To measure length distortion introduced by a registration process, the stretch concept proposed by Sander et al. [128] is adopted and modified in this study. They considered the case of mapping from a 2D planar domain to 3D surface, while our case is to map a 3D surface to another 3D surface. Two singular values of the 3×3 Jacobian matrix were computed to represent the largest and smallest length distortions caused by this transformation. In our case, the length

distortion cost (LDC) C_s with respect to a given mesh mapping Γ from M to $M \circ \Gamma$, is defined as follows:

$$\Psi(M) = M \circ \Gamma, \tag{3.30}$$

$$C_l(M, \Psi(M)) = \sqrt{\frac{\sum_{t_i \in M}(\sigma_1(t_i)^2 + \frac{1}{\sigma_2(t_i)^2})A(\Psi(t_i))}{2A(\Psi(M))}}, \tag{3.31}$$

$$C_l^W(M, \Psi(M)) = max\left\{max\left(\sigma_1(t_i), \frac{1}{\sigma_2(t_i)}\right) | t_i \in M\right\}, \tag{3.32}$$

where $\sigma_1(t_i)$ and $\sigma_2(t_i)$ are the largest and smallest length distortions for a triangle t_i, $A(\cdot)$ is used to denote the area of a triangular or quadrilateral mesh. More details on calculating $\sigma_1(t_i)$ and $\sigma_2(t_i)$ are discussed in [128].

In the above definitions, $C_l(M, \Psi)$ measures the average length distortion cost (LDC) for the whole mesh M, while $C_l^W(M, \Psi)$ represents for the worst LDC. The largest and smallest length distortions are directly computed from the length of three corresponding sides between t_i and $\Psi(t_i)$. In the definitions, contraction and expansion are equally treated. Even though in the original method of [128], they claimed the transformation Γ as an affine, this method can also be extended for deformable mappings.

Another way to measure length distortion is to use Harmonic Energy mentioned in 3.2.3 as it evaluates the total stretching of the transformation. Another critical reason we adopted HE as length distortion criterion is because HE works well in deformable registration cases and Riemann space.

Area Distortion Measures: $A(\cdot)$ is used to denote the area of a triangle or a mesh. The area distortion cost (ArDC) C_{ar} with respect to the mapping $\Psi(M)$ is defined as follows:

For each triangle $t_i \in M$, it measures the local ArDC of a single triangle. For each mesh vertex v in M, we have:

$$C_{ar}(t_i, \Psi(M)) = \frac{A(\Psi(t_i))}{A(t_i)}. \tag{3.33}$$

For each mesh vertex v in M, we have:

$$C_{ar}(v, \Psi(M)) = \frac{\sum_{t_i \in M_v} A(\Psi(t_i))}{\sum_{t_i \in M_v} A(t_i)}, \tag{3.34}$$

where M_v is the set of triangle incident upon v. This measures the local ArDC around a single vertex.

For the whole warped mesh $\Psi(M)$, it measures the overall ArDC for the whole mesh:

$$C_{ar}(M, \Psi(M)) = \frac{\sum_{t_i \in M} max(C_{ar}(t_i, \Psi(M)), \frac{1}{C_{ar}(t_i, \Psi(M))}) A(\Psi(t_i))}{A(\Psi(M))}. \tag{3.35}$$

By taking $max\left(C_{ar}(t_i, \Psi(M)), \frac{1}{C_{ar}(t_i, \Psi(M))}\right)$ as the ArDC contribution from each triangle, we treat contraction and expansion equally, and so always have $C_a(M, \Psi) \geqslant 1$.

Similar to the LDC, the worst ArDC is defined as below:

$$C_{ar}^{W}(M, \Psi) = max\left\{max\left(C_{ar}(t_i, \Psi), \frac{1}{C_{ar}(t_i, \Psi)}\right) | t_i \in M\right\}. \tag{3.36}$$

Angle Distortion Measures: Preserving angles is also crucial in control of mesh quality. Assume a surface mesh contains vertex u, v, w. Thus, edges are $[u, v]$, $[v, w]$ and $[w, u]$, angle $\angle uvw$ is opposite to edge $[v, w]$, angle $\angle uwv$ is opposite to edge $[u, v]$, angle $\angle wvu$ is opposite to edge $[w, u]$.

For each angle a_j in triangle t_i and $t_i \in M$, it measures the local AnDC of a single angle:

$$C_{an}(a_j, \Psi(M)) = \frac{\angle(\Psi(a_j))}{\angle(a_j)}. \tag{3.37}$$

For each mesh vertex v in M, we have:

$$C_{an}(v, \Psi(M)) = \frac{\sum_{a_j \in M_v} \angle(\Psi(a_j))}{\sum_{a_j \in M_v} \angle(a_j)},$$

where M_v is the set of triangle incident upon v. This measures the local AnDC around a single vertex.

For the whole mesh M containing triangle t_i:

$$C_{an}(t_i, \Psi(M)) = \sqrt{\frac{\sum_{t_i \in M, a_j \in t_i} (C_{an}(a_j, \Psi(M))^2 + \frac{1}{C_{an}(a_j, \Psi(M))^2}) A(\Psi(t_i))}{2A(\Psi(M))}}. \tag{3.38}$$

The worst AnDC is defined as below:

$$C_{an}^{W}(M,\Psi) = max\left\{max\left(C_{an}(t_i,\Psi), \frac{1}{C_{an}(t_i,\Psi)}\right)|t_i \in M\right\}. \tag{3.39}$$

At each step of the proposed algorithm in Chapter 3.2.4, the averaged and worst ArDCs, AnDcs and LDCs are evaluated, defined by Equations 3.31, 3.32, 3.35, 3.36, 3.38 and 3.39 respectively. These standards are used to avoid extreme contraction or expansion due to severe mesh distortion. Thus, it helps in monitoring and maintaining the reasonable angle and area distortion as well as length distortion.

3.4 Tests on Synthetic Data

To validate our proposed method, we generated synthetic data based on three categories: 1) Diffusion-like Spherical demons, 2) fluid-like Spherical demons, and 3) Combined Spherical demons. In each category, five tests are performed: compositive demons, diffeomorphic demons, momentum-based demons, symmetric demons, and momentum-based symmetric demons.

3.4.1 Data and Materials

Spherical meshes are obtained from subdividing an icosahedron mesh, and it gives us the flexibility to achieve a multi-resolution scheme for registration. The number of mesh vertices quadruples with the number of subdivisions, so for an "ic4" (shown in Figure 3.5), "ic5" (shown in Figure 3.6) and "ic6" (shown in Figure 3.7) icosahedron meshes, they respectively contain 2562, 10242 and 40962 mesh vertices.

We perform the classic registration task "circle to C" by generating a circle and a shape of "C" on a "ic5" spherical surface. As shown in Figure 3.8, we define a sphere in Cartesian coordinates. In order to generate a circle, we can simply set a threshold θ_x for x coordinates, any x larger than θ_{x1} are marked as circle. Similarly, if we want to further generate a shape of "C", we set another θ_{x2} such that $\theta_{x2} > \theta_{x1}$, then mark x larger than θ_{x2} as background, then find an area satisfy both following conditions:

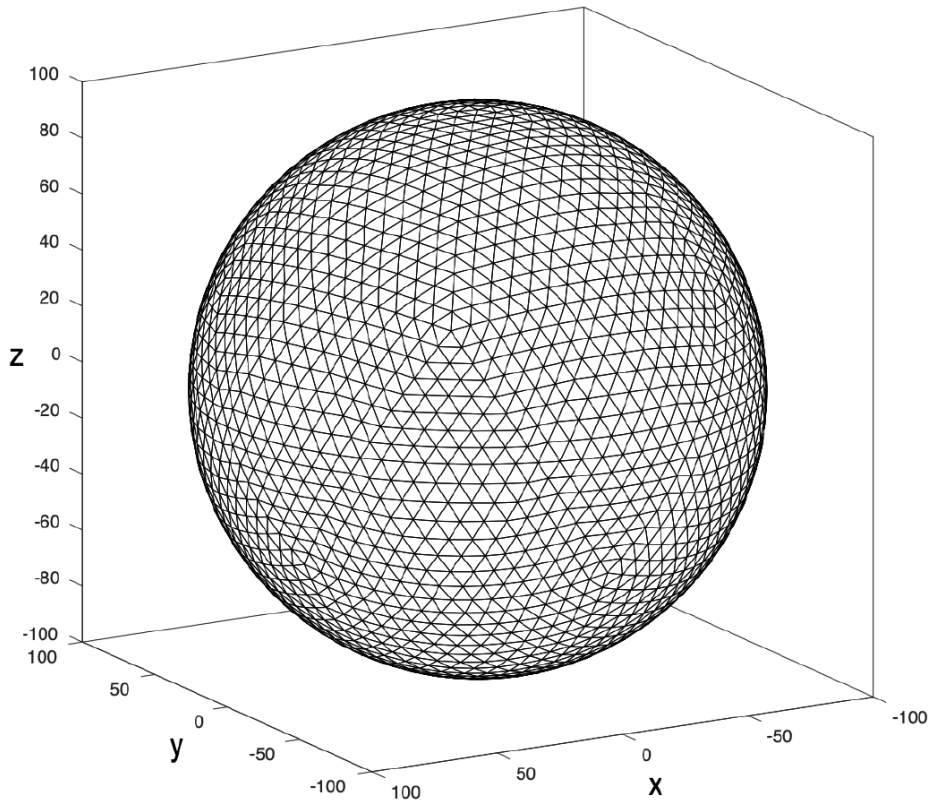

Fig. 3.5.: Subdivided icosahedron meshes at level 4.

$-\theta_y < y < \theta_y$ and $\theta_{z1} < z < \theta_{z2}$, this area is marked as a square area on Figure 3.8(b). Both "circle" and "C" are binary spherical images. At this point, we have generated synthetic data for surface registration. The synthetic data is generated in four levels of resolution, they are shown in Figure 3.9.

3.4.2 Experiments

Based on the regularization types, experiments are classified into three categories: diffusion-like demons, fluid-like demons, and regularization-combined demons. In each category, different demons forces are tested; it includes basic SD, compositive SD, momentum-based SD, symmetric SD, and momentum-based symmetric SD. In the experiments, we set a maximum iteration number to be one hundred, $tol. = -10^{-4}$.

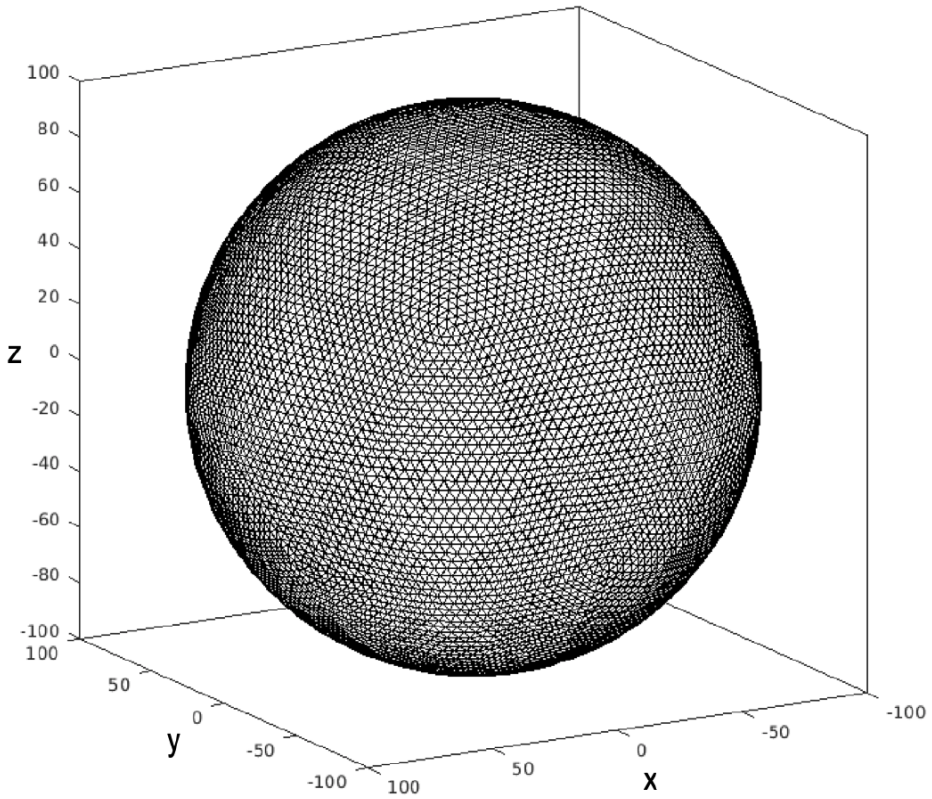

Fig. 3.6.: Subdivided icosahedron meshes at level 5.

Our registration adopted a multi-resolution scheme that during the four iterations, the first iteration is a coarse registration which downsampled the object surface, then for the remaining three iterations, the resolution increased level by level for more precise registrations.

Experimental results are summarized in Figures 3.10 - Figures 3.17. Harmonic Energy measures the smoothness of the transformation. Thus, it can be seen as an indicator for metric distortion between the spherical representation and the original cortical surface. With the idea of combining the definitions of HE in Chapter 3.2.3 and the stopping criterion defined in Equation 3.28, we examine distortion using the HE with the following strategy:

$$HE = \sum_{[v_i, v_j] \in K} \theta_{v_i v_j} \|\Gamma(v_i) - \Gamma(v_j)\|^2, i \neq j, \tag{3.40}$$

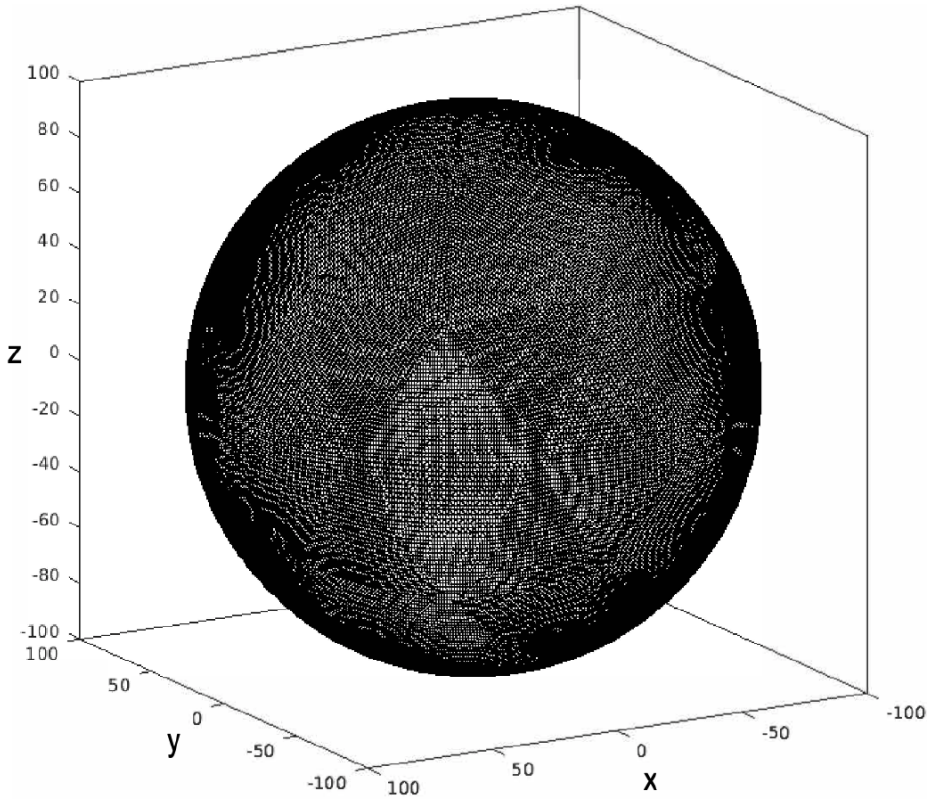

Fig. 3.7.: Subdivided icosahedron meshes at level 6.

where v_i and v_j are two vertices that define an edge, K is the triangle that contains v_i and v_j, and Γ is a transformation of current warp. Coefficients $\theta_{uv} = \cot\alpha + \cot\beta$, where α and β are the angles opposite to the edge $[v_i, v_j]$.

$$Distortion = \frac{\mathrm{HE}_n - \mathrm{HE}_1}{T}, \tag{3.41}$$

where n is the current warp of the image, and the numerator measures the overall length changes between the original vertices and the warped surface vertices, and the denominator T is a normalization term that represents for the total number of neighbours for all the vertices belongs to a surface.

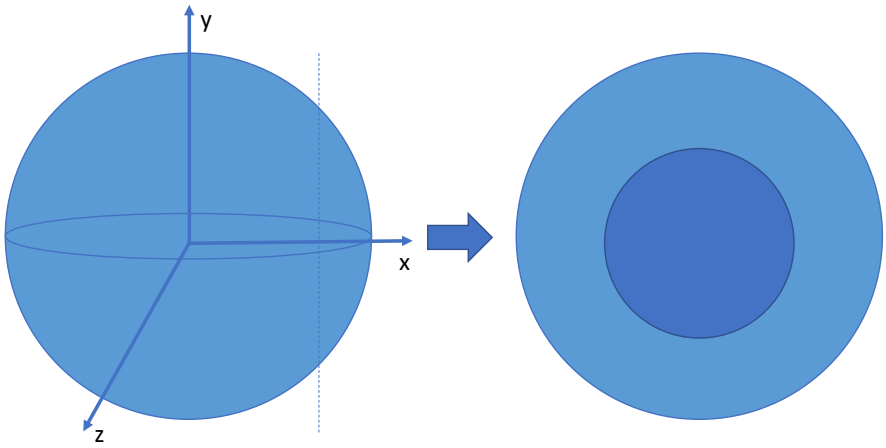

(a) A demonstration of generating a “circle” on sphere

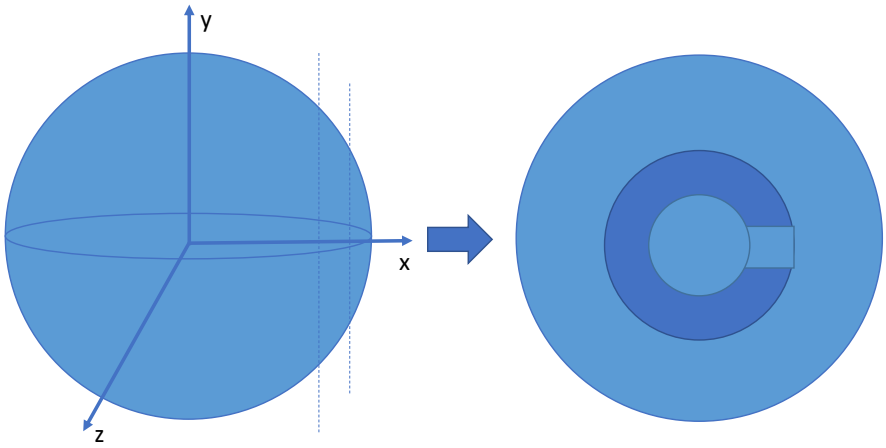

(b) A demonstration of generating a “C” on sphere

Fig. 3.8.: A demonstration of generating synthetic data for “circle to C” task.

We can see from the results, fluid-like demons achieved best results in RMSE, followed by combined demons and diffusion-like demons. However, it also scored the highest value for the harmonic energy, which means it has more severe mesh irregularity.

When we look deeper into each category, we firstly discuss the results from diffusion-like demons. In the coarse registration level (the 1st iteration) and “ic5” resolution level, compositive demons achieved distinct lower RMSE values while no

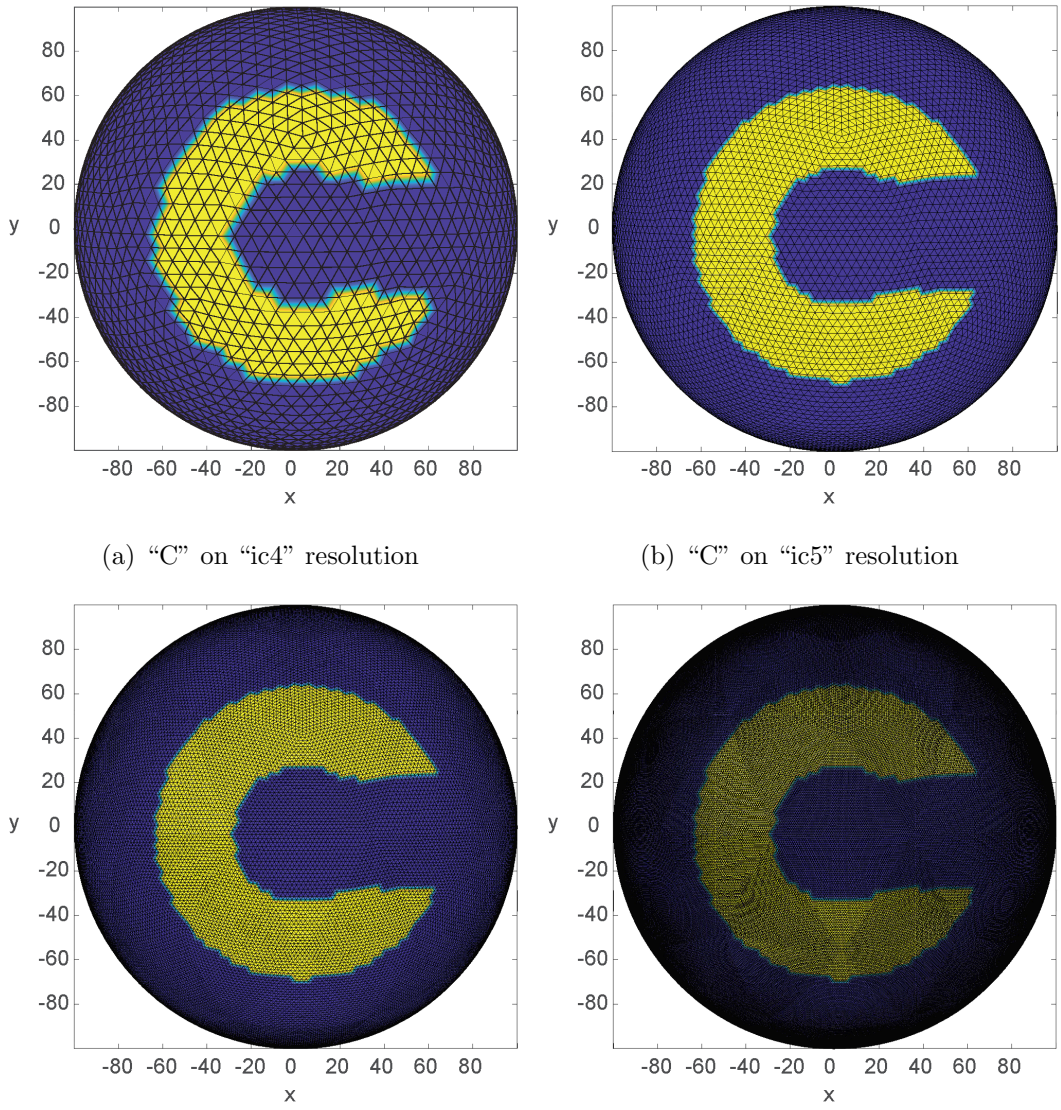

(a) "C" on "ic4" resolution

(b) "C" on "ic5" resolution

(c) "C" on "ic6" resolution

(d) "C" on "ic7" resolution

Fig. 3.9.: The generated "C" on spherical surface, we treat it as a template in registration.

noticeable HE differences to other methods. However, in a much higher resolution environment, the performance of compositive demons reduced rapidly, and it became the worst in RMSE at the end of the 4th iteration. The proposed method in this study

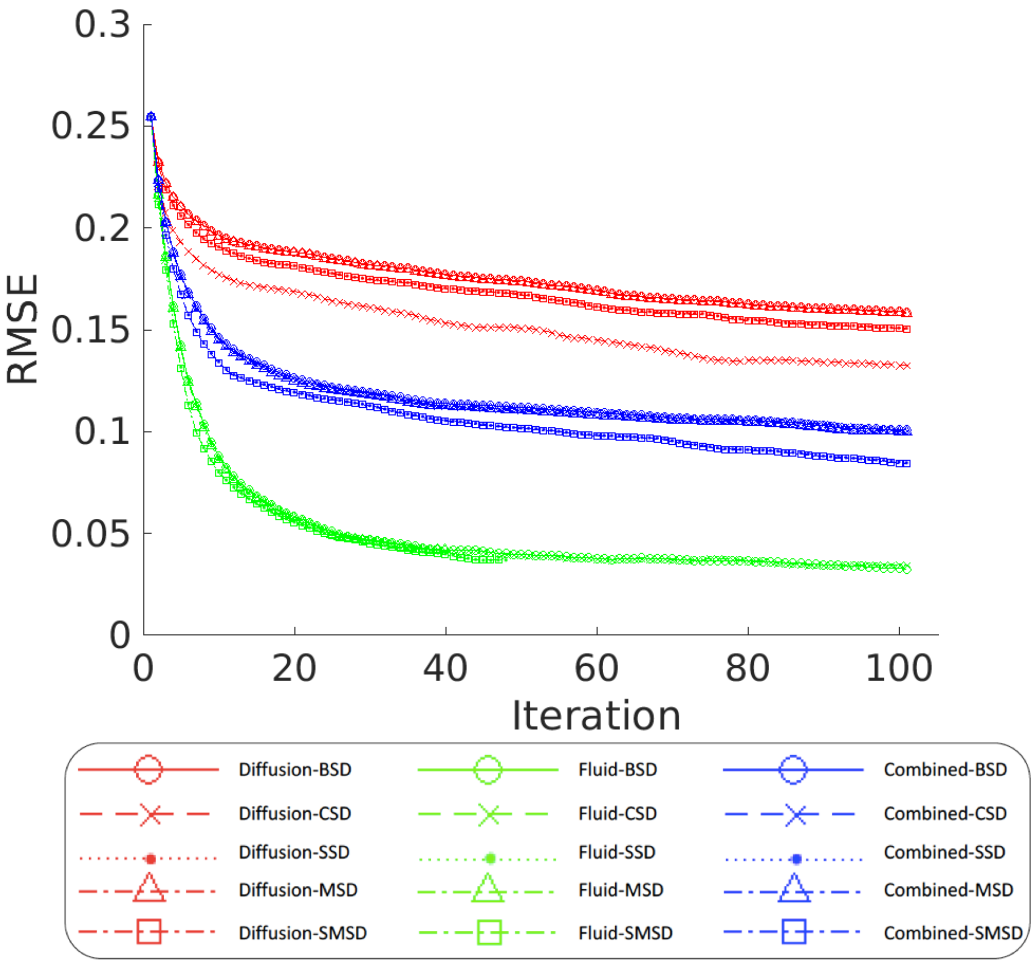

Fig. 3.10.: Root mean square error (RMSE) for synthetic warp results at level 1. RMSE is plotted against iteration.

achieved best RMSE values at the end of registration, during the meanwhile, its HE is only obviously higher than the compositive demons which scored the worst RMSE. The detailed warping paths for each experimental group are shown in Figure 3.19.

Secondly, we discuss the results from fluid-like demons. Compared to diffusion-like demons, the fluid-like demons features for less regularization; thus, it scored very low RMSE in all of four iterations; as a result, the surface mesh is exceptionally irregular. The meshes are shown in Figure 3.18. It is noteworthy that the stopping criteria we set in momentum-based demons, symmetric demons and momentum-based

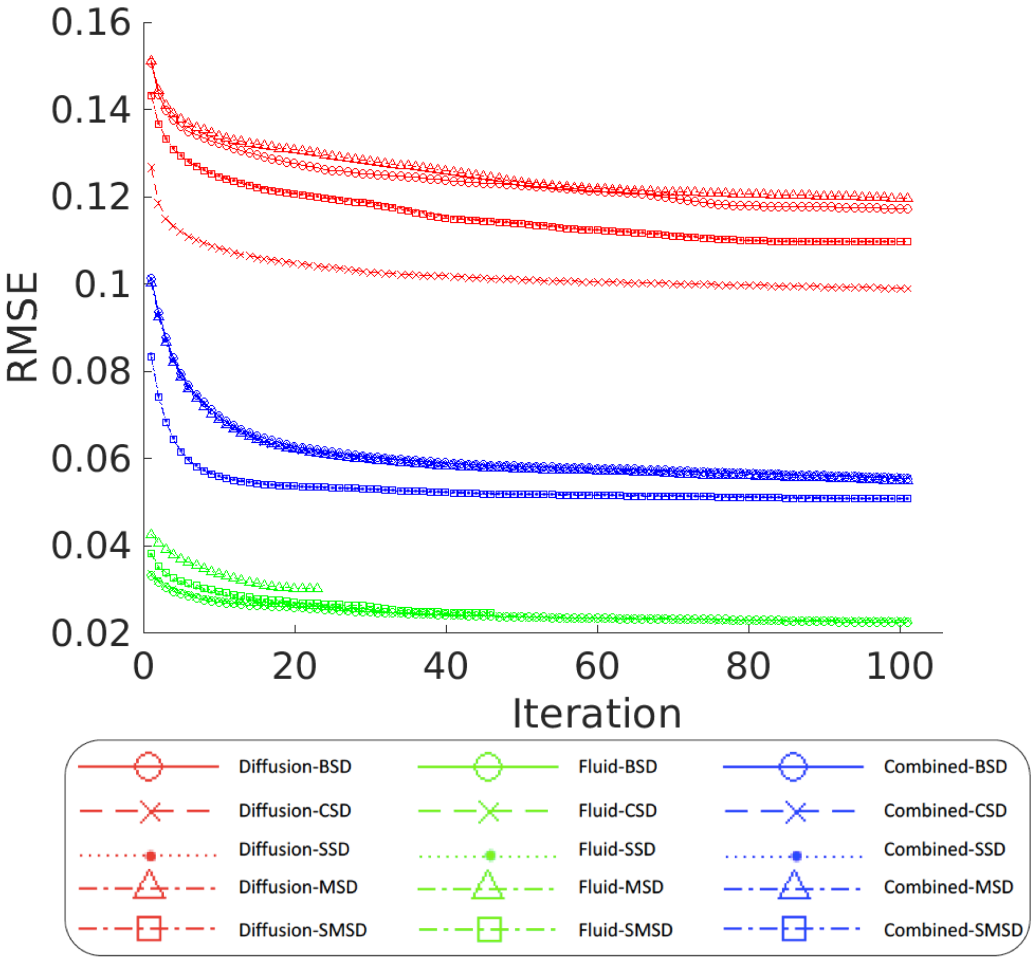

Fig. 3.11.: Root mean square error (RMSE) for synthetic warp results at level 2. RMSE is plotted against iteration.

symmetric demons prevented the extreme mesh distortion, and kept the RMSE in an ideal range. The detailed warping paths for each experimental group are shown in Figure 3.20.

Lastly, we discuss the results from combined demons. We applied a 3-level multi-resolution scheme, smoothing the surface features and regularizing the registration more at the first level, then we reduce regularization to relax the rest of subsequent levels, we removed regularization for displacement field and only kept regularization on updates in the last iteration. As a result, we can observe from Figure 3.10- 3.13,

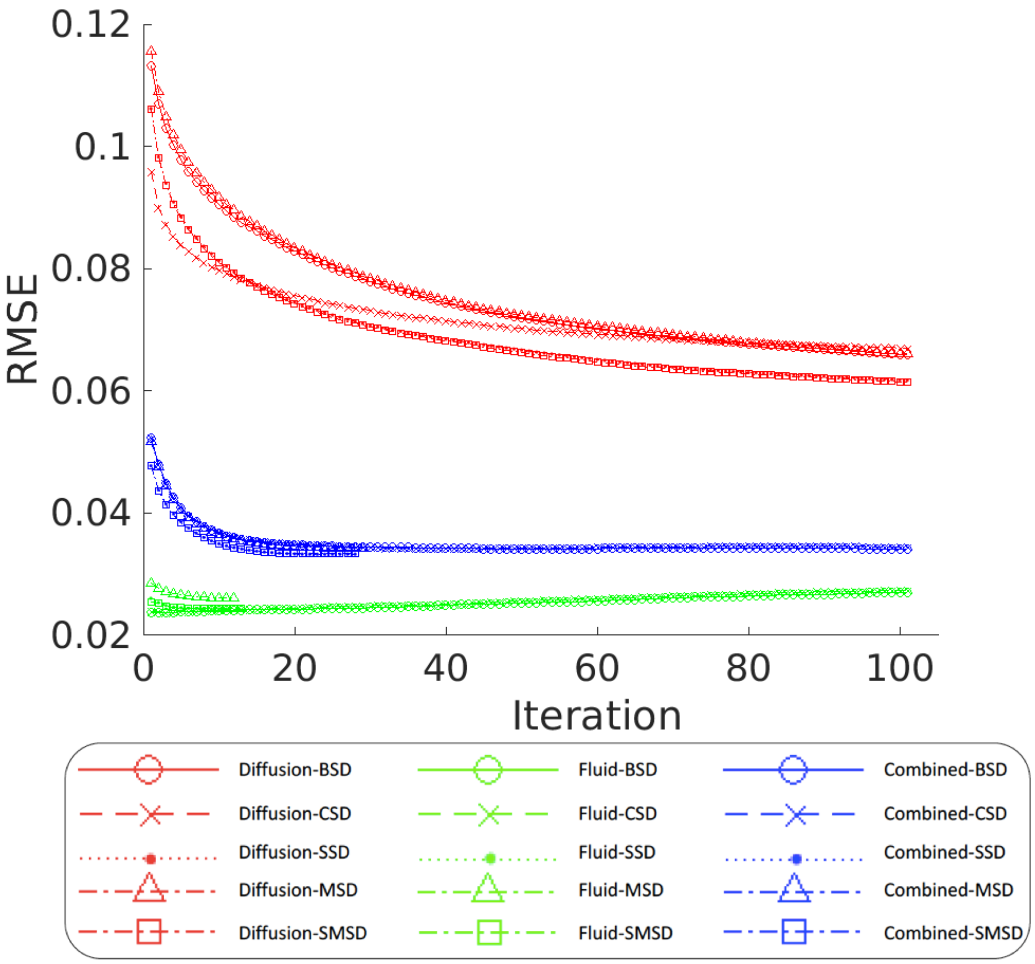

Fig. 3.12.: Root mean square error (RMSE) for synthetic warp results at level 3. RMSE is plotted against iteration.

the RMSE results of combined demons were approaching to fluid-like demons, while HE was reserved in a proper range. In this experimental set, our proposed methods (symmetric demons and MS demons) achieved the best RMSE results while keeping low HE values. The detailed warping paths for each experimental group are shown in Figure 3.21.

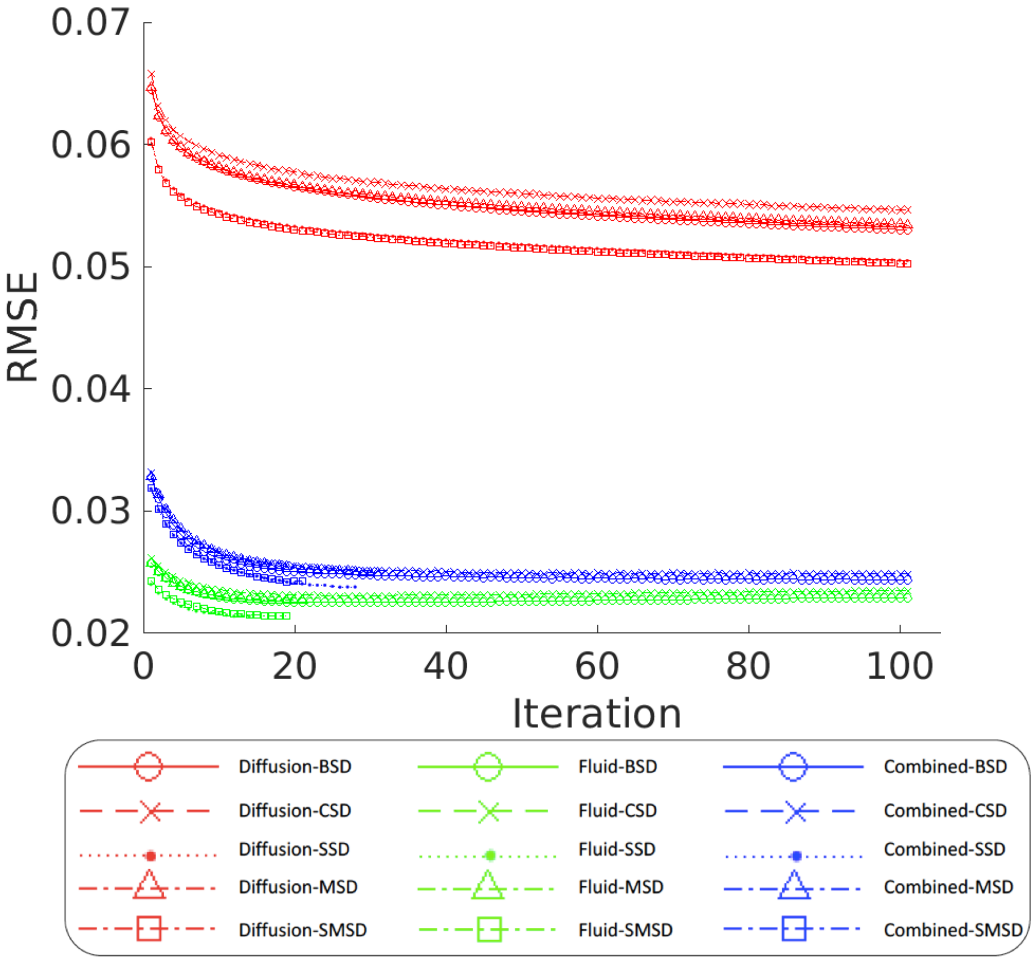

Fig. 3.13.: Root mean square error (RMSE) for synthetic warp results at level 4. RMSE is plotted against iteration.

3.4.3 Summary

In the experimental tests we compared the diffusion-like spherical demons with many other demons variants including the proposed methods, the comparison results suggest the proposed methods Symm SD and Symm-Momen SD are promising in aligning local regions on the spherical surfaces. Thus, the next stage of our study is to further applied on a set of real data in the subsequent studies.

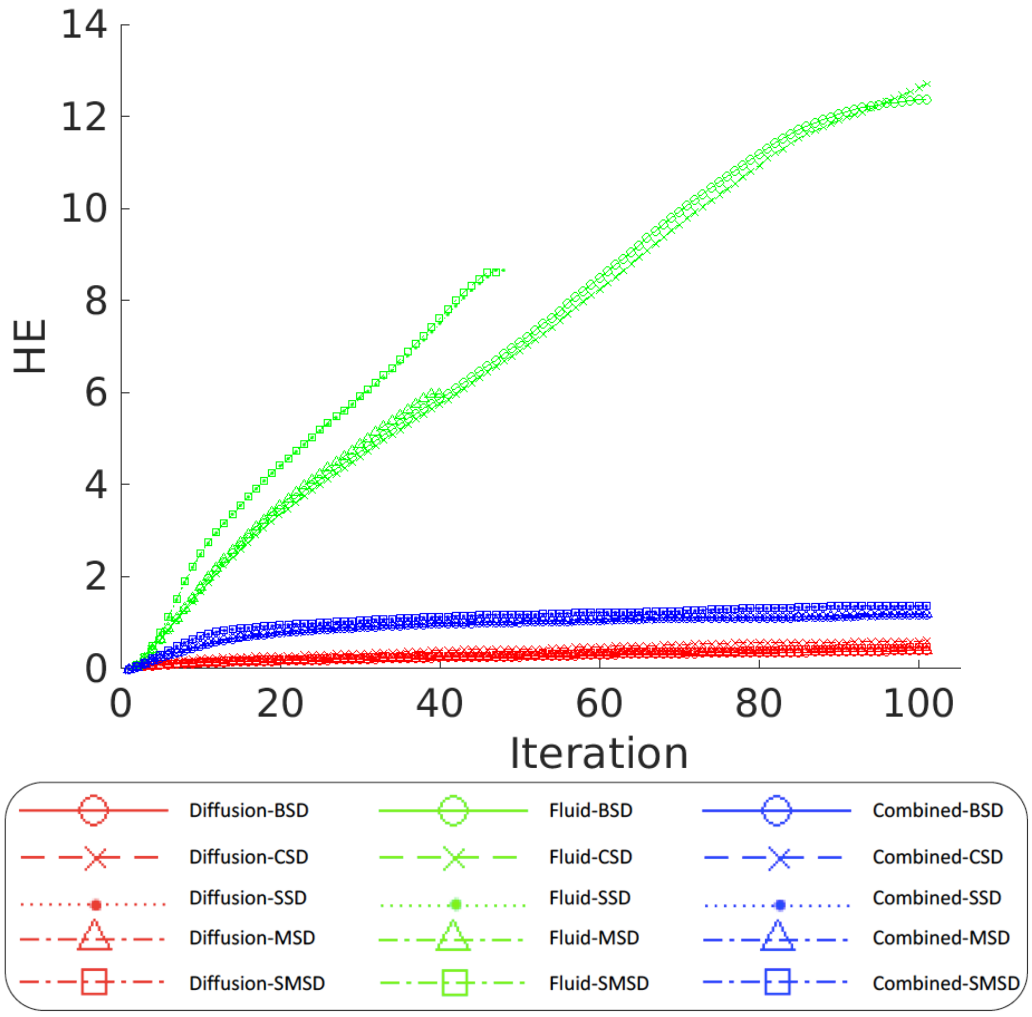

Fig. 3.14.: Harmonic energy (HE) for synthetic warp results at level 1. HE is plotted against iteration.

3.5 Summary of Chapter 3

Surface registration can be viewed as an extension of image registration, while additional geometric information and label information are provided to perform surface registration using a plentiful of mathematical tools. In this chapter, we introduced several widely used surface registration methods, discussed stopping criteria and evaluation strategies, we also tested our proposed method on a set of synthetic data. As the results showed in Chapter 3.4.2, our proposed methods (Symm SD and

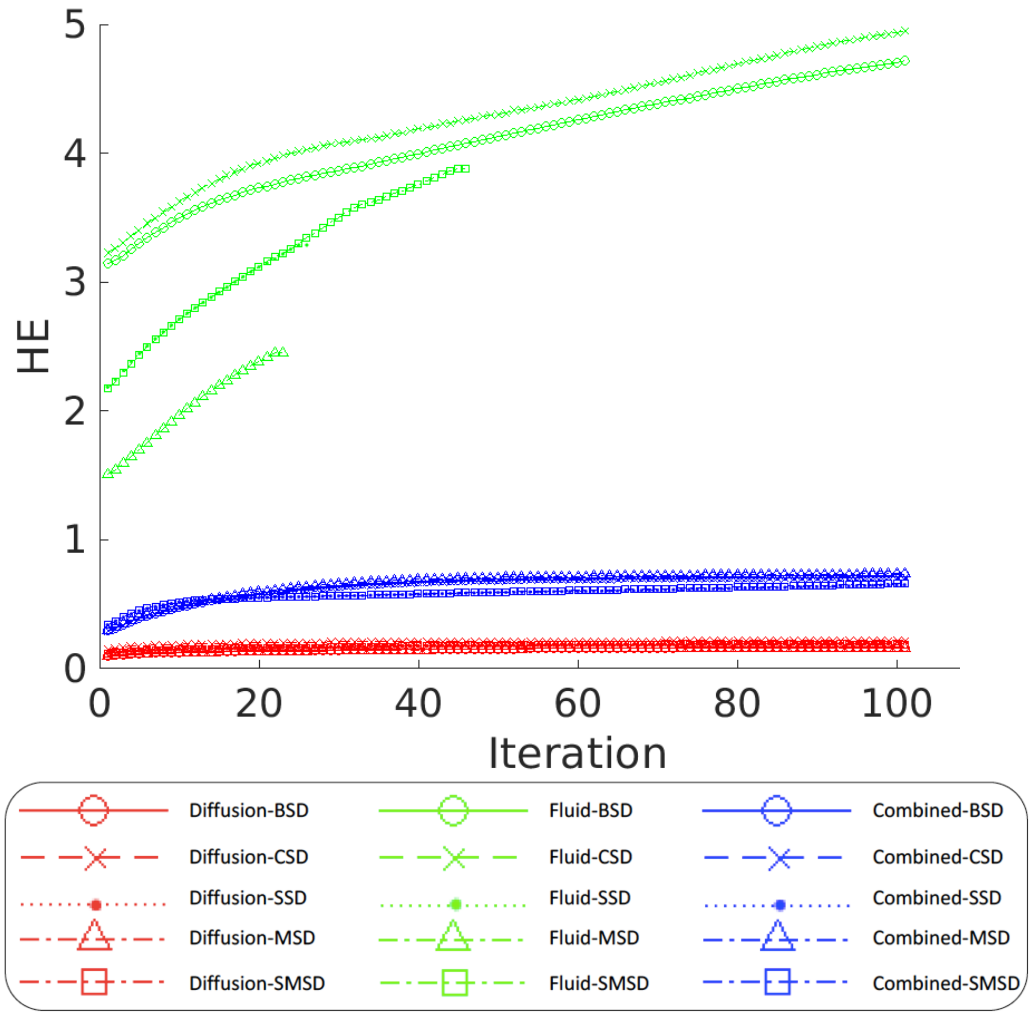

Fig. 3.15.: Harmonic energy (HE) for synthetic warp results at level 2. HE is plotted against iteration.

Symm-Momen SD) are promising in achieving best registration results while keeping relatively reasonable mesh distortion, also, the stopping criteria we chose was proved to be helpful in preventing the divergence of harmonic energy.

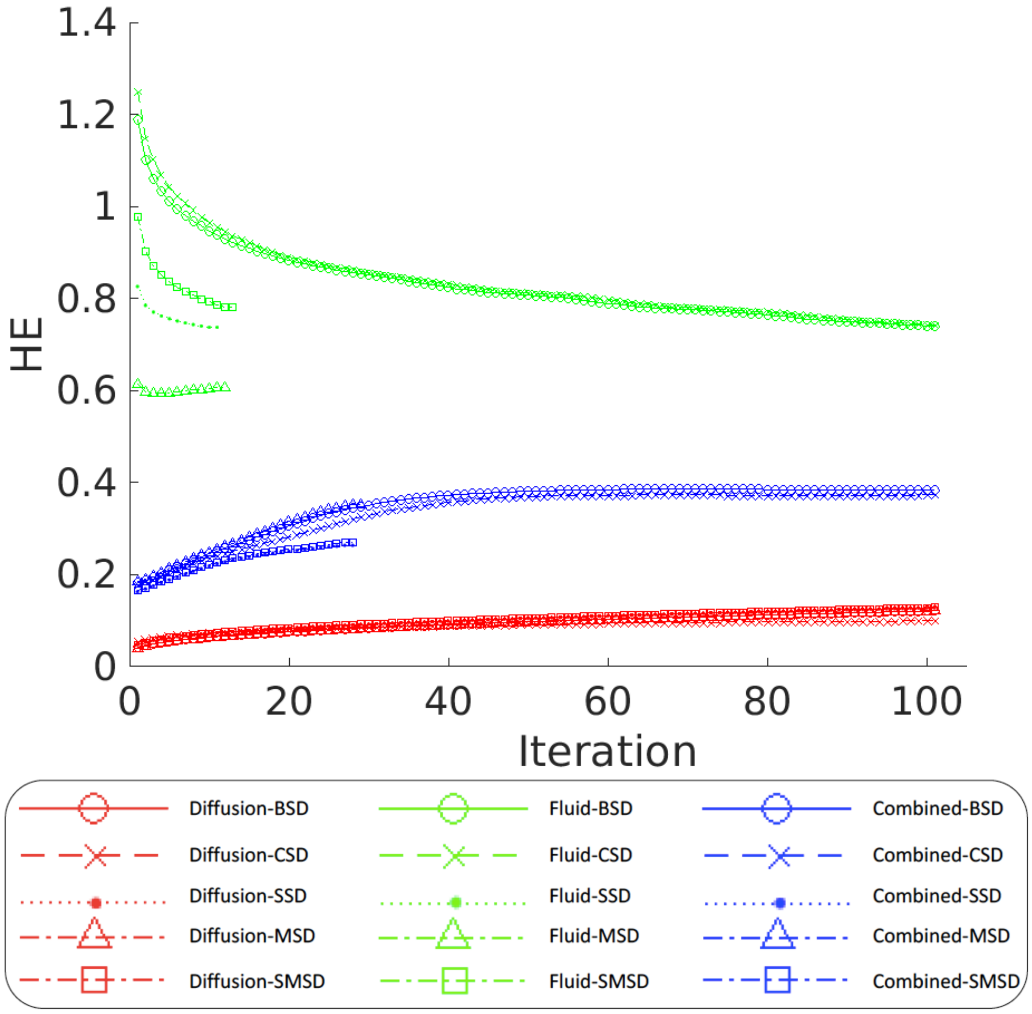

Fig. 3.16.: Harmonic energy (HE) for synthetic warp results at level 3. HE is plotted against iteration.

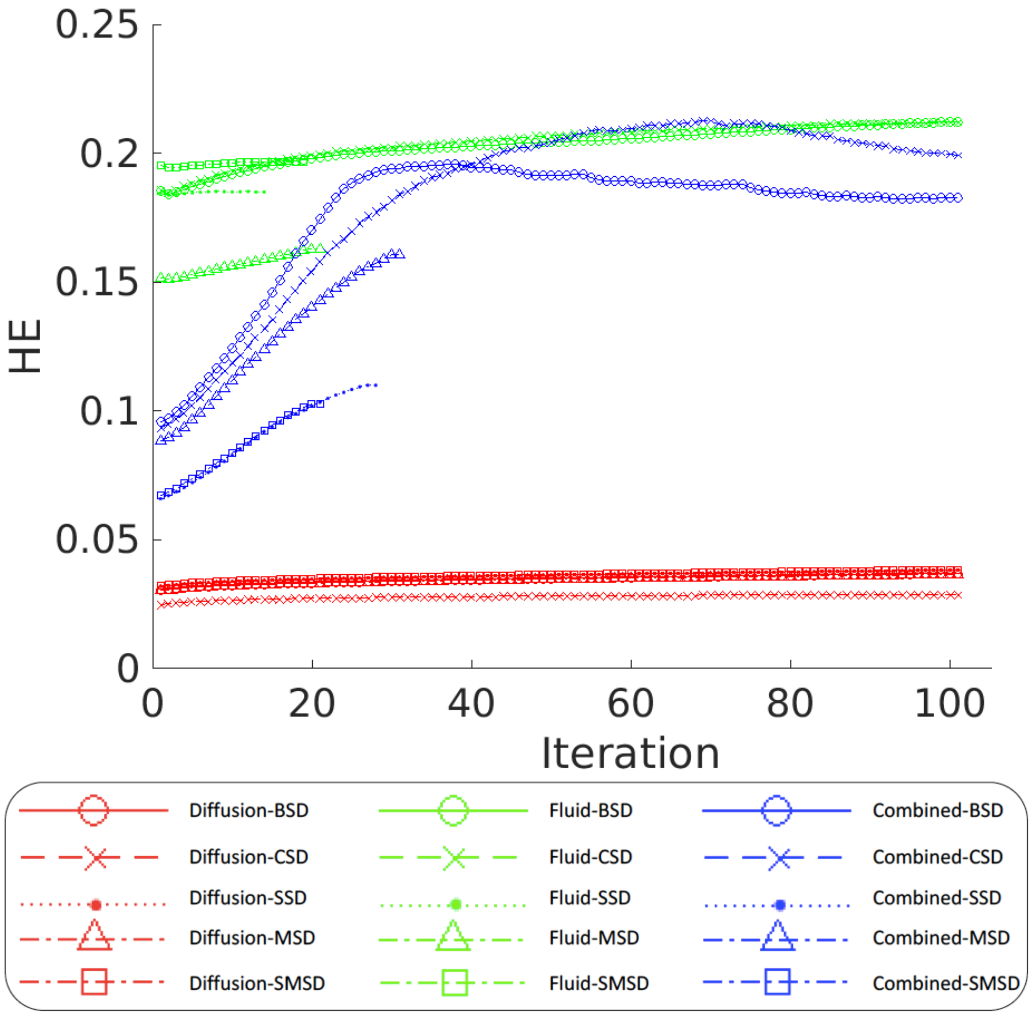

Fig. 3.17.: Harmonic energy (HE) for synthetic warp results at level 4. HE is plotted against iteration.

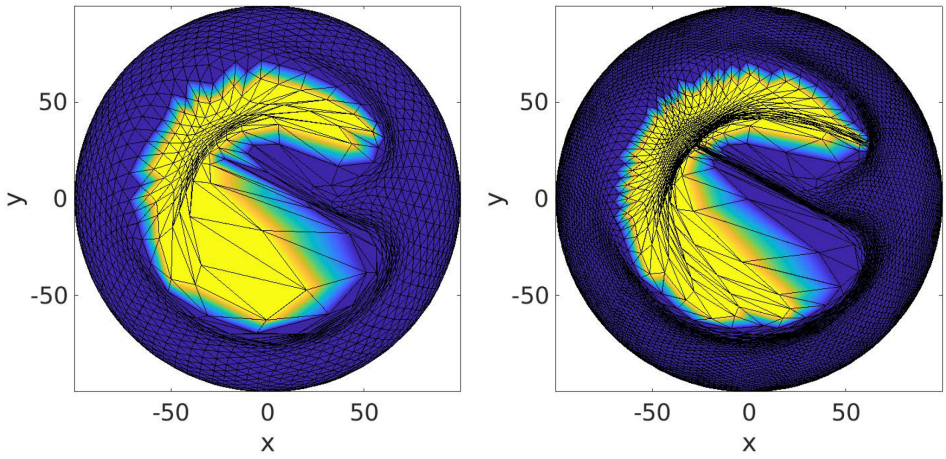

(a) Fluid-like Registration at level 1

(b) Fluid-like Registration at level 2

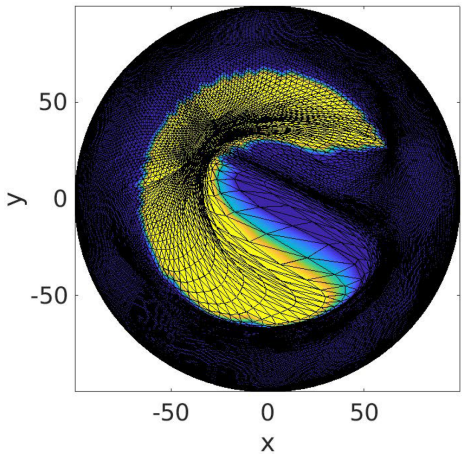

(c) Fluid-like Registration at level 3

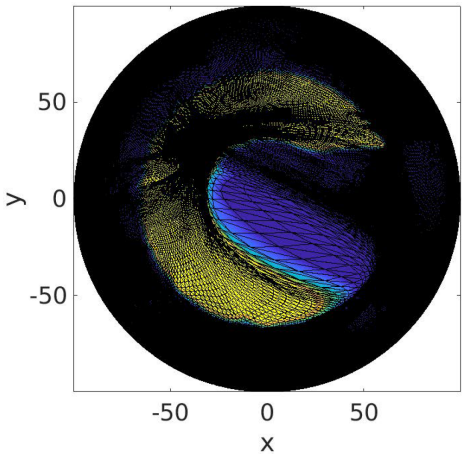

(d) Fluid-like Registration at level 4

Fig. 3.18.: Example results of fluid-like registration.

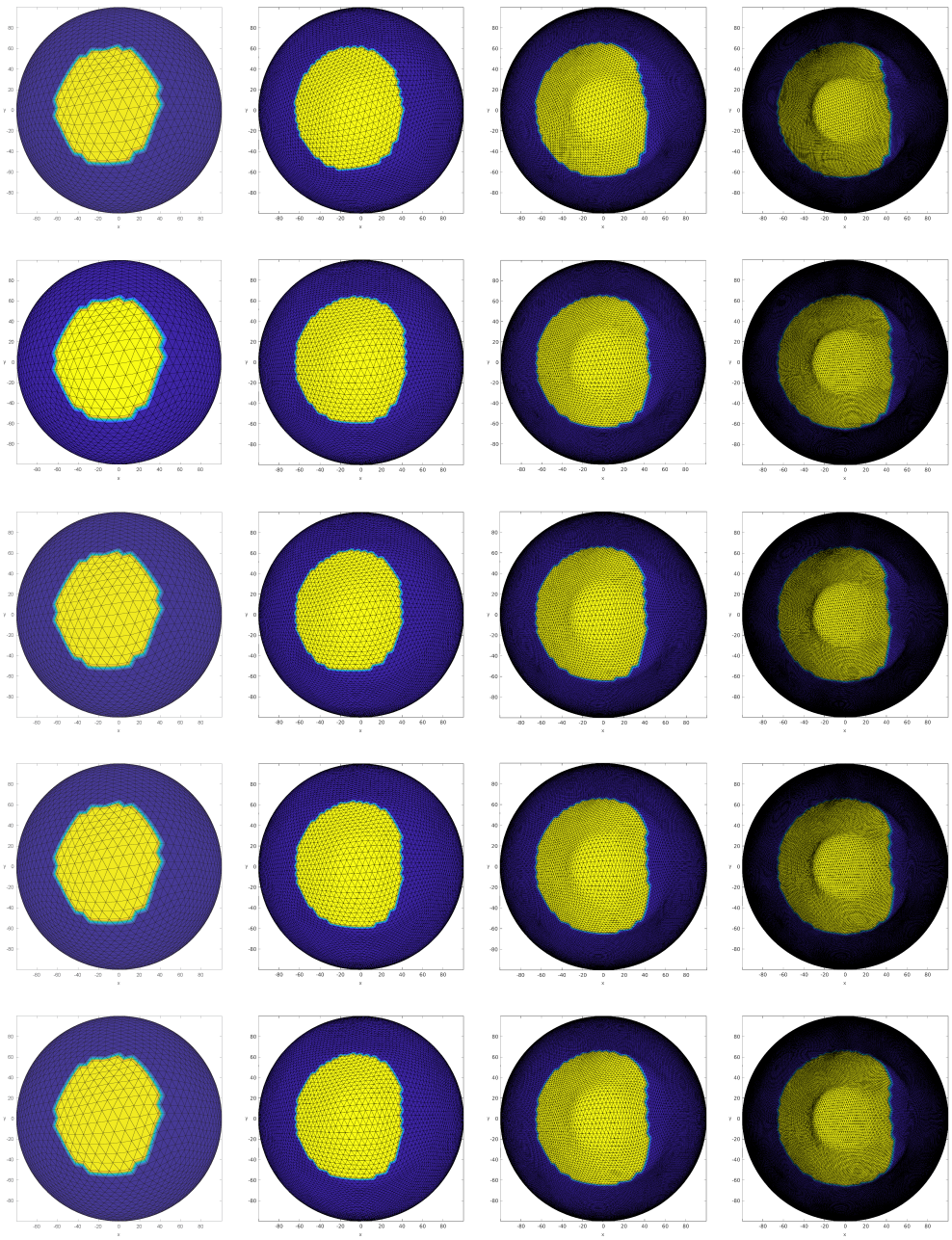

Fig. 3.19.: Registration results for diffusion-like methods using synthetic data. First row: basic diffeomorphic SD (BSD); second row: compositive SD (CSD); third row: momentum-based SD (MSD); fourth row: symmetric SD (SSD); fifth row: momentum-based symmetric SD (SMSD). Columns 1 to 4 represent resolution levels; the resolution increases with the increase of level numbers.

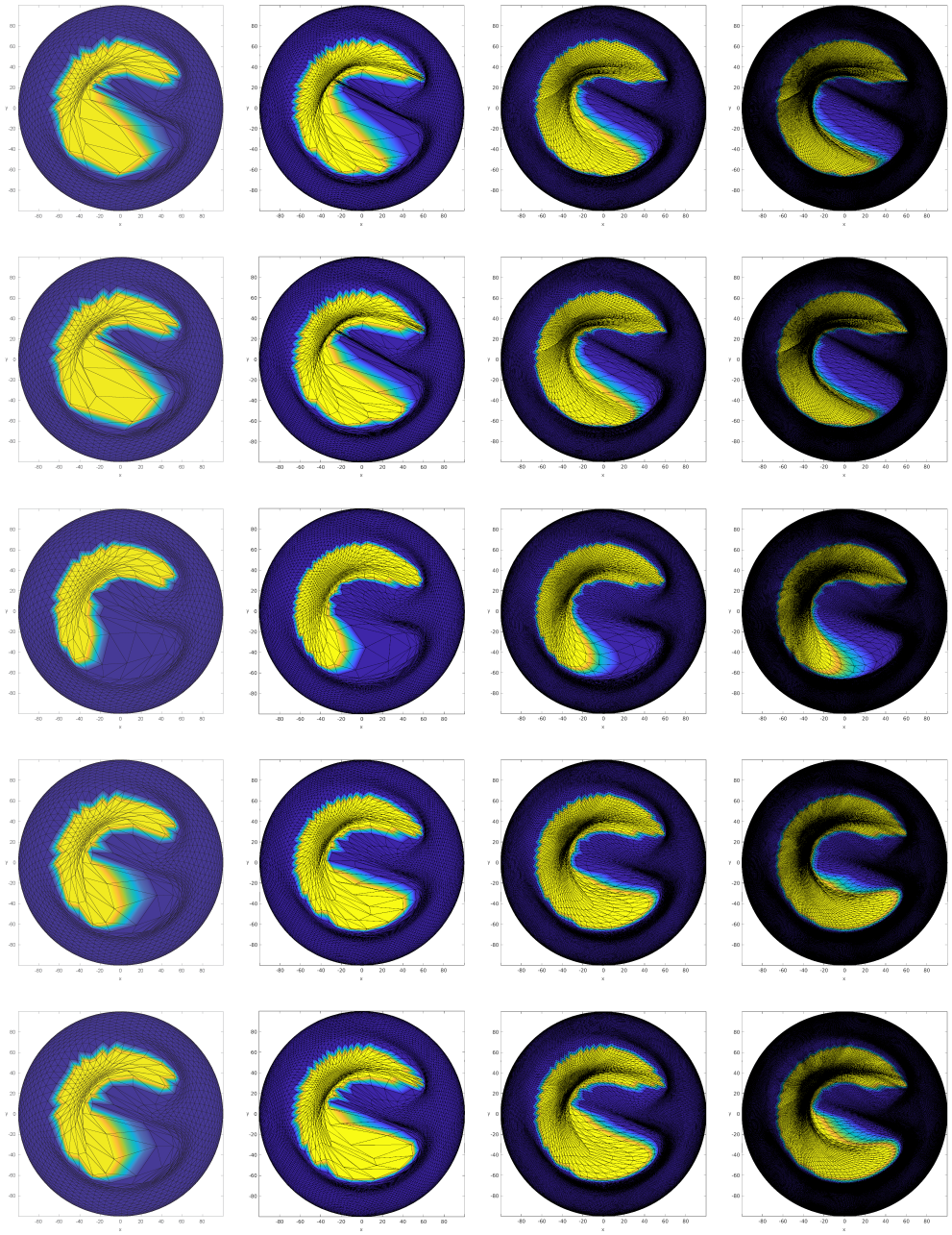

Fig. 3.20.: Registration results for fluid-like methods using synthetic data. First row: basic diffeomorphic SD (BSD); second row: compositive SD (CSD); third row: momentum-based SD (MSD); fourth row: symmetric SD (SSD); fifth row: momentum-based symmetric SD (SMSD). Columns 1 to 4 represent resolution levels; the resolution increases with the increase of level numbers.

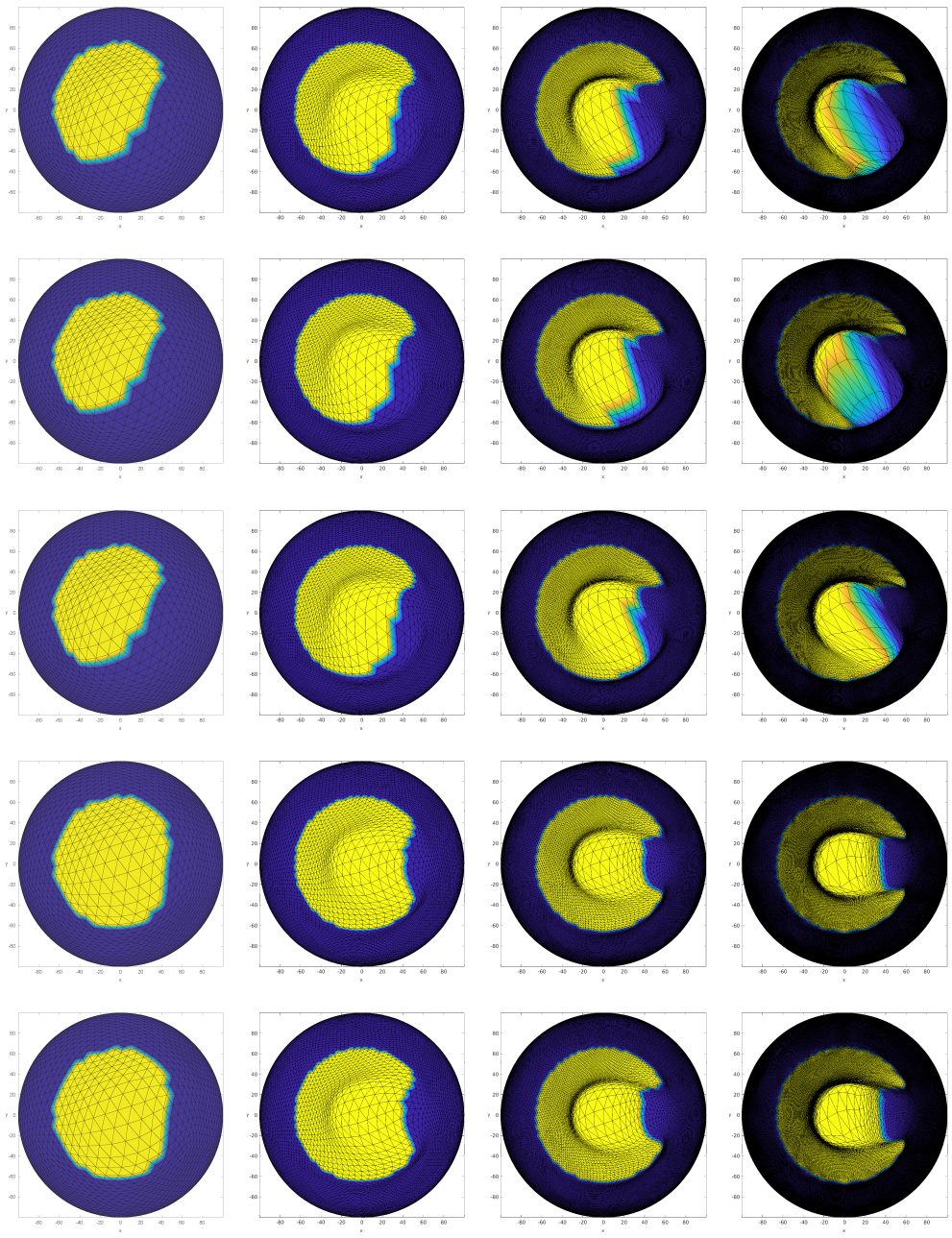

Fig. 3.21.: Registration results for combined methods using synthetic data. First row: basic deffeomorphic SD (BSD); second row: compositive SD (CSD); third row: momentum-based SD (MSD); fourth row: symmetric SD (SSD); fifth row: momentum-based symmetric SD (SMSD). Columns 1 to 4 represent resolution levels, the resolution increases with the increasing of level numbers.

4. BUILDING SURFACE ATLAS

4.1 Background

This section demonstrates the process of constructing a computational anatomical hippocampal atlas with subfield information on the surface. A detailed atlas of the hippocampal subfields is helpful in understanding and demonstrating the anatomy of hippocampal structures. It is proved to be highly complementary to morphological studies and essential for group comparisons. In the studies, our primary focus is to estimate atrophy on each subfield and identify significant subregions on the hippocampus that are profoundly affected by brain diseases (MCI and AD). An averaged synthetic template (atlas) is derived from the samples of clinically normal by shape averaging.

4.2 T1-Weighted Scans Only

4.2.1 Data and Materials

The magnetic resonance imaging (MRI) data were downloaded from the ADNI database. In this work, we analyzed the baseline MRI scans of 26 randomly selected healthy controls from the ADNI GO/2 cohort, where each subject had a pair of repeated scans (say A and B).

4.2.2 First Order Ellipsoid Registration

We introduced SPHARM parameterization and expansion in Sections 3.2.1 and 2.6.2, we also introduced FOE registration in Section 3.2.1. Based on the first order expansion of the SPHARM coefficients, FOE was introduced to perform a surface

registration task by employing geometric information of hippocampi. It aligns both of the spherical parametrizations in parameter space and orientations in object space; thus, it can establish correspondence across all hippocampal surfaces. In this section, we apply FOE to align all of the surfaces of objects to canonical positions by aligning both of surface parameterization in parameter space and object pose in object space.

4.2.3 Building Hippocampal Surface Atlas

After all of the surfaces are well aligned, given n hippocampal SPHARM models, we can calculate a mean SPHARM model and use that as our surface atlas. Now we describe our approach to map the subfield information onto the mean surface. The main idea is to apply the spherical harmonic basis functions to expand each subfield probability map. After that, for each surface location, we can assign it with the subfield label which has the largest probability among all eight subfields. In order to compute a SPHARM expansion for each probability map, we need to map a probability value to each vertex on the original voxel surface (see the left side of Figure 2.8). Note that each original probability value is defined for each voxel, and each face on the original surface has a unique probability value. Based on this, we can calculate a probability value for each vertex by averaging the probability values of its adjacent faces.

4.2.4 Experiments

Figure 1.2 shows the axial, coronal, and sagittal views of an example MRI scan. Left and right hippocampi are colored in brown and red separately. Figure 2.3 illustrates the probability distribution (red regions indicate nonzero probability) of each subfield on an example hippocampus. The probability maps were generated by Freesurfer, and mapped onto the surface of the hippocampus segmented by FIRST. Figure 2.8 shows the voxel surface of an example hippocampus segmented by FIRST and its spherical parameterization. In order to map the surface to a spherical ob-

ject, disconnected small components were removed, bad edge connectivity problem and bad vertex connectivity problem were fixed, and 3D holes were filled during the topology fix process.

Figure 2.8 shows an example spherical parameterization. The hippocampal surface is mapped to a unit sphere. The color indicates the correspondence between the surface and the sphere. The goal of parameterization is to create a continuous and uniform (bijective) mapping from the hippocampus surface to a unit sphere to establish surface correspondences across subjects. Figure 4.1 shows the steps of FOE registration process. Figure 2.10 shows the subfield mapping of an individual hippocampus, where subfields are mapped on the original mesh (left), its spherical parameterization (middle), and SPHARM reconstruction after FOE registration (right).

Figure 4.2 shows surface atlases of hippocampal subfields created from MRI scans of 26 healthy controls, where each individual has two repeated scans (A and B): (a) Atlas generated from using both scans, (b) atlas generated from using Scan A only, and (c) atlas generated from using Scan B only. Each of (a-c) visualizes the atlas from two different views. We can see the results are pretty consistent, demonstrating decent reproducibility of the proposed method.

4.2.5 Summary

In this section, we have proposed a method for building a surface atlas of hippocampal subfields from T1 weighted MRI scans using methods and tools including FreeSurfer, FIRST, and SPHARM. Using FreeSurfer, we have obtained valuable hippocampal subfield information. Using FIRST, we have extracted reliable hippocampal surface information. Using SPHARM, we have developed an approach to creating an atlas by mapping interpolated subfield information onto an average surface. The experimental result using ADNI data demonstrates good reproducibility of the proposed method.

4.3 T1 and T2-Weighted High Resolution Scans

In the last section, we proposed a method for hippocampal subfield morphometry by integrating FreeSurfer, FSL, and SPHARM tools. However, this method had some limitations, including the analysis of T1-weighted MRI scans without detailed subfield information and hippocampal registration without considering important subfield information. To bridge these gaps, in this work, we propose a new framework for building a surface atlas of hippocampal subfields from high-resolution T2-weighted MRI scans, and the proposed framework integrates variants of state-of-the-art methods for automated segmentation of hippocampal subfields and landmark-free, subfield-aware registration of hippocampal surfaces. Our experimental results have shown the promise of the new framework.

4.3.1 Data and Materials

We included two groups of data in our studies, and they were respectively acquired from Indiana Alzheimer's Disease Center (IADC) and Alzheimer's Disease Neuroimaging Initiative (ADNI). The two mentioned data centers are reputable for providing raw MRI data with high quality and relatively complete demographic and diagnostic information of patients. In our study, we initially applied the revised framework on the data from IADC, and we obtained promising results. With the consideration of the limited size of IADC data, we downloaded recently published ADNI 2 and 3 data set for further validation on our methods.

The sample in the initial tests includes 12 healthy control (HC) participants recruited at IADC. MRI scans were acquired on a Siemens MAGNETOM Prisma 3T MRI scanner. The scanning protocols include a T1-weighted (MPRAGE) whole-brain scan and a T2-weighted (TSE) partial-brain scan and an oblique coronal slice orientation (positioned orthogonally to the main axis of the hippocampus). Same protocols were adapted in [9, 78].

With the awareness of the limited data size, we downloaded 81 high-resolution data from ADNI 2 and ADNI 3. This data set contains 31 participants in the healthy control group, 30 participants in the MCI group, and 20 participants in the AD group. All of the imaging data comes with a T1-weighted regular 3T MRI scan and a T2-weighted high-resolution data; the T2-weighted high-resolution data does not cover the whole brain, it only covers the hippocampal regions in the left and right brain hemisphere to examine structural and functional changes in hippocampal regions. The scanning protocols and scanning procedures are the same as used at IADC.

4.3.2 Segmentation

Automatic Segmentation of Hippocampal Subfields (ASHS) is a software tool developed by Paul A Yushkevich, et al. [9] for automatically segmenting hippocampal subfields and their adjoining structures in the medial temporal lobe (MTL). The software has been used in several prior studies [129, 130]. This technique uses T1-weighted and high resolution T2-weighted MRI scans as inputs, and performs multi-atlas segmentation by implementing Joint Label Fusion method [33] and Corrective Learning [131]. ASHS has been shown to be able to produce accurate and reliable segmentation results in previous studies [9,129,132]. In this study, ASHS was used to segment the following hippocampal subfields and their adjoining regions from the un-accelerated and accelerated high resolution T2-weighted MRI scans coupled with the corresponding T1-weighted MRI scans (Figure 4.3): cornu ammonis 1 (CA1), CA2, CA3, dentate gyrus (DG), subiculum (SUB), entorhinal cortex (ERC), Brodmann areas 35 and 36 (BA35 and BA36, which together form the perirhinal cortex), and collateral sulcus (CS).

4.3.3 Spherical Parameterization

SPHARM PDM [47] Topology fix was performed on segmentation results to ensure a spherical topology for each hippocampus. The hippocampal surface was constructed from a voxel-based binary volume, and subfields were assigned to surface locations as "Cornu Ammonis (CA, including CA1-3)", "Dentate Gyrus (DG)", or "Subiculum + Miscellaneous (SUB+MISC)", using the strategy shown in [9]. Following section 2.6.1, spherical parametrization was performed to establish a bijective mapping between each surface location $v = (x, y, z)^T$ and a pair of spherical coordinates (θ, ϕ) while minimizing area distortion. This mapping can be represented as: $v(\theta, \phi) = (x(\theta, \phi), y(\theta, \phi), z(\theta, \phi))^T$. Figure 4.4(a-c) shows two example results of spherical parameterization with initial alignment.

4.3.4 Surface Signal Formulation

In our previous work, we directly utilized the subfield information returned from ASHS segmentation. Even though it worked, the method we discussed in previous studies were not sufficiently well proposed. The reason is, taking a label map from a segmentation tool as an input for registration brings inequality for different subfields. The label numbers returned from a segmentation tool only have literal meanings, but when we throw them directly into a registration algorithm, we treat them as numerical meanings. This leads to a problem of inequality.

For a more specific explanation, we assume the label for subfield CA is "1", the label for subfield DG is "2", and the label for subfield SUB is "3". When a registration algorithm tries to align the hippocampal surface based on these subfield label information, the algorithm will think the gap between CA and DG is smaller than the gap between CA and SUB, since the difference between CA and DG is 1, while the difference between CA and SUB is 2. To overcome this problem of inequality, we proposed three methods to vectorize the integer label map.

Binary Maps

The first idea is to binarize the integer labels. Instead of using one integer to represent a label, we use a $[3 \times 1]$ vector that binarize the integer. For example, the integeral label "1" can be binarized as $[\ 0 \quad 0 \quad 1\ ]$, similarly the labels "2" and "3" can be binarized as $[\ 0 \quad 1 \quad 0\ ]$ and $[\ 1 \quad 0 \quad 0\ ]$ respectively.

Distance Maps

The second strategy is to calculate a distance map for each subfield. We define the distance map by two steps: 1) identifying boundaries for each subfield, and 2) calculating the distance from each vertex to its nearest boundary point.

We first search through all the faces, we define a vertex which has at least one neighbor with different vertex label as a boundary vertex. Then for each subfield, we generate a boundary map, we assign value equals to one for the subfield, assign value equals to two for the boundaries and set the rest of vertices as zero. The results are shown in Figure 4.6.

For a vertex $v \in L_i$, L_i is the ith subfield returned from a segmentation tool. We calculate the distance from v to the nearest boundary of this subfield region. Thus, we have a $1 \times n$ feature vector, where n is the total number of surface mesh vertices. It assigns the weights a vertex belongs to a subfield, while the vertices outside of the region are given weights equals to zero. So for a total number of m subfields, we can formulate a $m \times n$ feature vector, and we name it as a distance map.

To better organize the surface signals across the whole data set, we further normalized the distance map and set the subfield regions as $(0, 1]$, the background regions as "-1", and the boundaries as zero. The results are shown in Figure 4.7.

Probability Maps

The last method to formulate surface signals is to utilize the probability maps directly from segmentation results. As the two of most popular hippocampi segmentation tools, FreeSurfer and ASHS are based on probability distributions, both of the tools returned probability maps for each hippocampal subfield. So we take each probability map of each subfield as a $1 \times n$ feature vector, so we can formulate a $m \times n$ vector as surface signals. The results of the probability maps are shown in Figure 4.8. We should note that the probability maps are not the final segmentation results, as each probability map indicates the probability of one single vertex belongs to the subfield, the final segmentation results were obtained by picking the largest probability from multiple probability maps of hippocampal subfields, it also compared them with a background map, which indicates the probability of one vertex belongs to the background. This means that the region of each probability map is larger than the actual segmented region.

As CA2 and CA3 were relatively small regions on the hippocampus, we combined the subfields of CA, and we calculated the combined probability of CA in the following way:

$$P_{CA} = 1 - (1 - P_{CA1})(1 - P_{CA2})(1 - P_{CA3}) \tag{4.1}$$

4.3.5 Spherical Registration using The Proposed Methods

As an indispensable component of the revised framework, one of the major difference is in the proposed framework; each surface will be aligned with the consideration of hippocampal subfield distributions. So we adopted the spherical demons registration mentioned in the Section 3.2.2. In the Section 3.2.2, we introduced the basic spherical demons (BSD) algorithm and its variants, and we also discussed the stopping criteria and distortion measurements. Then we proposed the improved method by taking the advantages of these concepts.

To illustrate the working procedures and compare different spherical registration techniques, we designed our experiments based on three categories: 1) diffusion-like spherical demons, 2) fluid-like spherical demons, and 3) combined spherical demons. In each category, five tests are performed: compositive spherical demons (CSD), basic diffeomorphic spherical demons (BSD), momentum-based spherical demons (MSD), symmetric spherical demons (SSD), and momentum-based symmetric spherical demons (SMSD). We also applied all of the mentioned fifteen methods on three types of surface features, which are binary maps, distance maps, and probability maps. In total, we performed forty-five registration tasks on the data set, and our goals are to identify 1) the best strategy to perform subfield-aware surface registration and 2) the best surface signal that can achieve best registration results.

4.3.6 Experiments

We separate our experiments into two parts. In the first part, we show some initial efforts to implement basic spherical demons (BSD) algorithm for spherical registrations, then a hippocampal subfield atlas on a spherical surface can be obtained. In the second part, we implement the proposed method introduced in Section 3.2.2.

Initial Efforts to Build Surface Atlas on Sphere: In order to demonstrate the SD algorithm can work well on a sphere using real hippocampal data, we first performed a simple test using spherical demons algorithm. The spherical demons algorithm took a multi-resolution scheme that it registered each onto an averaged template; the variance of the data set measured the registration results. As each individual surface was registered in each iteration, the group variance reduced.

In our experiments, the goal is to register five pairs of left and right hippocampi together. The registration scheme includes four iterations of multi-resolution alignment; it is the same strategy as we described in Section 3.2.2. The difference is in this set of tests, and we register all five subjects onto an averaged template. During each iteration, we first average all subjects as a template, then register each to this

template. Figure 4.4(d-e) showed registered 3D spherical surfaces and expanded 2D signal maps. However, the deformation on surface mesh is not obvious in this figure, so we take a deeper look at the registration process.

At the beginning of this process, we can observe blurred boundaries in the coarse registration as we demonstrate this in Figure 4.9, the boundaries of averaged template become more clear iteration by iteration when the algorithm achieves convergence, all of the individuals are well aligned, so the boundaries of the averaged template are clear.

The root mean square error (RMSE) is computed to evaluate the results of the SD registration:

$$\mathrm{RMSE}(F, M) = \sqrt{\frac{1}{k}\sum_{i=1}^{k} \|F(x_i) - M(x_i)\|^2} \tag{4.2}$$

where k is the total vertex number for each interpolated surface, and $F(x_i)$ and $M(x_i)$ are the corresponding label values at vertex x_i of template and individual respectively.

Figure 4.9 shows the mean spherical images at each iteration of the SD registration. These images are visualized using the interpolated results at Level 3 (i.e., containing 40,962 vertices). Figure 4.9(a) shows that subfields are roughly aligned at the beginning so that boundaries among them are blurred. Figure 4.9(b-e) show that boundaries on the mean spherical images are sharpened in each iteration since subfields are warped and better aligned by implementing SD algorithm as we presented in Algorithm 7. Figure 4.9(f) shows a 2D unfolded version of spherical images in Figure 4.9(e). The mean spherical images shown in Figure 4.9(e-f) are the converging results of SD method and chosen to be our hippocampal subfield atlas.

Figure 4.10 shows the RMSE at each iteration for each subject. The mean RMSEs of 12 subjects are 0.49 and 0.52 respectively for left and right hippocampi at the initial stage. They reduce to 0.32 and 0.34 after 1st iteration, then keep reducing until reaching 0.18 and 0.20 at the convengence.

Comparisons of Different Types of Registration Methods: Recall our goals are to identify the best strategy to perform subfield-aware surface registration and the best surface signal that can achieve best registration results. We have already demonstrated the success a basic SD (BSD) algorithm can achieve in spherical registration, and now we hope to further examine the improvements of our proposed methods can get by implementing the algorithms on a real hippocampal data set. We introduced the theoretical background of each algorithm in Section 3.2.2. In this section, different SD registration algorithms are implemented and compared in several aspects of registration quality and regularization on mesh distortion.

Based on the regularization types we discussed in Chapter 3, we categorize our experiments into three types: diffusion-like demons, fluid like demons, and regularization combined demons. In each category, five different demons forces are tested; it includes basic SD (BSD), compositive SD (CSD), momentum-based SD (MSD), symmetric SD (SSD), and momentum based symmetric SD (SMSD). We also applied all of the mentioned fifteen methods on three types of surface features, which are binary maps, distance maps, and probability maps. In total, we performed forty five registration tasks on the data set.

In the experiments, we set maximum iteration number to be 30, and tolerance of the updated step size to be $tol. = -10^{-4}$. Our registration adopted a multi-resolution scheme that during the four iterations, the first iteration is a coarse registration which downsampled the object surface, then for the remaining three iterations, the resolution increased level by level for more precise registrations. We adopted an all-to-one registration strategy that all of the individual surfaces are registered to one single template. The way we select the template is that we randomly pick one subject from the group of health control.

We evaluate our experimental results in three aspects: 1) the dice similarity between moving image and fixed image (shown in Figure 4.11), 2) the root mean square error (RMSE) between two images (shown in Figure 4.12), and 3) harmonic energy for mesh quality control (shown in Figure 4.13).

As shown in Figure 4.11, we calculated the dice similarity coefficients, which is defined as the followings equation: For a fixed image F and a moving image M:

$$DSC = \frac{2|V_F \cap V_M|}{|V_F| + |V_M|}, \tag{4.3}$$

where $V_F \cap V_M$ is the overlap between fixed image and moving image, $|V_F| + |V_M|$ is the total number of vertices on both surface meshes.

Root mean square error (RMSE) is defined in Section 4.3.6 as the following equation:

$$\text{RMSE}(F, M) = \sqrt{\frac{1}{k}\sum_{i=1}^{k} \|F(x_i) - M(x_i)\|^2}, \tag{4.4}$$

where k is the total vertex number for each interpolated surface, and $F(x_i)$ and $M(x_i)$ are the corresponding label values at vertex x_i of template and individual respectively.

From the Equation 4.4 we can see, the RMSE measures the distance between the fixed image and the moving image in each iteration. We recorded the RMSE iteratively and it is shown in Figure 4.12.

Harmonic Energy measures the smoothness of the transformation. Thus, it can be seen as an indicator for metric distortion between the spherical representation and the original cortical surface. In the Section 3.4.2, it has been defined in Equation 3.27 and 3.28. In the experiments, we examine HE and evaluate the mesh distortion with HE by combining the following two equations:

$$HE = \sum_{[v_i, v_j] \in K} \theta_{v_i v_j} \|\Gamma(v_i) - \Gamma(v_j)\|^2, i \neq j, \tag{4.5}$$

where v_i and v_j are two vertices that define an edge, K is the triangle that contains v_i and v_j, and Γ is a transformation of current warp. Coefficients $\theta_{uv} = \cot\alpha + \cot\beta$, where α and β are the angles opposite to the edge $[v_i, v_j]$.

$$Distortion = \frac{\text{HE}_n - \text{HE}_1}{T}, \tag{4.6}$$

where n is the current warp of the image, and the numerator measures the overall length changes between the original vertices and the warped surface vertices, and the denominator T is a normalization term that represents for the total number of neighbours for all the vertices belongs to a surface. The results of evaluating HE in each iteration are demonstrated in the Figure 4.13.

Experiments Based on Binary Maps: In the first division of the experiments, we hope to check the spherical surface registration methods using the binary maps formulated in Section 4.3.4. As an overview, We can see the iterative results on Figures 4.11 4.12 4.13, they showed three major categories and five sub-divisions in each category, totally fifteen methods we compared in our studies. From the results, we can directly observe that fluid-like demons (color in green) achieved best results in RMSE, followed by combined demons (color in blue), the diffusion-like demons (color in red) scored the worst dice similarity and RMSE. However, achieving the best DSC and RMSE is not necessary to conclude, because we need to consider the tradeoffs between image similarity and mesh regularization. Thus, we also need to evaluate the level of mesh distortion. As we can see from the Figure 4.13, fluid-like demons achieved the highest values of the harmonic energy; these results indicated more severe mesh distortion using fluid-like demons. The severe mesh distortion may cause mesh irregularity in the process of mesh reconstruction, and bring errors in further statistical analyses since our analyses are based on shape changes.

When we look deeper in each of the three major categories, we can find that due to the nice properties of second derivative LM algorithm, our algorithms converged fast in each category. Even though we set 30 iterations on each resolution level, we realized this number was far than enough for the convergence. However, by keeping the $iter = 30$, we hope to illustrate the behavior of the algorithm without a stopping criterion, and compare the results with the algorithms with stopping criteria.

We start the group comparisons by discussing the results from diffusion-like spherical demons. We can see from the red lines in Figure 4.11 and Figure 4.12, they demonstrated the results of DSC and RMSE respectively, our experiments did not benefit from diffeomorphic as we can see, the compositive demons achieved better results in reducing RMSE than the basic diffeomorphic spherical demons (BSD). The proposed methods Symm SD (SSD) and Symm-momen SD (SMSD) achieved best results in RMSE and DSC, and a conclusion is derived from this set of experiments that the momentum term played a positive role in reducing RMSE. We can also observe from the Figure 4.13, the diffusion-like registrations achieved the lowest scores in the evaluations of HE. We can also validate this by checking the mesh visually.

Secondly, we illustrate the results from fluid-like demons. Compared to diffusion-like demons, the fluid-like demon's features for less regularization. Thus, it scored very low RMSE in all of four levels. As a result, the surface mesh is extremely irregular due to large deformation in a lower resolution as shown in Figure 3.18(a-b).

Lastly, we demonstrate the results from combined demons. We applied a 3-level multi-resolution scheme, smoothing the surface features and regularizing the registration more at the first level, then we reduce regularization to relax the rest of subsequent levels, we removed regularization for displacement field and only kept regularization on updates at the last level of registration. As a result, we can observe from Figure 4.12, the RMSE results of combined demons were approaching to fluid-like demons, while HE was reserved in a proper range. In this experimental set, our proposed methods (SSD and SMSD) achieved the best RMSE results while keeping low HE values.

An example of the final registration results using binary maps is demonstrated in Figure 4.14. Each surface mesh has the same resolution with the original surface of the subject, which means the final registration result is interpolated from "ic7" (the 4th level of registration) to the original resolution of the subject's surface mesh. As we can see from the results, the proposed method works well in aligning the moving surface to match the template.

Experiments Based on Distance Maps: In the second division of the experiments, we hope to check the spherical surface registration methods using the distance maps formulated in Section 4.3.4.

We start the group comparisons by examining the results from diffusion-like spherical demons. We can see from the red lines in Figure 4.15 and Figure 4.16, our experiments did not benefit from diffeomorphic as we can see, the compositive demons achieved equal or better results in reducing RMSE than the basic diffeomorphic spherical demons (BSD). The proposed methods Symm SD (SSD) and Symm-momen SD (SMSD) achieved best results in RMSE and DSC. Thus, in this set of experiments, the momentum term played a positive role in reducing RMSE. We can also observe from FigureFigure 4.17, the diffusion-like registrations achieved the lowest scores in the evaluations of HE. We can also validate this by checking the mesh visually.

Secondly, we discuss the results from fluid-like demons. Similar to our previous tests using binary maps, the fuild-like registration methods scored very low RMSE in all of four levels, it also achieved high HE scores. The proposed methods Symm SD (SSD) and Symm-momen SD (SMSD) achieved best results in RMSE and DSC, while the rest of the three methods achieved similar registration results.

Lastly, we discuss the results from combined demons. we can observe from Figure 4.15, Figure 4.16, and Figure 4.17, the RMSE results of combined demons were approaching to fluid-like demons, while HE was reserved in a proper range. In this experimental set, our proposed methods (SSD and SMSD) achieved the best RMSE results while keeping low HE values.

Experiments Based on Probability Maps: In the third division of the experiments, we hope to check the spherical surface registration methods using the probabilistic maps formulated in Section 4.3.4.

As we can see from the Figure 4.18, 4.19 and 4.20 the probability maps returned from ASHS segmentation results are not well regularly distributed. Even though the yellow and cyan colored regions provided a relatively stable pattern for hippocampal subfield distributions, the probability values within the region are not well regularized. This type of pattern severely affected the accuracy of the registration.

We start the group comparisons by examining the results from diffusion-like spherical demons. We can see from the red lines in Figure 4.18 and Figure 4.19, our experiments were not benefit from deffeomorphic as we can see the compositive demons achieved better results in reducing RMSE than the basic deffeomorphic spherical demons (BSD). The proposed methods Symm SD (SSD) and Symm-momen SD (SMSD) achieved best results in RMSE and DSC. Thus, in this set of experiments the momentum term played a positive role in reducing RMSE. We can also observe from the Figure 4.20, the diffusion-like registrations achieved the lowest scores in the evaluations of HE. We can also validate this by checking the mesh visually.

Secondly, we discuss the results from fluid-like demons. Compared to the other two groups, the five methods using fluid-like demons scored overall lowest RMSE and highest DSC in all of four registration levels, similar to the previous comparisons, the methods in this category achieved overall highest HE. The proposed methods Symm SD (SSD) and Symm-momen SD (SMSD) achieved best results in DSC, and Symm SD (SSD) achieved the lowest scores in RMSE.

Lastly we discuss the results from combined demons. we can see from Figure 4.18, 4.19 and 4.20, the RMSE, DSC and HE results of combined demons were in between of fluid-like methods and diffusion-like demons. The combined demons take a good compromise between registration similarity and mesh regularity. Our proposed methods (SSD and SMSD) achieved the best RMSE results while keeping relatively low HE values.

Discussions on Comparison Results: In the previous parts we compared the basic spherical demons (BSD) algorithm with other variants, the results shown in Figures 4.11, 4.12, 4.13, 4.15, 4.16, 4.17, 4.18, 4.19 and 4.20 demonstrated the proposed methods achieved improvements compared to the original spherical demons. However, the improvement is meaningless if it is too small. So we performed some further analyses on the experimental results to examine if the improvement is statistically significant.

In Figures 4.21, 4.22, 4.23, 4.24, 4.25, 4.26, 4.27, 4.28 and 4.29, we demonstrated the DSC, RMSE, and HE values of each subject, while the individual subjects are grouped based on the surface features we used and the regularization types. We also calculated the mean and variance of each experimental group. We can see from the figures, Symm SD (SSD) and Symm-Momen SD (SMSD) achieved the best RMSE and DSC in the comparisons for both left and right hippocampi. Symm SD (SSD) usually can achieve lower HE scores compared with Symm-Momen SD (SMSD).

For the comparisons among surface signals binary maps, distance maps, and probability maps, we can see the tests using binary maps achieved best DSC and RMSE results. Even though we realized that using binary maps lead to a higher HE score, we find the mesh quality was acceptable.

For three types of surface signals and three regularization methods, The initial intend is to perform t-test on the evaluations of the registration results such as DSC, RMSE and HE to see if these measurements are significantly different for different demons registration strategies. As t-test requires an assumption that the data should obey a normal distribution, we performed Lilliefors test [133, 134] to check the normality of the evaluation results. Even though we assumed the evaluation results were normally distributed or at least normally-like distributed, we found some of the data were not strictly normally distributed (but visually normal-like) due to the sizes of the data sets. So we performed a Box-Cox transformation [135, 136] on the data that were not strictly normal, it transforms non-normally distributed variables into a normal distribution. Then we performed t-test on the transformed data sets: the

transformed data were used for both groups in comparisons when at least one group of data was non-normal. Similarly, as we treated BSD as the benchmark in the comparisons, the transformed data were used in all of the comparisons (BSD vs. CSD, BSD vs. SSD, BSD vs. MSD and BSD vs. SMSD) as long as the original data set of BSD was non-normal. The statistical results for DSC, RMSE, and HE measures are summarized in the Tables 4.1, 4.2 and 4.3. The results marked with a star indicates they were obtained from transformed data sets. Conversely, the results without a star were from original measures. From the results we can see, compared to the basic SD (BSD) algorithm, our proposed Symm SD (SSD) and Symm-Momen SD (SMSD) improved on DSC and RMSE significantly, while few significant differences were noticed on the measurements of HE.

4.3.7 Building Hippocampal Surface Atlas

After the surface signals are well aligned in parameter space, our next step is to align them in the object space. We still use FOE to align the spatial orientation of each subject by utilizing their first order reconstruction. Then we reconstruct each hippocampal surface with a degree of 15 reconstruction. Each reconstructed surface contains 2562 vertices and 5120 faces. At the last step, we averaged all subjects from the healthy control group and obtained a surface atlas based on healthy people. The averaged left, and the right atlas is shown in Figure 4.30.

4.3.8 Summary

A novel computational framework has been presented to build a surface atlas of hippocampal subfields from high-resolution T2-weighted MRI scans. Compared with previous studies, the major contributions of this work are fourfold: (1) it demonstrates detailed and accurate hippocampal subfield partitions by using high-resolution T2-weighted data. (2) It maps complex surface anatomical topology onto a sphere to establish surface correspondence across individuals. (3) It formulates different types

Table 4.1.: t-test results to examine the improvements on dice similarity coefficient (DSC). A Box-Cox transformation was applied to transfer the non-normally distributed data to normal distribution. Comparisons based on the transformed data are marked with a star.

Study	Dice Similarity Coefficient			
	BSD vs.CSD	BSD vs.SSD	BSD vs.MSD	BSD vs.SMSD
Binary_comb_r	1.00E+00	4.04E-24	3.31E-01	3.47E-27
Binary_comb	1.00E+00*	1.13E-04*	1.00E+00*	9.09E-01*
Binary_fluid_r	1.00E+00	8.48E-13	7.41E-02	1.34E-14
Binary_fluid	7.85E-01	1.20E-13	1.18E-03	1.02E-13
Binary_diff_r	1.70E-02	2.16E-28	5.80E-01	5.59E-37
Binary_diff	3.37E-02	1.51E-26	3.19E-01	4.15E-56*
DistMap_comb_r	1.00E+00	2.63E-25	4.93E-01	9.69E-32
DistMap_comb	1.00E+00	5.63E-29	8.42E-01	3.11E-29
DistMap_fluid_r	9.99E-01	4.01E-24*	3.40E-01	4.82E-26*
DistMap_fluid	6.52E-19*	4.20E-23*	1.00E+00*	2.78E-31*
DistMap_diff_r	1.00E+00	1.89E-31	9.80E-01	2.33E-40
DistMap_diff	9.97E-01	1.05E-32	8.43E-01	9.24E-43
ProbMap_comb_r	9.38E-01	2.94E-10	7.93E-01	5.79E-13
ProbMap_comb	8.29E-01	4.79E-19	1.21E-01	3.49E-24
ProbMap_fluid_r	9.75E-01	1.00E+00*	8.27E-01	7.35E-01
ProbMap_fluid	1.00E+00*	1.00E+00*	2.28E-23*	1.00E+00*
ProbMap_diff_r	3.13E-03	1.67E-14	8.02E-01	4.18E-19
ProbMap_diff	2.69E-01	8.40E-27	1.00E+00	4.26E-35

Table 4.2.: t-test results to examine the improvements on root mean square error (RMSE). A Box-Cox transformation was applied to transfer the non-normally distributed data to normal distribution. Comparisons based on the transformed data are marked with a star.

Study	Root Mean Square Error			
	BSD vs.CSD	BSD vs.SSD	BSD vs.MSD	BSD vs.SMSD
Binary_comb_r	9.97E-01	9.53E-27	1.00E+00	2.16E-37
Binary_comb	9.99E-01*	1.93E-21	4.61E-01	7.26E-31
Binary_fluid_r	7.48E-02	1.06E-07	9.99E-01	1.31E-05
Binary_fluid	2.59E-04	1.10E-06	3.66E-04	1.01E-07
Binary_diff_r	7.38E-07	4.12E-28	5.12E-01	1.23E-35
Binary_diff	4.63E-04*	2.63E-32*	3.03E-01*	2.05E-42*
DistMap_comb_r	9.05E-01	3.83E-30	4.45E-01	4.85E-39
DistMap_comb	9.18E-01*	9.13E-34	5.43E-01	1.44E-38
DistMap_fluid_r	7.94E-01	8.49E-14	3.96E-01	7.37E-20
DistMap_fluid	6.20E-01*	6.90E-19*	8.54E-01*	6.55E-24*
DistMap_diff_r	1.76E-01	3.04E-31	9.71E-01	1.37E-40
DistMap_diff	1.39E-01*	1.04E-37*	6.64E-01*	1.64E-49*
ProbMap_comb_r	9.39E-01	2.25E-21*	8.56E-01	1.95E-28
ProbMap_comb	5.98E-01*	4.17E-22*	6.81E-02*	5.22E-27*
ProbMap_fluid_r	9.90E-01	1.56E-01	5.82E-01	6.56E-01*
ProbMap_fluid	6.68E-01	3.77E-01	2.29E-01	3.59E-01*
ProbMap_diff_r	8.30E-02	3.93E-24	8.03E-01	1.66E-30
ProbMap_diff	4.48E-01*	1.69E-30	9.86E-01	3.82E-43*

Table 4.3.: t-test results to examine the significant difference on harmonic energy (HE). A Box-Cox transformation was applied to transfer the non-normally distributed data to normal distribution. Comparisons based on the transformed data are marked with a star.

Study	Harmonic Energy			
	BSD vs.CSD	BSD vs.SSD	BSD vs.MSD	BSD vs.SMSD
Binary_comb_r	8.49E-11	1.00E+00*	4.81E-01	1.00E+00*
Binary_comb	9.57E-08*	1.00E+00*	7.90E-01*	1.00E+00*
Binary_fluid_r	8.90E-02*	1.00E+00	9.93E-01*	1.00E+00*
Binary_fluid	1.44E-01	1.00E+00	1.00E+00	1.00E+00
Binary_diff_r	1.30E-23	1.00E+00	4.70E-09	1.00E+00
Binary_diff	6.66E-17*	1.00E+00*	3.16E-04*	1.00E+00*
DistMap_comb_r	9.54E-11	1.00E+00*	7.09E-02	1.00E+00*
DistMap_comb	4.99E-05*	1.00E+00*	9.84E-02*	1.00E+00*
DistMap_fluid_r	1.67E-01	1.00E+00	7.70E-02	1.00E+00
DistMap_fluid	6.69E-01*	1.00E+00*	9.49E-01*	1.00E+00*
DistMap_diff_r	4.55E-19	1.00E+00	1.58E-09	1.00E+00
DistMap_diff	2.11E-18*	1.00E+00*	4.69E-08*	1.00E+00*
ProbMap_comb_r	9.91E-06	1.00E+00	6.02E-01	1.00E+00
ProbMap_comb	7.67E-05	1.00E+00*	6.46E-01*	1.00E+00*
ProbMap_fluid_r	2.26E-01	1.00E+00	4.03E-01	1.00E+00
ProbMap_fluid	9.09E-02	1.00E+00	2.16E-01	1.00E+00
ProbMap_diff_r	1.43E-13*	1.00E+00*	3.28E-05*	1.00E+00*
ProbMap_diff	1.28E-05*	1.00E+00*	9.88E-05*	1.00E+00*

of surface signals that can better describe the subfield distributions than using label maps directly. And (4) it provides a pathway for fast and accurate landmark free registration that embraces, rather than ignores, the precious subfield information. We have demonstrated its effectiveness by applying it to both of the IADC and ADNI data. Instead of identifying landmarks on subfield boundaries, the landmark free registration makes use of surface label information to guide registration.

4.4 Summary of Chapter 4

In this section, we introduced our initial efforts on building a framework based on traditional T1-weighted MRI scans. This framework showed the feasibility of surface morphometric analyses and gave us the confidence for further explorations. After those initial efforts, we were aware that recently released high-resolution MRI scans could provide more detailed information for hippocampal subfields and adjacent regions. Also, these high-resolution data got widely recognized and appreciated in recent year studies. The quality of alignment has a high effect on group studies. Based on our goals of research, we are aiming to examine the structural changes of hippocampal subfields; this motivated us to develop a registration method based on hippocampal subfield information. So we performed some preliminary work on processing these high-resolution data using IADC data and applied basic Spherical demons (BSD) methods for hippocampal subfield guided registration. The experimental results showed to be more promising compared with our work only based on T1-weighted data. Then we applied the proposed methods Symm SD (SSD) and Symm-Momen SD (SMSD) on a more extensive data set from ADNI. We compared our proposed methods with popular registration strategies, in most of the tests using different surface signals, our proposed outperformed the basic spherical demons (BSD) algorithm, our proposed methods achieved higher subfield matching rate and lower RMSE, in the meanwhile they kept the harmonic energy in a proper range. We

also validated that the improvements were statistically significant. This encourages us to work on a more in-depth investigation of hippocampal subfield morphometric analyses based on high-resolution MRI scans.

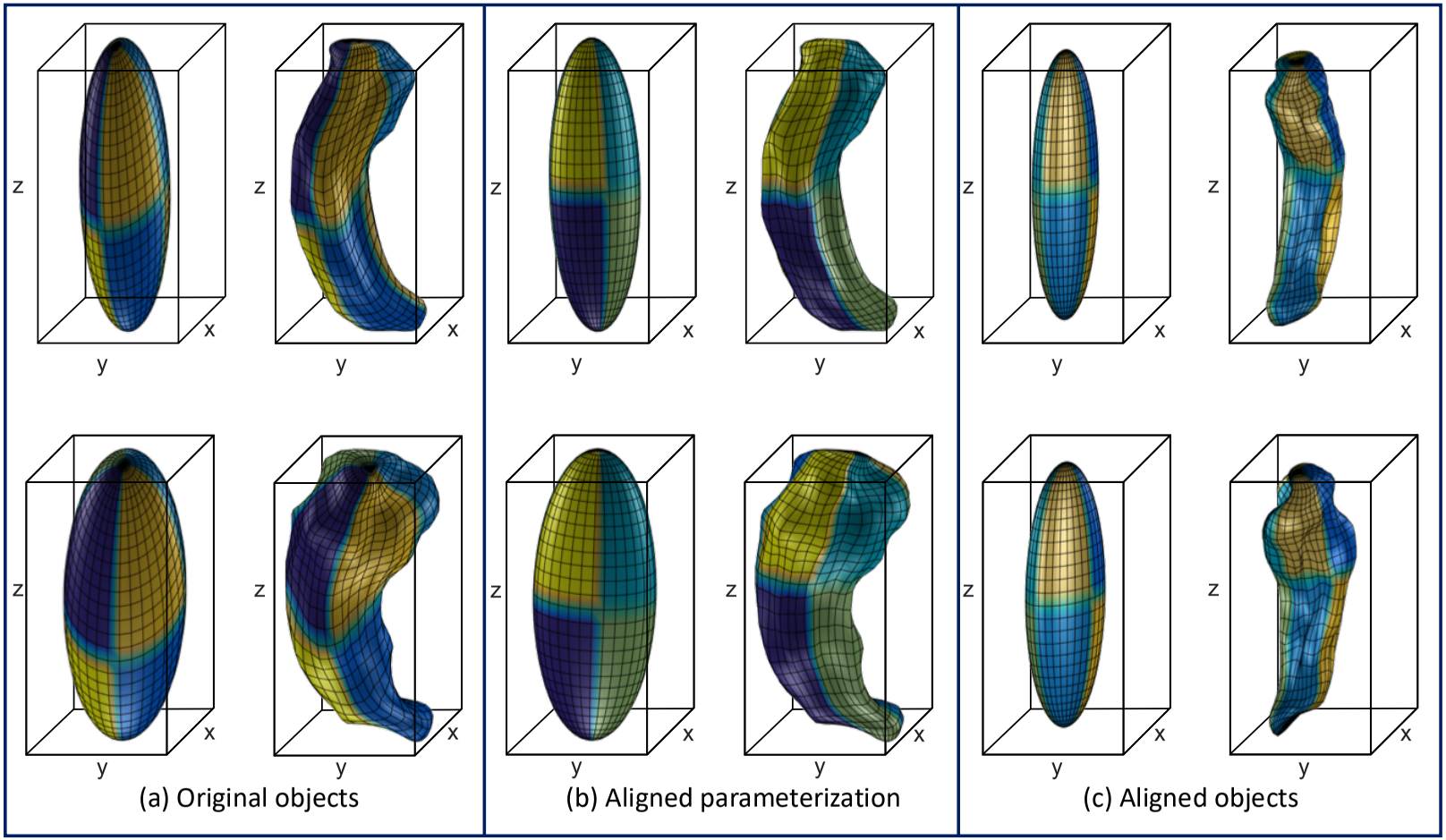

Fig. 4.1.: SPHARM registration using first order ellipsoids (FOEs). Each of (a-c) indicates the FOE on left and 15th degree reconstruction on right. Parameterization is shown by the mesh and color on the surface.

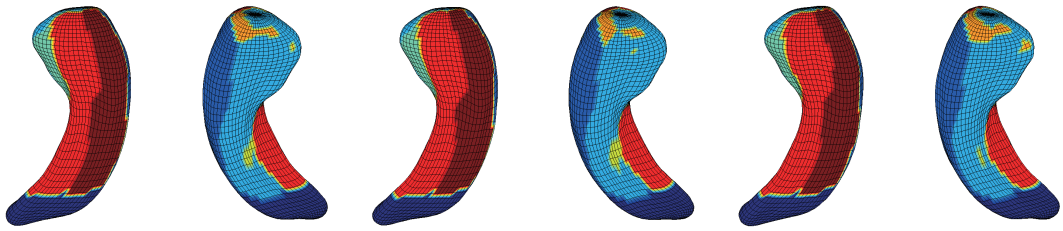

(a) using both scans (b) using Scan A (c) using Scan B

Fig. 4.2.: Surface atlases of hippocampal subfields created from MRI scans of 26 healthy controls, where each individual was scanned twice. (a) Atlas generated from using both scans, (b) atlas generated from using Scan A only, and (c) atlas generated from using Scan B only. Each of (a-c) visualizes the atlas from two different views.

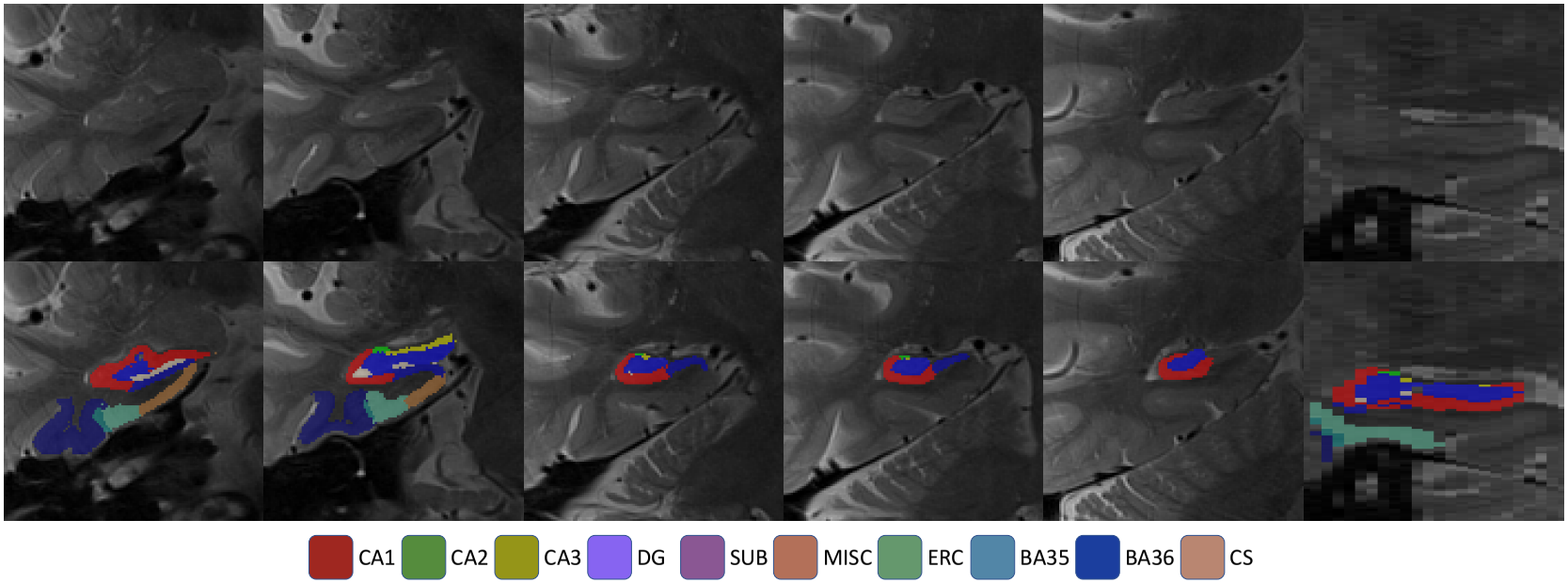

Fig. 4.3.: Examples of automatic segmentation results from high resolution MRI scans: Five coronal slices and one sagittal slice are shown.

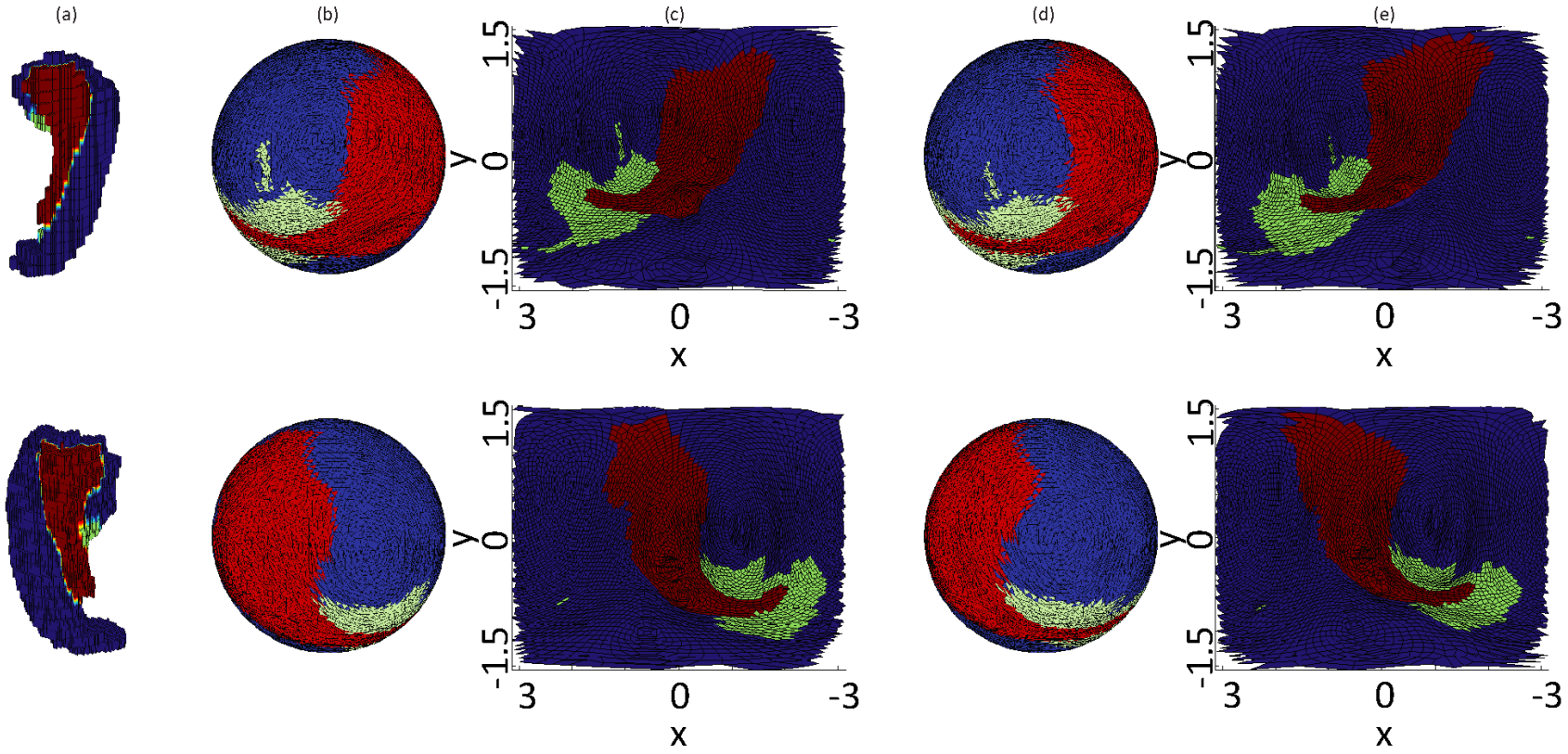

Fig. 4.4.: Example results of spherical parameterization (b-c) and SD registration (d-e): (a) Original object in Euclidean space, (b) original spherical mapping, (c) original spherical mapping unfolded to 2D plane, (d) registered spherical mapping using SD method, (e) registered spherical mapping unfolded to 2D plane. Red, blue, and green colors correspond to SUB+MISC, CA, and DG, respectively.

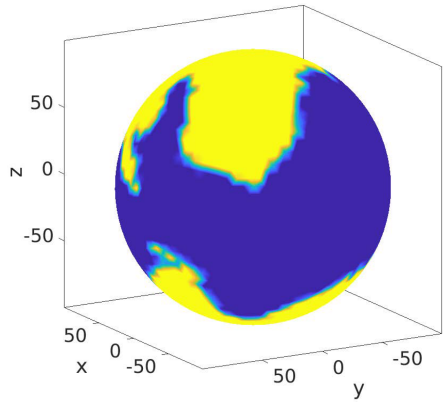

(a) Binary map for CA

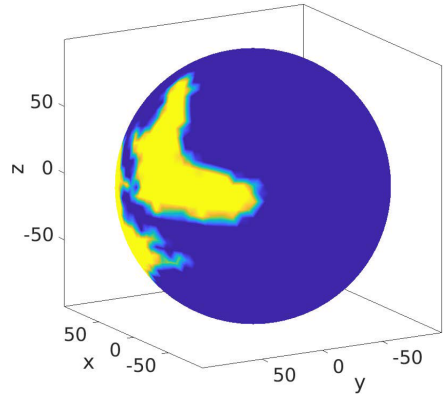

(b) Binary map for DG

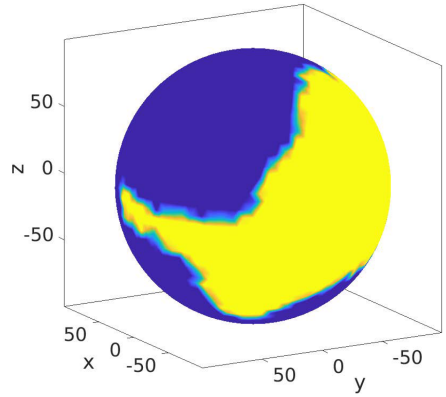

(c) Binary map for SUB

Fig. 4.5.: Some examples of generated binary maps for each hippocampal subfield. The regions with yellow color have values equal to one, the regions with blue color have values equal to zero.

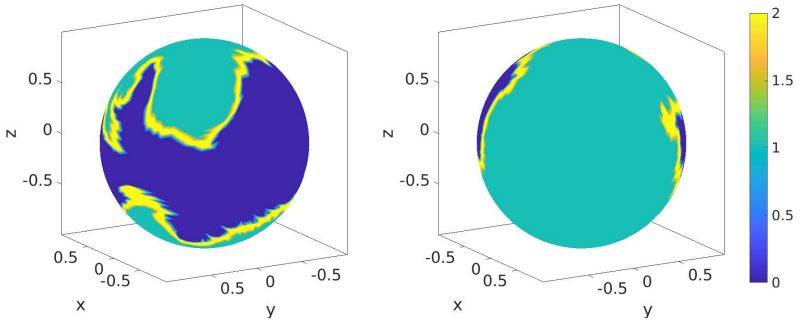

(a) Boundary map for CA

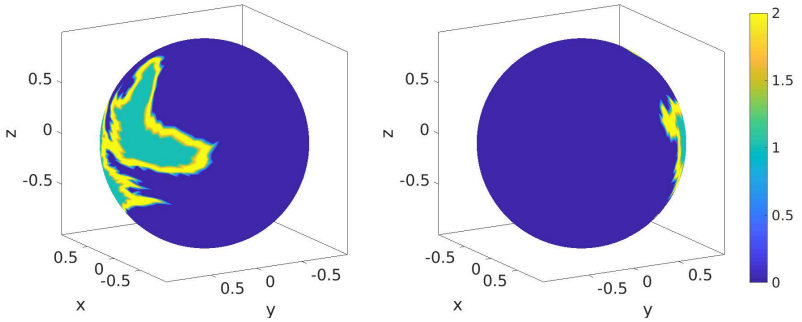

(b) Boundary map for DG

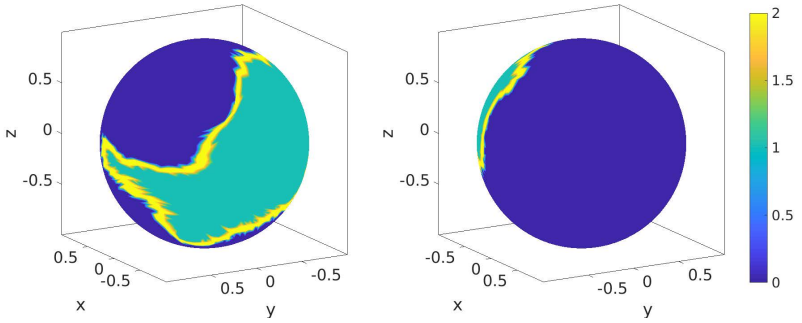

(c) Boundary map for SUB

Fig. 4.6.: Some examples of generated boundary maps for each hippocampal subfield. The regions with cyan color have values equal to one, the regions with blue color have values equal to zero, and the regions with yellow color have values equal to 2.

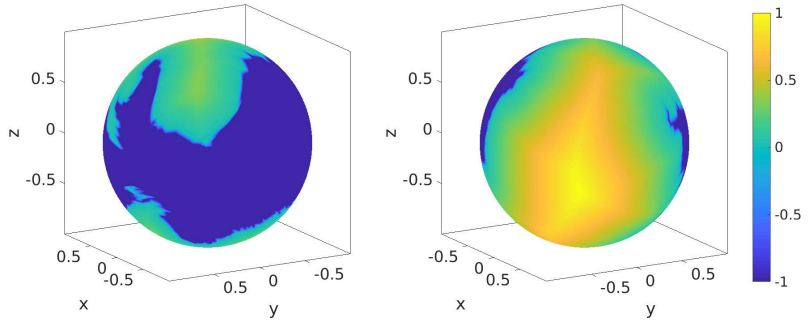

(a) Distance map for CA

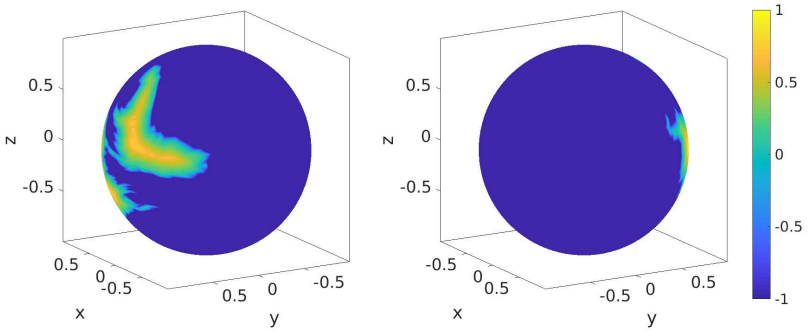

(b) Distance map for DG

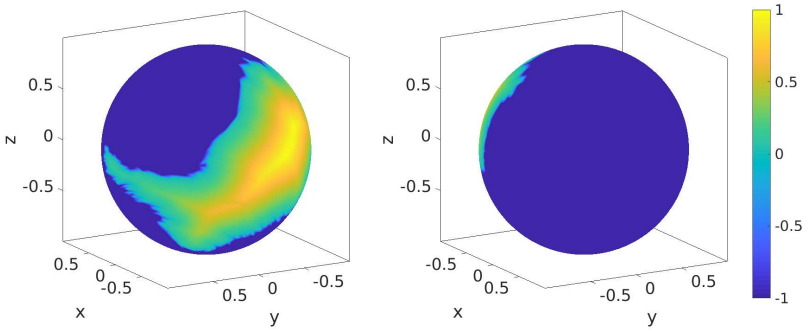

(c) Distance map for SUB

Fig. 4.7.: Some examples of normalized distance maps for each hippocampal subfield. The subfield regions are marked value between $(0, 1]$, the background regions are marked value equals as -1, and the boundaries are marked as zero.

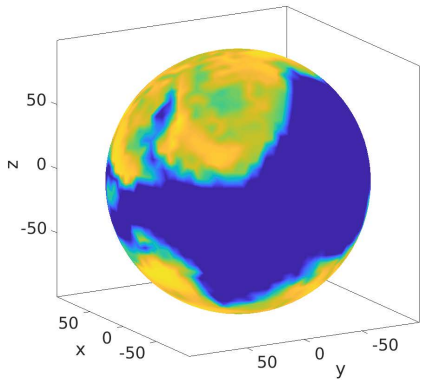

(a) Probability map for CA

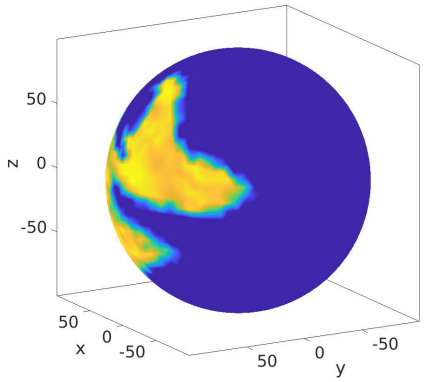

(b) Probability map for DG

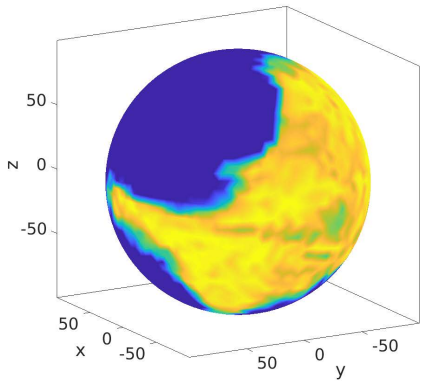

(c) Probability map for SUB

Fig. 4.8.: Some examples of probability maps for each hippocampal subfield. The subfield regions are marked as yellow and cyan; the background regions are marked as blue.

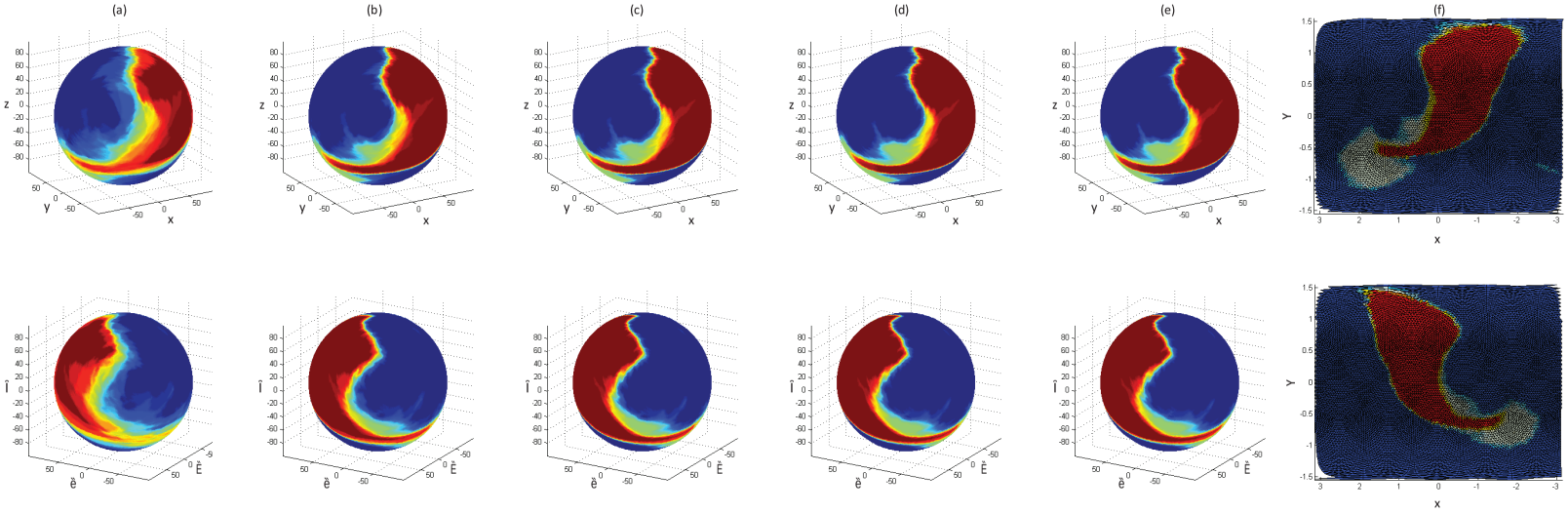

Fig. 4.9.: The top and bottom rows correspond to the left and right sides, respectively. (a) Mean spherical images after spherical parameterization and FOE alignment. (b-e) Mean spherical images after 1st-4th iterations in SD registration. (f) Spherical images in (e) unfolded to 2D space. Red, blue, and green colors correspond to SUB+MISC, CA, and DG, respectively. The mean spherical images shown in (e-f) are the converging results of SD method and are chosen to be our hippocampal subfield atlases.

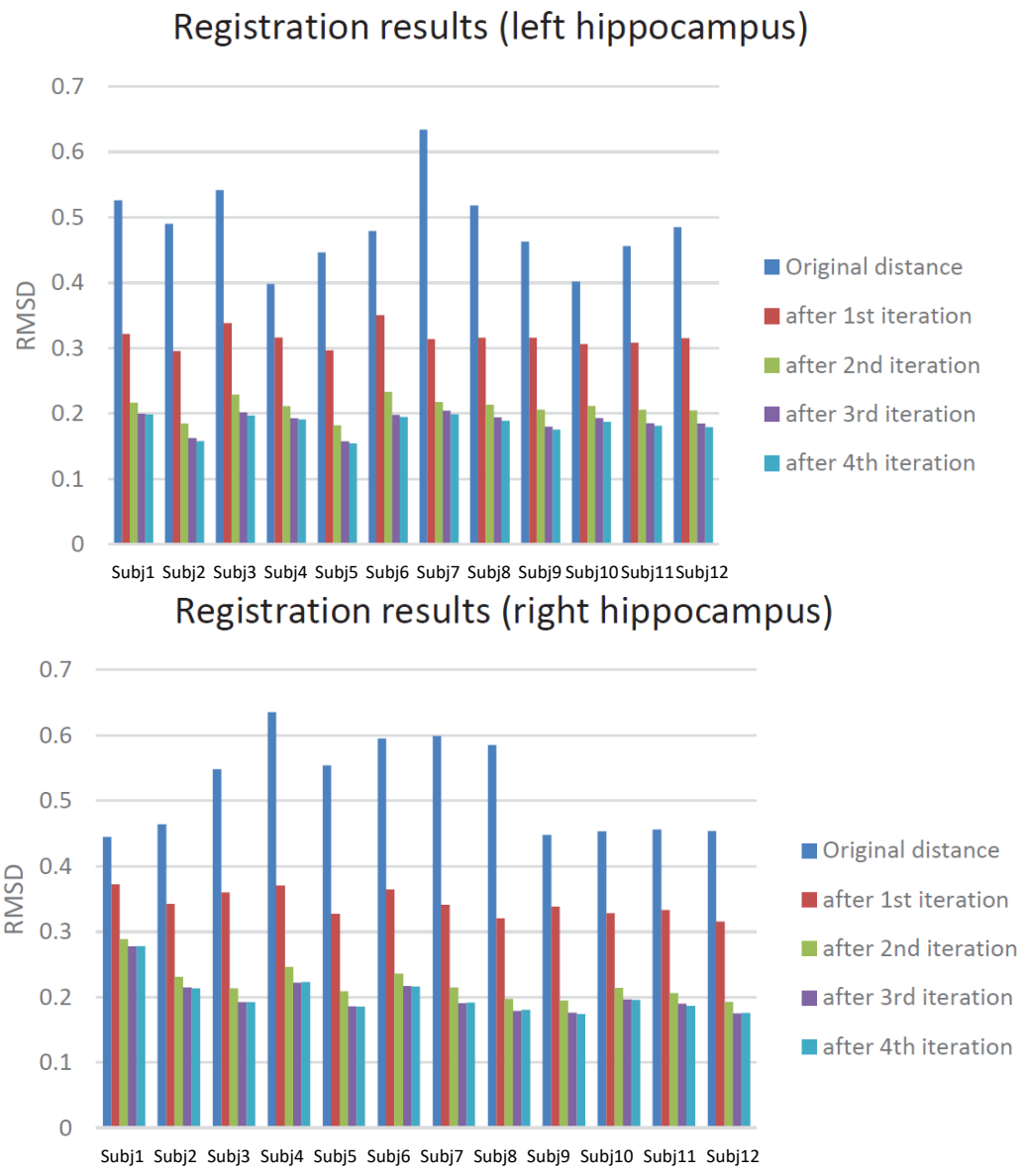

Fig. 4.10.: Root mean square error (RMSE) at each iteration for each subject.

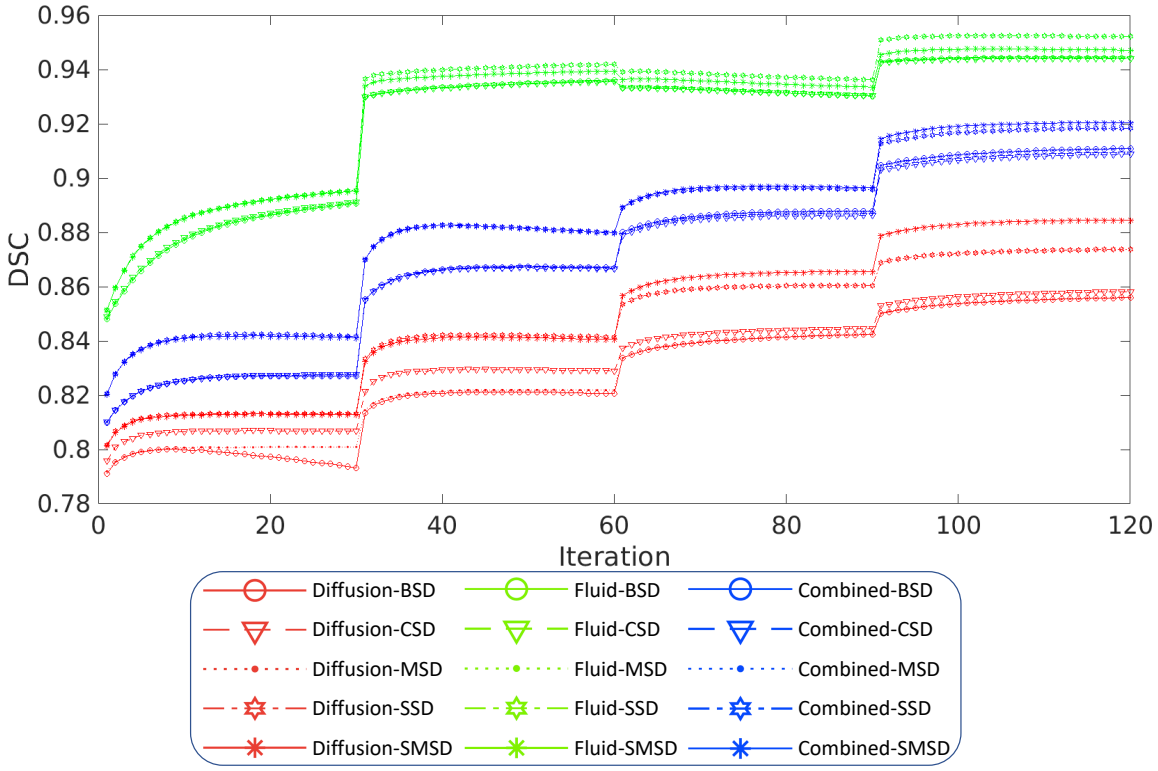

Fig. 4.11.: Summary of comparisons using binary maps: dice similarity coefficients (DSC). DSC is plotted against iteration.

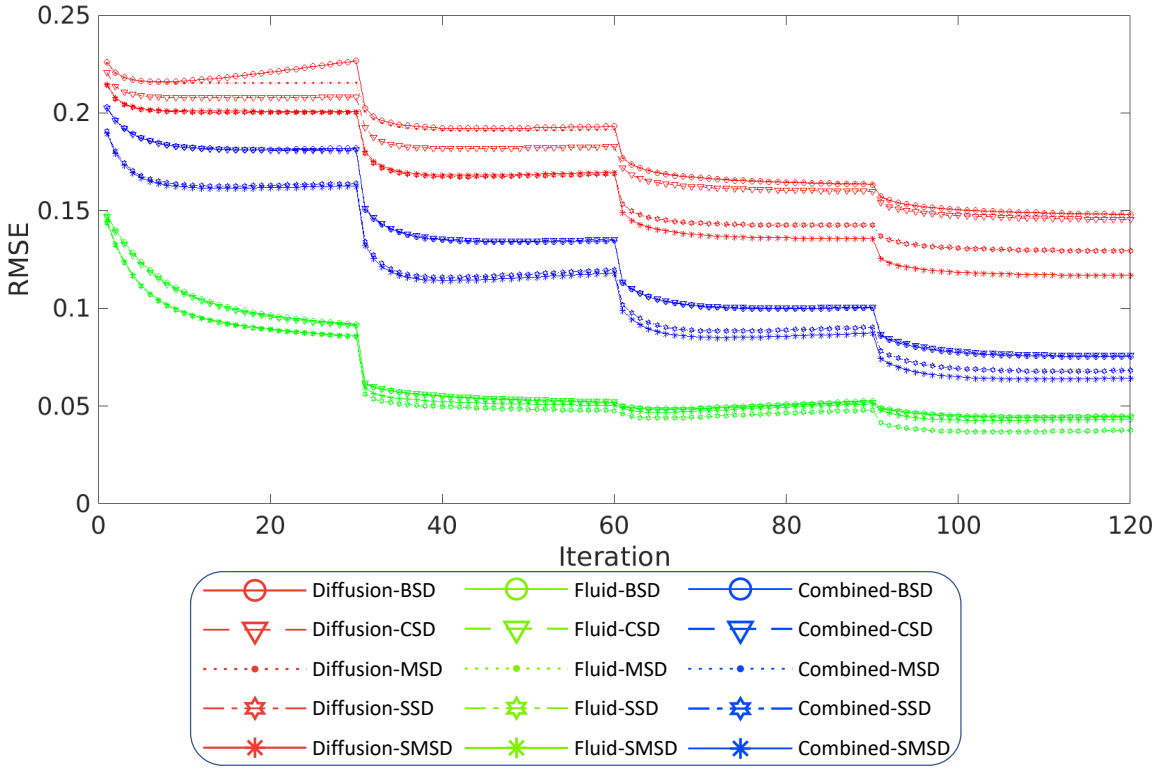

Fig. 4.12.: Summary of comparisons using binary maps: root mean square error (RMSE). RMSE is plotted against iteration.

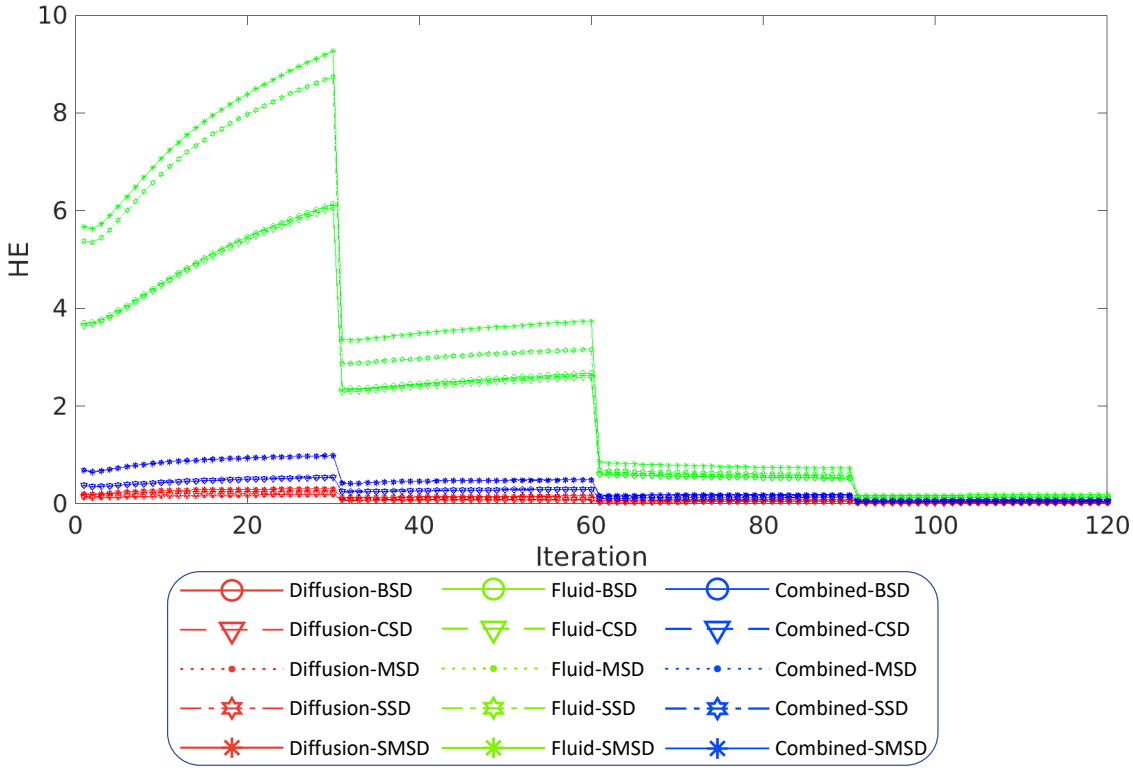

Fig. 4.13.: Summary of comparisons using binary maps: harmonic energy (HE). HE is plotted against iteration.

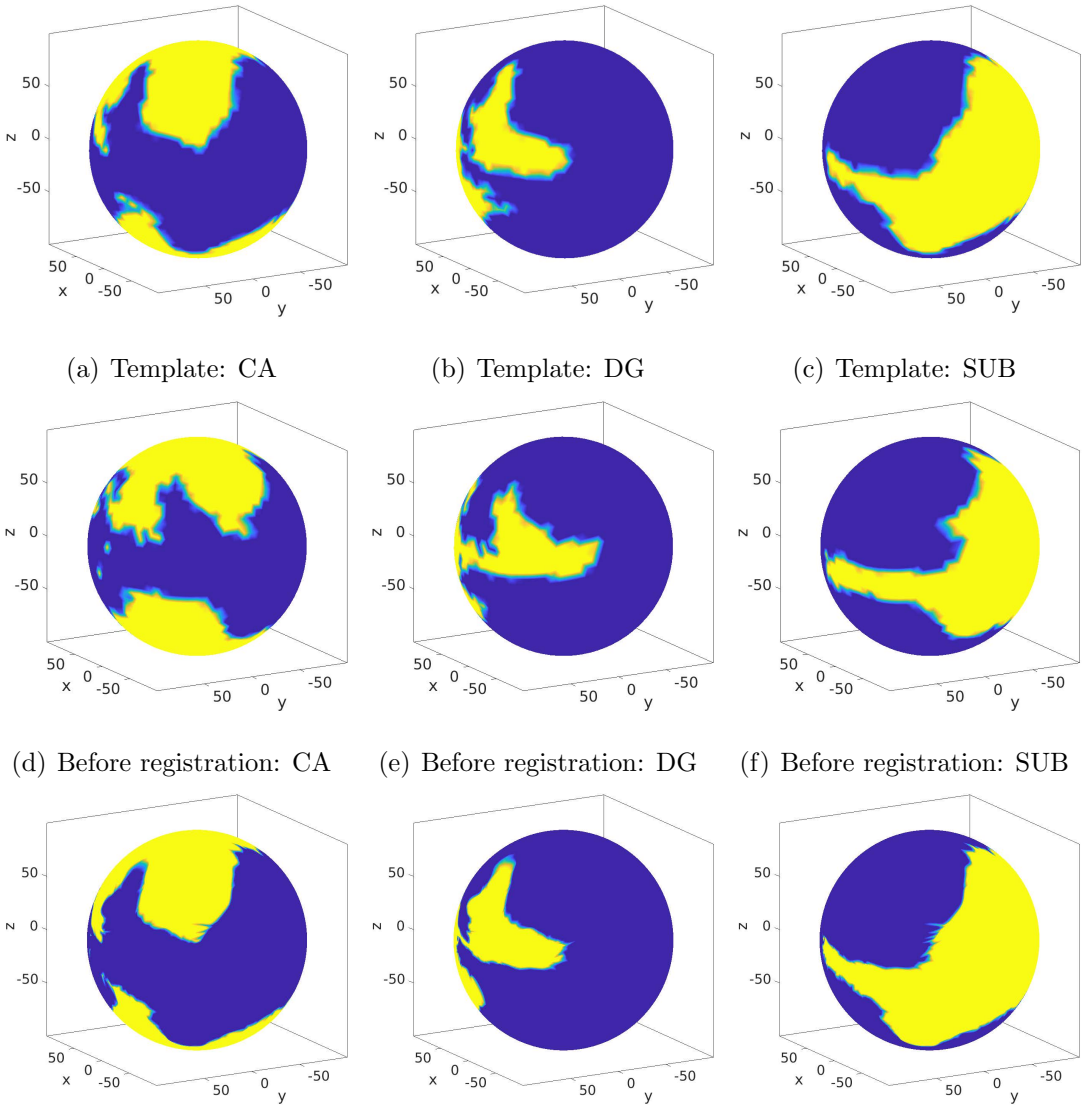

(a) Template: CA (b) Template: DG (c) Template: SUB

(d) Before registration: CA (e) Before registration: DG (f) Before registration: SUB

(g) After registration: CA (h) After registration: DG (i) After registration: SUB

Fig. 4.14.: An example of registration using binary maps.

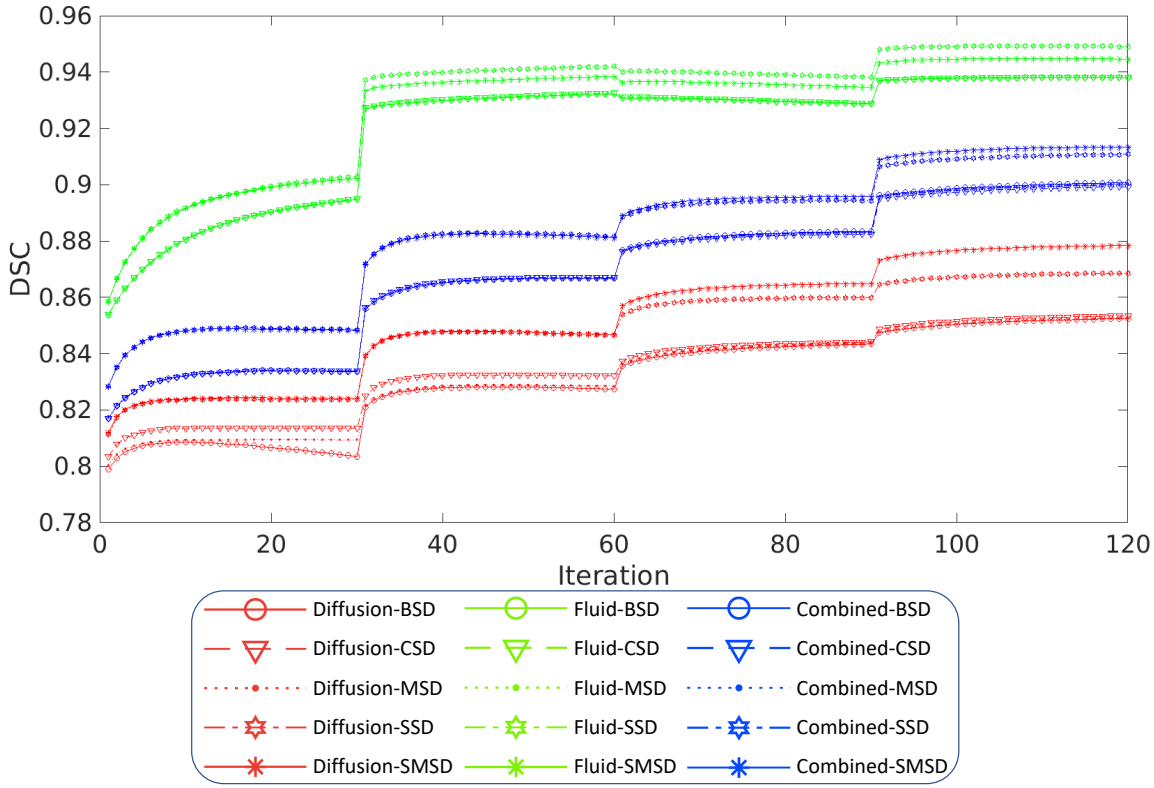

Fig. 4.15.: A summary of comparison results using distance maps: dice similarity coefficients (DSC). DSC is plotted against iteration.

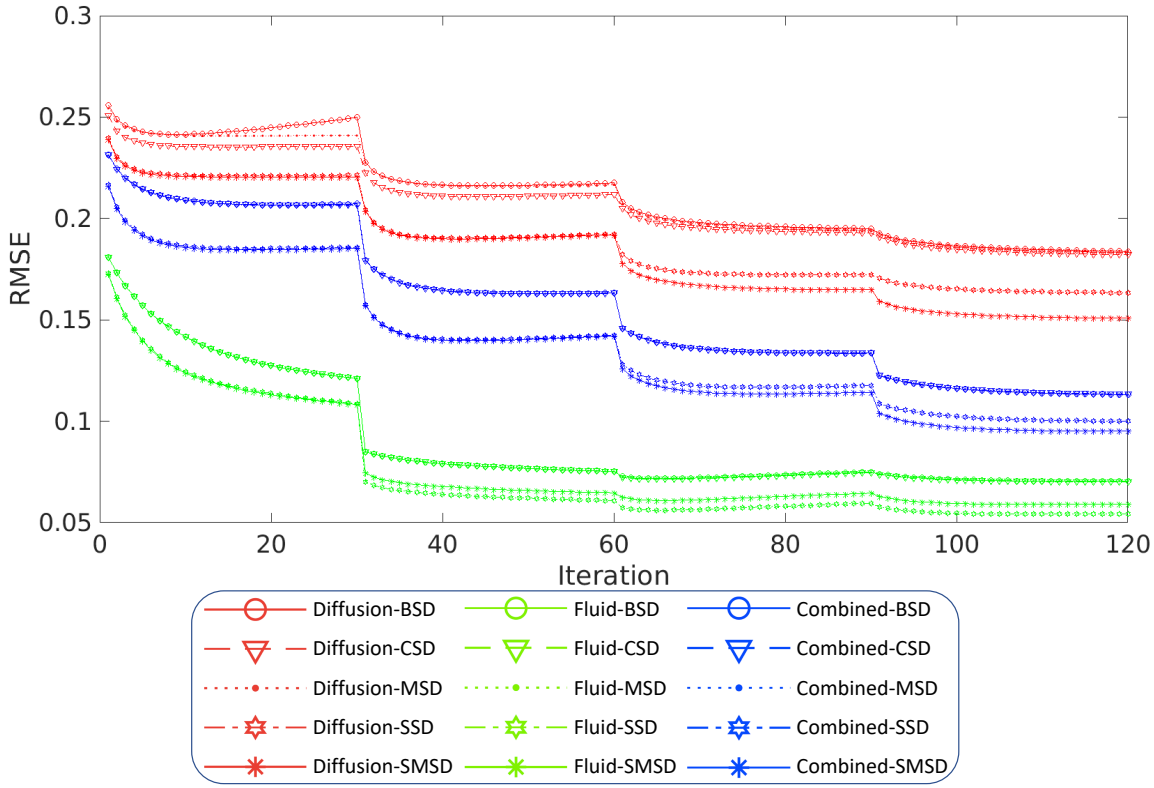

Fig. 4.16.: A summary of comparison results using distance maps: root mean square error (RMSE). RMSE is plotted against iteration.

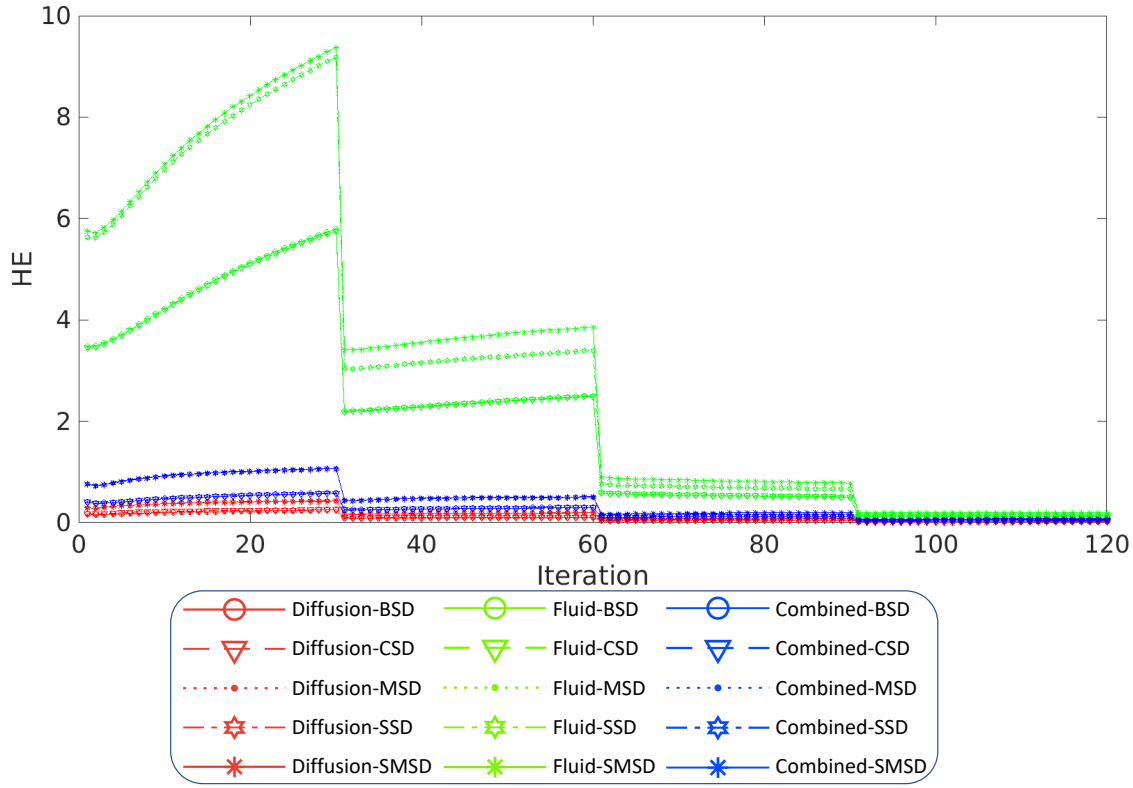

Fig. 4.17.: A summary of comparison results using distance maps: harmonic energy (HE). HE is plotted against iteration.

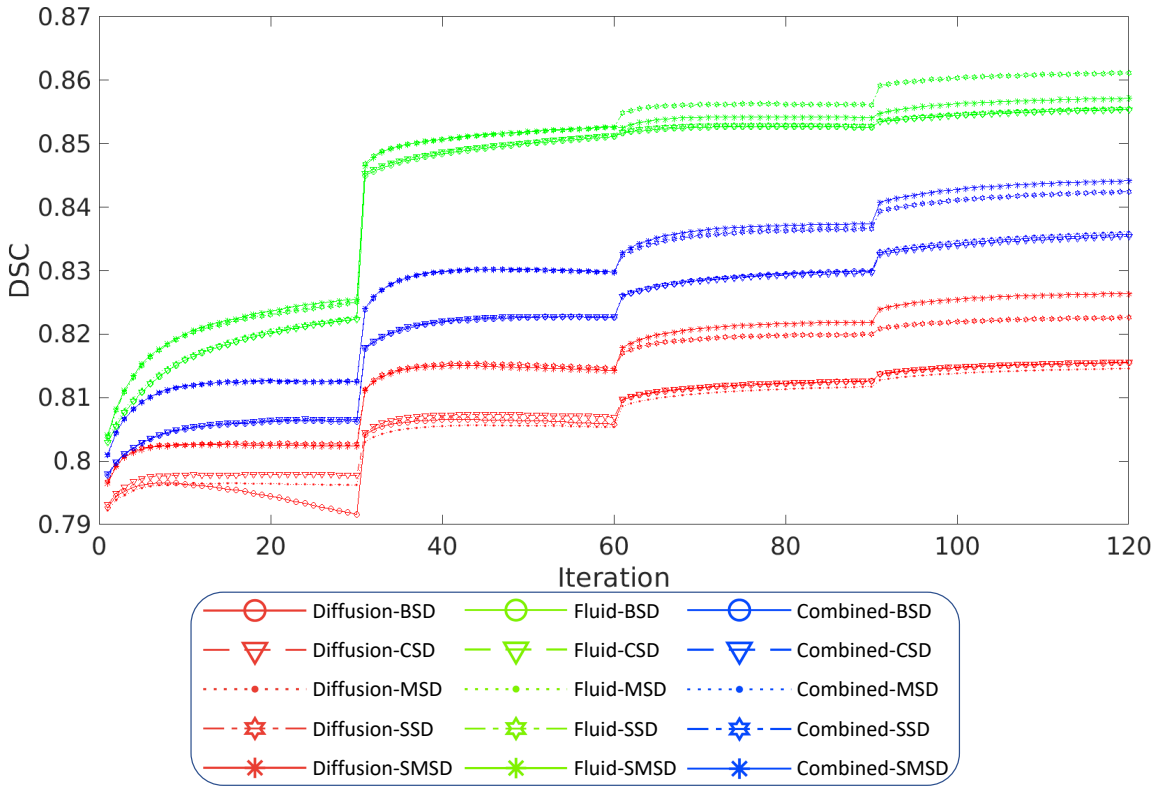

Fig. 4.18.: A summary of comparison results using probabilistic maps: dice similarity coefficients (DSC).

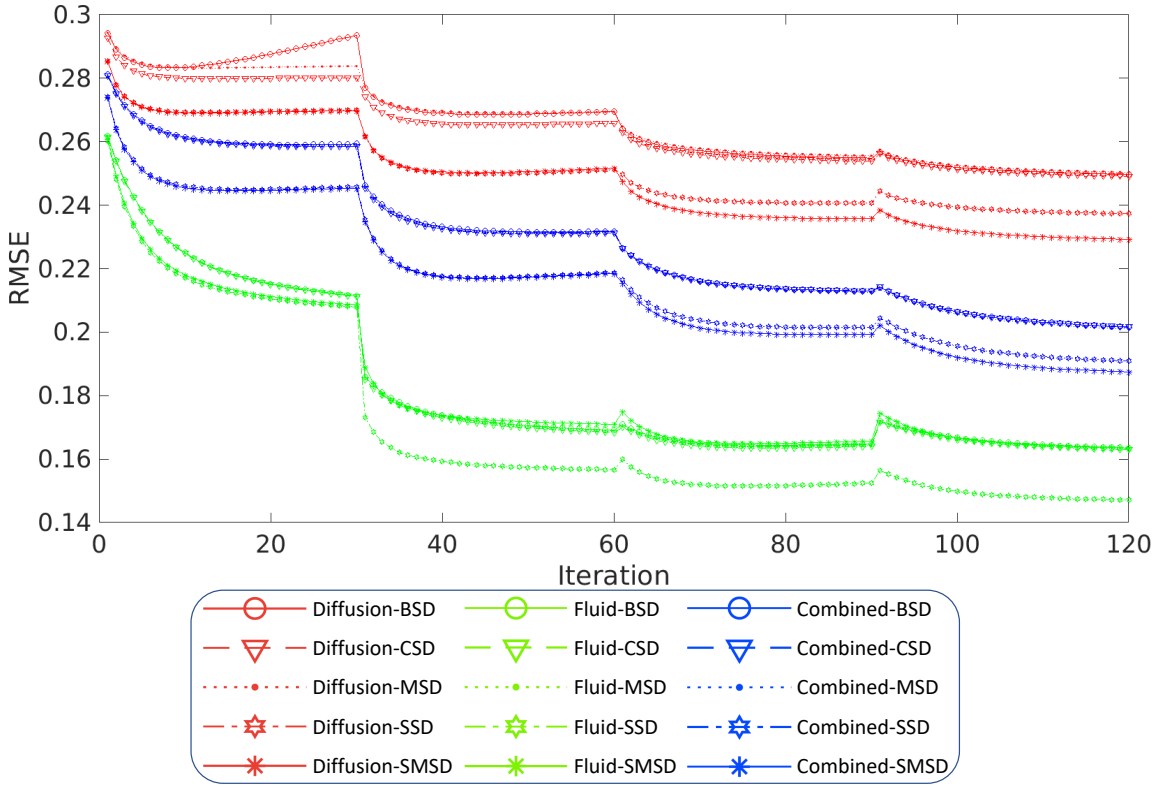

Fig. 4.19.: A summary of comparison results using probabilistic maps: root mean square error (RMSE).

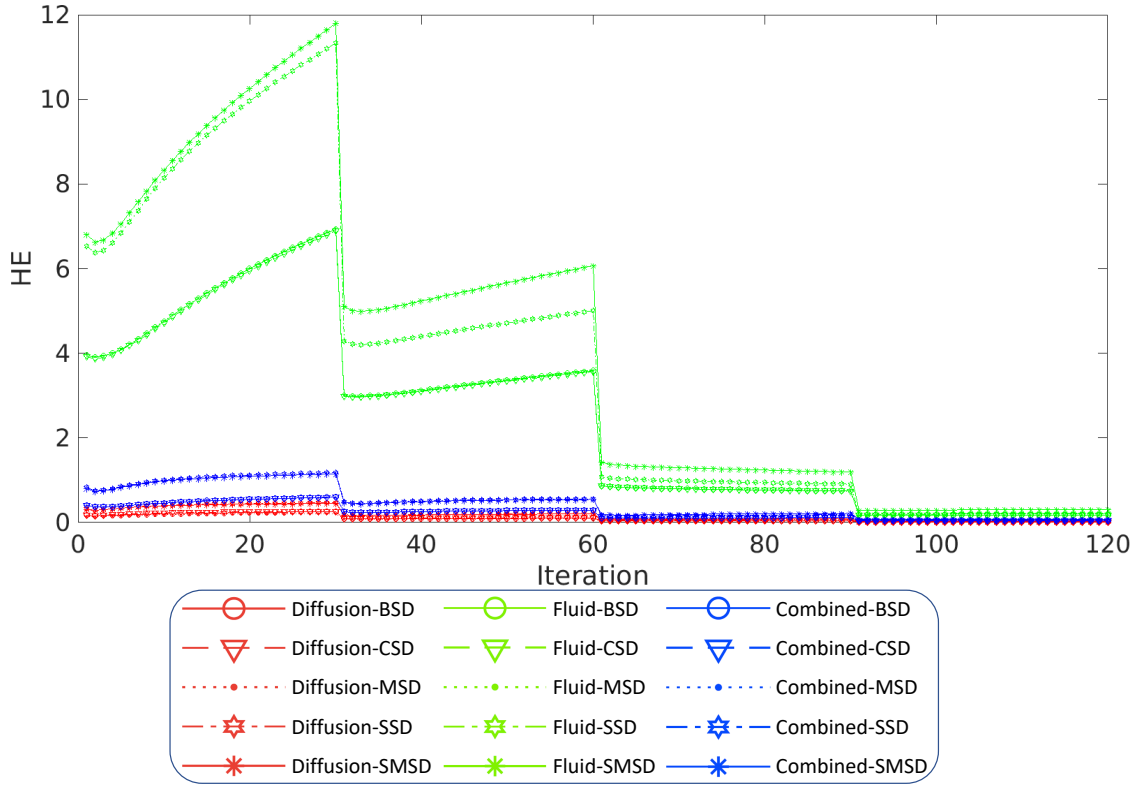

Fig. 4.20.: A summary of comparison results using probabilistic maps: harmonic energy (HE).

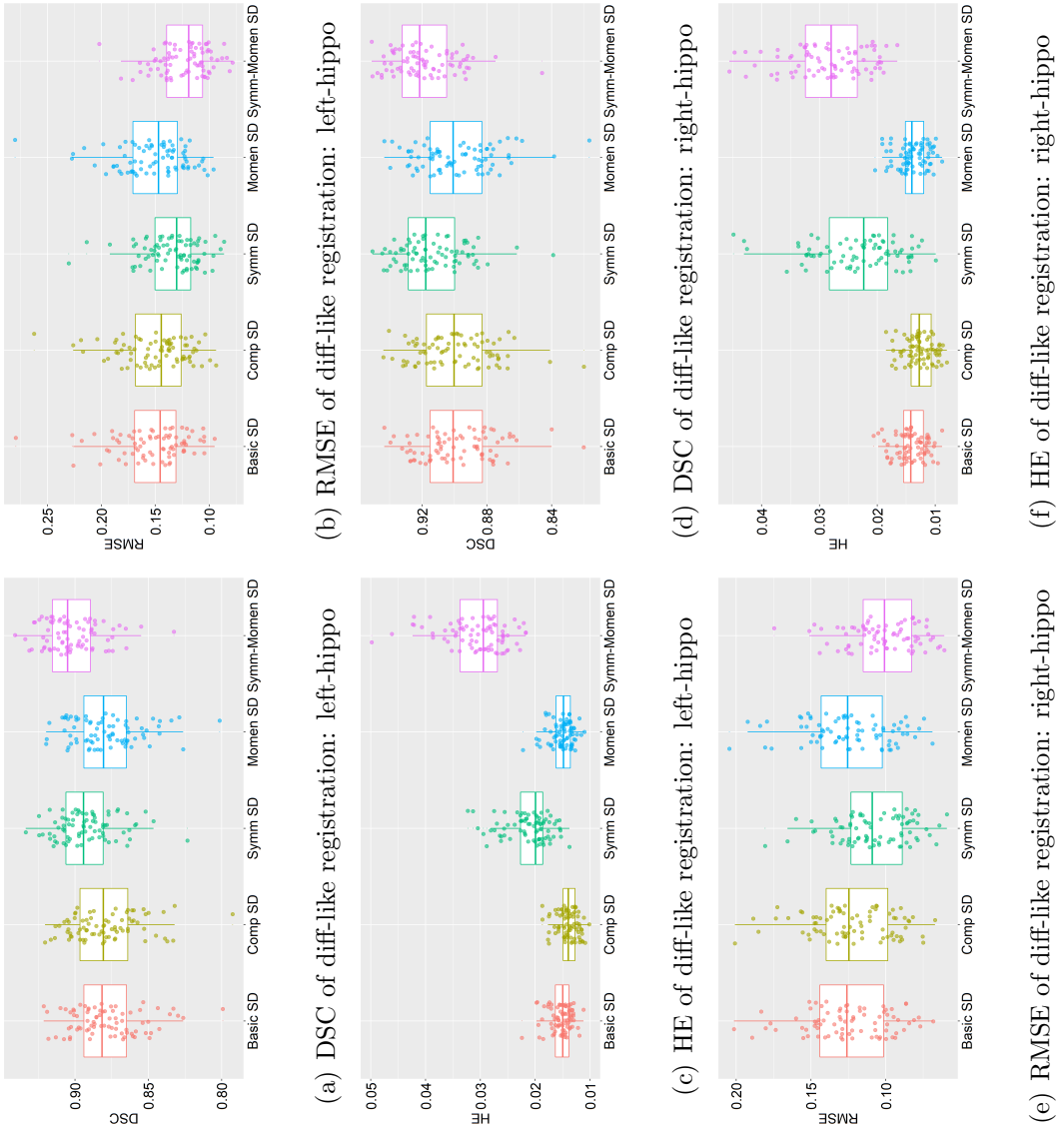

(a) DSC of diff-like registration: left-hippo

(b) RMSE of diff-like registration: left-hippo

(c) HE of diff-like registration: left-hippo

(d) DSC of diff-like registration: right-hippo

(e) RMSE of diff-like registration: right-hippo

(f) HE of diff-like registration: right-hippo

Fig. 4.21.: Diff-like registration results using binary maps.

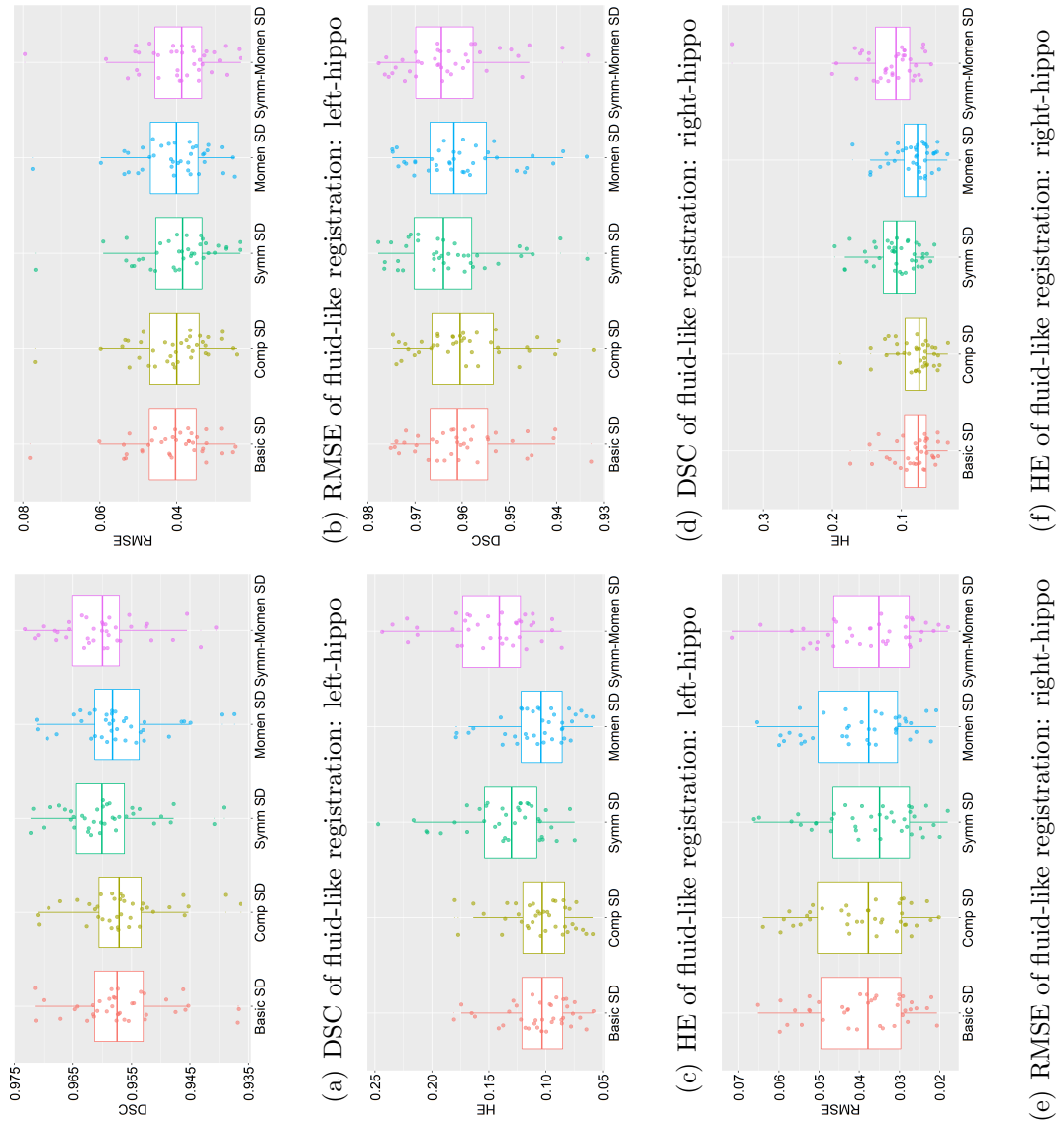

(a) DSC of fluid-like registration: left-hippo
(b) RMSE of fluid-like registration: left-hippo
(c) HE of fluid-like registration: left-hippo
(d) DSC of fluid-like registration: right-hippo
(e) RMSE of fluid-like registration: right-hippo
(f) HE of fluid-like registration: right-hippo

Fig. 4.22.: Fluid-like registration results using binary maps.

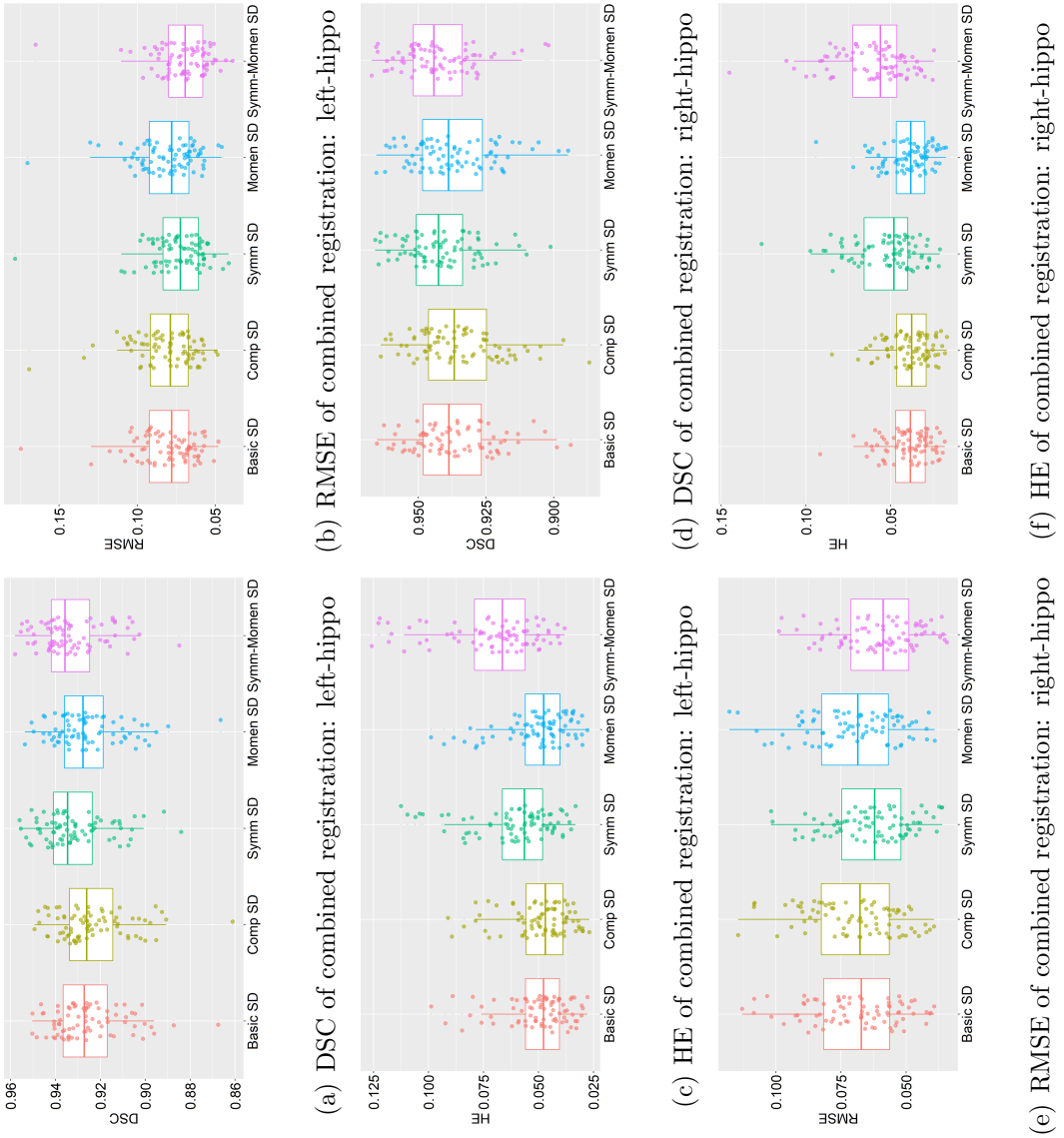

(a) DSC of combined registration: left-hippo
(b) RMSE of combined registration: left-hippo
(c) HE of combined registration: left-hippo
(d) DSC of combined registration: right-hippo
(e) RMSE of combined registration: right-hippo
(f) HE of combined registration: right-hippo

Fig. 4.23.: Combined registration results using binary maps.

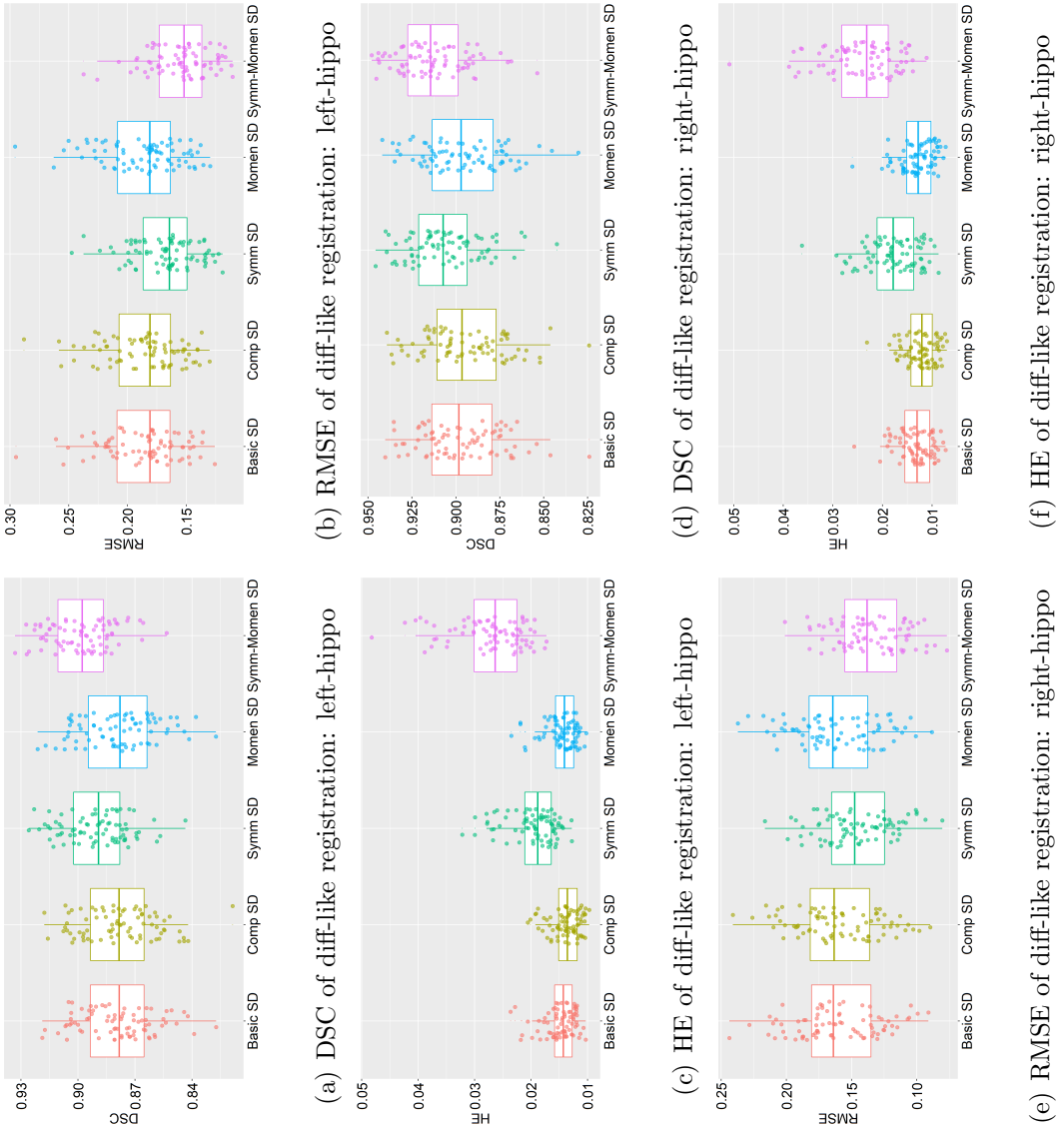

(a) DSC of diff-like registration: left-hippo

(b) RMSE of diff-like registration: left-hippo

(c) HE of diff-like registration: left-hippo

(d) DSC of diff-like registration: right-hippo

(e) RMSE of diff-like registration: right-hippo

(f) HE of diff-like registration: right-hippo

Fig. 4.24.: Diff-like registration results using distance maps.

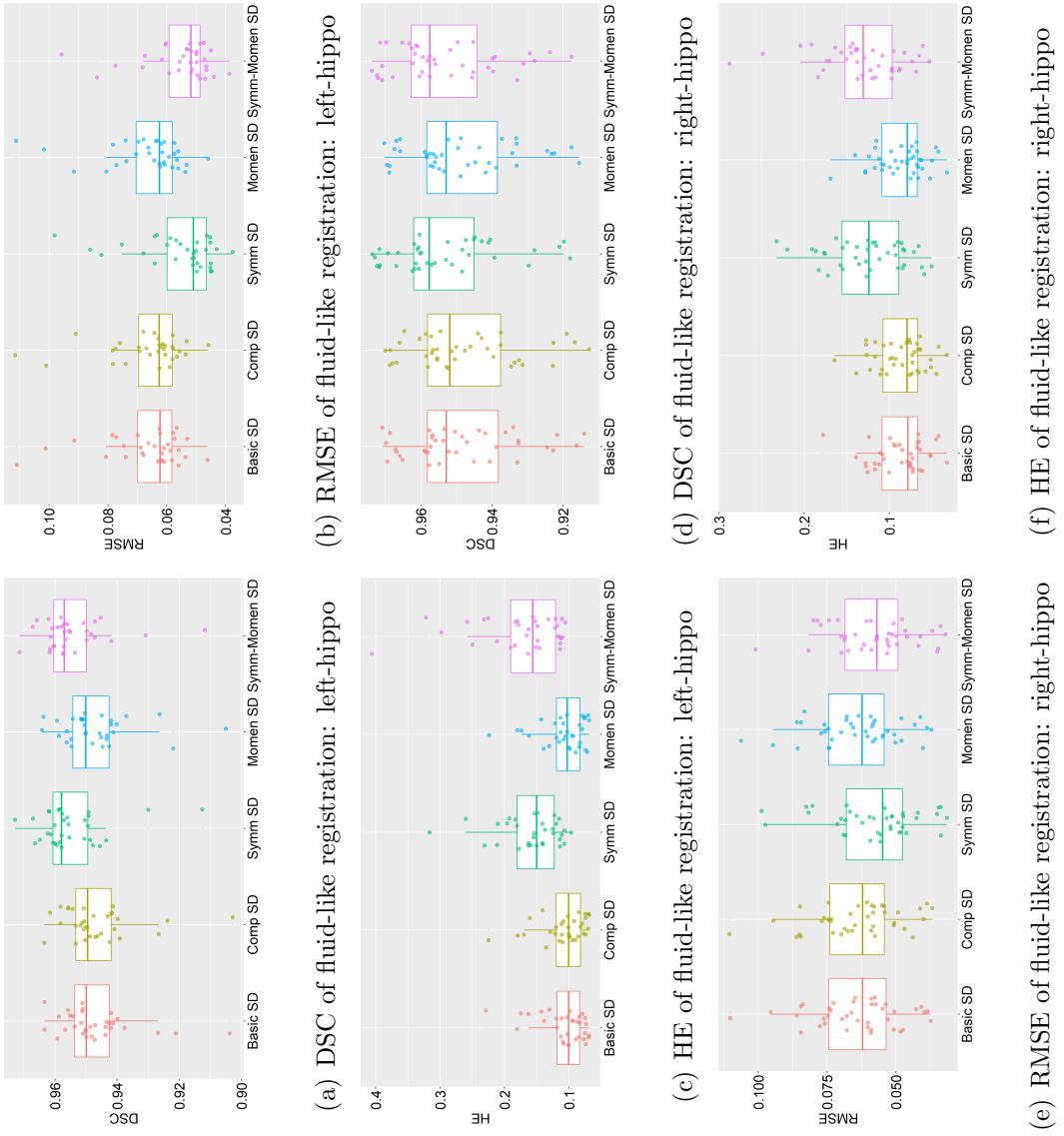

(a) DSC of fluid-like registration: left-hippo
(b) RMSE of fluid-like registration: left-hippo
(c) HE of fluid-like registration: left-hippo
(d) DSC of fluid-like registration: right-hippo
(e) RMSE of fluid-like registration: right-hippo
(f) HE of fluid-like registration: right-hippo

Fig. 4.25.: Fluid-like registration results using distance maps.

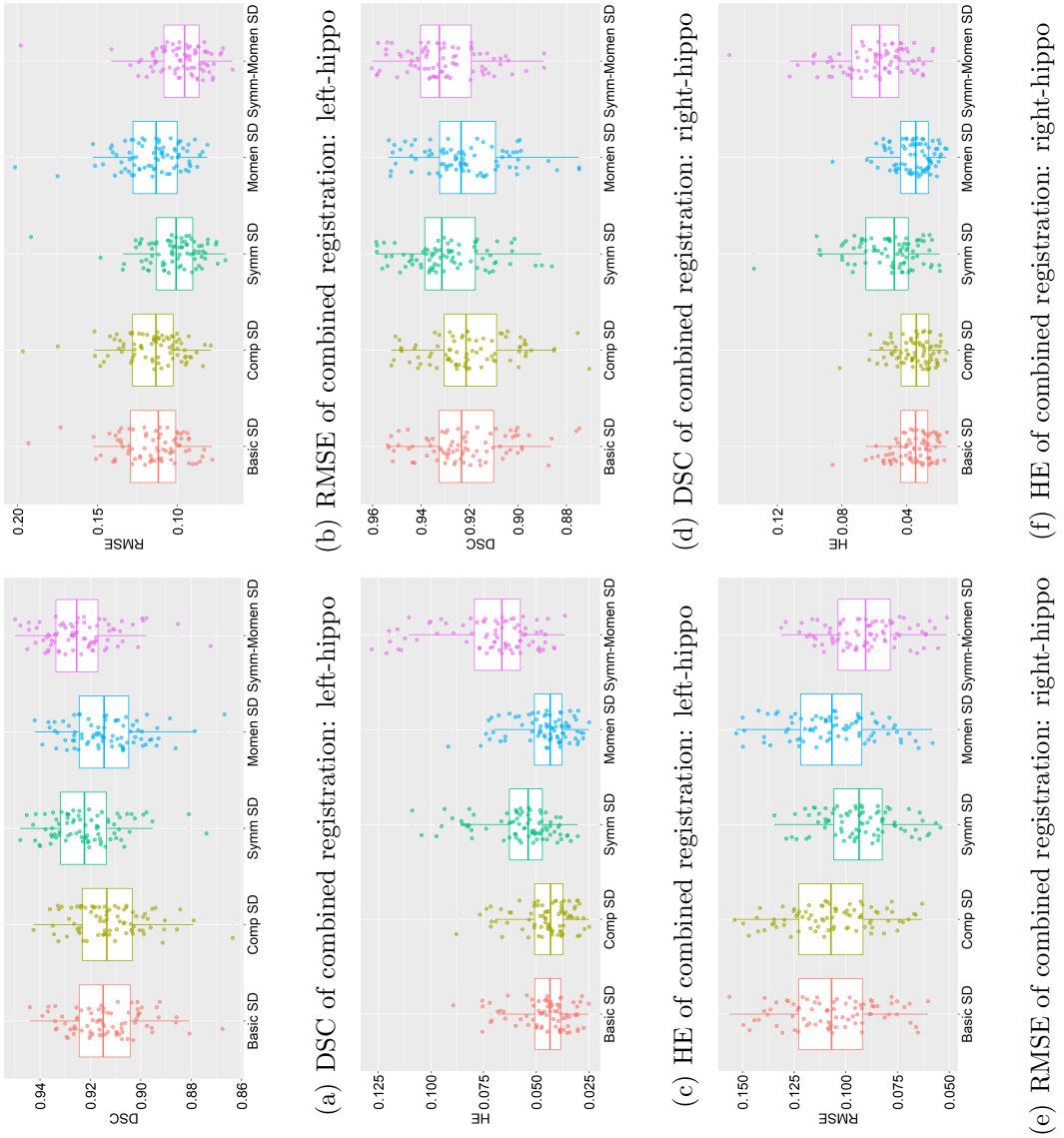

(a) DSC of combined registration: left-hippo (b) RMSE of combined registration: left-hippo (c) HE of combined registration: left-hippo (d) DSC of combined registration: right-hippo (e) RMSE of combined registration: right-hippo (f) HE of combined registration: right-hippo

Fig. 4.26.: Combined registration results using distance maps.

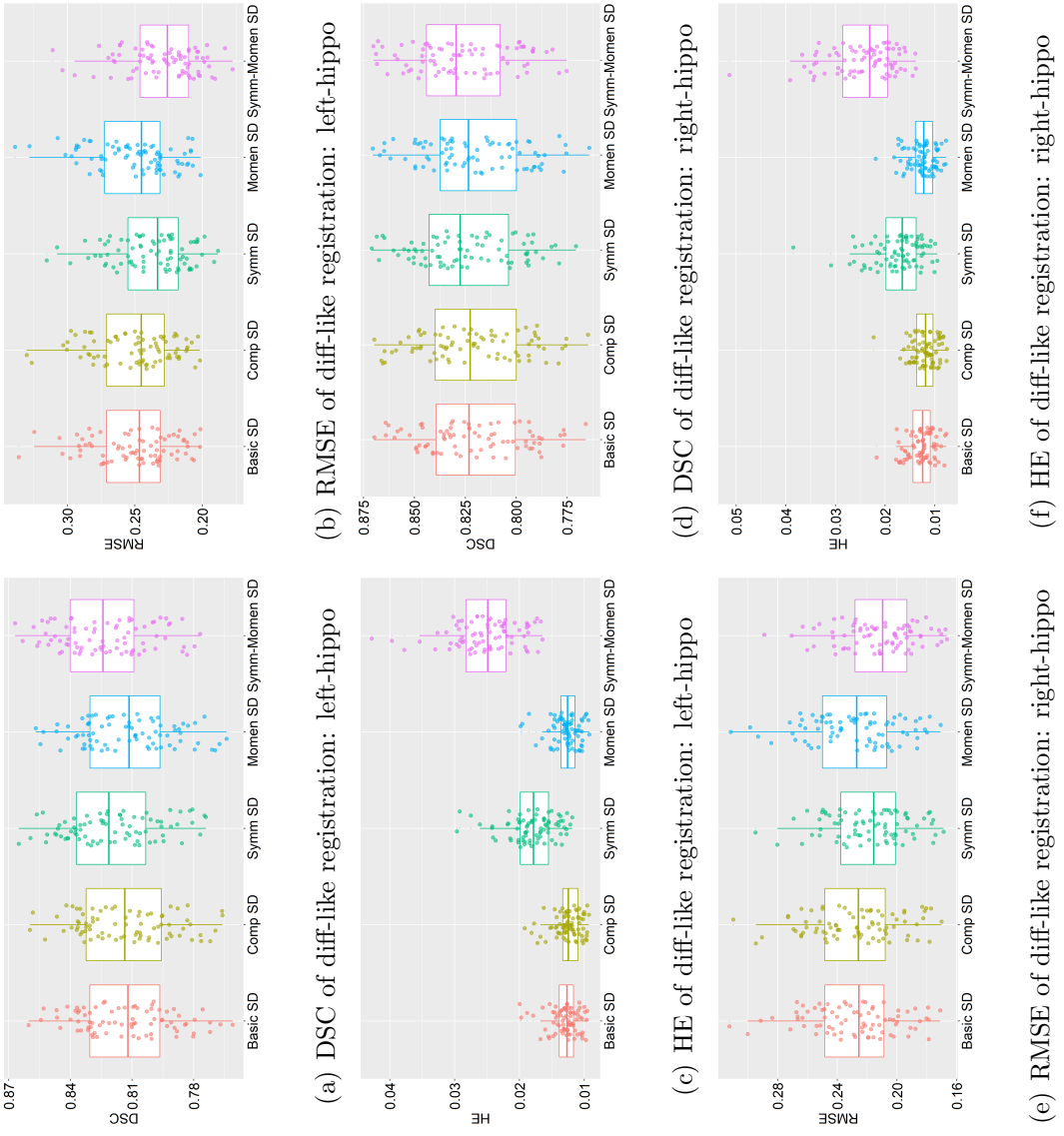

(a) DSC of diff-like registration: left-hippo

(b) RMSE of diff-like registration: left-hippo

(c) HE of diff-like registration: left-hippo

(d) DSC of diff-like registration: right-hippo

(e) RMSE of diff-like registration: right-hippo

(f) HE of diff-like registration: right-hippo

Fig. 4.27.: Diff-like registration results using probability maps.

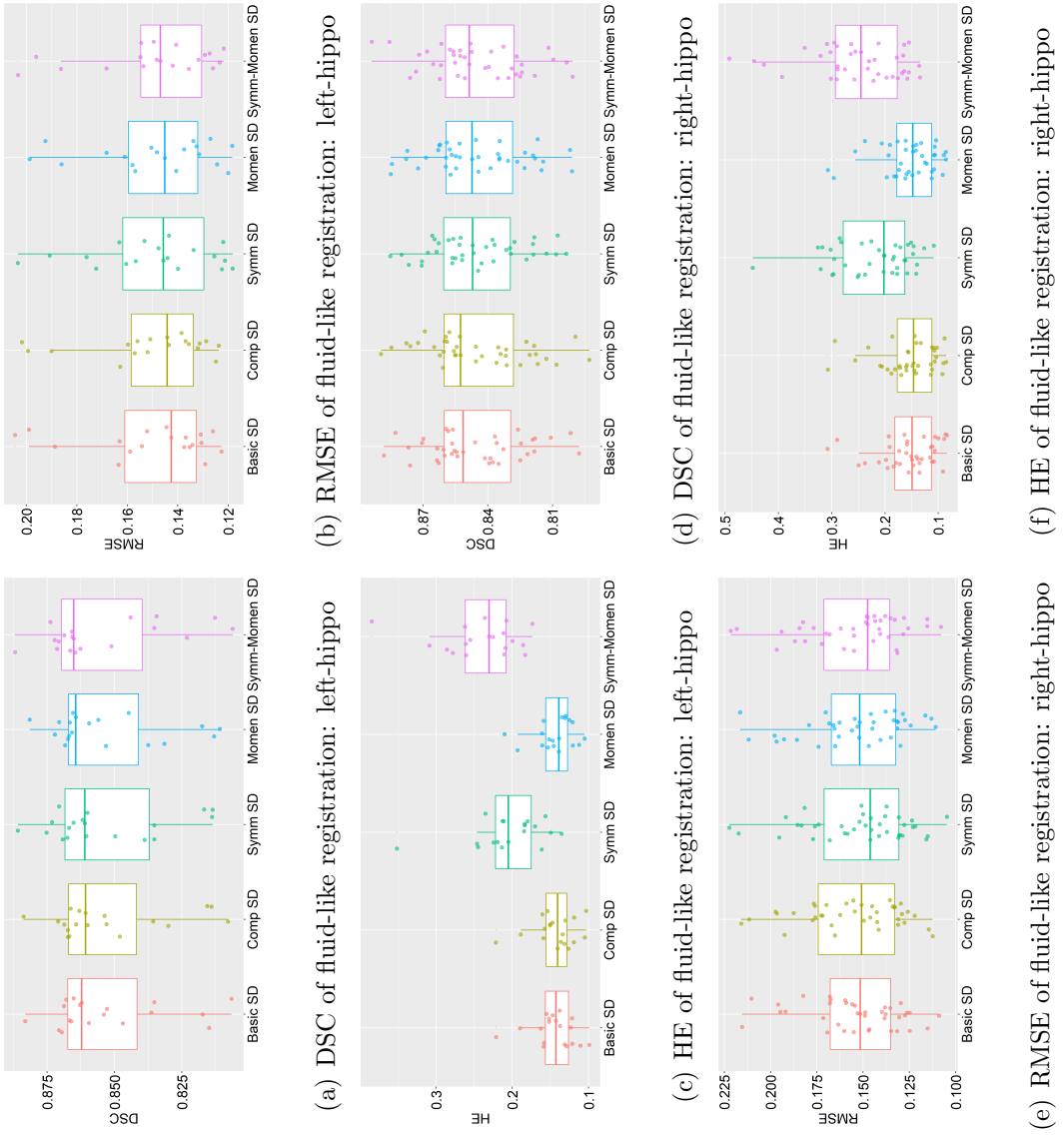

(a) DSC of fluid-like registration: left-hippo

(b) RMSE of fluid-like registration: left-hippo

(c) HE of fluid-like registration: left-hippo

(d) DSC of fluid-like registration: right-hippo

(e) RMSE of fluid-like registration: right-hippo

(f) HE of fluid-like registration: right-hippo

Fig. 4.28.: Fluid-like registration results using probability maps.

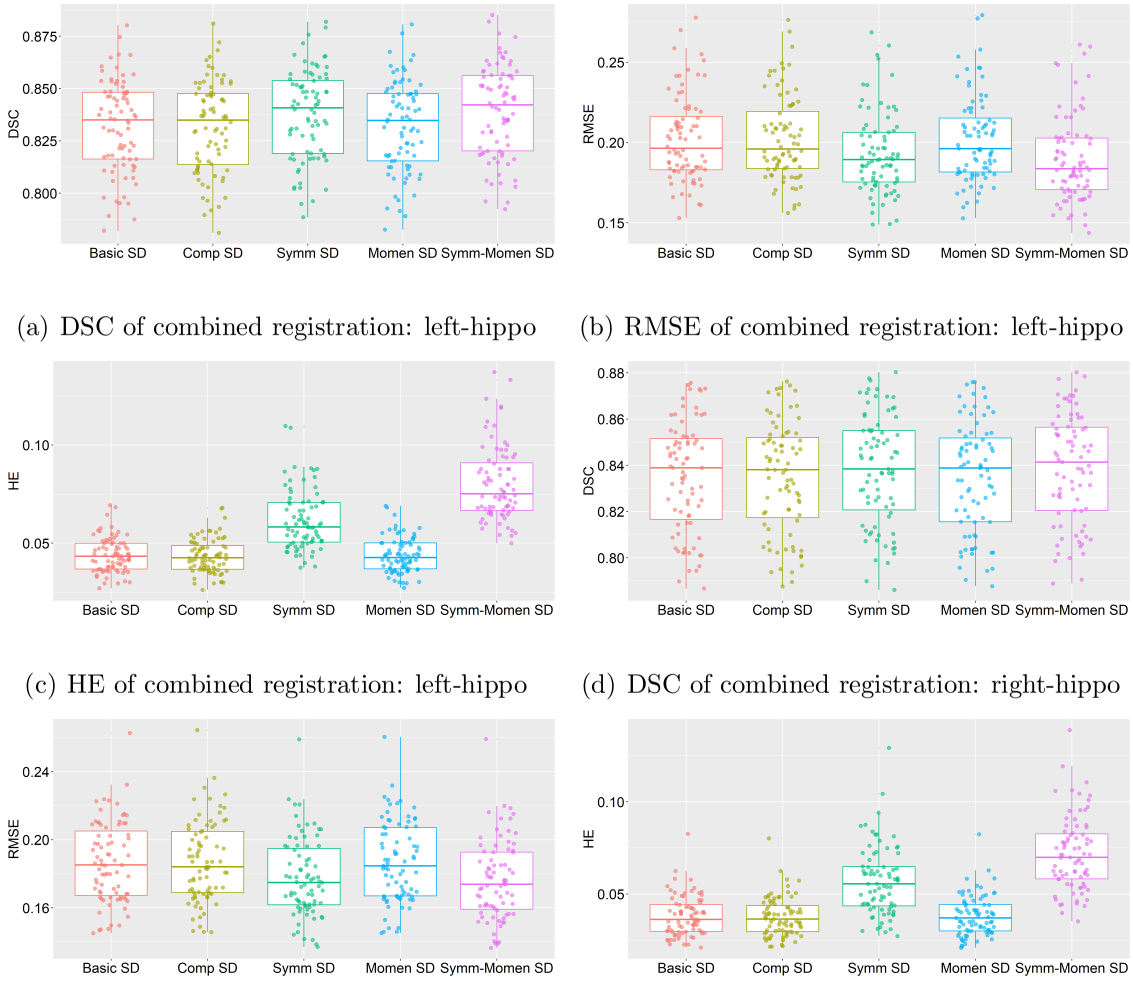

(a) DSC of combined registration: left-hippo

(b) RMSE of combined registration: left-hippo

(c) HE of combined registration: left-hippo

(d) DSC of combined registration: right-hippo

(e) RMSE of combined registration: right-hippo

(f) HE of combined registration: right-hippo

Fig. 4.29.: Combined registration results using probability maps.

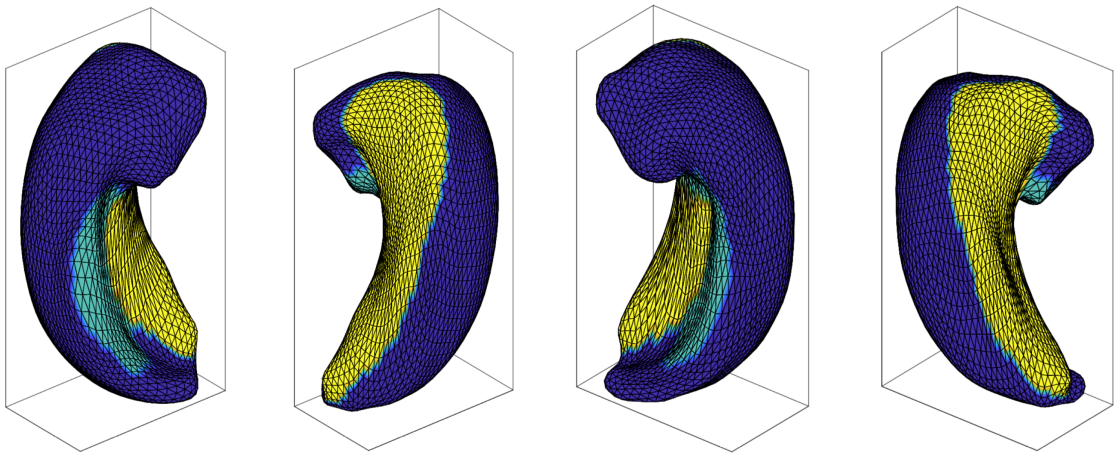

(a) Left hippocampal surface atlas (b) Right hippocampal surface atlas

Fig. 4.30.: The averaged left and right hippocampal surface atlas. Each of the subfigure (a) and (b) shows two orientations. For example, the latter one in (a) is flipped 180 degree by vertical axis from the first one. Color blue represents for subfield CA, color yellow represents for subfield SUB, color cyan represents for subfield DG.

5. MORPHOMETRIC ANALYSES OF HIPPOCAMPAL SUBFIELDS

5.1 Background

Morphometrics analysis is one type of quantitative analysis, a concept that encompasses size and shape. Morphometric analyses are useful in analyzing both developmental and degeneration changes, correlations between shape changes and related variants, as well as relationships between brain structural changes and genetic variations or cognitive score measurements. A major goal of the morphometric analysis is to statistically test hypotheses on the factors which affect the shape.

We compute the surface morphometric difference of the hippocampus pair-wisely between health control (HC), early MCI (EMCI), late MCI (LMCI) and AD groups. We also compute the volumetric morphometric difference of the hippocampus pair-wisely between HC, subjective cognitive decline (SCD), MCI and AD groups to evaluate the degeneration affection of cognitive decline to hippocampal subfields.

5.2 Surface-Based Morphometric Analyses

5.2.1 Data and Materials

The data used in this study were downloaded from the ADNI database [93] as discussed in Section 2.2. For this study, we downloaded baseline 3T MRI scans of 172 HC, 267 EMCI, 140 LMCI and 108 AD participants aging between 55 and 90, along with demographic and diagnostic information. All the raw data are 3D T1-weighted scans with voxel resolution of $1.2 \times 1.0 \times 1.0$ mm^3 and dimension of $196 \times 256 \times 256$.

We also performed statistical analyses on high resolution MRI scans, the data were downloaded from ADNI 2 and 3. Each subject contains two MRI scans, namely one T1-weighted and one T2-weighted MRI scans. The data set we used for this study included 30 HC, 30 MCI and 20 AD participants aging from 58 to 94, along with demographic and diagnostic information. The T1-weighted MRI scan (MPRAGE) had an acquisition matrix of 240 $\times$ 256 $\times$ 176 and voxel size of 1.05 $\times$ 1.05 $\times$ 1.2 mm^3; the T2-weighted scan had an acquisition matrix of 448 $\times$ 448 $\times$ 30 or 448 $\times$ 448 $\times$ 24, where the differences were caused by different imaging sites. The voxel size for high resolution T2-weighted scans is 0.4 $\times$ 0.4 $\times$ 2 mm^3 with TR/TE 8020/50 ms, 24 or 30 interleaved slices with no gap.

5.2.2 Feature Extraction

In neuroimaging, morphometric features include summary statistics of imaging measures (e.g., volume, thickness, gray matter density), surface deformations, and detailed voxel-wise measures. Dealing with different morphometric features, morphometric studies can be categorized to "traditional" morphometry, surface-based morphometry (SBM), and voxel-based morphometry (VBM). They have been used in biomedical imaging and other domains to identify significant patterns related to certain conditions, assisting with diagnosis and treatment.

In modeling the surface deformation, we take the L^2-norm for the difference between two corresponding vertices on a test subject and the template. The way to compute surface deformation on each vertex is described as follows:

$$\delta(x) = \|(x - x_t)\|^2, \tag{5.1}$$

where $\delta(x)$ describes the deformation field, x and x_t are individual subject surface and atlas respectively.

5.2.3 General Linear Model

Tests using T1-weighted scans only

We use $\mathbf{x_t}$ to denote the atlas, and $\mathbf{x}$ to denote an individual surface registered to the atlas. Although the deformation field $\delta(\mathbf{x}) = \mathbf{x} - \mathbf{x_t}$ can be used to describe the individual shape, there are three related elements (corresponding to x, y, z coordinates) in $\delta(\mathbf{x})$ that are needed to capture local shape changes. For simplicity, we look at only the deformation signal along the surface normal direction to decrease the number of variables considered for each surface position. We apply heat kernel smoothing, which generalizes Gaussian kernel smoothing to arbitrary Riemannian manifolds [137], to smooth the surface signals and increase the signal-to-noise ratio. We use a kernel size of 5mm full-width-half-max (FWHM) in the smoothing.

We perform statistical surface analysis to detect: (a) age or gender effect on surface deformation, and (b) group difference (HC vs. EMCI, HC vs. LMCI, and HC vs. AD) on surface deformation after removing the age and gender effects. We consider the following general linear model (GLM):

$$y = X\Psi + Z\Phi + \epsilon, \tag{5.2}$$

where the dependent variable y is our surface signal; $X = (x_1, \cdots, x_p)$ are the variables of interest such as group; $Z = (z_1, \cdots, z_k)$ are the variables whose effects we want to exclude, such as age and gender; and $\Psi = (\psi_1, \cdots, \psi_k)^T$, $\Phi = (\phi_1, \cdots, \phi_p)^T$ and ϵ are the coefficients. The goal is to test if X is significant (i.e., $\Psi \neq 0$) for some $y \in \partial\Omega$, where $\partial\Omega$ indicates the atlas surface manifold. We use SurfStat [138] to test our GLMs. SurfStat is a Matlab toolbox that applies linear mixed effects models and random field theory (RFT, for multiple comparison correction) for the statistical analysis of univariate and multivariate surface and volumetric data [138, 139].

RFT Surface Analysis employs random field theory (RFT) implemented in Surfstat, the surface signals $N_{i,j}$ are analyzed using the regression model:

$$N_{i,j} = \beta_0 + \beta_{1,j} I_i + \beta_{2,j} age_i + \beta_{3,j} gender_i + \epsilon_{i,j}, i = 1, ..., n, j = 1, ..., m \tag{5.3}$$

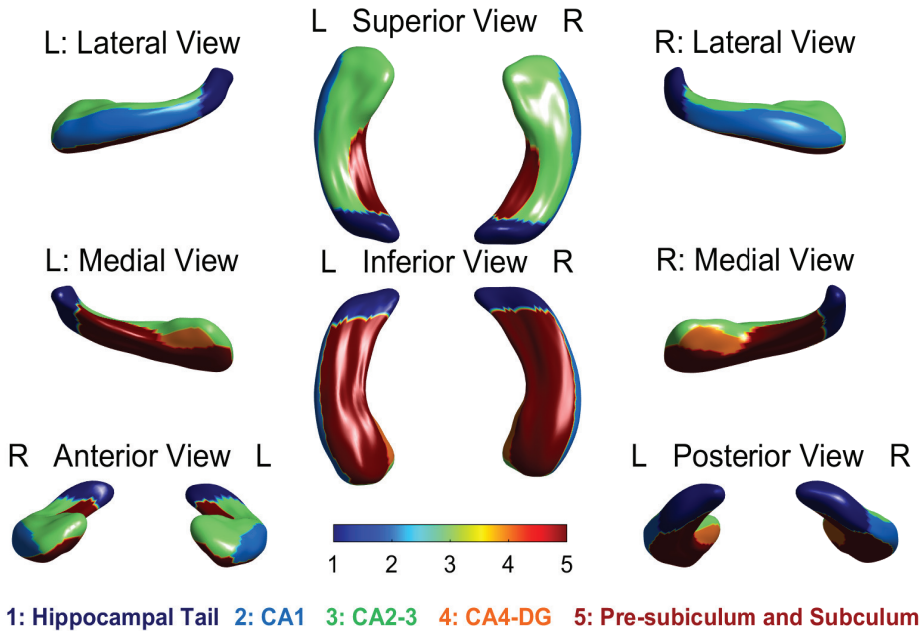

Fig. 5.1.: Hippocampal surface atlas: five subfields color mapped on to the mean hippocampal surface of all HC participants in the studied cohort.

where I_i is the group indicator (e.g., 1 if EMCI and 0 if HC), n is the number of subjects and m is the number of surface vertices. The SPM consisting of the t statistics for testing $H_0 : \beta_{1,j} = 0, j = 1, \ldots, m$, is then analyzed using both peak amplitude and cluster size statistics as implemented by Surfstat.

The GLM is employed to estimate the parameters that can describe the data in the same way as in the conventional analysis of discrete data. RFT is employed to tackle the multiple comparison problem to control the type I error, or the statistical results would not be sufficiently convincing when making inferences over a surface mesh of the brain. RFT theory provides a method for correcting p values for the search surface vertex and plays the same role for continuous data (i.e., images) as the Bonferroni correction for the number of discontinuous or discrete statistical tests [140].

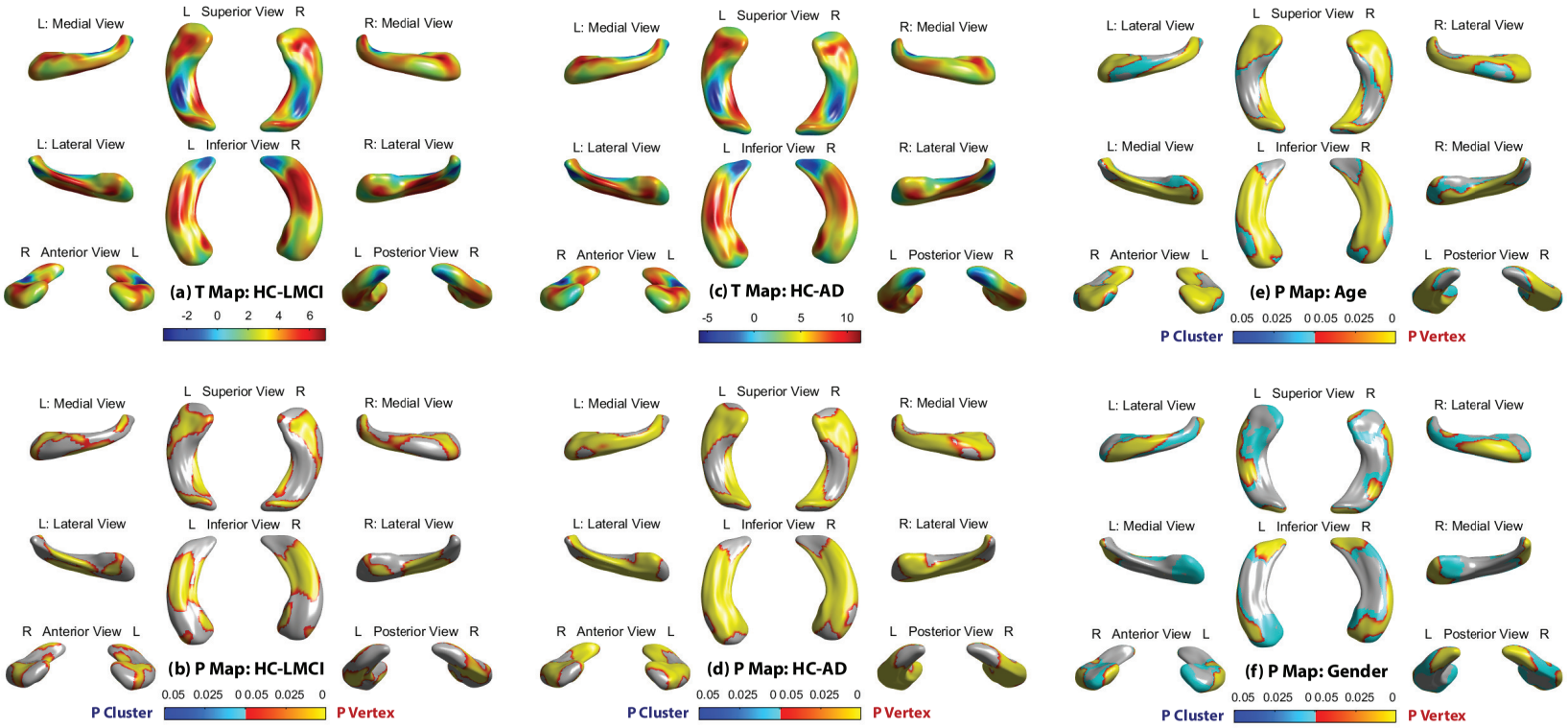

Fig. 5.2.: (a-b) The t-map and p-map of the diagnostic effect (HC-LMCI) on surface signals after removing the effects of age and gender. (c-d) The t-map and p-map of the diagnostic effect (HC-AD) on surface signals after removing the effects of age and gender. (e) The p-map of age effect on surface signals. (f) The p-map of gender effect on surface signals. In t-maps (a and c), red/blue colors respectively indicate expansion/contraction in HC compared with LMCI or AD.

Shown in Figure 5.1 is the resulting surface atlas color-mapped with five hippocampal subfields. Shown in Figure 5.2 are example T-maps (maps of t statistics) and P-maps (maps of p values, only significant p-values shown, corrected by RFT at both vertex and cluster levels) of selected analyses. Shown in Table 5.1 are the numbers of significant surface vertices in each of five analyses.

Below we briefly review the results of three diagnostic effects (covaried for age and gender) on surface signals. (1) HC vs EMCI: there was no significant shape change on the entire surface. (2) HC vs LMCI: LMCI demonstrated significant atrophy patterns in 25% of Tail, 38% of CA1, 30% of CA2-3, 32% of CA4-DG, and 55% of SUB. (3) HC vs AD: AD demonstrated significant atrophy patterns in 49% of Tail, 87% of CA1, 50% of CA2-3, 94% of CA4-DG, and 84% of SUB. While SUB was among the top atrophy regions at both LMCI and AD stages, CA1 and CA4-DG showed modest atrophy at the LMCI stage but severe atrophy at the AD stage.

Regarding the age, it affected 83% of SUB, 50-56% of Tail, CA1 and CA2-3, and 39% of CA4-DG. The overall pattern was similar to diagnostic effects of LMCI and AD. As to the gender, it affected 47-62% of Tail and CA1, 14-16% of CA2-3 and SUB, and 5% of CA4-DG.

Tests using T1- and T2-weighted high resolution scans

Similar to the previous section, we performed statistical analyses on the high resolution data, and the deformation fields were captured by calculating the deformation between each subject and the template, where the template was generated based on the pipeline described in Section 4.3.7.

Figure 5.3 demonstrates the t statistics and p statistics from the comparisons between HC and MCI groups. As we can see from the figure, not many subfield surface regions are marked as "significant" (marked as yellow) in Figure 5.3(b). However, we still can see from Figure 5.3(a), CA and SUB showed a trend of atrophy.

Table 5.1.: The number of significant surface vertices in each subfield for five different analyses. SUB = pre-subicumlum and subiculum

Hemisphere		Left					Right				
Subfields		Tail	CA1	CA2-3	CA4-DG	SUB	Tail	CA1	CA2-3	CA4-DG	SUB
Number of vertices		398	389	728	91	956	405	362	735	119	941
Significant Region (number of vertices)	HC vs EMCI	0	0	0	0	0	0	0	0	0	0
	HC vs LMCI	89	135	236	33	550	112	151	210	35	494
	HC vs AD	201	343	365	88	837	193	307	365	110	762
	Age	223	195	346	52	803	201	225	389	29	766
	Gender	181	235	111	0	81	196	231	120	10	184

Figure 5.4 summarizes the t statistics and p statistics from the comparisons between HC and AD groups. As we can see from the figure, CA and SUB are the most affected regions by the progression of AD. The "significant" regions in Figure 5.4(b) are corresponded to the red regions in Figure 5.4(a), which means these regions are significantly related to the disease.

Based on the statitical results, we again validated our statistical findings in Section 5.2.3 using a different data set. The promising statistical results proved the feasibility and advantages of the proposed framework described in Chapter 3 and 4.

5.2.4 Statistical Parametric Mapping Distribution Analysis

Investigation of hippocampal morphometry as an early biomarker for detecting EMCI is a significant but yet under-explored topic. We have discussed this topic using random field theory [138, 139] and surface-based morphometry in last section, but identified no significant difference between HC and EMCI participants.

To bridge this gap, in this section, we propose a novel and powerful image analysis framework for hippocampal morphometry in EMCI. We create a hippocampal surface atlas with subfield information using the method described in Chapter 3. We model each hippocampus using the SPHARM techniques and register it to the atlas for subsequent analyses. We propose a new alternative to standard random field theory (RFT) and permutation image analysis methods, Statistical Parametric Mapping (SPM) Distribution Analysis or SPM-DA, to perform statistical shape analysis and compare its performance with that of RFT methods on both simulated and real hippocampal surface data. The major strengths of this framework are twofold: (a) SPM-DA is designed to be more powerful than current RFT and permutation methods for detecting low signal-to-noise ratio signals and (b) the framework embraces, rather than ignores, the important hippocampal subfield information for improved interpretation of the identified pattern.

Table 5.2.: Statistical results for group compasisions

Hemisphere		Left				Right			
Subfields		CA	DG	SUB	Total	CA	DG	SUB	Total
Number of Vertices		1703	217	642	2562	1697	232	633	2562
Significant Region (Number of Vertices)	HC vs. MCI	120	31	108	259	230	1	51	282
	HC vs. AD	242	42	156	440	485	0	61	546
Percentage of the significant vertices	HC vs. MCI	7.05	14.29	16.82	10.11	13.56	0.43	8.06	11.01
	HC vs. AD	14.21	19.36	24.3	17.17	28.58	0	9.64	21.31

We demonstrate the effectiveness of our method through an application to the Alzheimer's Disease Neuroimaging Initiative (ADNI) data, where the proposed SPMDA can identify subtle hippocampal shape difference between HC and EMCI that cannot be detected by standard RFT methods.

SPM Distribution Analysis (SPM-DA): SPM-DA begins by estimating the distribution of the SPM statistics with a frequency histogram. The histogram bin boundaries are chosen so that each bin is equally likely under the null distribution, here the t distribution. The bin frequencies are then analyzed to detect departures from count uniformity. In these analyses, two regression models are employed:

$$F_i = \beta_\mu x_{\mu,i} + \epsilon_i,\ i = 1, \ldots, n, \tag{5.4}$$

$$F_i = \beta_l x_{l,i} + \epsilon_i,\ i = 1, \ldots, n, \tag{5.5}$$

where F_i denotes the frequency of the i-th of n = 12 bins. see Figure 5.6 for a few examples bin counts computed from the real hippocampal data (i.e., the "." values) and predictor data (i.e., the solid line). The first model in Equation 5.4, with $x'_\mu = (0, 0, 0, 0, 0, 0, 0, 1, 2, 3, 4, 5)'$ be our predictor. Thus, the coefficient μ will be positive when there is an overabundance of positive SPM statistics (right-tail values) indicating a positive relationship between image values and the predictor of interest. Similarly, for the second model in Eq (5.5), we let $x'_l = (5, 4, 3, 2, 1, 0, 0, 0, 0, 0, 0, 0)'$ be our predictor. Thus, the coefficient l will be positive when there is an overabundance of negative (left-tail) values indicating a negative relationship.

To detect a relationship between the image and the predictor of interest generating the SPM, the following com-positive hypotheses are tested:

$$H_0 = \beta_\mu \leqslant 0 \quad and \quad \beta_l \leqslant 0 \quad versus \quad H_1 = \beta_\mu > 0 \quad and \quad \beta_l > 0. \tag{5.6}$$

Let $\hat{\beta}_\mu$ and $\hat{\beta}_l$ denote the least squares estimates of β_μ and β_l from the un-permuted data. The corresponding one-sided p-values, $p_u = P(\beta_\mu \geqslant \hat{\beta}_\mu)$ and $p_l = P(\beta_l \geqslant \hat{\beta}_l)$, are combined using Bonferroni to get the p-value for testing H_0 vs. H_1, $p =$

$2min(p_l, p_u)$. Simulation is used to compute p_u and p_l by randomly permuting the predictor (after it's orthogonalized with respect to covariates if they are present [139]) with respect to the surface data, recomputing the SPM, and then computing the corresponding permutation coefficient estimates $\hat{\beta_{\mu}}*$ and $\hat{\beta_l}*$. This process is repeated N times and then p_u is estimated by:

$$p_\mu = \frac{(Number \quad of \quad \hat{\beta}_\mu^{*\prime} s \geqslant \hat{\beta}_\mu)}{N}. \tag{5.7}$$

And p_l is estimated similarly. The only requirement for p-values p_u and p_l to be valid is the usual permutation assumption of exchangeability. Exchangeability is satisfied much more readily than the stringent RFT assumptions [139].

If, in addition, the distributions of the permutation coecient estimates $\hat{\beta_{\mu}}*$ and $\hat{\beta_l}*$ are normal, as will often be the case for large samples [141] (e.g., those shown in Figure 5.3(a-b)) then p_u and p_l can be computed using the t distribution:

$$p_\mu = P(t_{N-1} \geqslant \frac{\hat{\beta}_\mu - \hat{X}}{S\sqrt{1+\frac{1}{N}}}), \tag{5.8}$$

in which $\hat{X}$ and S are the sample mean and sample standard deviation of the N $\hat{\beta}_\mu^{*\prime} s$. The factor$\sqrt{1+\frac{1}{N}}$ in the denominator is needed since $Var[\hat{\beta}_\mu - \hat{X}] = \sigma^2(1+\frac{1}{N})$ under the null hypothesis. Using this approach small p-values can be accurately estimated with N as small as 30 or so. This procedure, implemented in R, is also used to analyze the hippocampal surface normals and the results compared with the Surfstat RFT results.

Simulation Studies: SPM-DA and RFT peak and cluster methods are compared using two simulation studies. For both studies random data on a hippocampal template surface with 652 vertices are generated for 72 subjects according to the model:

$$S_{i,j} = \beta_{x_i} + \epsilon_{i,j}, i = 1, \ldots, 72, j = 1, \ldots, 126, \tag{5.9}$$

$$= \epsilon_{i,j}, i = 1, \ldots, 72, j = 127, \ldots, 652, \tag{5.10}$$

in which $S_{i,j}$ represents the surface value at location j for subject i. Both studies simulate two-sample data with xi equal to -1 for $i = 1, \ldots, 36$ and 1 for $i = 37, \ldots, 72$. Thus, the signal which extends across 126 contiguous locations is constant with a

magnitude determined by β. For both studies, values for are 0, 1/12, 1/6, and 1/3. In the first study the random errors $\epsilon_{i,j}$ are independent standard normal ($\mu = 0, \sigma^2 = 1$) pseudorandom numbers. In the second study the $\epsilon_{i,j}$ are also independent standard normals ($\mu = 0, \sigma^2 = 1$) but are smoothed prior to the signal being added using the heat kernel smoothing method [142] applied to the hippocampal surface atlas. The resulting data sets are analyzed using SPM-DA (programmed in R) and RFT peak and cluster statistics as implemented by Surfstat [138, 139]. For each combination of and choice of unsmoothed or smoothed random errors, 100 data sets were constructed and analyzed by SPM-DA and RFT methods to compare their power.

Table 5.3.: Simulation study results: the number of rejections (out of 100 runs) based on SPM-DA, RFT peak, and RFT cluster p-values. The null is rejected when $p \leqslant 0.05$.

Signal Strength	Unsmoothed Data			Smoothed Data		
	SPM-DA	RFT Peak	RFT Cluster	SPM-DA	RFT Peak	RFT Cluster
0	5	1	0	3	2	0
1/12	92	7	1	83	10	0
1/6	100	57	6	100	47	51
1/3	100	100	5	100	100	49

In our simulation study, the distribution of the permutation coefficient estimates by SPM-DA is always normal (see Figure 5.5(a-b) for a couple of examples). Thus, the p_u and p_l are computed using a fast approach shown in Equation 5.8. However, in the real data study, the distribution of the permutation coefficient estimates by SPM-DA is no longer normal (see Figure 5.5(c) for one example). In this case, we compute pu and pl based on Equation 5.7 using 10,000 permutation tests.

Table 5.3 presents the results of our simulation studies by providing the number of rejections (out of 100 runs) of the SPM-DA, RFT Peak, and RFT Cluster methods for the various scenarios. All tests have significance level $\alpha = 0.05$. For the null (signal

Table 5.4.: Statistical analysis results on real data using three approaches: SPM-DA, RFT Peak and RFT Cluster. P values are shown for pairwise comparison among three groups HC, EMCI and LMCI. N.S. indicates not significant.

Comparison	P from SPM-DA	Smallest P	
		RFT Peak	RFT Cluster
HC vs EMCI	9.20E-03	1.51E-01	N.S.
EMCI vs LMCI	<2E-04	9.46E-08	N.S.
HC vs LMCI	<2E-04	1.72E-08	N.S.

strength = 0) scenarios none of the three methods have type I error rates exceeding $\alpha = 0.05$ although the RFT methods appear conservative. For all non-null scenarios the SPM-DA method dominates the RFT Cluster method, exhibiting substantially greater power at all signal strengths. It also dominates the RFT Peak method in all but the strongest signal case. In particular, its power is about eight times greater than RFT Peak for the weakest signals.

Table 5.4 presents the results of analyzing the three hippocampal pairwise comparisons using the three methods. The SPM-DA method was the most powerful, detecting shape differences at level $\alpha = 0.05$ for all three comparisons in contrast to RFT Peak which detected two and RFT cluster which detected none. We believe that SPM-DA would yield smaller p-values than RFT Peak for the EMCI vs LMCI and HC vs LMCI comparisons if sufficient permutations (e.g., 10^9) were used. The encouraging fact that the SPM-DA method was able to detect HC vs EMCI shape differences demonstrates the promise of SPM-DA for detecting early biomarkers in AD studies.

Figure 5.6 shows the Equation 5.4 predictor data (i.e., the solid line) and the bin counts generated by SPM-DA for each of the three comparisons. It is obvious that the shape differences were detected by the first regression model (see Equation 5.4) in each case. In other words, SPM-DA detected trends toward an overabundance of

SPM values in the upper tail of the distribution, indicating hippocampal atrophy in EMCI compared with HC, in LMCI compared with EMCI, and in LMCI compared with HC.

Figure 5.6(b) shows the surface map of the SPM values for HC vs EMCI, where the red color indicates the atrophy region in EMCI compared with HC. For comparison, Figure 5.7(a) shows the t-map of the SurfStat analysis (p-map not shown due to lack of signal). Although capturing a similar pattern, the RFT methods used by SurfStat cannot claim the group differences between HC and EMCI are significant. However, the RFT Peak method used by SurfStat was able to identify statistical shape differences between EMCI and LMCI (t-map and p-map shown in Figure 5.7(c-d)) and between HC and LMCI (t-map and p-map similar to Figure 5.7(c-d) and thus not shown).

Given that we have a surface atlas of hippocampal subfields, Table 5.5 shows the signal region size in each subfield using RFT Peak and SPM-DA methods, i.e., number of vertices with $p < 0.05$ and number of vertices with bin value (bv) = 12 respectively. Below we summarize the amount of the subfield atrophy region detected by SPM-DA. (1) HC vs EMCI: EMCI demonstrated atrophy patterns compared with HC in 27% of Tail, 51% of CA1, 36% of CA2-3, 79% of CA4-DG and 51% of SUB. (2) EMCI vs LMCI: LMCI demonstrated atrophy patterns compared with EMCI in 66% of Tail, 91% of CA1, 61% of CA2-3, 70% of CA4-DG and 90% of SUB. (3) HC vs LMCI: LMCI demonstrated atrophy patterns compared with HC in 70% of Tail, 100% of CA1, 69% of CA2-3, 99% of CA4-DG and 98% of SUB.

In summary, We have proposed a novel and powerful image analysis method, Statistical Parametric Mapping (SPM) Distribution Analysis or SPM-DA, and applied it to statistical shape analysis in hippocampal morphometry coupled with subfield information. We have compared its performance with that of standard random field theory (RFT) in surface-based morphometry. Empirical studies on both simulated and real hippocampal data have shown that the proposed SPM-DA outperformed both RFT Peak method and RFT Cluster method. SPM-DA, by making more ex-

Table 5.5.: Comparison between RFT Peak and SPM-DA on the signal region size (i.e., number of vertices with p ¡ 0.05 and number of vertices with bin value (bv) = 12 respectively) in each subfield. No data is shown for RFT Cluster method, since no signals were identified in any RFT cluster analysis on real data.

Hemisphere		Left					Right				
Subfield		Tail	CA1	CA2-3	CA4-DG	SUB	Tail	CA1	CA2-3	CA4-DG	SUB
Total # of vertices		398	389	728	91	956	405	362	735	119	941
RFT Peak: # of vertices with p <0.05	HC vs EMCI	0	0	0	0	0	0	0	0	0	0
	EMCI vs LMCI	48	15	39	0	92	15	0	49	3	351
	HC vs LMCI	64	92	204	27	501	94	116	184	28	450
SPM-DA: # of vertices with bv = 12	HC vs EMCI	87	113	260	85	572	128	273	263	80	393
	EMCI vs LMCI	291	389	441	49	896	242	295	450	97	805
	HC vs LMCI	283	389	507	91	914	278	362	509	117	903

tensive use of the information provided by the SPM distribution, was more powerful than either of the standard RFT methods. It dominated the other methods in the simulation power studies and was able to detect meaningful HC vs. EMCI differences missed by them. The key idea behind the new method is to make better use of the information provided by the distribution of the General Linear Model (GLM) statistics in the SPM. Standard RFT methods just look at the distribution maximum (vertex peak) or the number of contiguous supra threshold vertices (clusters) and thus ignoring much information. This approach avoids all that. In this work, we constructed a histogram to capture the distribution information. One future direction is to explore other ways of using the distribution information. Given that the proposed method is generic, another future direction is to apply it to other image and/or shape analysis studies.

We also performed the statistical analyses using high resolution data set. The statistical results were not promising enough because (1) the data set was relatively too small (50 subjects for HC vs AD and 60 subjects for HC vs MCI), this could reduce the statistical power dramatically, and (2) the process of surface parameterization introduced errors that reduced the sensitivity of surface analysis. For the second point, we will conduct a new study to design a better surface parameterization strategy to overcome the current issue. However, the statistical results proved the feasibility of the proposed framework to build hippocampal surface atlas and the followed surface morphometric analyses.

5.3 Volume-Based Morphometric Analyses

In this section, statistical group analyses are performed to identify if any discriminative patterns can be discovered from high-resolution scans. All the statistical analyses were performed using IBM SPSS 23 (SPSS Statistics 23, IBM Corporation, Somers, NY).

In our analyses, we examined primary hippocampal subfields and adjoining regions segmented directly from the ASHS software, as well as several composite regions of interest (ROIs). Specifically, we included the following nine primary regions: CA1, CA2, CA3, DG, SUB, ERC, BA35, BA36, and CS. Also, we examined the following three composite regions: cornu ammonis (CA) containing CA1, CA2, and CA3, hippocampus (HIPP) containing CA, DG and SUB, and perirhinal cortex (PRC) containing BA35 and BA36.

5.3.1 Data and Materials

The sample (n=35) included research subjects from four categories: cognitively normal (CN, n=10), subjective cognitive decline (SCD, n=9), mild cognitive impairment (MCI, n=10), and Alzheimer's disease (AD, n=6). All participants were recruited from the Clinical Core of the Indiana Alzheimer's Disease Center (IADC). All procedures were approved by the Indiana University Institutional Review Board. All subjects signed a written informed consent form. Participant characteristics are shown in Table 5.6.

5.3.2 Image Acquisition

MRI scans were acquired on a Siemens MAGNETOM Prisma 3T MRI scanner. The scanning protocols included a T1-weighted MPRAGE sequence with whole-brain coverage and a T2-weighted TSE sequence with partial-brain coverage and an oblique coronal slice orientation (positioned orthogonally to the main axis of the hippocampus). The following MRI sequence parameters were used: the MPRAGE had an acquisition matrix of 240 $\times$ 256 $\times$ 176 and voxel size of 1.05 $\times$ 1.05 $\times$ 1.2 mm^3; the T2 scan had an acquisition matrix of 448 $\times$ 448 $\times$ 30 and voxel size of 0.4 $\times$ 0.4 $\times$ 2 mm^3 with TR/TE 8020/50 ms, 30 interleaved slices with no gap. The acquisition time of the conventional protocol is 8 minutes and 11 seconds.

Table 5.6.: Participant characteristics regarding age, gender and intracranial volume (ICV).

	Age(mean±std, in years)	Gender(M, F)	ICV(cm^3)
Cognitively normal control (CN, n=10)	69.2±5.7	1, 9	1437±146
Subjective cognitive decline (SCD, n=9)	71.3±6.4	5, 4	1469±201
Mild cognitive impairment (MCI, n=10)	72.9±6.2	5, 5	1464±255
Alzheimer's disease (AD, n=6)	64.5±12.9	2, 4	1407±174
p-value	0.197*	0.157**	0.993*

*One-way ANOVA. **Chi-square test.

5.3.3 Statistical Group Analyses

Segmentation was performed based on the methods discussed in Section4.3.2. We performed volumetric analyses to evaluate differences between diagnostic groups using SPSS General linear model (GLM). Specifically, our goal was to investigate whether there were significant regional volume differences between CN, SCD, MCI, and AD participants. Further, we evaluated whether the pattern of differences between groups using subfield volumetric estimates from ASHS. In our experiments, we employed a multivariate regression model with diagnosis (DX) as a fixed factor; age, sex, and total intracranial volume (ICV) as covariates; and primary and composite regional volumes as dependent variables.

To further examine the volume based morphometric differences between diagnostic groups, pairwise comparisons of effect sizes were performed for CN, SCD, MCI, and AD groups. Effect sizes were calculated using Cohen's d [143]. The effect size of each group difference was computed after covarying for age, gender and ICV.

5.3.4 Results

Figure 5.9 shows mean volume for each sub-region adjusted by age, sex and ICV by DX group, where error bars indicate standard error. Table5.7 shows the p-values of pairwise group comparison covaried for age, sex, and ICV for high resolution MRI scan data. Given our modest sample size, we used the nominal $p < 0.05$ as the threshold to identify significant regions (see red cells in Table 5.7).

Table 5.8 show the effect size results (Cohen's d) for each pairwise comparison among four diagnosis groups (CN, SCD, MCI and AD). According to [144], an effect size with d = 1.2 is considered to be "very large", and thus is colored in red in Table 5.8. The effect size pattern shown in Table 5.8 is very similar to the significance pattern described in Table 5.7. Graphical effect size results are shown in Figure 5.10.

Table 5.7.: P value of diagnosis effect on subfield volume covaried for age, gender and ICV.

Subfield	CN vs SCD	CN vs MCI	CN vs AD	SCD vs MCI	SCD vs AD	MCI vs AD
L_CA1	0.115	0.147	0.006	0.003	0.000	0.140
R_CA1	0.106	0.260	0.024	0.006	0.010	0.259
L_CA2	0.420	0.413	0.045	0.163	0.443	0.669
R_CA2	0.641	0.473	0.098	0.033	0.918	0.731
L_CA3	0.793	0.589	0.025	0.255	0.340	0.358
R_CA3	0.311	0.949	0.613	0.255	0.978	0.897
L_DG	0.153	0.236	0.021	0.001	0.036	0.161
R_DG	0.030	0.105	0.040	0.000	0.015	0.521
L_SUB	0.194	0.118	0.049	0.004	0.018	0.324
R_SUB	0.107	0.232	0.229	0.014	0.115	0.791
L_ERC	0.397	0.248	0.026	0.012	0.154	0.213
R_ERC	0.112	0.788	0.237	0.004	0.332	0.602
L_BA35	0.716	0.642	0.115	0.476	0.178	0.020
R_BA35	0.035	0.654	0.152	0.034	0.016	0.062
L_BA36	0.836	0.320	0.051	0.278	0.019	0.087
R_BA36	0.457	0.302	0.083	0.089	0.030	0.160
L_CS	0.848	0.165	0.683	0.169	0.617	0.402
R_CS	0.785	0.809	0.511	0.766	0.835	0.987
L_CA	0.123	0.142	0.006	0.002	0.000	0.123
R_CA	0.094	0.280	0.029	0.006	0.014	0.273
L_HIPP	0.117	0.143	0.011	0.001	0.002	0.130
R_HIPP	0.046	0.202	0.040	0.000	0.014	0.372
L_PRC	0.929	0.457	0.047	0.275	0.020	0.047
R_PRC	0.236	0.393	0.069	0.033	0.009	0.080

Table 5.8.: Effect size of diagnosis effect on subfield volume covaried for age, gender and ICV, where |cohen's d| > 1.2 is shown as red, indicating "very large" effect size.

Subfield	CN vs SCD	CN vs MCI	CN vs AD	SCD vs MCI	SCD vs AD	MCI vs AD
L_CA1	-0.43	1.11	2.21	1.79	3.98	0.98
R_CA1	-0.56	0.93	1.68	1.59	2.71	0.66
L_CA2	0.04	0.84	1.22	0.78	1.14	0.53
R_CA2	-0.04	0.94	0.91	1.12	0.99	0.28
L_CA3	-0.19	0.55	1.25	0.63	1.17	0.43
R_CA3	-0.30	0.12	0.16	0.56	0.56	0.09
L_DG	-0.67	1.19	1.70	1.94	2.28	0.82
R_DG	-1.10	1.42	1.47	3.05	2.70	0.36
L_SUB	-0.32	1.08	1.49	1.71	2.18	0.74
R_SUB	-0.50	0.82	0.86	1.45	1.35	0.23
L_ERC	-0.13	1.05	1.38	1.46	1.67	0.83
R_ERC	-0.59	0.56	0.69	1.55	1.38	0.31
L_BA35	-0.20	0.20	1.19	0.45	1.50	1.27
R_BA35	-1.10	0.17	1.17	1.18	2.07	0.90
L_BA36	0.19	0.65	1.36	0.60	1.55	1.07
R_BA36	0.06	0.59	1.09	0.79	1.51	0.95
L_CS	0.13	0.56	0.15	0.62	0.06	-0.43
R_CS	0.28	0.02	0.09	-0.24	-0.15	0.07
L_CA	-0.43	1.14	2.20	1.86	3.92	1.01
R_CA	-0.57	0.91	1.59	1.62	2.61	0.64
L_HIPP	-0.52	1.19	1.97	2.14	3.31	0.98
R_HIPP	-0.78	1.08	1.48	2.21	2.66	0.53
L_PRC	0.11	0.59	1.42	0.62	1.74	1.23
R_PRC	-0.19	0.57	1.21	1.14	1.98	1.10

To detect significant volumetric differences between diagnostic groups, we applied the general linear model (GLM) to examine the regional volume changes related to diagnosis while covarying for age, sex, and ICV. This pair-wise comparison study was performed among four diagnostic groups: CN, SCD, MCI and AD.

Given the small sample size in this study, we adopted a nominal significance level of $p < 0.05$ to evaluate the group differences. While comparing CN and SCD, a majority of regions demonstrate a trend of increased volume in the SCD group (Figure 5.9), some of which were statistically significant (i.e., right DG, right BA35, and right HIPP; see the CN vs SCD column in Table 5.7). These findings suggest that this group might demonstrate increased regional volumes, potentially as a compensatory mechanism to delay the process of conversion into MCI for this group of subjects with relatively high risk. Similar statistical patterns were observed in [145].

The major affected regions in AD include CA1, dentate gyrus, left subiculum, and left entorhinal cortex, as well as the composite CA, hippocampus and left perirhinal cortex. No regional significance between CN and SCD was identified. Also, we did not detect any regional significance between CN and MCI, unlike in [9], which demonstrated significant volumetric reductions in the dentate gyrus. Our lack of replication may be due to the small sample size of our study, making it under-powered to detect subtle changes.

Compared with previous results [9,78,146], our analyses confirmed the importance of CA1, BA35, subiculum, and dentate gyrus as AD biomarkers. For example, in our study, BA35 turned out to be the only marker showing large difference between MCI and AD. This region was reported in [146, 147] as the first cortical site affected by neurofibrillary tangle pathology. Also, we found that CA1 and the left subiculum could distinguish AD from CN and SCD, which is in accordance with the findings in [78]. In addition, we identified the dentate gyrus as a marker that distinguishes AD from CN and SCD. The dentate gyrus was identified in [9] as a marker showing differences between CN and MCI and the present results indicate sensitivity of this region to early through later stages. One potential application of a time efficient

and robust scan acquisition enabling hippocampal subfield investigation is the area of MRI markers related to adult neurogenesis, a process that interacts with AD pathophysiology [148].

5.4 Genome-Wide Association Studies

5.4.1 Background

Genetics has played an important role in AD research over the past few decades. Studies have demonstrated the genetic factors impact AD pathogenesis, Where the cognitive phenotypes are thought to have substantial heritability (up to 80%) based on twin studies [149]. It is critical to understand the genetic molecular mechanisms underlying the AD. The hippocampus have attracted the most attention in the AD study, as it is the one of the first areas in the brain affected in AD. Imaging genetic analysis of the hippocampus, typically focusing on the whole region, have identified a few of genetic risk factors associated with hippocampal lobe atrophy [150], while there is still substantial portion of missing heritability.

Given the heterogeneous structure of the human hippocampal complex and its relevance to AD, we proposed to characterize the hippocampal subfields' genetic architecture, to help improve the molecular interpretation of AD. We performed a genome-wide association study (GWAS) of hippocampal subfield volumes as well as those of neighboring cortical structures using high-resolution MRI data, for determining genetic contributions to structural changes in this important region.

5.4.2 Data and Materials

Data used in the preparation of hippocampal subfields' GWAS were obtained from the ADNI database. The ADNI was launched in 2003 as a public-private partnership, led by Principal Investigator Michael W. Weiner, MD. The primary goal of ADNI

has been to test whether serial MRI, PET, other biological markers, and clinical and neuropsychological assessment can be combined to measure the progression of mild cognitive impairment (MCI) and early AD.

Participants included 136 non-Hispanic Caucasian subjects from the ADNI cohort with both high-resolution MRI scans and genotype data available, including 42 HC, 45 EMCI, 23 LMCI and 26 AD participants. Detailed characteristic information and the number of subjects in each sub-group are shown in Table 5.9. MRI data included T1-weighted MPRAGE scans with an acquisition matrix of $240 \times 256 \times 176$ and voxel size $1.05 \times 1.05 \times 1.2$ mm^3 and T2-weighted scans containing 24 or 30 coronal slices with an acquisition matrix of 448×448 and voxel size $0.39 \times 0.39 \times 2$ mm^3.

Genotyping data were obtained from the ADNI database. They were quality-controlled, imputed and combined as described in [151]. Briefly, genotyping was performed on all ADNI participants following manufacturer's protocol using blood genomic DNA samples and Illumina GWAS arrays (610-Quad, OmniExpress, or HumanOmni2.5-4v1) [149]. Quality control was performed in PLINK v1.90 [152] using the following criteria: 1) call rate per marker $\geqslant 95\%$, 2) minor allele frequency (MAF) $\geqslant 5\%$, 3) Hardy Weinberg Equilibrium (HWE) test P $\geqslant$ 1.0E-6, and 4) call rate per participant $\geqslant 95\%$.

5.4.3 Methods

Automatic Segmentation of Hippocampal Subfields (ASHS) software [153] was employed to segment 14 primary labeled regions including hippocampal subfields and neighboring cortical structures. Associations between 565,373 SNPs and 14 volumetric measures on these subfields and structures were examined by performing GWAS using PLINK [152], where a linear regression model with age, gender, education, ICV and diagnosis as covariates.

Table 5.9.: Participant characteristics regarding age, gender, and intracranial volume (ICV).

Diagnosis	HC	EMCI	LMCI	AD	P
Number	42	45	23	26	-
Gender(M/F)	20/22	26/19	10/13	16/10	0.48
Age(mean±sd)	75.88±6.94	73.96±7.14	71.83±7.34	74.42±7.62	0.19
Education(mean±sd)	16.90±2.36	17.16±2.66	16.35±3.11	16.35±2.50	0.51
ICV(mean±sd)	1511021±153661	1543125±120714	1466828±132155	1523602±183138	0.25

HC=Healthy Control; EMCI=Early Mild Cognitive Complaint;

LMCI=Late Mild Cognitive Complaint; AD=Alzheimer's disease.

5.4.4 Results

We identified a novel locus rs2968869 in *ERC1* on Chromosome 12 (p = 3.43E-9; Bonferroni corrected p = 2.71E-2) significantly associated with right BA36 volume (Figure 5.11). Right BA36 volume was previously reported to be associated with tau deposition in right temporal lobe [154]. Perirhinal cortex (PRC), formed by BA35 and BA36, is a part of the memory system and has shown a significant correlation with broad tau deposition [154]. This evidence indicates that BA36 might play a role in AD pathology. The minor allele C of rs2968869 was associated with greater right BA36 volume, suggesting a protective effect for AD. This aligns well with the IGAP finding [155] that rs2968869 is a protective locus for AD (p = 4.47E-2). Our study demonstrated that high-resolution MRI provided more detailed neuroanatomical information that could promote the identification of disease relevant molecular factors. GWAS of these quantitative neuroimaging phenotypes identified a novel protective locus in the *ERC1* gene which is implicated in regulation of neurotransmitter release and the NF-κB signaling pathway. After independent replication, *ERC1* could be explored as a potential therapeutic target.

5.5 Summary of Chapter 5

In summary, this section demonstrates the work procedures to perform our group analyses in two aspects: surface based and volume based hippocampal subfield morphometric analyses. Our work shows that statistical significant hippocampal subfields and adjacent regions between cognitively normal older adults and those with MCI (EMCI, LMCI) and/or AD are detected.

A more powerful statistical analysis method named SPM-DA is discussed and proved to be more powerful by successfully detecting the overall statistical significance between HC and EMCI participants. This method will be tested in our further studies for statistical analyses for the contributions on early AD detection.

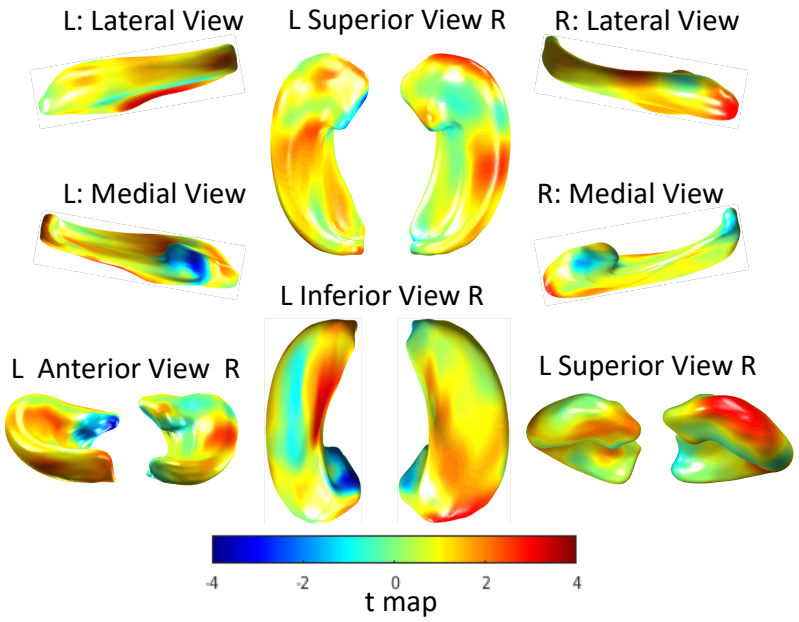

(a) T statistics

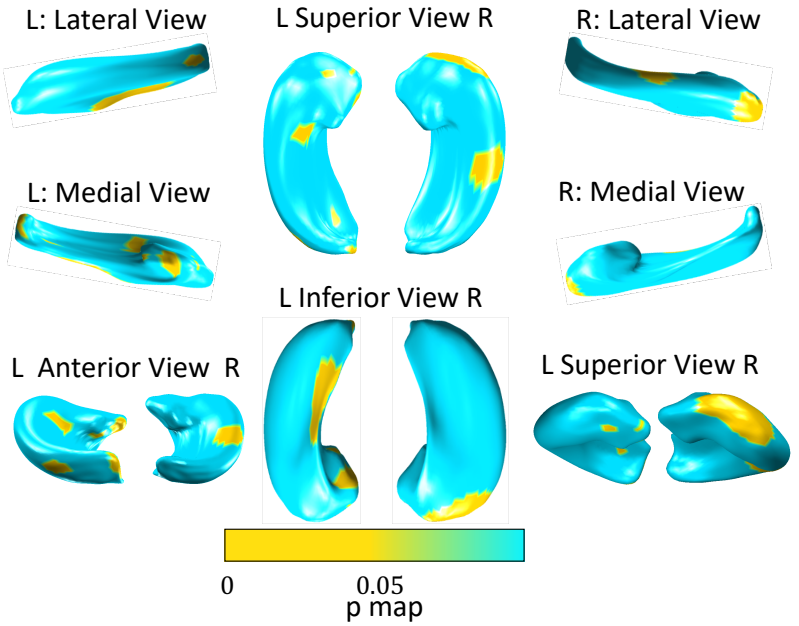

(b) P statistics

Fig. 5.3.: Results of t tests for the comparisons between HC and MCI: (a) is t statistics and (b) is p statistics.

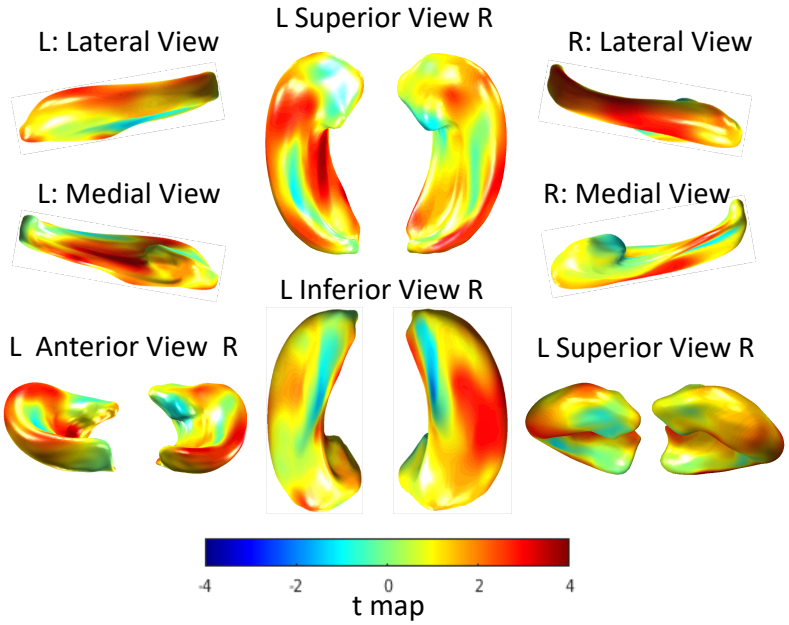

(a) T statistics

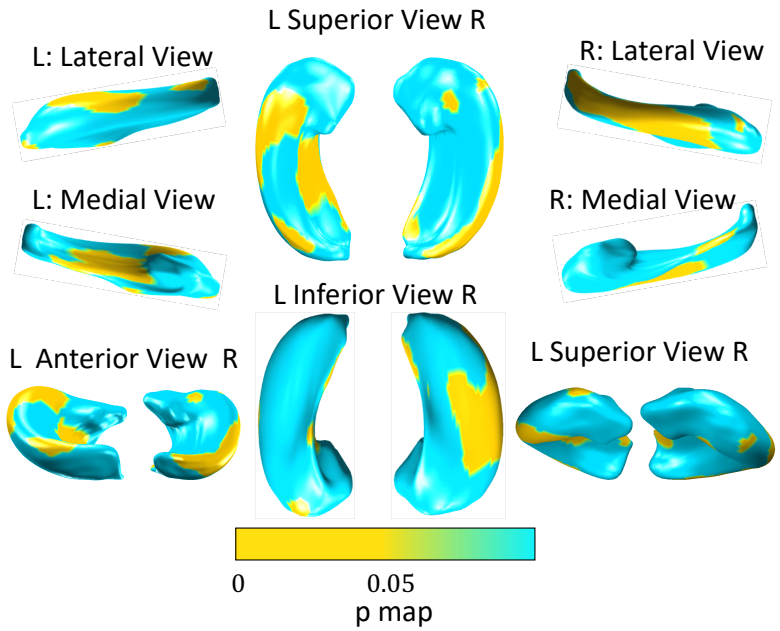

(b) P statistics

Fig. 5.4.: Results of t tests for the comparisons between HC and AD: (a) is t statistics and (b) is p statistics.

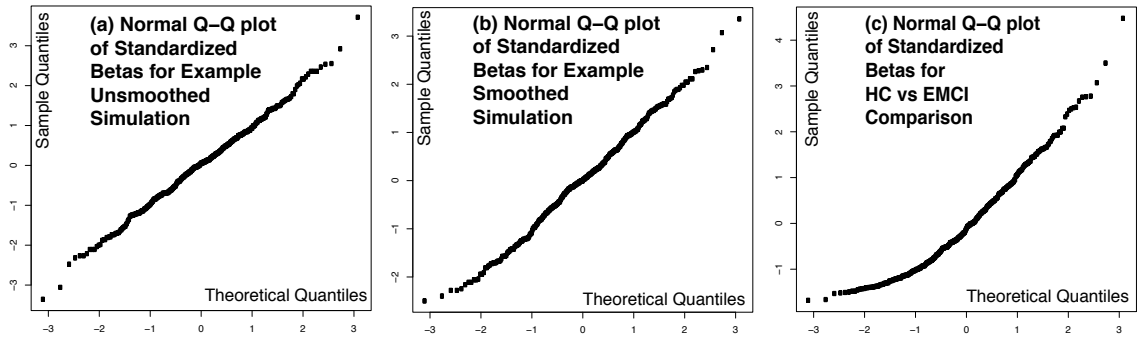

Fig. 5.5.: Normal Q-Q plot of standardized betas for (a-b) example unsmoothed and smoothed simulations, and (c) HC vs EMCI comparison.

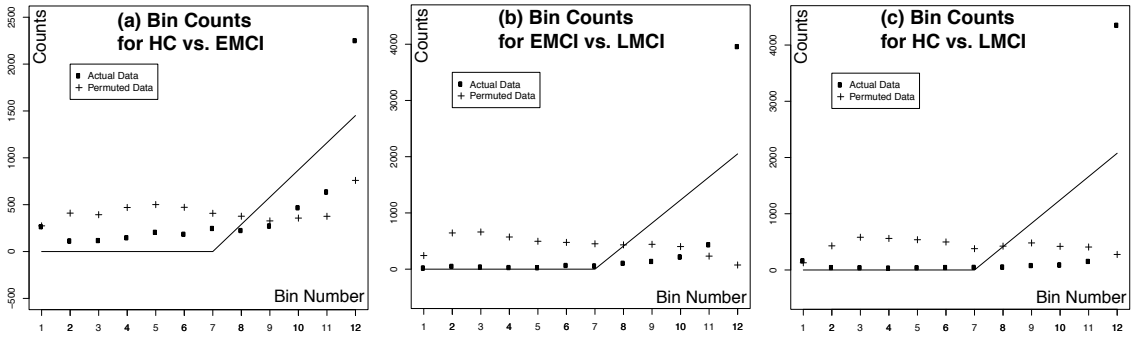

Fig. 5.6.: Bin counts for (a) HC vs EMCI, (b) EMCI vs LMCI and (c) HC vs LMCI. Our linear model in Eq (1) aims to use the values on the solid line to predict the "+" values (for permuted data) or the "·" values (for real data). Note that the count scales on the y-axis are di erent across these three cases, and the signi cance of the group difference is driven mainly by the "·" value on the 12^{th} bin in each case.

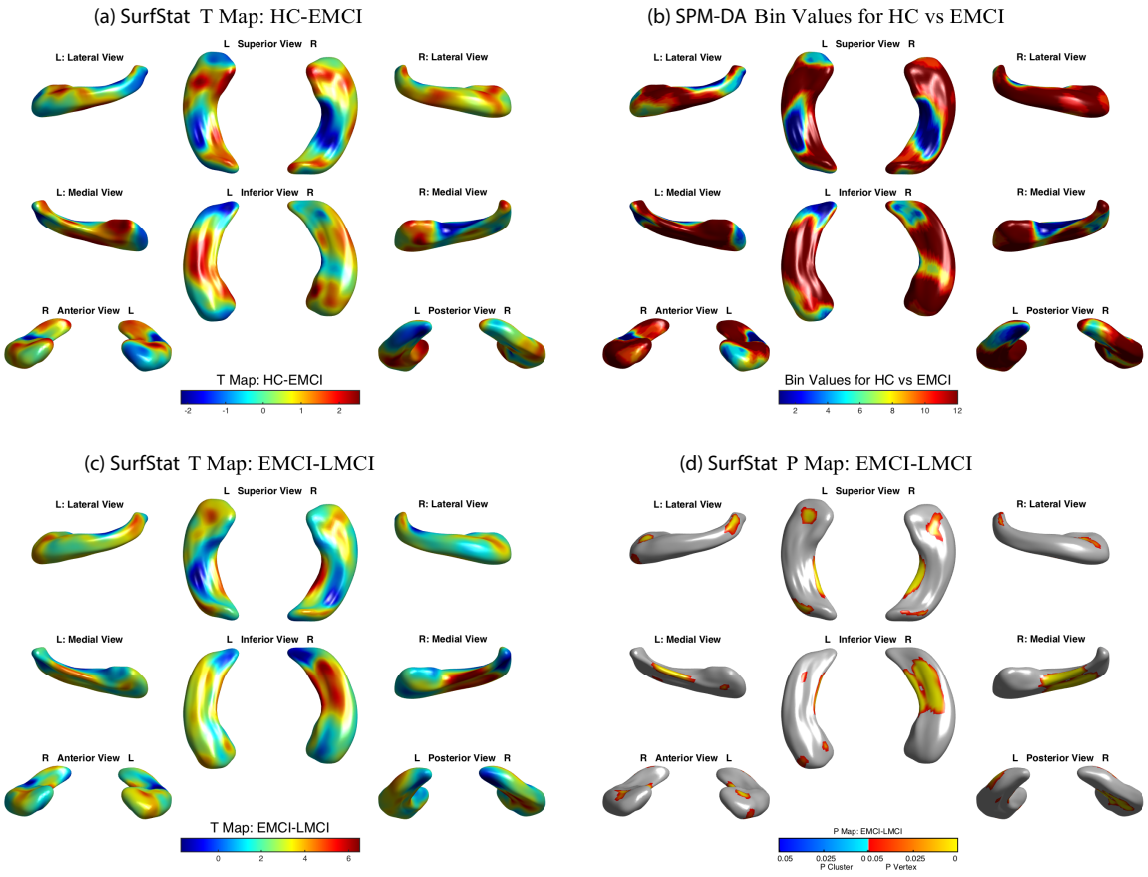

Fig. 5.7.: (a) The SurfStat t-map of the diagnostic effect (HC-LMCI) on surface signals after removing the effects of age and gender. (b) The SPM-DA bin value map for the comparison of HC vs EMCI after removing effects of age and gender. (c-d) The SurfStat t-map and p-map of the diagnostic effect (EMCI-LMCI) on surface signals after removing the effects of age and gender.

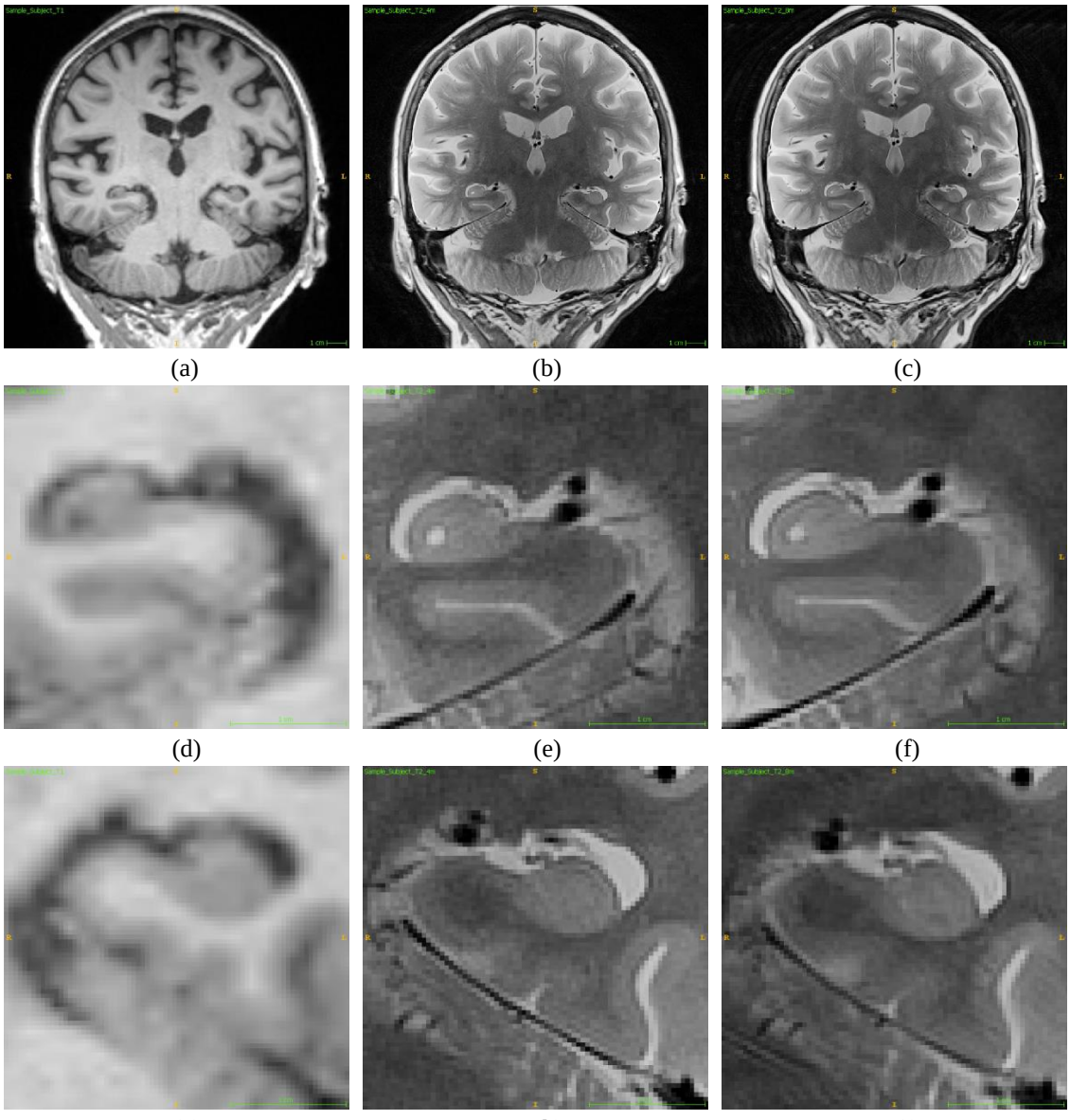

Fig. 5.8.: Coronal views: (a-c) Conventional MRI, high resolution MRI, and repeated high resolution MRI. (d-f) Left hippocampal area on conventional MRI, high resolution MRI, and repeated high resolution MRI. (g-i) Right hippocampal area on conventional MRI, high resolution MRI, and repeated high resolution MRI.

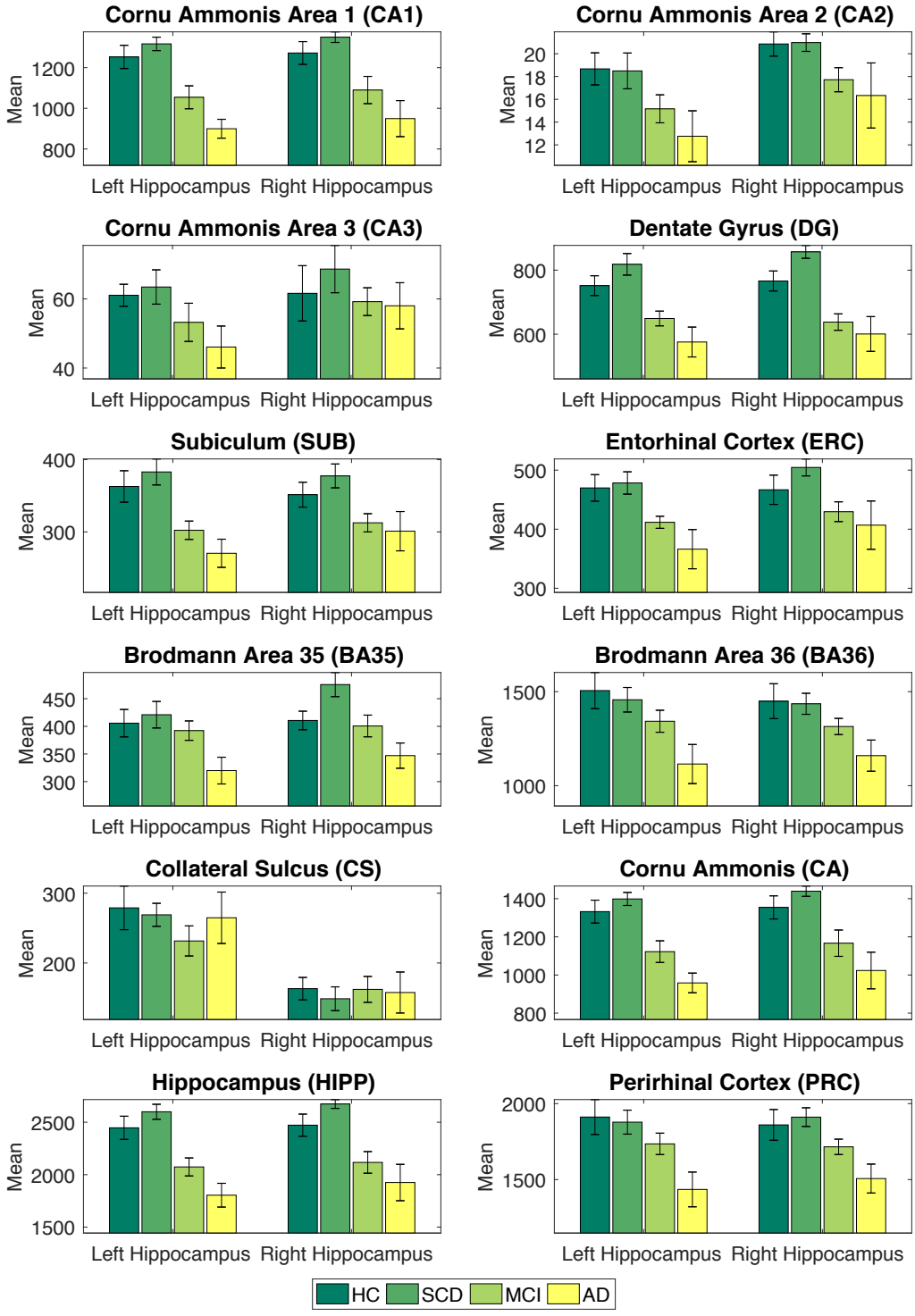

Fig. 5.9.: Group comparison for each of primary labels and compound labels. Mean and standard error (as error bar) are shown for each group (HC, SCD, MCI and AD).

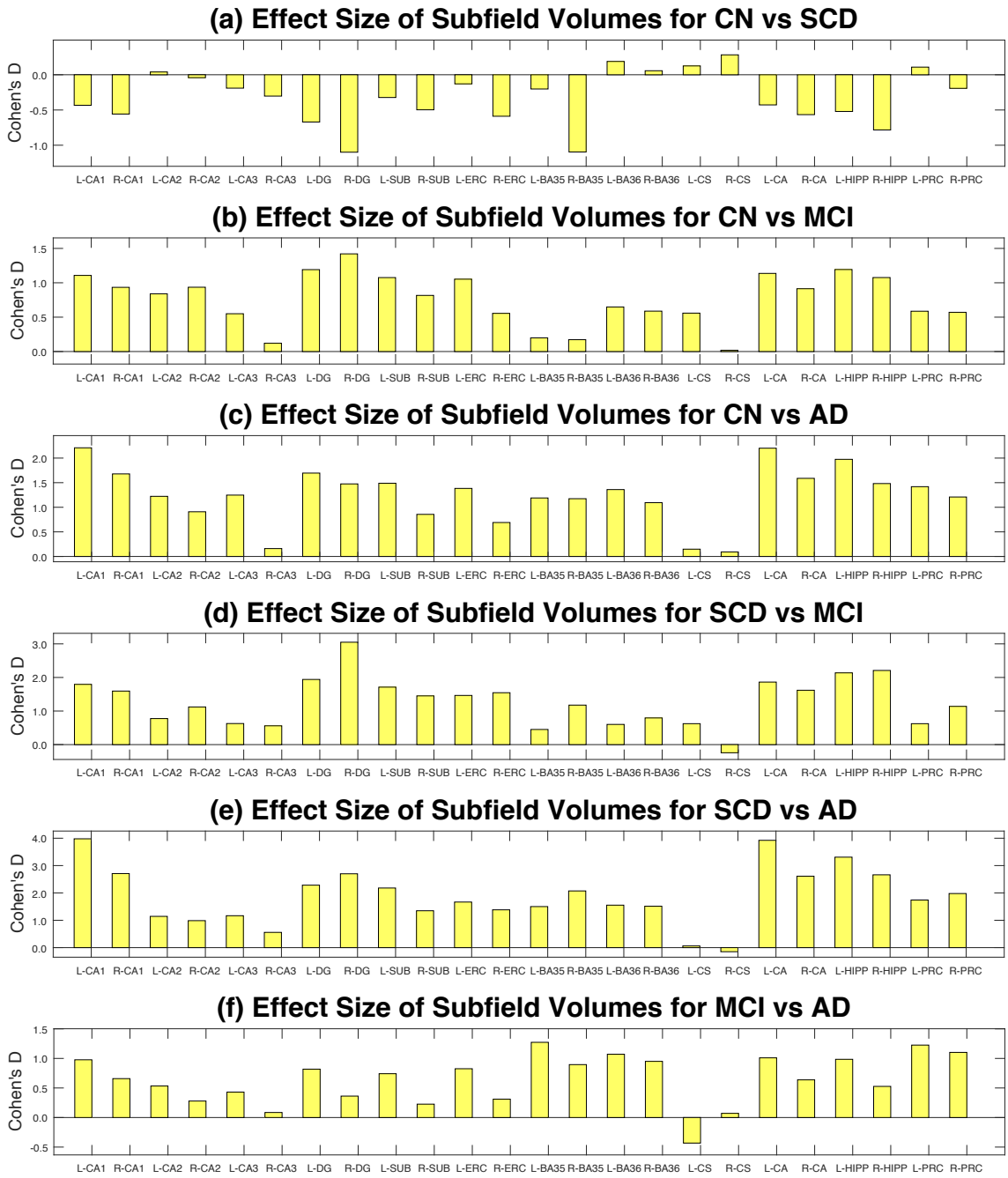

Fig. 5.10.: Effect sizes (Cohen's d) of the pair-wised comparisons between four diagnosis groups (CN, SCD, MCI and AD) evaluated for hippocampal subfield volumes. Subfield volumes are adjusted by age, gender and ICV by DX group.

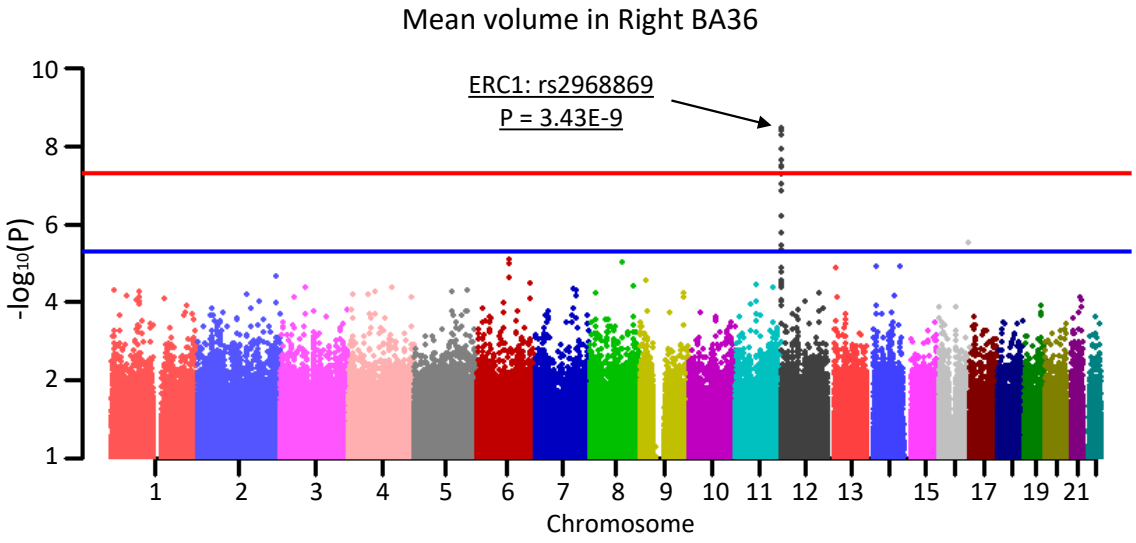

Fig. 5.11.: Manhattan plot for genome-wide association studies (GWAS) results: We identified a novel locus rs2968869 in *ERC1* on Chromosome 12 significantly associated with right BA36 volume. Blue and red lines correspond to the p-value of 5E-6 and 5E-8, respectively.

6. DISCUSSIONS AND CONCLUSIONS

In this study, we have proposed two computational frameworks to build a surface atlas of hippocampal subfields from T1, and T2 weighted MRI scans using FreeSurfer, FIRST, ASHS and SPHARM methods and tools. Using FreeSurfer, we have obtained valuable hippocampal subfield information. Using FIRST, we have extracted reliable hippocampal surface information. Using ASHS, we can extract accurate hippocampal shape and subfield information at the same time, which provides the possibility to demonstrate detailed and accurate hippocampal subfield partitions by using high-resolution T2-weighted data. Using SPHARM, it maps complex surface anatomical topology onto a sphere to establish surface correspondence across individuals. We have developed an approach to creating an atlas by mapping interpolated subfield information onto an average surface.

We have proposed and implemented an improved surface registration strategy based on demons method for fast and accurate landmark free registration that embraces, rather than ignores, the very valuable subfield information. We have demonstrated its effectiveness by applying it to the IADC and ADNI data, as well as the synthetic data. Instead of identifying landmarks on subfield boundaries, the landmark free registration makes use of surface label information to guide registration. With the awareness of the limitation of using labels directly, we formulated three types of surface features from subfield labels and used the generated features for the registration tests. Based on the experimental results illustrated in Section 4.3.6, we chose binary maps as the surface features to build the final atlas and used our proposed method Symm-Momen SD for spherical registration.

Surface-based and volumetric-based morphometric analysis of hippocampal subfields has been performed. Our studies identified statistically significant areas related to cognitive brain disorders, which match clinical evidence. We also identified genetic associations with subfield volume loss and Alzheimer's. Those findings can be seen as good biomarkers to detect AD, especially in the very early stage of AD.

The major strengths of this study are as follows:

1) We proposed a novel computational framework that integrates the high quality data cohorts and latest image processing techniques for building a hippocampal surface atlas. The generated 3D surface atlas can be seen as a reference in group analyses and it can demonstrate detailed and accurate hippocampal subfield partitions for visual inspection.

2) The popular volumetric studies usually measured global shape changes which ignores the local shape variations. The proposed methods in this study bridged this issue by taking each individual surface vertex as a measurement so it can numerically and visually indicate the degree of atrophy.

3) With the goal of achieving a better alignment for hippocampal subfields and examining local shape deformations, we demonstrated the feasibility of fast and accurate landmark free registration using hippocampal subfield information.

4) As the subfield measures are obtained directly from segmentation results, and using integer labels directly for registration can introduce errors, we resolved this problem by generating proper surface feature representations such binary maps, distance maps and probability maps.

5) With awareness of several limitations of current registration works, we proposed a new surface registration method that takes advantages of invertible transformation and momentum term. We designed detailed experiments to illustrate that the proposed methods achieved more accurate subfield matching results while keeping mesh regularity in control.

However, we are aware that there are some limitations and possible extensions of the study, some interesting future directions are described below to better achieve the goals introduced in Chapter 1. As a reminder, there are three major goals in this study: 1) taking hippocampal subfield information to guide registration; 2) creating a 3D surface atlas of the hippocampus as a reference; 3) building a framework for hippocampal morphometric analysis and identifying statistically significant regions of the hippocampus.

1-1. For the first goal of developing a subfield-guided registration method, currently only three combined subfields are used for registration. More specifically partitioned subfields can be used in both processes of the registration and shape analysis.

1-2. Another direction of the first goal is to further optimize the shape similarity while maintaining mesh regularity.

1-3. The surface registration methods ignore the interior information of the hippocampus as they only measure surface features. A volume-based registration method that considers interior information of the hippocampus can potentially be a promising study direction.

2-1. For the second goal of generating a reference, creating a reference for group analyses is one way to perform morphometric analyses, while another way to be explored is reference-free, which may lead to a different result in pair-wised group analyses.

3-1. For the third goal of building a framework for shape analyses, as the proposed approaches in this study can be generally applied in a wide range of surface analysis tasks, we hope to seek for more applications in medical imaging analysis.

3-2. Another direction in the third goal is that we only performed several simple analyses in this study, but more complicated association analyses can be conduct with the proposed framework such as longitudinal analyses, genetic association and brain connectivity analyses.

3-3. In this study, we examined the significant subfield regions and developed the AD biomarkers that were highly related to cognitive diseases. The next extension in the third goal is to classify and predict the patients given a data set.

REFERENCES

[1] J. Gaugler, B. James, T. Johnson, A. Marin, and J. Weuve, "2019 alzheimer's disease facts and figures," *ALZHEIMERS & DEMENTIA*, vol. 15, no. 3, pp. 321–387, 2019.

[2] R. C. Petersen, G. E. Smith, S. C. Waring, R. J. Ivnik, E. G. Tangalos, and E. Kokmen, "Mild cognitive impairment: clinical characterization and outcome," *Arch Neurol*, vol. 56, no. 3, pp. 303–8, 1999.

[3] B. C. Bernhardt, S.-J. Hong, A. Bernasconi, and N. Bernasconi, "Magnetic resonance imaging pattern learning in temporal lobe epilepsy: classification and prognostics," *Annals of neurology*, vol. 77, no. 3, pp. 436–446, 2015.

[4] B. C. Bernhardt, A. Bernasconi, M. Liu, S.-J. Hong, B. Caldairou, M. Goubran, M. C. Guiot, J. Hall, and N. Bernasconi, "The spectrum of structural and functional imaging abnormalities in temporal lobe epilepsy," *Annals of neurology*, vol. 80, no. 1, pp. 142–153, 2016.

[5] D. Koshiyama, M. Fukunaga, N. Okada, F. Yamashita, H. Yamamori, Y. Yasuda, M. Fujimoto, K. Ohi, H. Fujino, Y. Watanabe *et al.*, "Subcortical association with memory performance in schizophrenia: a structural magnetic resonance imaging study," *Translational psychiatry*, vol. 8, no. 1, p. 20, 2018.

[6] J. Pluta, P. Yushkevich, S. Das, and D. Wolk, "In vivo analysis of hippocampal subfield atrophy in mild cognitive impairment via semi-automatic segmentation of t2-weighted mri," *Journal of Alzheimer's Disease*, vol. 31, no. 1, pp. 85–99, 2012.

[7] L. Shen, A. J. Saykin, S. Kim, H. A. Firpi, J. D. West, S. L. Risacher, B. C. McDonald, T. L. McHugh, H. A. Wishart, and L. A. Flashman, "Comparison of manual and automated determination of hippocampal volumes in mci and early ad," *Brain imaging and behavior*, vol. 4, no. 1, pp. 86–95, 2010.

[8] C. Testa, M. P. Laakso, F. Sabattoli, R. Rossi, A. Beltramello, H. Soininen, and G. B. Frisoni, "A comparison between the accuracy of voxel-based morphometry and hippocampal volumetry in alzheimer's disease," *Journal of Magnetic Resonance Imaging*, vol. 19, no. 3, pp. 274–282, 2004.

[9] P. A. Yushkevich, J. B. Pluta, H. Wang, L. Xie, S. Ding, E. C. Gertje, L. Mancuso, D. Kliot, S. R. Das, and D. A. Wolk, "Automated volumetry and regional thickness analysis of hippocampal subfields and medial temporal cortical structures in mild cognitive impairment," *Human brain mapping*, vol. 36, no. 1, pp. 258–287, 2015.

[10] H.-K. Lim, S. C. Hong, W. S. Jung, K. J. Ahn, W. Y. Won, C. Hahn, I. S. Kim, and C. U. Lee, "Hippocampal shape and cognitive performance in amnestic mild cognitive impairment," *Neuroreport*, vol. 23, no. 6, pp. 364–368, 2012.

[11] P. A. Yushkevich, J. B. Pluta, H. Wang, L. Xie, S.-L. Ding, E. C. Gertje, L. Mancuso, D. Kliot, S. R. Das, and D. A. Wolk, "Automated volumetry and regional thickness analysis of hippocampal subfields and medial temporal cortical structures in mild cognitive impairment," *Human brain mapping*, vol. 36, no. 1, pp. 258–287, 2015.

[12] A. Perrotin, R. de Flores, F. Lamberton, G. Poisnel, R. La Joie, V. de la Sayette, F. Mezenge, C. Tomadesso, B. Landeau, B. Desgranges *et al.*, "Hippocampal subfield volumetry and 3d surface mapping in subjective cognitive decline," *Journal of Alzheimer's Disease*, vol. 48, no. s1, pp. S141–S150, 2015.

[13] S. G. Mueller, L. Chao, B. Berman, and M. W. Weiner, "Evidence for functional specialization of hippocampal subfields detected by mr subfield volumetry on high resolution images at 4t," *Neuroimage*, vol. 56, no. 3, pp. 851–857, 2011.

[14] M. J. West, C. H. Kawas, W. F. Stewart, G. L. Rudow, and J. C. Troncoso, "Hippocampal neurons in pre-clinical alzheimers disease," *Neurobiology of aging*, vol. 25, no. 9, pp. 1205–1212, 2004.

[15] T. Bartsch, J. Döhring, A. Rohr, O. Jansen, and G. Deuschl, "Ca1 neurons in the human hippocampus are critical for autobiographical memory, mental time travel, and autonoetic consciousness," *Proceedings of the National Academy of Sciences*, vol. 108, no. 42, pp. 17 562–17 567, 2011.

[16] M. Rössler, R. Zarski, J. Bohl, and T. G. Ohm, "Stage-dependent and sector-specific neuronal loss in hippocampus during alzheimer's disease," *Acta neuropathologica*, vol. 103, no. 4, pp. 363–369, 2002.

[17] M. Hoogman, J. Bralten, D. P. Hibar, M. Mennes, M. P. Zwiers, L. S. Schweren, K. J. van Hulzen, S. E. Medland, E. Shumskaya, N. Jahanshad *et al.*, "Subcortical brain volume differences in participants with attention deficit hyperactivity disorder in children and adults: a cross-sectional mega-analysis," *The Lancet Psychiatry*, vol. 4, no. 4, pp. 310–319, 2017.

[18] T. Wise, J. Radua, E. Via, N. Cardoner, O. Abe, T. Adams, F. Amico, Y. Cheng, J. Cole, C. d. A. M. Périco *et al.*, "Common and distinct patterns of grey-matter volume alteration in major depression and bipolar disorder: evidence from voxel-based meta-analysis," *Molecular psychiatry*, vol. 22, no. 10, p. 1455, 2017.

[19] J. Firth, B. Stubbs, D. Vancampfort, F. Schuch, J. Lagopoulos, S. Rosenbaum, and P. B. Ward, "Effect of aerobic exercise on hippocampal volume in humans: a systematic review and meta-analysis," *Neuroimage*, vol. 166, pp. 230–238, 2018.

[20] D. P. Hibar, H. H. Adams, N. Jahanshad, G. Chauhan, J. L. Stein, E. Hofer, M. E. Renteria, J. C. Bis, A. Arias-Vasquez, M. K. Ikram *et al.*, "Novel genetic loci associated with hippocampal volume," *Nature communications*, vol. 8, p. 13624, 2017.

[21] A. Scher, Y. Xu, E. Korf, L. White, P. Scheltens, A. Toga, P. Thompson, S. Hartley, M. Witter, D. Valentino *et al.*, "Hippocampal shape analysis in alzheimers disease: a population-based study," *Neuroimage*, vol. 36, no. 1, pp. 8–18, 2007.

[22] J. Winterburn, J. C. Pruessner, C. Sofia, M. M. Schira, N. J. Lobaugh, A. N. Voineskos, and M. M. Chakravarty, "High-resolution in vivo manual segmentation protocol for human hippocampal subfields using 3t magnetic resonance imaging," *Journal of Visualized Experiments*, no. 105, pp. e51 861–e51 861, 2015.

[23] P. A. Yushkevich, R. S. Amaral, J. C. Augustinack, A. R. Bender, J. D. Bernstein, M. Boccardi, M. Bocchetta, A. C. Burggren, V. A. Carr, M. M. Chakravarty *et al.*, "Quantitative comparison of 21 protocols for labeling hippocampal subfields and parahippocampal subregions in in vivo mri: towards a harmonized segmentation protocol," *Neuroimage*, vol. 111, pp. 526–541, 2015.

[24] J. L. Winterburn, J. C. Pruessner, S. Chavez, M. M. Schira, N. J. Lobaugh, A. N. Voineskos, and M. M. Chakravarty, "A novel in vivo atlas of human hippocampal subfields using high-resolution 3t magnetic resonance imaging," *Neuroimage*, vol. 74, pp. 254–265, 2013.

[25] L. Wisse, L. Gerritsen *et al.*, "Subfields of the hippocampal formation at 7t mri: In vivo volumetric assessment," *Neuroimage*, vol. 61, no. 4, pp. 1043–1049, 2012.

[26] R. La Joie, M. Fouquet, F. Mézenge, B. Landeau, N. Villain, K. Mevel, A. Pélerin, F. Eustache, B. Desgranges, and G. Chételat, "Differential effect of age on hippocampal subfields assessed using a new high-resolution 3t mr sequence," *Neuroimage*, vol. 53, no. 2, pp. 506–514, 2010.

[27] M. R. Hunsaker and D. G. Amaral, "A semi-automated pipeline for the segmentation of rhesus macaque hippocampus: Validation across a wide age range," *PloS one*, vol. 9, no. 2, p. e89456, 2014.

[28] B. Merkel, C. Steward, L. Vivash, C. B. Malpas, P. Phal, B. A. Moffat, K. L. Cox, K. A. Ellis, D. J. Ames, E. V. Cyarto *et al.*, "Semi-automated hippocampal segmentation in people with cognitive impairment using an age appropriate template for registration," *Journal of Magnetic Resonance Imaging*, vol. 42, no. 6, pp. 1631–1638, 2015.

[29] K. Van Leemput, A. Bakkour, T. Benner, G. Wiggins, L. L. Wald, J. Augustinack, B. C. Dickerson, P. Golland, and B. Fischl, "Automated segmentation of hippocampal subfields from ultra-high resolution in vivo mri," *Hippocampus*, vol. 19, no. 6, pp. 549–57, 2009.

[30] J. E. Iglesias, J. C. Augustinack, K. Nguyen, C. M. Player, A. Player, M. Wright, N. Roy, M. P. Frosch, A. C. McKee, L. L. Wald *et al.*, "A computational atlas of the hippocampal formation using ex vivo, ultra-high resolution mri: application to adaptive segmentation of in vivo mri," *NeuroImage*, vol. 115, pp. 117–137, 2015.

[31] D. Sone, N. Sato, N. Maikusa, M. Ota, K. Sumida, K. Yokoyama, Y. Kimura, E. Imabayashi, Y. Watanabe, M. Watanabe *et al.*, "Automated subfield volumetric analysis of hippocampus in temporal lobe epilepsy using high-resolution t2-weighed mr imaging," *NeuroImage: Clinical*, vol. 12, pp. 57–64, 2016.

[32] J. Pipitone, M. T. M. Park, J. Winterburn, T. A. Lett, J. P. Lerch, J. C. Pruessner, M. Lepage, A. N. Voineskos, M. M. Chakravarty, A. D. N. Initiative *et al.*, "Multi-atlas segmentation of the whole hippocampus and subfields using multiple automatically generated templates," *Neuroimage*, vol. 101, pp. 494–512, 2014.

[33] H. Wang, J. W. Suh *et al.*, "Multi-atlas segmentation with joint label fusion," *Pattern Analysis and Machine Intelligence, IEEE Transactions on*, vol. 35, no. 3, pp. 611–623, 2013.

[34] P. Coupe, V. Fonov, S. Eskildsen, J. Manjón, D. Arnold, and L. Collins, "Influence of the training library composition on a patch-based label fusion method: Application to hippocampus segmentation on the adni dataset," *Alzheimer's & Dementia: The Journal of the Alzheimer's Association*, vol. 7, no. 4, p. S316, 2011.

[35] G. Wu, Q. Wang, D. Zhang, F. Nie, H. Huang, and D. Shen, "A generative probability model of joint label fusion for multi-atlas based brain segmentation," *Medical image analysis*, vol. 18, no. 6, pp. 881–890, 2014.

[36] B. A. Gutman, N. Jahanshad, C. R. Ching, Y. Wang, P. V. Kochunov, T. E. Nichols, and P. M. Thompson, "Medial demons registration localizes the degree of genetic influence over subcortical shape variability: an n= 1480 meta-analysis," in *Proceedings of the 12th International Symposium on Biomedical Imaging (ISBI)*. IEEE, 2015, pp. 1402–1406.

[37] B. T. Yeo, M. R. Sabuncu, T. Vercauteren, N. Ayache, B. Fischl, and P. Golland, "Spherical demons: fast diffeomorphic landmark-free surface registration," *IEEE transactions on medical imaging*, vol. 29, no. 3, pp. 650–668, 2010.

[38] Y. Wang, J. Shi, X. Yin, X. Gu, T. F. Chan, S.-T. Yau, A. W. Toga, and P. M. Thompson, "Brain surface conformal parameterization with the ricci flow," *IEEE transactions on medical imaging*, vol. 31, no. 2, pp. 251–264, 2011.

[39] K. Hett, V.-T. Ta, J. V. Manjón, and P. Coupé, "Graph of hippocampal subfields grading for alzheimers disease prediction," in *International Workshop on Machine Learning in Medical Imaging*. Springer, 2018, pp. 259–266.

[40] M. Shakeri, H. Lombaert, A. N. Datta, N. Oser, L. Létourneau-Guillon, L. V. Lapointe, F. Martin, D. Malfait, A. Tucholka, S. Lippé *et al.*, "Statistical shape analysis of subcortical structures using spectral matching," *Computerized Medical Imaging and Graphics*, vol. 52, pp. 58–71, 2016.

[41] S. Cong, M. Rizkalla, P. Salama, S. L. Risacher, J. D. West, Y.-C. Wu, L. Apostolova, E. Tallman, A. J. Saykin, and L. Shen, "Building a surface atlas of hippocampal subfields from high resolution t2-weighted mri scans using landmark-free surface registration," in *2016 IEEE 59th International Midwest Symposium on Circuits and Systems (MWSCAS)*. IEEE, 2016, pp. 1–4.

[42] M. Shakeri, H. Lombaert, S. Tripathi, S. Kadoury, A. D. N. Initiative *et al.*, "Deep spectral-based shape features for alzheimers disease classification," in *International Workshop on Spectral and Shape Analysis in Medical Imaging*. Springer, 2016, pp. 15–24.

[43] O. Litany, E. Rodolà, A. M. Bronstein, and M. M. Bronstein, "Fully spectral partial shape matching," in *Computer Graphics Forum*, vol. 36, no. 2. Wiley Online Library, 2017, pp. 247–258.

[44] J. Zhang, M. Liu, L. An, Y. Gao, and D. Shen, "Alzheimer's disease diagnosis using landmark-based features from longitudinal structural mr images," *IEEE journal of biomedical and health informatics*, vol. 21, no. 6, pp. 1607–1616, 2017.

[45] J. Shi, P. M. Thompson, B. Gutman, and Y. Wang, "Surface fluid registration of conformal representation: Application to detect disease burden and genetic influence on hippocampus," *Neuroimage*, vol. 78, pp. 111–134, 2013.

[46] L. Shen, H. A. Firpi, A. J. Saykin, and J. D. West, "Parametric surface modeling and registration for comparison of manual and automated segmentation of the hippocampus," *Hippocampus*, vol. 19, no. 6, pp. 588–595, 2009.

[47] M. Styner, I. Oguz, S. Xu, C. Brechbühler, D. Pantazis, J. J. Levitt, M. E. Shenton, and G. Gerig, "Framework for the statistical shape analysis of brain structures using spharm-pdm," *The insight journal*, no. 1071, p. 242, 2006.

[48] A. A. Goshtasby, *2-D and 3-D image registration: for medical, remote sensing, and industrial applications*. John Wiley & Sons, 2005.

[49] X. Yang, J. Li, B. Liu, Y. Li, and T. Jiang, "Impact of picalm and clu on hippocampal degeneration," *Human brain mapping*, vol. 37, no. 7, pp. 2419–2430, 2016.

[50] R. Zhang, X. Chen, T. Shiratori, X. Tong, and L. Liu, "An efficient volumetric method for non-rigid registration," *Graphical Models*, vol. 79, pp. 1–11, 2015.

[51] W. Zeng and X. D. Gu, "Registration for 3d surfaces with large deformations using quasi-conformal curvature flow," in *Computer Vision and Pattern Recognition (CVPR), 2011 IEEE Conference on*. IEEE, 2011, pp. 2457–2464.

[52] S. Arguillere, M. I. Miller, and L. Younes, "Diffeomorphic surface registration with atrophy constraints," *SIAM Journal on Imaging Sciences*, vol. 9, no. 3, pp. 975–1003, 2016.

[53] R. Shi, W. Zeng, Z. Su, J. Jiang, H. Damasio, Z. Lu, Y. Wang, S.-T. Yau, and X. Gu, "Hyperbolic harmonic mapping for surface registration," *IEEE transactions on pattern analysis and machine intelligence*, vol. 39, no. 5, pp. 965–980, 2017.

[54] M. Sergejeva, E. A. Papp, R. Bakker, M. A. Gaudnek, Y. Okamura-Oho, J. Boline, J. G. Bjaalie, and A. Hess, "Anatomical landmarks for registration of experimental image data to volumetric rodent brain atlasing templates," *Journal of neuroscience methods*, vol. 240, pp. 161–169, 2015.

[55] D. Chetverikov, D. Svirko, D. Stepanov, and P. Krsek, "The trimmed iterative closest point algorithm," in *Proceeding of 16th International Conference on Pattern Recognition*, vol. 3. IEEE, 2002, pp. 545–548.

[56] S. J. Hsu, L. Fan, and K. M. Sekins, "High intensity focused ultrasound registration with imaging," 2016, uS Patent 9,392,992.

[57] M.-M. Rohé, M. Datar, T. Heimann, M. Sermesant, and X. Pennec, "Svf-net: learning deformable image registration using shape matching," in *International Conference on Medical Image Computing and Computer-Assisted Intervention*. Springer, 2017, pp. 266–274.

[58] M. Bruveris and D. D. Holm, "Geometry of image registration: The diffeomorphism group and momentum maps," in *Geometry, Mechanics, and Dynamics*. Springer, 2015, pp. 19–56.

[59] M. Zhang and P. T. Fletcher, "Finite-dimensional lie algebras for fast diffeomorphic image registration," in *International Conference on Information Processing in Medical Imaging*. Springer, 2015, pp. 249–260.

[60] H. Lombaert, L. Grady, X. Pennec, N. Ayache, and F. Cheriet, "Spectral log-demons: diffeomorphic image registration with very large deformations," *International journal of computer vision*, vol. 107, no. 3, pp. 254–271, 2014.

[61] T. Ohtani, P. G. Nestor, S. Bouix, D. Newell, E. D. Melonakos, R. W. McCarley, M. E. Shenton, and M. Kubicki, "Exploring the neural substrates of attentional control and human intelligence: Diffusion tensor imaging of prefrontal white matter tractography in healthy cognition," *Neuroscience*, vol. 341, pp. 52–60, 2017.

[62] L. J. ODonnell and C.-F. Westin, "An introduction to diffusion tensor image analysis," *Neurosurgery Clinics*, vol. 22, no. 2, pp. 185–196, 2011.

[63] G. Fichtinger, A. Jain, T. Mustufa, K. Wyrobek, G. Chirikjian, Y. Zhou, and E. C. Burdette, "Image registration of multiple medical imaging modalities using a multiple degree-of-freedom-encoded fiducial device," 2015, uS Patent 8,948,471.

[64] Y. Yamaguchi, Y. Takeda, T. Hara, X. Zhou, M. Matsusako, Y. Tanaka, K. Hosoya, T. Nihei, T. Katafuchi, and H. Fujita, "Three modality image registration of brain spect/ct and mr images for quantitative analysis of dopamine transporter imaging," in *Medical Imaging 2016: Biomedical Applications in Molecular, Structural, and Functional Imaging*, vol. 9788. International Society for Optics and Photonics, 2016, p. 97881V.

[65] P. Fallavollita, G. Fichtinger, P. Abolmaesumi, and E. C. BURDETTE, "C-arm pose estimation using intensity-based registration of imaging modalities," 2016, uS Patent 9,282,944.

[66] S. Haker, S. Angenent, A. Tannenbaum, R. Kikinis, G. Sapiro, and M. Halle, "Conformal surface parameterization for texture mapping," *IEEE Transactions on Visualization and Computer Graphics*, vol. 6, no. 2, pp. 181–189, 2000.

[67] X. Gu, Y. Wang, T. F. Chan, P. M. Thompson, and S.-T. Yau, "Genus zero surface conformal mapping and its application to brain surface mapping," *IEEE Transactions on Medical Imaging*, vol. 23, no. 8, pp. 949–958, 2004.

[68] S. Durrleman, X. Pennec, A. Trouvé, and N. Ayache, "A forward model to build unbiased atlases from curves and surfaces," in *2nd MICCAI Workshop on Mathematical Foundations of Computational Anatomy*, 2008, pp. 68–79.

[69] L. M. Lui, T. W. Wong, P. Thompson, T. Chan, X. Gu, and S.-T. Yau, "Shape-based diffeomorphic registration on hippocampal surfaces using beltrami holomorphic flow," in *International Conference on Medical Image Computing and Computer-Assisted Intervention*. Springer, 2010, pp. 323–330.

[70] M. I. Restrepo, A. O. Ulusoy, and J. L. Mundy, "Evaluation of feature-based 3-d registration of probabilistic volumetric scenes," *ISPRS Journal of Photogrammetry and Remote Sensing*, vol. 98, pp. 1–18, 2014.

[71] S. S. Ghosh, S. Kakunoori, J. Augustinack, A. Nieto-Castanon, I. Kovelman, N. Gaab, J. A. Christodoulou, C. Triantafyllou, J. D. Gabrieli, and B. Fischl, "Evaluating the validity of volume-based and surface-based brain image registration for developmental cognitive neuroscience studies in children 4 to 11 years of age," *Neuroimage*, vol. 53, no. 1, pp. 85–93, 2010.

[72] G. Postelnicu, L. Zollei, and B. Fischl, "Combined volumetric and surface registration," *IEEE transactions on medical imaging*, vol. 28, no. 4, pp. 508–522, 2009.

[73] W. Zhang, J. Shi, C. Stonnington, R. J. Bauer, B. A. Gutman, K. Chen, P. M. Thompson, E. M. Reiman, R. J. Caselli, and Y. Wang, "Morphometric analysis of hippocampus and lateral ventricle reveals regional difference between cognitively stable and declining persons," in *Proceedings of 13th International Symposium on Biomedical Imaging (ISBI),*. IEEE, 2016, pp. 14–18.

[74] J. Shi, N. Leporé, B. A. Gutman, P. M. Thompson, L. C. Baxter, R. J. Caselli, and Y. Wang, "Genetic influence of apolipoprotein e4 genotype on hippocampal morphometry: An n= 725 surface-based alzheimer's disease neuroimaging initiative study," *Human brain mapping*, vol. 35, no. 8, pp. 3903–3918, 2014.

[75] S. M. Gold, M.-F. O'Connor, R. Gill, K. C. Kern, Y. Shi, R. G. Henry, D. Pelletier, D. C. Mohr, and N. L. Sicotte, "Detection of altered hippocampal morphology in multiple sclerosis-associated depression using automated surface mesh modeling," *Human brain mapping*, vol. 35, no. 1, pp. 30–37, 2014.

[76] L. W. Chen, D. Sun *et al.*, "Smaller hippocampal ca1 subfield volume in posttraumatic stress disorder," *Depression and anxiety*, vol. 35, no. 11, pp. 1018–1029, 2018.

[77] U. K. Haukvik, L. T. Westlye, L. Mørch-Johnsen, K. N. Jørgensen, E. H. Lange, A. M. Dale, I. Melle, O. A. Andreassen, and I. Agartz, "In vivo hippocampal subfield volumes in schizophrenia and bipolar disorder," *Biological psychiatry*, vol. 77, no. 6, pp. 581–588, 2015.

[78] S. G. Mueller, N. Schuff, K. Yaffe, C. Madison, B. Miller, and M. W. Weiner, "Hippocampal atrophy patterns in mild cognitive impairment and alzheimer's disease," *Hum Brain Mapp*, vol. 31, no. 9, pp. 1339–47, 2010.

[79] S. G. Costafreda, I. D. Dinov, Z. Tu, Y. Shi, C.-Y. Liu, I. Kloszewska, P. Mecocci, H. Soininen, M. Tsolaki, B. Vellas *et al.*, "Automated hippocampal shape analysis predicts the onset of dementia in mild cognitive impairment," *Neuroimage*, vol. 56, no. 1, pp. 212–219, 2011.

[80] K. Ning, B. Chen, F. Sun, Z. Hobel, L. Zhao, W. Matloff, A. W. Toga, A. D. N. Initiative *et al.*, "Classifying alzheimer's disease with brain imaging and genetic data using a neural network framework," *Neurobiology of aging*, vol. 68, pp. 151–158, 2018.

[81] R. Han, T. De Silva, M. Ketcha, A. Uneri, and J. Siewerdsen, "A momentum-based diffeomorphic demons framework for deformable mr-ct image registration," *Physics in Medicine & Biology*, vol. 63, no. 21, p. 215006, 2018.

[82] B. W. Papież, J. M. Franklin, M. P. Heinrich, F. V. Gleeson, M. Brady, and J. A. Schnabel, "Gifted demons: deformable image registration with local structure-preserving regularization using supervoxels for liver applications," *Journal of Medical Imaging*, vol. 5, no. 2, p. 024001, 2018.

[83] L. Pishchulin, S. Wuhrer, T. Helten, C. Theobalt, and B. Schiele, "Building statistical shape spaces for 3d human modeling," *Pattern Recognition*, vol. 67, pp. 276–286, 2017.

[84] A. P. Tafti, A. B. Kirkpatrick, Z. Alavi, H. A. Owen, and Z. Yu, "Recent advances in 3d sem surface reconstruction," *Micron*, vol. 78, pp. 54–66, 2015.

[85] T. Heimann and H.-P. Meinzer, "Statistical shape models for 3d medical image segmentation: a review," *Medical image analysis*, vol. 13, no. 4, pp. 543–563, 2009.

[86] S. G. Mueller, L. Stables, A. T. Du, N. Schuff, D. Truran, N. Cashdollar, and M. W. Weiner, "Measurement of hippocampal subfields and age-related changes with high resolution MRI at 4T," *Neurobiol Aging*, vol. 28, no. 5, pp. 719–26, 2007.

[87] P. A. Yushkevich, B. B. Avants, J. Pluta, S. Das, D. Minkoff, D. Mechanic-Hamilton, S. Glynn, S. Pickup, W. Liu, J. C. Gee, M. Grossman, and J. A. Detre, "A high-resolution computational atlas of the human hippocampus from postmortem magnetic resonance imaging at 9.4 T," *Neuroimage*, vol. 44, no. 2, pp. 385–98, 2009.

[88] R. La Joie, M. Fouquet, F. Mezenge, B. Landeau, N. Villain, K. Mevel, A. Pelerin, F. Eustache, B. Desgranges, and G. Chetelat, "Differential effect of age on hippocampal subfields assessed using a new high-resolution 3T MR sequence," *Neuroimage*, vol. 53, no. 2, pp. 506–14, 2010.

[89] J. L. Winterburn, J. C. Pruessner, S. Chavez, M. M. Schira, N. J. Lobaugh, A. N. Voineskos, and M. M. Chakravarty, "A novel in vivo atlas of human hippocampal subfields using high-resolution 3 t magnetic resonance imaging," *Neuroimage*, vol. 74, pp. 254–65, 2013.

[90] L. Shen, S. Kim, J. Wan, J. D. West, and A. J. Saykin, "Fourier methods for 3d surface modeling and analysis," *Emerging Topics in Computer Vision and Its Applications*, vol. 1, p. 175, 2011.

[91] C. Brechbühler, G. Gerig, and O. Kübler, "Parametrization of closed surfaces for 3-d shape description," *Computer vision and image understanding*, vol. 61, no. 2, pp. 154–170, 1995.

[92] L. Shen, S. Kim, and A. J. Saykin, "Fourier method for large-scale surface modeling and registration," *Computers & graphics*, vol. 33, no. 3, pp. 299–311, 2009.

[93] M. W. Weiner, D. P. Veitch *et al.*, "The alzheimer's disease neuroimaging initiative: a review of papers published since its inception," *Alzheimers Dement*, vol. 9, no. 5, pp. e111–94, 2013.

[94] K. Van Leemput, A. Bakkour, T. Benner, G. Wiggins, L. L. Wald, J. Augustinack, B. C. Dickerson, P. Golland, and B. Fischl, "Automated segmentation of hippocampal subfields from ultra-high resolution in vivo mri," *Hippocampus*, vol. 19, no. 6, pp. 549–557, 2009.

[95] A. P. Dempster, N. M. Laird, and D. B. Rubin, "Maximum likelihood from incomplete data via the em algorithm," *Journal of the Royal Statistical Society: Series B (Methodological)*, vol. 39, no. 1, pp. 1–22, 1977.

[96] B. Patenaude, S. M. Smith, D. N. Kennedy, and M. Jenkinson, "A bayesian model of shape and appearance for subcortical brain segmentation," *Neuroimage*, vol. 56, no. 3, pp. 907–922, 2011.

[97] M. Quicken, C. Brechbuhler, J. Hug, H. Blattmann, and G. Székely, "Parameterization of closed surfaces for parametric surface description," in *Proceedings IEEE Conference on Computer Vision and Pattern Recognition. CVPR 2000 (Cat. No. PR00662)*, vol. 1. IEEE, 2000, pp. 354–360.

[98] G. Bertrand and G. Malandain, "A new characterization of three-dimensional simple points," *Pattern Recognition Letters*, vol. 15, no. 2, pp. 169–175, 1994.

[99] M. K. Chung, P. Bubenik, and P. T. Kim, "Persistence diagrams of cortical surface data," in *International Conference on Information Processing in Medical Imaging*. Springer, 2009, pp. 386–397.

[100] M.-H. Yueh, W.-W. Lin, C.-T. Wu, and S.-T. Yau, "An efficient energy minimization for conformal parameterizations," *Journal of Scientific Computing*, vol. 73, no. 1, pp. 203–227, 2017.

[101] K. Tapp, *Differential Geometry of curves and surfaces*. Springer, 2016.

[102] M. P. Do Carmo, G. Fischer, U. Pinkall, and H. Reckziegel, "Differential geometry," in *Mathematical Models*. Springer, 2017, pp. 155–180.

[103] E. Abbena, S. Salamon, and A. Gray, *Modern differential geometry of curves and surfaces with Mathematica*. Chapman and Hall/CRC, 2017.

[104] M. P. Do Carmo, *Differential Geometry of Curves and Surfaces: Revised and Updated Second Edition*. Courier Dover Publications, 2016.

[105] E. W. Weisstein, ""spherical harmonic." from mathworldA Wolfram Web Resource," http://mathworld.wolfram.com/SphericalHarmonic.html/, website Update Date: March 20, 2014; Last Date Accessed: April, 2014.

[106] E. C. Robinson, K. Garcia, M. F. Glasser, Z. Chen, T. S. Coalson, A. Makropoulos, J. Bozek, R. Wright, A. Schuh, M. Webster *et al.*, "Multimodal surface matching with higher-order smoothness constraints," *NeuroImage*, vol. 167, pp. 453–465, 2018.

[107] I. Peterlík, H. Courtecuisse, R. Rohling, P. Abolmaesumi, C. Nguan, S. Cotin, and S. Salcudean, "Fast elastic registration of soft tissues under large deformations," *Medical image analysis*, vol. 45, pp. 24–40, 2018.

[108] Y. Lu, S. Zhao, N. Younes, and J. K. Hahn, "Accurate nonrigid 3d human body surface reconstruction using commodity depth sensors," *Computer Animation and Virtual Worlds*, vol. 29, no. 5, p. e1807, 2018.

[109] L. Shen, S. Kim, J. Wan, J. D. West, and A. J. Saykin, *Fourier methods for 3D surface modeling and analysis*. World Scientific, 2011, pp. 175–196.

[110] J.-P. Thirion, "Image matching as a diffusion process: an analogy with maxwell's demons," *Medical image analysis*, vol. 2, no. 3, pp. 243–260, 1998.

[111] T. Vercauteren, X. Pennec, A. Perchant, and N. Ayache, "Diffeomorphic demons: Efficient non-parametric image registration," *NeuroImage*, vol. 45, no. 1, pp. S61–S72, 2009.

[112] A. Santos-Ribeiro, D. J. Nutt, and J. McGonigle, "Inertial demons: a momentum-based diffeomorphic registration framework," in *International Conference on Medical Image Computing and Computer-Assisted Intervention*. Springer, 2016, pp. 37–45.

[113] J. J. Moré, "The levenberg-marquardt algorithm: implementation and theory," in *Numerical analysis*. Springer, 1978, pp. 105–116.

[114] P. Cachier, E. Bardinet, D. Dormont, X. Pennec, and N. Ayache, "Iconic feature based nonrigid registration: the pasha algorithm," *Computer vision and image understanding*, vol. 89, no. 2-3, pp. 272–298, 2003.

[115] M. Bro-Nielsen and C. Gramkow, "Fast fluid registration of medical images," in *International Conference on Visualization in Biomedical Computing*. Springer, 1996, pp. 265–276.

[116] B. A. Gutman, S. K. Madsen, A. W. Toga, and P. M. Thompson, "A family of fast spherical registration algorithms for cortical shapes," in *International Workshop on Multimodal Brain Image Analysis*. Springer, 2013, pp. 246–257.

[117] N. J. Higham, "The scaling and squaring method for the matrix exponential revisited," *SIAM review*, vol. 51, no. 4, pp. 747–764, 2009.

[118] C. Moler and C. Van Loan, "Nineteen dubious ways to compute the exponential of a matrix, twenty-five years later," *SIAM review*, vol. 45, no. 1, pp. 3–49, 2003.

[119] M. Lorenzi, N. Ayache *et al.*, "Lcc-demons: a robust and accurate symmetric diffeomorphic registration algorithm," *NeuroImage*, vol. 81, pp. 470–483, 2013.

[120] L. Zhao and K. Jia, "Deep adaptive log-demons: diffeomorphic image registration with very large deformations," *Computational and Mathematical Methods in Medicine*, 2015.

[121] D. Forsberg, M. Andersson, and H. Knutsson, "Non-rigid diffeomorphic image registration of medical images using polynomial expansion," in *International Conference Image Analysis and Recognition*. Springer, 2012, pp. 304–312.

[122] J. Modersitzki, *Numerical methods for image registration*. Oxford University Press on Demand, 2004.

[123] D. Yang, H. Li, D. A. Low, J. O. Deasy, and I. El Naqa, "A fast inverse consistent deformable image registration method based on symmetric optical flow computation," *Physics in Medicine & Biology*, vol. 53, no. 21, p. 6143, 2008.

[124] P. Harjulehto, P. Hästö, M. Koskenoja, and S. Varonen, "The dirichlet energy integral and variable exponent sobolev spaces with zero boundary values," *Potential Analysis*, vol. 25, no. 3, p. 205, 2006.

[125] A. Jahanbani and H. H. Raz, "On the harmonic energy and estrada index of graphs," *MATI*, vol. 1, no. 1, pp. 1–20, 2019.

[126] P. T. Choi, K. C. Lam, and L. M. Lui, "Flash: Fast landmark aligned spherical harmonic parameterization for genus-0 closed brain surfaces," *SIAM Journal on Imaging Sciences*, vol. 8, no. 1, pp. 67–94, 2015.

[127] M. Peroni, P. Golland, G. Sharp, and G. Baroni, "Stopping criteria for log-domain diffeomorphic demons registration: an experimental survey for radiotherapy application," *Technology in cancer research & treatment*, vol. 15, no. 1, pp. 77–90, 2016.

[128] P. V. Sander, J. Snyder, S. J. Gortler, and H. Hoppe, "Texture mapping progressive meshes," in *Proceedings of the 28th annual conference on Computer graphics and interactive techniques*. ACM, 2001, pp. 409–416.

[129] R. de Flores, R. La Joie, and G. Chetelat, "Structural imaging of hippocampal subfields in healthy aging and alzheimer's disease," *Neuroscience*, vol. 309, pp. 29–50, 2015.

[130] N. C. Hindy, F. Y. Ng, and N. B. Turk-Browne, "Linking pattern completion in the hippocampus to predictive coding in visual cortex," *Nat Neurosci*, vol. 19, no. 5, pp. 665–7, 2016.

[131] H. Wang, S. R. Das *et al.*, "A learning-based wrapper method to correct systematic errors in automatic image segmentation: consistently improved performance in hippocampus, cortex and brain segmentation," *Neuroimage*, vol. 55, no. 3, pp. 968–985, 2011.

[132] P. A. Yushkevich, R. S. C. Amaral, Augustinack *et al.*, "Quantitative comparison of 21 protocols for labeling hippocampal subfields and parahippocampal subregions in vivo mri towards a harmonized segmentation protocol," *NeuroImage*, vol. 111, pp. 526–541, 2015.

[133] H. W. Lilliefors, "On the kolmogorov-smirnov test for the exponential distribution with mean unknown," *Journal of the American Statistical Association*, vol. 64, no. 325, pp. 387–389, 1969.

[134] A. Ghasemi and S. Zahediasl, "Normality tests for statistical analysis: a guide for non-statisticians," *International journal of endocrinology and metabolism*, vol. 10, no. 2, p. 486, 2012.

[135] G. E. Box and D. R. Cox, "An analysis of transformations," *Journal of the Royal Statistical Society: Series B (Methodological)*, vol. 26, no. 2, pp. 211–243, 1964.

[136] J. W. Osborne, "Improving your data transformations: Applying the box-cox transformation," *Practical Assessment, Research & Evaluation*, vol. 15, no. 12, pp. 1–9, 2010.

[137] M. K. Chung, S. Robbins, K. M. Dalton *et al.*, "Cortical thickness analysis in autism via heat kernel smoothing," *NeuroImage*, vol. 25, pp. 1256–1265, 2005.

[138] R. J. Adler and J. E. Taylor, *Random fields and geometry*. Springer Science & Business Media, 2009.

[139] A. M. Winkler, G. R. Ridgway, M. A. Webster, S. M. Smith, and T. E. Nichols, "Permutation inference for the general linear model," *Neuroimage*, vol. 92, pp. 381–397, 2014.

[140] L. Landini, V. Positano, and M. Santarelli, *Advanced image processing in magnetic resonance imaging*. CRC press, 2018.

[141] P. K. Sen and J. M. Singer, *Large sample methods in statistics: an introduction with applications*. CRC Press, 1994, vol. 25.

[142] M. K. Chung, S. M. Robbins, K. M. Dalton, R. J. Davidson, A. L. Alexander, and A. C. Evans, "Cortical thickness analysis in autism with heat kernel smoothing," *Neuroimage*, vol. 25, no. 4, pp. 1256–1265, 2005.

[143] J. Cohen, "Statistical power analysis for the behavioral sciences lawrence earlbaum associates," *Hillsdale, NJ*, pp. 20–26, 1988.

[144] S. S. Sawilowsky, "New effect size rules of thumb," *J Mod Appl Stat Methods*, vol. 8, p. 467474, 2009.

[145] S. L. Risacher, S. Kim, K. Nho, T. Foroud, L. Shen, R. C. Petersen *et al.*, "Apoe effect on alzheimer's disease biomarkers in older adults with significant memory concern," *Alzheimer's and Dementia*, vol. 11, no. 12, pp. 1417–1429, 2015.

[146] H. Braak and E. Braak, "Staging of alzheimer's disease-related neurofibrillary changes," *Neurobiology of aging*, vol. 16, no. 3, pp. 271–278, 1995.

[147] L. Xie, S. R. Das, L. E. Wisse, R. Ittyerah, P. A. Yushkevich, and D. A. Wolk, "Tau burden correlates with longitudinal structural change in regions affected by earliest neurofibrillary tangle pathology in amyloid-β-positive adni subjects," *Alzheimer's & Dementia*, vol. 13, no. 7, pp. P1373–P1374, 2017.

[148] E. Horgusluoglu, K. Nudelman, K. Nho, and A. J. Saykin, "Adult neurogenesis and neurodegenerative diseases: A systems biology perspective," *Am J Med Genet B Neuropsychiatr Genet*, vol. 174, no. 1, pp. 93–112, 2017.

[149] A. J. Saykin, L. Shen, X. Yao, S. Kim, K. Nho, S. L. Risacher *et al.*, "Genetic studies of quantitative MCI and AD phenotypes in ADNI: Progress, opportunities, and plans," *Alzheimers Dement.*, vol. 11, no. 7, pp. 792–814, 2015.

[150] L. Shen *et al.*, "Genetic analysis of quantitative phenotypes in AD and MCI: imaging, cognition and biomarkers," *Brain Imaging Behav.*, vol. 8, no. 2, pp. 183–207, 2014.

[151] S. Kim, S. Swaminathan *et al.*, "Influence of genetic variation on plasma protein levels in older adults using a multi-analyte panel," *PLoS ONE*, vol. 8, no. 7, p. e70269, 2013.

[152] S. Purcell *et al.*, "PLINK: a tool set for whole-genome association and population-based linkage analyses," *Am. J. Hum. Genet.*, vol. 81, no. 3, pp. 559–75, 2007.

[153] L. E. Wisse, H. J. Kuijf *et al.*, "Automated hippocampal subfield segmentation at 7t mri," *American Journal of Neuroradiology*, vol. 37, no. 6, pp. 1050–1057, 2016.

[154] D. Sone, E. Imabayashi *et al.*, "Regional tau deposition and subregion atrophy of medial temporal structures in early Alzheimer's disease: A combined positron emission tomography/magnetic resonance imaging study," *Alzheimer's & Dementia: Diagnosis, Assessment & Disease Monitoring*, vol. 9, pp. 35–40, 2017.

[155] J. C. Lambert *et al.*, "Meta-analysis of 74,046 individuals identifies 11 new susceptibility loci for Alzheimer's disease," *Nat. Genet.*, vol. 45, no. 12, pp. 1452–1458, 2013.

VITA

Education

2014 - 2019	Ph.D. in Electrical & Computer Engr.	Purdue Univ., West Lafayette
2012 - 2014	M.S. in Electrical & Computer Engr.	Purdue Univ., Indianapolis
2008 - 2012	B.S. in Electrical & Electronic Engr.	Harbin Univ. of S & T

Research Interests

He is currently working toward the Ph.D. degree in Electrical and Computer Engineering, Purdue University since 2014. His research interests are in the broad areas of image shape modeling, pattern recognition, image registration, and data analysis.

Peer-Reviewed Publications

1. **Cong S**, Risacher S, West J, Wu Y, Apostolova L, Tallman E, Rizkalla M, Salama P, Saykin A, Shen L. Volumetric Comparison of Hippocampal Subfields Extracted from 4-Minute Accelerated versus 8-Minute High-resolution T2-weighted 3T MRI Scans. *Brain Imaging and Behavior*. 2018;12(6): pp. 1583-1595.

2. **Cong S**, Rizkalla M, Salama P, Risacher SL, West JD, Wu YC, Apostolova L, Tallman E, Saykin AJ, Shen L. Building A Surface Atlas of Hippocampal Subfields from High Resolution T2-weighted MRI Scans Using Landmark-free Surface Registration. Circuits and Systems (MWSCAS), 2016 IEEE 59th International Midwest Symposium on 2016 Oct 16 (pp. 1-4). IEEE.

3. **Cong S**, Rizkalla M, Salama P, West J, Risacher S, Saykin A, Shen L. Surface-based Morphometric Analysis of Hippocampal Subfields in Mild Cognitive Impairment and Alzheimer's Disease. Circuits and Systems (MWSCAS), 2015 IEEE 58th International Midwest Symposium on 2015 Aug 2 (pp. 1-4). IEEE.

4. **Cong S**, Rizkalla M, Du EY, West J, Risacher S, Saykin A, Shen L. Building a Surface Atlas of Hippocampal Subfields from MRI Scans Using FreeSurfer, FIRST and SPHARM. Circuits and Systems (MWSCAS), 2014 IEEE 57th International Midwest Symposium on 2014 Aug 3 (pp. 813-816). IEEE.

5. Yao X, **Cong S**, Yan J, Risacher SL, Saykin AJ, Moore J, Shen L. Mining Regional Imaging Genetic Associations via Voxel-wise Enrichment Analysis. IEEE-EMBS International Conference on Biomedical and Health Informatics (BHI19). 2019, accepted.

6. Inlow M, **Cong S**, Risacher SL, West J, Rizkalla M, Salama P, Saykin AJ, Shen L. A New Statistical Image Analysis Approach and Its Application to Hippocampal Morphometry. InInternational Conference on Medical Imaging and Virtual Reality 2016 Aug 24 (pp. 302-310). Springer International Publishing.

7. Mussabayeva A, Kroshnin A, Kurmukov A, Denisova Y, Shen L, **Cong S**, Wang L, Gutman B. Image Registration and Predictive Modeling: Learning the Metric on the Space of Diffeomorphisms. International Workshop on Shape in Medical Imaging 2018 Aug 24 (pp. 160–168). Springer International Publishing.

8. Petrov D, Gutman B, and et int. and **Cong S**, and others. Machine Learning for Large-Scale Quality Control of 3D Shape Models in Neuroimaging. International Workshop on Machine Learning in Medical Imaging 2017 (pp. 371–378). Springer International Publishing.

Book Chapter

Shen L, **Cong S**, Inlow M. Statistical Shape Analysis for Brain Structures. Statistical Shape and Deformation Analysis: Methods, Implementation and Applications. 2017 Mar 23:351.

Conference Abstracts

1. **Cong S**, Yao X., Risacher SL., Nho K., Saykin AJ., Shen L.. GWAS of Hippocampal Subfield and Neighboring Cortical Structure Volumes Identifies an *ERC1* Locus

Using ADNI High-Resolution MRI Data. *Alzheimer's & Dementia: The Journal of the Alzheimer's Association*. 2019 accepted. Travel fellowship awarded.

2. **Cong S**, Risacher SL, West JD, Wu YC, Apostolova LG, Tallman EF, Rizkalla M, Salama P, Saykin AJ, Shen L. Volumetric Comparison of Automatically Segmented Hippocampal Subfields from 4-Min Accelerated versus. 8-Min T2-weighted 3T-MRI Scans. Alzheimer's & Dementia: The Journal of the Alzheimer's Association. 2016 Jul 1;12(7):P1167.

3. **Cong S**, Rizkalla M, Yan J, West J, Kim S, Risacher S, Saykin A, Shen L. Reproducibility of Hippocampal Subfield Segmentation using FreeSurfer and FIRST. 2014 IEEE International Symposium on Biomedical Imaging.